

Full Tokamak Discharge Simulation and Kinetic Plasma Profile Control for ITER

THÈSE N° 4500 (2009)

PRÉSENTÉE LE 9 OCTOBRE 2009
À LA FACULTÉ SCIENCES DE BASE
CRPP ASSOCIATION EURATOM
PROGRAMME DOCTORAL EN PHYSIQUE

ÉCOLE POLYTECHNIQUE FÉDÉRALE DE LAUSANNE

POUR L'OBTENTION DU GRADE DE DOCTEUR ÈS SCIENCES

PAR

Sun HEE KIM

acceptée sur proposition du jury:

Prof. O. Schneider, président du jury
Dr J. B. Lister, directeur de thèse
Dr T. Casper, rapporteur
Dr T. Hoang, rapporteur
Prof. L. Villard, rapporteur



ÉCOLE POLYTECHNIQUE
FÉDÉRALE DE LAUSANNE

Suisse
2009

La compréhension du couplage non-linéaire des phénomènes physiques engendrés par le transport du plasma et ceux liés à l'évolution à frontière non-prescrite de l'équilibre est essentielle dans l'optique de faire fonctionner de futurs tokamaks tels qu'ITER et DEMO dans les régimes d'opération avancés. Afin d'étudier ce couplage non-linéaire, nous nécessitons un outil de simulation capable de calculer d'une manière cohérente tous les phénomènes physiques principaux ayant lieu dans le plasma, tout en tenant compte des contraintes opérationnelles. La partie principale de ce travail de thèse a été dédiée au développement d'un simulateur de décharges tokamak qui réalise ces simulations de manière complète. Un tel simulateur a été réalisé en combinant un code à évolution non-linéaire et à frontière non-prescrite de l'équilibre, DINA-CH, à un code avancé décrivant le transport du plasma, CRONOS. Ce simulateur de décharges tokamak a été utilisé afin de vérifier la faisabilité de l'implémentation de différents scénarii d'opération d'ITER, ainsi que différentes autres questions spécifiques liées au fonctionnement d'ITER. En parallèle, DINA-CH a été utilisé pour l'étude des problèmes de physique des plasmas à frontière non-prescrite, tels que le déclenchement magnétique des modes localisés au bord du plasma (Edge Localized Modes, ELMs) et la réponse dynamique du plasma à des perturbations. Un autre obstacle majeur qu'ITER doit affronter est celui du contrôle actif des profils cinétiques du plasma. Ce problème a lui aussi été étudié.

Dans la partie de ce travail dédiée à la simulation de décharges tokamak à frontière non-prescrite, nous avons étudié la réponse dynamique de l'équilibre à frontière non-prescrite du plasma à des perturbations des tensions externes ainsi qu'à des perturbations internes au sein du plasma. Ce travail a été réalisé en utilisant DINA-CH. Tout d'abord, le comportement opposé observé entre TCV et ASDEX Upgrade lors du déclenchement magnétique des ELMs est examiné. Les deux plasmas observent des expansions des flux de surface locaux près de la bobine-G supérieure et de la boucle de stabilisation passive (Passive Stabilisation Loop, PSL) lorsque les ELMs sont déclenchés, de par la présence des PSLs situées à l'intérieur de la chambre à vide d'ASDEX Upgrade. Puis, nous étudions la réponse dynamique du plasma aux fortes perturbations envisagée lors de l'opération d'ITER, afin d'examiner la capacité du système de contrôle à rejeter ces perturbations. Des ELMs spécifiées et non contrôlées sont contrôlables par les systèmes de contrôle. Toutefois, les spécifications pour les transitions rapides entre les modes H et L ne sont pas complètement réalisables de par la présence d'un

évènement de déplacement vertical (Vertical Displacement Event, VDE) causé par un fort mouvement du plasma vers l'intérieur.

Dans la partie de ce travail dédiée à la simulation de manière complète de décharges tokamak, nous avons introduit tout d'abord le simulateur de décharges tokamak complètes DINA-CH/CRONOS. DINA-CH calcule l'évolution non-linéaire du plasma à frontière non-prescrite de manière consistante avec la diffusion du courant du plasma, répondant aux courants contrôlés au sein bobines poloïdales (Poloidal Fields coils, PF) et aux courants induits dans les systèmes conducteurs environnants. CRONOS fournit l'évolution des profils du plasma en résolvant le transport de chaleur et de particules de manière consistante avec les profils des sources. Nous avons simulé avec succès le scénario d'opération d'ITER 2, démontrant ainsi les possibilités d'un tel simulateur combiné. Cette étude a par la même occasion un intérêt d'un point de vue du design. Le ratio de puissance de fusion sur la puissance totale auxiliaire, Q , est d'environ 10 avec une puissance auxiliaire appliquée de 53 MW répartie en chauffage auxiliaire et conduite du courant (Heating and Current Drive, H&CD). Nous avons examiné plusieurs problèmes spécifiques liés à l'opération du tokamak, tels que l'instabilité verticale, les limites de courant des bobines PF, et la consommation en flux poloïdaux lors de la phase d'augmentation du courant plasma. L'application de puissance sous forme d'ondes hybrides inférieures (Lower Hybrid, LH) à partir de la phase initiale de l'augmentation du courant plasma a augmenté les marges de sécurité lors de l'opération des bobines PF superconductrices en réduisant la consommation résistive du flux ohmique ainsi qu'en conduisant le courant plasma de manière non-inductive. Finalement, nous avons étudié le mode d'opération hybride d'ITER en nous concentrant sur la capacité opérationnelle d'obtenir un facteur de sécurité (q) stationnaire et plat au début de la phase flat-top (Start Of Flat-top, SOF), en le maintenant aussi longtemps que possible par la combinaison de différentes source de conduction du courant plasma non-inductive. L'application d'une conduction de courant plasma par electron-cyclotron (Electron Cyclotron Current Drive, ECCD) légèrement désaxée semble être efficace en comparaison à la conduction de courant lointaine et désaxée par LH, du moins sur des échelles de temps courtes.

Dans la partie de ce travail dédiée au contrôle actif des profil du plasma, nous avons développé une technique de contrôle robuste qui simplifie le contrôle actif en temps réel de plusieurs profils cinétiques du plasma dans ITER. La réponse des profils du plasma au modifications de la puissance auxiliaire des systèmes H&CD est modélisée. Afin de permettre la mise à jour en temps réel de la modélisation de la réponse des profils du plasma, la

description physique du système est simplifiée par l'introduction de plusieurs hypothèses. La réponse du profil de température électronique est modélisée en simplifiant l'équation de transport de la chaleur électronique. La réponse du profil du facteur de sécurité q est modélisée en la mettant en relation directe avec les modifications du profil de la source de densité de courant. Les modifications requises de la puissance des actuateurs sont calculées en utilisant la technique de décomposition en valeurs singulières (Singular Value Decomposition, SVD), et en tenant compte de la saturation de la puissance des actuateurs. Les possibilités de cette technique de contrôle sont montrées en les appliquant à des simulations d'ITER en mode d'opération hybride.

Mots-clés: Tokamak, ITER, non-linéaire, frontière non-prescrite, simulateur de décharges tokamak complètes, régime d'opération de tokamak avancé, contrôle actif des profils plasma

Abstract

Understanding non-linearly coupled physics between plasma transport and free-boundary equilibrium evolution is essential to operating future tokamak devices, such as ITER and DEMO, in the advanced tokamak operation regimes. To study the non-linearly coupled physics, we need a simulation tool which can self-consistently calculate all the main plasma physics, taking the operational constraints into account. As the main part of this thesis work, we have developed a full tokamak discharge simulator by combining a non-linear free-boundary plasma equilibrium evolution code, DINA-CH, and an advanced transport modelling code, CRONOS. This tokamak discharge simulator has been used to study the feasibility of ITER operation scenarios and several specific issues related to ITER operation. In parallel, DINA-CH has been used to study free-boundary physics questions, such as the magnetic triggering of edge localized modes (ELMs) and plasma dynamic response to disturbances. One of the very challenging tasks in ITER, the active control of kinetic plasma profiles, has also been studied.

In the part devoted to free-boundary tokamak discharge simulations, we have studied dynamic responses of the free-boundary plasma equilibrium to either external voltage perturbations or internal plasma disturbances using DINA-CH. Firstly, the opposite plasma behaviour observed in the magnetic triggering of ELMs between TCV and ASDEX Upgrade has been investigated. Both plasmas experience similar local flux surface expansions near the upper G-coil set and passive stabilization loop (PSL) when the ELMs are triggered, due to the presence of the PSLs located inside the vacuum vessel of ASDEX Upgrade. Secondly, plasma dynamic responses to strong disturbances anticipated in ITER are examined to study the capability of the feedback control system in rejecting the disturbances. Specified uncontrolled ELMs were controllable with the feedback control systems. However, the specifications for fast H-L mode transitions were not fully achievable due to a vertical displacement event (VDE) caused by a strong inward plasma movement.

In the part dedicated to full tokamak discharge simulations, firstly, we have introduced the combined DINA-CH/CRONOS tokamak discharge simulator. DINA-CH self-consistently calculates the non-linear evolution of the free-boundary plasma equilibrium with the plasma current diffusion, in response to both controlled poloidal field (PF) coil currents and inductively driven currents in the surrounding conducting system. CRONOS provides the evolution of the plasma profiles by self-consistently solving heat and particle transport with

source profiles. Secondly, we have successfully simulated ITER operation scenario 2 as a demonstration of the capabilities of the combined simulator, as well as being a design study in itself. The fusion power ratio to the total auxiliary power Q was about 10 with the application of 53MW of auxiliary heating and current drive (H&CD) power. We have investigated several specific issues related to the tokamak operation, such as the vertical instability, PF coil current limits and poloidal flux consumption during the current ramp-up. Lower hybrid (LH) applied from the initial phase of the plasma current ramp-up increased the safety margins in operating the superconducting PF coils both by reducing resistive ohmic flux consumption and by providing non-inductively driven plasma current. Lastly, we have studied ITER hybrid mode operation, focusing on the operational capability of obtaining a stationary flat safety factor (q) profile at the start of flat-top (SOF) phase and sustaining it as long as possible by combining various non-inductively driven current sources. Application of a near on-axis electron cyclotron current drive (ECCD) appears to be effective compared to the far off-axis lower hybrid current drive (LHCD), at least on short time scales.

In the active plasma profile control part, we have developed a robust control technique that simplifies the active real-time control of several kinetic plasma profiles in ITER. The response of the plasma profiles to power changes of auxiliary H&CD systems is modelled. To allow real-time update of the plasma profile response model, the related physics are simplified with several assumptions. The electron temperature profile response is modelled by simplifying the electron heat transport equation. The q profile response is modelled by directly relating it to the changes of source current density profiles. The required actuator power changes are calculated using the singular value decomposition (SVD) technique, taking the saturation of the actuator powers into account. The potential of this control technique has been shown by applying it to simulations of the ITER hybrid mode operation.

Keywords: Tokamak, ITER, non-linear, free-boundary, full tokamak discharge simulator, advanced tokamak operation regime, active plasma profile control

Contents

1	Introduction	1
1.1	Nuclear fusion and tokamak	1
1.2	Motivation	5
1.2.1	Free-boundary tokamak discharge simulation	6
1.2.2	Full tokamak discharge simulation	7
1.2.3	Kinetic plasma profile control	8
1.3	Outline	9
I	Free-boundary tokamak discharge simulations	13
2	Comparing magnetic triggering of ELMs in TCV and ASDEX Upgrade	15
2.1	Introduction	15
2.2	Simulating the magnetic triggering of ELMs	18
2.2.1	Scope of the simulations	18
2.2.2	Magnetic triggering of ELMs in TCV	18
2.2.3	Magnetic triggering of ELMs in ASDEX Upgrade	22
2.3	Comparing the two cases of magnetic triggering of ELMs	24
2.3.1	Perturbed plasma current density in the edge region	25
2.3.2	Perturbed local plasma pressure gradient in the edge region	26
2.3.3	Flux surface deformation and its pattern in the edge region	28
2.4	Magnetic perturbation with radial plasma movements in ASDEX Upgrade	31
2.5	Discussion	33
3	Plasma dynamic response to disturbances	37
3.1	Introduction	37

3.2	Pre-programming appropriate plasma disturbances	38
3.2.1	Uncontrolled ELMs	39
3.2.2	Fast H-L mode transitions	40
3.2.3	Transport simulation with frozen heat conductivity profiles	41
3.3	Dynamic plasma responses	42
3.3.1	First trial simulations and a bug	44
3.3.2	Uncontrolled ELMs	46
3.3.3	Fast H-L mode transition	47
3.4	Discussion	53
II	Full tokamak discharge simulations	57
4	Full tokamak discharge simulator	59
4.1	Plasma equilibrium	59
4.1.1	Non-linear Grad-Shafranov equation	60
4.1.2	Free-boundary plasma equilibrium	62
4.2	Plasma transport	62
4.2.1	Magnetic flux surface averaging technique	62
4.2.2	Magnetic field diffusion	63
4.2.3	Particle transport	66
4.2.4	Electron heat transport	67
4.2.5	Ion heat transport	68
4.3	Plasma transport evolution scheme in CRONOS	69
4.4	Free-boundary plasma equilibrium evolution scheme in DINA-CH	71
4.4.1	Circuit equations	71
4.4.2	Free-boundary plasma equilibrium evolution algorithm	73
4.5	Combined tokamak discharge simulator	74
4.5.1	Code coupling scheme	74
4.5.2	Challenges met during the code coupling	76
5	Full tokamak discharge simulation of ITER scenario 2	81
5.1	Introduction	81
5.2	Setting up the simulation of ITER operation scenario 2	82
5.3	Full tokamak discharge simulation results	86

5.4	Issues related to the ITER tokamak operation	88
5.4.1	Avoiding the PF coil current limit	89
5.4.2	Vertical stability with high l_i	92
5.4.3	Reducing the poloidal flux consumption	94
5.5	Summary and Discussion	96
6	Lower Hybrid assisted plasma current ramp-up in ITER	99
6.1	Introduction	99
6.2	Modelling the plasma current ramp-up	100
6.3	Lower Hybrid assisted plasma current ramp-up	102
6.4	Free-boundary plasma evolution	107
6.5	Conclusions	109
7	ITER hybrid mode operation	111
7.1	Introduction	111
7.2	Modelling the plasma current ramp-up	112
7.3	Achieved plasma parameters	116
7.4	q profile evolution	119
7.5	Coil current limits	119
7.6	Summary and discussion	122
III	Active control of the kinetic plasma profiles	123
8	Simplifying plasma profile control in ITER	125
8.1	Introduction	125
8.2	Plasma profile response models	126
8.2.1	Incremental electron temperature profile response model	127
8.2.2	Incremental q profile response model	129
8.2.3	Simultaneous control of the electron temperature and q profiles	132
8.3	Plasma profile responses in ITER hybrid mode operation	134
8.3.1	Plasma profile responses to additional H&CD power	135
8.3.2	Application of both ECH&CD and LHH&CD	138
8.4	Active control of kinetic plasma profiles	139
8.4.1	Controlling the electron temperature profile	139

8.4.2	Controlling the q profile	142
8.4.3	Simultaneous control of the electron temperature and q profiles . . .	143
8.5	Summary and Discussion	145
9	Conclusions	149
9.1	Summary	149
9.2	Perspective	153
A	Details in deriving the theoretical formulations	155
A.1	Non-linear Grad-Shafranov equation	155
A.1.1	DINA-CH : CGS units	155
A.1.2	CRONOS : MKS units	157
A.2	Flux surface average properties	158
A.3	The magnetic field diffusion equation	159
A.3.1	Derivation of $\langle \mathbf{j} \cdot \mathbf{B} \rangle$ and $\langle \mathbf{E} \cdot \mathbf{B} \rangle$	159
A.3.2	DINA-CH : CGS units	162
A.3.3	CRONOS : MKS units	163
A.4	Plasma current	164
A.4.1	Standard : MKS units	164
A.4.2	DINA-CH : CGS units	164
A.5	Electron heat transport equation	165
A.6	Ion heat transport equation	166
A.7	Plasma transport evolution scheme in CRONOS	167

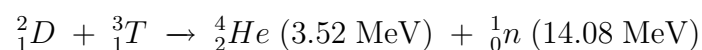
Chapter 1

Introduction

1.1 Nuclear fusion and tokamak

The goal of nuclear fusion is to produce reliable electricity by building a commercial power plant which is environmentally safe and cost-effective. Recent research activities are mainly focused on demonstrating the feasibility of such a future commercial power plant by studying either the tokamak [1] or the stellarator [2]. Among the future research activities, the International Thermonuclear Experimental Reactor (ITER) [3] is seen as one of the most plausible approach to DEMO (DEMONstration power plant). Its construction has already been initiated by means of an international collaboration. It is foreseen to be the world largest tokamak facility in near future.

ITER is a device based on the concept of magnetic confinement fusion, ‘tokamak’. In this concept, the fuel, a mixture of deuterium (D) and tritium (T), is ionized and constitutes a plasma with fast ions and electrons. These ionized particles follow spiral orbits around helical magnetic field lines generated by the external toroidal field (TF) coil currents and the toroidal plasma current. Application of a strong plasma heating accelerates the positively charged ions and enables them to overcome the repelling force between them, which is very strong at close distance. The fast ions then fuse releasing about 17.6MeV of energy, as well as producing fusion products such as helium (He) and neutrons. This reaction is given by



The neutrons carrying 80% of the released energy leave the plasma without interaction and generate the electricity by converting their kinetic energy into the heat. The ionized alpha particles stay in the plasma and transfer 20% of the released energy to the plasma through collisions. This process is called ‘alpha particle self-heating’. If the alpha particle self-heating power (P_α) is greater than the total energy loss from the plasma, the plasma is self-heated without requiring any external plasma heating. This is called ‘ignition’.

The ignition condition is generally given by

$$n T \tau_E > 5 \times 10^{21} \text{ m}^{-3} \text{ keV s} \quad (1.1)$$

where n and T are the peak values of ion density and temperature, τ_E is the energy confinement time. Present-day tokamak devices have not yet reached this condition and therefore need additional external plasma heating systems to sustain their operation. ITER will be the first device which studies this capability with various tokamak operation scenarios and test blanket modules. A measure of the success in approaching the reactor conditions is given by the fusion power (P_{fusion}) ratio to the applied additional heating power (P_{add}), Q , given by

$$Q = \frac{P_{fusion}}{P_{add}} = \frac{5P_\alpha}{P_{add}} \quad (1.2)$$

If the plasma ignites, Q approaches infinity. In ITER, this value is about 10 for the inductive 15MA baseline operation.

Besides heating the plasma, generating a toroidal plasma current which produces the poloidal magnetic field is indispensable in the tokamak concept. This toroidal plasma current is closely linked to the plasma confinement, transport and instabilities.

The variation of currents in the poloidal field (PF) coils drives the plasma current through the magnetic induction and heats the plasma by Joule effect. The central solenoid (CS) coils, which are located on the inboard side of the torus, mainly induce a toroidal electric field which drives the plasma current. This plasma current generates poloidal magnetic fields and the TF coil currents generate toroidal magnetic fields. These magnetic fields finally create a nested helical magnetic field structure improving the plasma confinement. However, the use of magnetic induction in driving the plasma current makes the tokamak operation unavoidably pulsed. Once the volt-seconds provided by the PF coil system are fully consumed, the tokamak discharge should be terminated to recharge the power supplies.

In order to elongate this pulse duration and possibly to operate a tokamak in steady-state, we need an additional method which can provide non-inductively driven currents. The inductive component of the plasma current can be completely replaced by a combination of several non-inductive external current sources [4] and self-generated bootstrap current [5]. We also need external plasma heating sources since the efficiency of ohmic heating quickly decreases as the plasma approaches the ignition condition. The plasma conductivity becomes very high as the electron temperature increases ($\sim T_e^{\frac{3}{2}}$).

In ITER, various auxiliary heating and current drive (H&CD) systems will provide plasma heating sources and non-inductively driven currents [6]. Neutral beam injection (NBI) heats the plasma and provides non-inductively driven current by transferring the energy and momentum of the injected beams of neutral particles to the plasma. 33MW of NBI with 1MeV of the beam energy will be used in ITER [6]. Electromagnetic waves can also heat the plasma and provide non-inductively driven currents in various schemes. Ion and electron cyclotron (IC and EC) waves transfer the injected power to the plasma species, ions and electrons respectively, at their resonance frequencies. In these schemes, the current can be driven by the asymmetry in the velocity distribution function of the heated particles. Lower hybrid (LH) waves can transfer the injected power and momentum to the electrons at a frequency between IC and EC resonance frequencies, therefore providing plasma heat sources and non-inductively driven currents. IC resonance heating (ICH)/fast wave current drive (FWCD), EC resonance heating and current drive (ECH&ECCD), LH resonance heating and current drive (LHH&LHCD) will be used in ITER. 20MW is specified as the baseline power for each wave H&CD system, while upgrading these powers for the advanced tokamak operations is being taken into consideration.

In order to achieve controlled fusion in a tokamak, the plasma heating sources and inductively/non-inductively driven currents have to be adequately provided together with a tokamak operation scenario. The plasma heating, which is indispensable for both initiating the plasma burn and approaching the ignition condition, is closely linked to many physics issues, such as the plasma confinement, transport and instabilities, as well as to several specific issues, such as the confinement mode transition, build-up of bootstrap current, consumption of the poloidal flux provided by the PF coil system and heat loads to the wall and divertor plates. Application of inductive/non-inductive current sources is also closely linked to many physics and tokamak operation issues, such as the anomalous plasma transport, improved plasma confinement regimes and onset of MHD instabilities. These

critical issues can be studied by tailoring the plasma current density profile using various inductive/non-inductive current sources. Active control of kinetic plasma profiles, such as the plasma pressure and current profiles, will be essential to achieving the steady-state operation in future tokamaks.

Besides the kinetic plasma profiles, dynamic response of the plasma has to be adequately controlled throughout a tokamak discharge [7, 8, 9]. The PF coil system not only generates the plasma current, but also provides the control of the plasma position and shape. The vertical instability of elongated plasmas, which might lead the plasma to a disruptive vertical displacement event (VDE) [10], can be handled by a plasma position control system. The controllability of the control system is generally enhanced by placing the toroidally conducting structures close to the plasma. Eddy currents flowing in the toroidally conducting structures effectively slow down the fast vertical plasma movements so that the feedback control system can control the plasma position. The plasma shape control system guides the desired evolution of the plasma boundary by controlling several gaps between the plasma boundary and wall. Various magnetic diagnostic measurements provide information on the plasma parameters to be controlled.

Finally, tokamak operation scenarios have to be designed including all the engineering constraints and operational limits. The coil current and voltage limits, electromagnetic forces on the coils and vacuum vessels, thermal heat loads on the wall and divertors, maximum available poloidal flux provided by the coil systems, and density and beta limits have to be taken into account. These constraints and limits add additional non-linearities to the plasma evolution which is intrinsically non-linear. Therefore, all the knowledge on the main plasma physics, techniques and know-how from the past researches should be assembled for successful operation of ITER.

In order to study the burning plasma physics and the feasibility of reactor relevant tokamak operation in ITER, several operation scenarios [3] are proposed considering all the main physics and engineering aspects.

The baseline operation scenario of ITER is a high confinement mode (H-mode) operation in which the plasma experiences repetitive onsets of the edge localized modes (ELMs) [11]. This type of ELMy H-mode is routinely achieved in many present tokamaks as one of the improved plasma confinement modes. In this scenario, the plasma current is inductively

ramped up to 15MA and the current flat-top is maintained for about 400s producing a significant amount of fusion power ($Q = 10$). H-mode physics, such as the H-mode pedestal in the plasma edge [12], plasma confinement mode transitions [13], sawtooth crashes [14] and ELMs, and burning plasma physics, such as the energetic particle physics and alpha particle self-heating [15, 16, 17], are main research subjects.

A hybrid mode operation is proposed to extend the discharge pulse duration over 1000s with $Q = 5$. In this scenario, the plasma is operated at a lower plasma current compared with the inductive 15MA ELMy H-mode operation, to provide the poloidal flux for a long time. A significant fraction of the plasma current is substituted by non-inductively driven currents and self-generated bootstrap current. An improved confinement regime can be achieved by tailoring the plasma current during the plasma current ramp-up phase in such a way of avoiding undesirable MHD instabilities. Achieving a stationary flat safety factor (q) profile at the beginning of the flat-top phase and sustaining it for a long time is the key element in this operation.

A steady-state operation is possible in ITER by fully substituting the inductive component of the plasma current with non-inductively driven currents and self-generated bootstrap current. In this operation, internal transport barriers (ITBs) [18, 19, 20] are generally observed with the reduction of micro-turbulent instabilities in a reversed q profile configuration. Several MHD instabilities, such as the neoclassical tearing modes (NTMs) [21] and resistive wall modes (RWMs) [22] should be avoided. This operation will require a robust method which can maintain ITBs by actively controlling both the plasma pressure and current profiles.

1.2 Motivation

This thesis work is divided into 3 parts. In the first part, we study two free-boundary physics questions which require a non-linear free-boundary plasma equilibrium evolution code, such as DINA-CH [23, 24]. In the second part, we couple DINA-CH with an advanced transport modelling code, CRONOS [25], in order to achieve an extended capability of performing full tokamak discharge simulations. In the last part, we develop a robust control technique that simplifies the active control of plasma profiles in ITER.

1.2.1 Free-boundary tokamak discharge simulation

Studying plasma dynamic response to internal and/or external disturbances requires a non-linear free-boundary plasma equilibrium evolution code, such as DINA-CH.

Magnetic triggering of ELMs was first demonstrated in TCV experiments [26] by injecting a pre-programmed voltage perturbations on PF coils. The voltage perturbation injected on the G-coil sets located inside the vacuum vessel for the active control of the vertical instability induced vertical plasma movements delaying and/or triggering ELMs. This technique was repeated in ASDEX Upgrade experiments [27], in which the plasma was forced to move vertically following an imposed reference waveform. Both experiments were successful in triggering ELMs and controlling the ELM frequency. However, the ELMs were triggered in ASDEX Upgrade when the plasma was moving down towards the X-point with a consequent decrease of the plasma current density in the edge region, contrary to the previous observation on TCV in which ELMs were triggered when the edge current was increased by an upward plasma movement. In order to investigate this opposite behaviour, we need to study free-boundary features which have previously received little attention, such as the plasma shape deformation. We also have to examine the spatial pressure and current gradients, edge current density (averaged and local), plasma column size and its position, in order not to erroneously exclude any possible mechanism. Recently, the magnetic triggering of ELMs has been repeated in JET experiments [61].

Strong plasma disturbances anticipated in ITER, such as uncontrolled ELMs and fast H-L mode transitions, force the plasma to release its stored energy and particles on plasma facing components, and result in strong fluctuations of plasma properties such as the plasma current, position, shape, internal inductance ($l_i(3) = 2 \int B_p^2 dV / \mu_0^2 I_p^2 R$ is referred to as l_i) and poloidal plasma beta ($\beta_p = (\int p dS / \int dS) / (B_p^2 / 2\mu_0)$). If the magnitude of these plasma disturbances is beyond the capability of the feedback control systems, the plasma inevitably experiences a disruptive VDE. Specifications of the plasma disturbances in ITER have been recently updated to cover a wider range of disturbances observed in present tokamak experiments [28]. Therefore, the capability of the feedback control systems in rejecting the plasma perturbations has to be re-examined. In this thesis work, we will study non-linear dynamic responses of the free-boundary plasma equilibrium to the uncontrolled ELMs and fast H-L mode transitions using DINA-CH.

1.2.2 Full tokamak discharge simulation

Studying the feasibility of the ITER operation scenarios and non-linearly coupled physics issues requires a tool which can self-consistently calculate all the main physics, taking the operational limits and engineering constraints into account. This tool is called ‘full tokamak discharge simulator’. However, there was a little interest in developing this type of simulator in the past, since huge time and effort are required to integrate all the main physics using adequate numerical schemes and to include a model of entire tokamak system. A few number of full tokamak discharge simulators have been developed. TSC and PTRANSP have been combined to form a full tokamak discharge simulator, TSC/PTRANPS [29, 30]. CORSICA [31, 32, 33] is developed with a capability of coupling core and edge transport. These two codes use different assumptions in modelling the evolution of the free-boundary plasma equilibrium. TSC/PTRANSP gives the plasma a finite mass and solves the acceleration of the plasma in the presence of a net force on the plasma, while CORSICA give the plasma a zero mass to instantly move to a new free-boundary equilibrium, similarly with DINA-CH.

As the main part of this thesis work, we develop a new full tokamak discharge simulator by combining the free-boundary plasma equilibrium evolution code, DINA-CH, and an advanced transport modelling code, CRONOS. Both codes has previously shown good accuracy and performance in solving the coupled physics in each research area. DINA-CH has been mainly used to study the non-linear dynamic response of the plasma to disturbances, as well as to investigate several plasma control issues [34, 35, 36]. CRONOS has been used for interpretative or predictive plasma transport simulations and source profile calculation [37, 38, 39].

This combined simulator can self-consistently calculate the non-linear evolution of the free-boundary plasma equilibrium with the plasma transport and source profiles, in response to currents flowing in the PF coil and surrounding conducting systems. The operational constraints can be used as inputs to the control system which follows a given reference operation scenario. This full tokamak discharge simulator therefore allows us to study a vast number of physics and control issues anticipated in operating ITER. Optimizing the plasma current ramp-up and ramp-down scenarios, achieving improved plasma confinement modes, producing an internal transport barrier and sustaining it with an active control of the plasma profiles, would be typical physics interests. Rejecting possible plasma disturbances with the control system and avoiding dangerous disruptive plasma conditions will be critical control

issues for successful tokamak operation.

In this thesis work, we will study the feasibility of ITER operation scenarios and several issues related to the tokamak operation using the extended capability of the combined tokamak discharge simulator. Our experience acquired while developing the combined tokamak discharge simulator and simulating ITER tokamak discharges can give insight and guidance to a recently initiated activity of developing a new tokamak discharge simulator, European Integrated Tokamak Modelling (EU-ITM) [40].

1.2.3 Kinetic plasma profile control

Controlling the kinetic plasma profiles is one of the very challenging issues for the success of controlled nuclear fusion. The steady-state and hybrid mode operations in ITER require an active real-time control of kinetic plasma profiles to achieve the advanced tokamak regimes for sustained operation. Experiments on this active plasma profile control have been conducted on several devices, including JET [41, 42], Tore-Supra [43, 44] and DIII-D [45, 46]. A model-based technique for integrated real-time kinetic plasma profile control, which appears to be the most promising technique, has been developed and demonstrated in JET experiments and simulations [47, 48, 49, 50]. In this technique, the response model of the plasma profiles to power changes of auxiliary H&CD systems is deduced from identification experiments and is then used to control the plasma profiles. However, the range of applicability of this experimentally deduced plasma profile response model is still in question. This model might be not valid if the plasma state varies away from the reference state achieved in the identification experiments. Real-time update of the plasma profile response model would be the most plausible approach to resolving this difficulty. This is possible either by selecting an adequate plasma profile response model from an existing database or by identifying one in real-time.

In this thesis work, we develop a robust control technique that simplifies the active control of plasma profiles in ITER. We propose fast incremental plasma profile response models developed by simplifying the related physics. The potential of this control technique will be shown by applying it to simulations of the ITER hybrid mode operation.

1.3 Outline

Part I: Free-boundary tokamak discharge simulations

In this first part, free-boundary tokamak discharge simulations performed using DINA-CH are presented. These simulations show the capability of a non-linear free-boundary plasma equilibrium evolution code in studying the free-boundary physics issues.

In chapter 2, magnetic triggering of ELMs in TCV and ASDEX Upgrade is investigated to get a possible explanation for the observed opposite plasma behaviour between the two experiments. Free-boundary plasma equilibrium responses to the external voltage perturbations are compared and kink-ballooning mode stability at the plasma edge is investigated. All the possible candidates which can explain the observed opposite behaviour are investigated not to erroneously attribute causality in the presence of all correlated plasma responses. The results of this work have been published as a journal article:

Kim S H, Cavinato M M, Dokuka V, Ivanov A A, Khayrutdinov R R, Lang P T, Lister J B, Lukash V E, Martin Y R, Medvedev S Yu and Villard L Comparing magnetic triggering of ELMs in TCV and ASDEX Upgrade 2009 *Plasma Phys. Control. Fusion* **51** 055021

In chapter 3, plasma dynamic responses to disturbances anticipated in ITER are examined. Giant ELMs and fast H-L mode transitions specified for the inductive 15MA ELMy H-mode ITER operation are pre-programmed and the plasma responses are investigated focusing on the capability of the feedback control system in rejecting the disturbances. The results of this work have been published as a project report:

Kim S H, Artaud J-F, Basiuk V, Dokuka V, Khayrutdinov R R, Lister J B and Lukash V E Plasma position and shape control for ITER scenarios 2008 *Contract TW6-TPO-PLASMADYN2*

Part II: Full tokamak discharge simulations

In this second part, theoretical and technical details of the combined tokamak discharge simulator are first introduced and its applications to ITER discharges are presented. We have also investigated several issues related to the tokamak operation.

In chapter 4, firstly, theoretical formulations of the plasma equilibrium and transport used in the two codes are introduced and directly compared. Secondly, numerical algorithms used for the free-boundary plasma equilibrium evolution in DINA-CH and for the coupled particle and heat transport in CRONOS are explained. Finally, code coupling scheme used to combine the two codes and several challenges met during developing the combined tokamak discharge simulator are presented.

In chapter 5, the feasibility of the inductive 15MA ELMy H-mode ITER operation scenario is studied. All the tokamak operation phases including the plasma current ramp-up, flat-top and ramp-down phases are successfully simulated. Many issues related to the plasma physics and tokamak operation, such as the coil current limits, vertical instability, poloidal flux consumption, confinement mode transition, application of H&CD power, free-boundary plasma evolution and plasma control, are investigated to achieve a full tokamak discharge simulation with the ITER operation scenario.

In chapter 6, LH assisted plasma current ramp-up is studied to investigate the capability of effectively reducing the poloidal flux consumption and lowering l_i . An application of LH starting from the early phase of the plasma current ramp-up is very effective for both. However, the plasma boundary evolution and shape transition are modified due to this early LH application. As a possible solution of recovering the desired plasma shape evolution, modifying the evolution of the PF coil currents is tested. The results of this work have been published as a journal article:

Kim S H, Artaud J F, Basiuk V, Bécoulet A, Dokuka V, Hoang G T, Imbeaux F, Khayrutdinov R R, Lister J B and Lukash V E Lower hybrid assisted plasma current ramp-up in ITER 2009 *Plasma Phys. Control. Fusion* **51** 065020

In chapter 7, 12MA hybrid mode ITER operation is simulated including the plasma current ramp-up and flat-top phases. The range of the plasma parameter achievable in the hybrid mode operation is examined with different assumptions on the pedestal, heat conductivity and plasma confinement. The capability of achieving a stationary flat q profile at the beginning of the flat-top phase and sustaining it as long as possible by combining several H&CD schemes is investigated.

An article presenting the combined tokamak discharge simulator (chapter 4), 15MA ITER

ELMy H-mode simulation results (chapter 5) and 12MA ITER hybrid mode simulation results (chapter 7) has been submitted to a journal:

Kim S H, Artaud J F, Basiuk V, Dokuka V, Khayrutdinov R R, Lister J B and Lukash V E Full tokamak discharge simulation of ITER by combining DINA-CH and CRONOS 2009 submitted to *Plasma Phys. and Control. Fusion*

Part III: Active control of the kinetic plasma profiles

In chapter 8, active control of kinetic plasma profiles in ITER is studied. A robust control technique allowing the real-time active plasma profile control in ITER is developed. The plasma profile response models developed by simplifying the related physics are applied to simulations of the 12MA ITER hybrid mode operation. The results of this work are to be submitted to a journal:

Kim S H and Lister J B Simplifying plasma profile control in ITER 2009 to be submitted to *Plasma Phys. and Control. Fusion*

In chapter 9, conclusions of this thesis work are presented.

Part I

Free-boundary tokamak discharge simulations

Chapter 2

Comparing magnetic triggering of ELMs in TCV and ASDEX Upgrade

2.1 Introduction

The H-mode observed in many tokamak plasmas is characterized by a pedestal region in which the plasma density and temperature profiles have strong radial gradients. While in the standard/baseline scenarios pressure gradients in the core are limited by micro-turbulent effects leading to profile stiffness, the pedestal pressure gradient is increased by a spontaneous formation of edge transport barriers (ETBs), resulting in the localization of large bootstrap currents in the edge region. However, these continuous increases of the pressure gradient and the bootstrap current make the plasma edge susceptible to MHD instabilities. The onset of unstable MHD modes breaks the edge transport barriers and causes the plasma to release its stored energy and particles rapidly, in a few milliseconds. This fast repetitive regulation of the plasma energy and particle balances is known as ELMs and various types of ELMs have been identified in many tokamaks [11].

The ELMs, although degrading the plasma confinement, have some beneficial influences which allow quasi-stationary tokamak operation. Dangerous disruptive behaviour, such as an uncontrollable rise of plasma density or an accumulation of impurities in the plasma interior, is avoided by repetitive ELMs. This aspect made ITER consider an ELMy H-mode as its baseline operation. However, type-I ELMs anticipated during the main heating phase

of ITER will produce unacceptably large heat loads on the plasma facing components, if the present scaling laws are extrapolated to ITER.

Although alternatives to the large type-I ELMs, such as grassy type-II ELMs and mixed type-I and type-II ELMs, are being studied, they still have very narrow operational windows [51, 52]. Substantial progress has been made in the study of controlling the ELM frequency which is found to be inversely related to the heat load per ELM. Pellet injection into the pedestal region in ASDEX Upgrade [53], ergodization of magnetic field in DIII-D [54] and magnetic triggering of ELMs in TCV [26] were successful in modifying and controlling the ELM frequency. In particular, the magnetic triggering of ELMs is relatively easy to apply in a vertically elongated plasma, without the need of any additional systems.

In the TCV experiments, a pre-programmed voltage perturbation was injected on the G-coil sets located inside the vacuum vessel for the active control of the vertical instability [26]. The induced vertical plasma movements locked the ELM frequency to the magnetic perturbation by delaying and/or triggering ELMs. Similar experiments were carried out in ASDEX Upgrade by forcing the plasma to move vertically following an imposed reference waveform [27]. Both experiments were successful in triggering ELMs and controlling the ELM frequency. However, an unexpected and so far unexplained opposite behaviour was identified. In ASDEX, ELMs are triggered when the plasma is moving down towards the X-point with a decrease of plasma current density in the edge region, contrary to the TCV experiments in which ELMs are triggered when the plasma moves up with an increase of edge current density. Since the divertor current has the same sign as the plasma current, reducing their separation causes an increase of the flux linking the plasma, and vice versa. This linking flux is compensated by an inductively driven current at the plasma surface which has an opposite sign to the plasma current. Moving towards the X-point therefore always creates a negative induction by Lenz's law. In this chapter, the sign of the plasma current is assumed to be positive for both tokamak plasmas.

This study focuses on understanding this opposite behaviour observed in the magnetic triggering of ELMs and the possible physics reasons behind it. The geometries of TCV and ASDEX Upgrade used in our studies are shown in figure 2.1, including the separatrices of the plasmas studied in these simulations. Free-boundary features which have previously received little attention, such as plasma shape deformation, are investigated using the DINA-CH free-boundary tokamak simulator [24]. Analysis of the kink-ballooning modes (toroidal

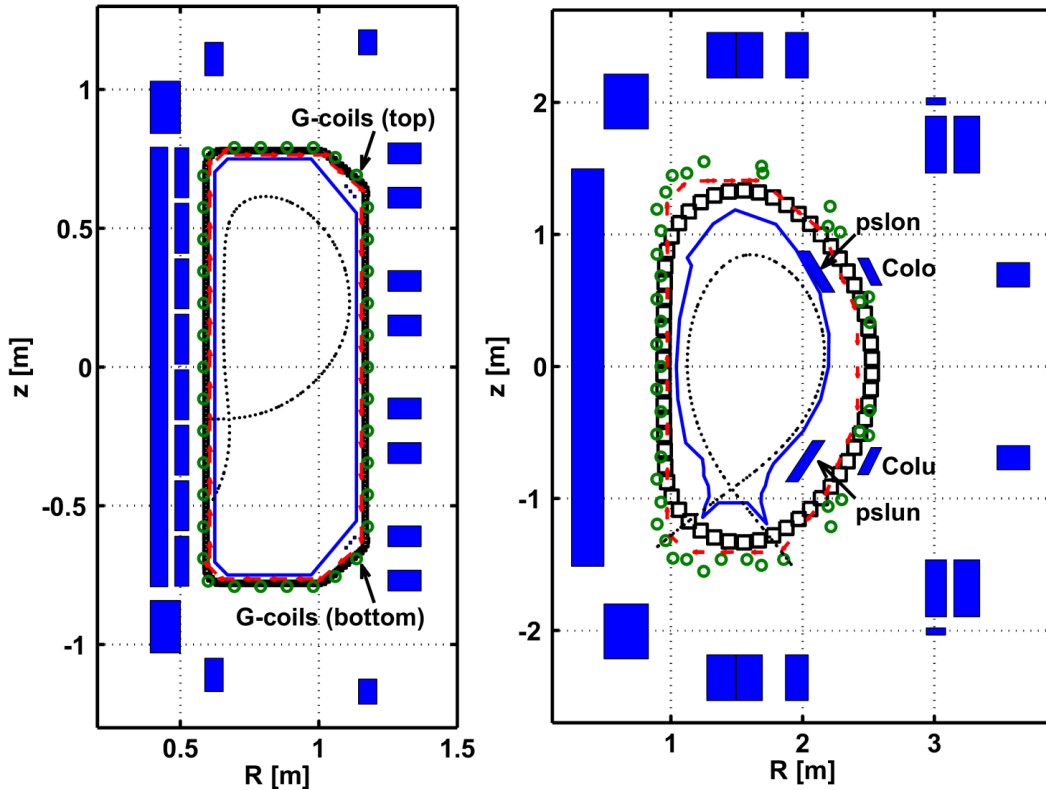


Figure 2.1: Definitions of TCV (left) and ASDEX Upgrade (right) used in the DINA-CH free-boundary tokamak simulations. The poloidal field coils (blue), vacuum vessels (black), limiters (blue), separatrixes (black dots), flux loops (green circles) and magnetic probes (red arrows) are shown. The G-coil sets are located inside the vacuum vessel of TCV. The passive stabilization loops (PSLs), $pslon$ and $pslun$, and active control coils, $CoIo$ and $CoIu$, are located inside and outside the vacuum vessel of ASDEX Upgrade, respectively.

mode numbers up to 60) possibly involved in ELM destabilization is provided by the KINX ideal MHD stability code [55].

In section 2.2, the magnetic triggering of ELMs is simulated for TCV and ASDEX Upgrade. These simulations are compared in section 2.3, to examine possible causes of the observed opposite behaviour. Driving radial plasma movements as another possible technique of magnetic ELM triggering is studied in section 2.4. A discussion is presented in section 2.5.

2.2 Simulating the magnetic triggering of ELMs

2.2.1 Scope of the simulations

Our major concern is to look for plausible mechanisms behind the opposite behaviour observed in the magnetic triggering of ELMs in two tokamaks. We do not model the ELMs themselves. The approach is simply to look for changes provoked by the magnetic perturbations which might reasonably be considered as candidates for influencing the ELM triggering conditions.

ELMs are not simulated in detail for two principal reasons. First, the cyclic ELM process is not yet completely understood. The onset conditions of ELMs and the transport processes of heat and particles across the pedestal region still have major uncertainties. Second, temporal variations of the pedestal current and pressure profiles during the ELM cycle can non-linearly interact with injected magnetic perturbations. This increases the complexity in the system being modelled and makes it very difficult to distinguish the influences contributed by the magnetic perturbations.

Including realistic pedestal profiles in the simulations was found not to be critical for investigating the dynamic plasma response, if the global plasma parameters, such as the total plasma current, I_i and β_p , are prescribed to be close to the values measured in the experiments. For convenience, the plasma density and temperature profiles are assumed to be monotonic from the plasma core to the separatrix. The absence of a detailed description of the pedestal region and the resulting underestimated pressure gradient and bootstrap current in the edge region does not significantly change the free-boundary features of the plasma responses. This was verified by free-boundary simulations done by the PET code integrated into the DINA-CH Simulink environment with differently designed pedestal profiles and increased numerical resolution, which led to similar qualitative plasma responses [56].

2.2.2 Magnetic triggering of ELMs in TCV

TCV discharge #20333 was chosen to investigate the magnetic triggering of ELMs in TCV. A comparison between this discharge and its first simulation was originally reported in detail in reference [26]. This discharge, in which the plasma is in a single-null lower configuration (SNL) with a magnetic centre shifted upward from the mid-plane ($z_{mag} = 0.2\text{m}$), shows

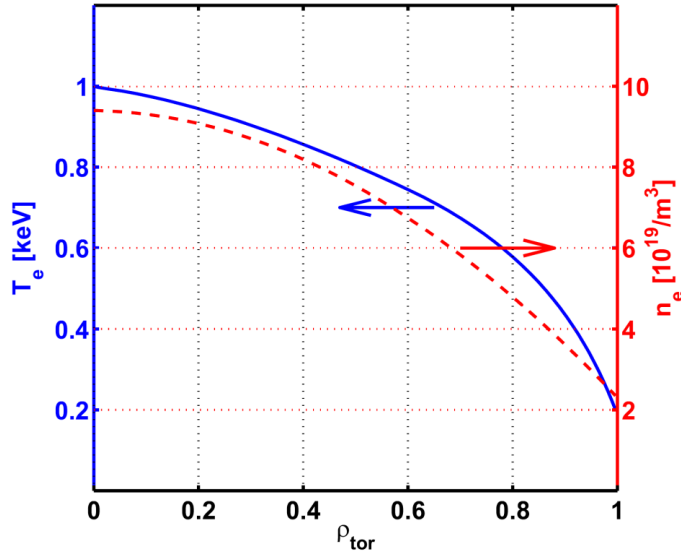


Figure 2.2: Prescribed monotonic electron temperature (blue solid line) and density (red dashed line) profiles used in the simulation of TCV discharge #20333. These profiles are arbitrarily chosen to represent a typical H-mode TCV plasma.

successful ELM frequency locking to the vertical plasma movement induced by magnetic perturbations. In the simulation of this discharge, monotonic plasma density and temperature profiles representing typical H-mode core plasmas in TCV are prescribed as shown in figure 2.2. Transport of heat and particles is not modelled. The free-boundary plasma evolution is self-consistently calculated with the currents in the poloidal field coils and surrounding conducting systems using the DINA-CH tokamak simulator.

The plasma responses observed in the experiment [26] were successfully reproduced. The voltage applied to the G-coil sets (V_G) is perturbed by a short and strong signal input (V_{pert}). The perturbed current (I_G) flowing in G-coil sets induces a vertical plasma movement (Δ_z and v_z) and results in a variation of the plasma current in the edge region (ΔI_{edge} which is an integrated plasma current outside $\rho_{tor} > 0.95$) as shown in figure 2.3. The plasma experiences repetitive vertical excursions of its magnetic centre (z_{mag}) of a few millimetres in response to G-coil current fluctuations of about 2kA. The magnetic axis and the plasma centroid calculated taking the plasma current distribution into account show very similar responses. In the experiment, ELMs are triggered when the plasma moved up at the end of each magnetic perturbation.

The increase of edge current density resulting from positively induced currents due to

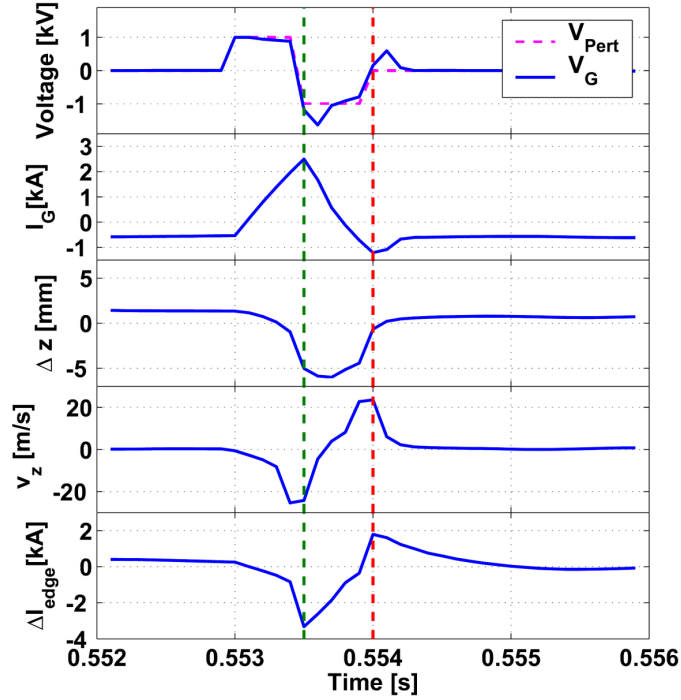


Figure 2.3: Magnetic triggering of ELMs in TCV discharge #20333 is simulated. Time traces of the voltage and current in the G-coil sets, the vertical position of the magnetic centre, the velocity of the vertical movement and the variation of the edge current which is integrated outside $\rho_{tor} > 0.95$ are shown. ELMs are triggered in the experiment when the plasma moved up with a consequent increase of edge current density (red dashed). The edge current density is correspondingly decreased with a downward plasma movement (green dashed).

an upward plasma movement away from the X-point was originally proposed as a candidate mechanism which triggers ELMs [26]. This was further emphasized by experiments in a single null upper configuration (SNU), in which ELMs were triggered with downward plasma movements away from the X-point which again induce positive currents in the edge region. Besides the vertical plasma motion sweeping the up-down asymmetric vacuum field, there is another direct source of current. A net change of external flux linking the plasma, resulting from the proximity of the plasma column to one or other of the two G-coil sets, can drive current in the edge region. These drive a surface loop voltage V_{surf} as given in reference [26] by

$$V_{surf} = -\frac{d}{dt}\langle\psi_{ext}\rangle = -\frac{\partial}{\partial t}\langle\psi_{ext}\rangle - \langle\mathbf{u} \cdot \nabla\psi_{ext}\rangle = V_{surf}^{direct} + V_{surf}^{motional} \quad (2.1)$$

where, V_{ext} is the external poloidal flux and the brackets represent averaging over the last

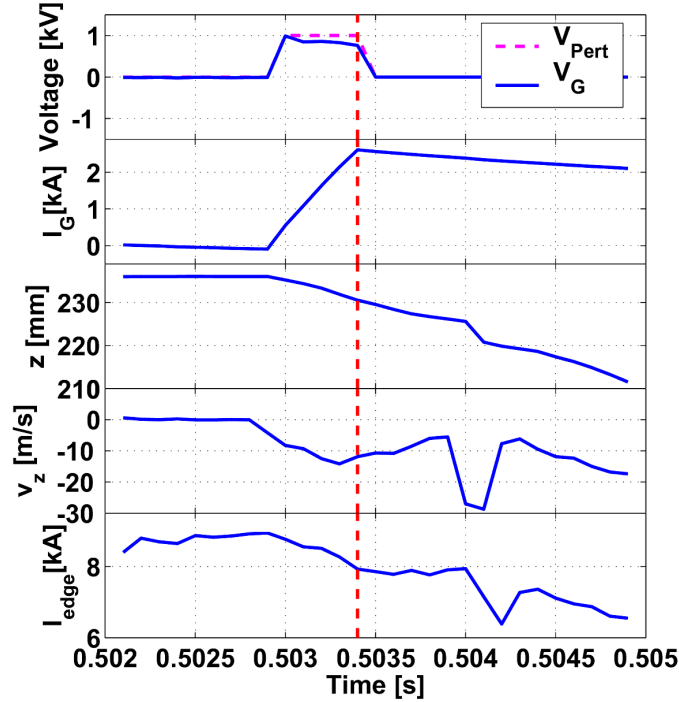


Figure 2.4: A downward VDE is triggered in TCV discharge #20333 simulation. Time traces of the voltage and current of G-coil, the vertical position of magnetic centre, the velocity of the vertical movement and the variation of the edge current are shown. The feedback control systems are disabled for the plasma to continue the vertical displacement ($V_G = 0$ after the red dashed line).

closed flux surface. However, the voltage directly driven by the external source considering no plasma motion, V_{surf}^{direct} , is relatively small and has the opposite sign to the voltage induced by the vertical plasma motion sweeping the vacuum field, $V_{surf}^{motional}$. For example, if the plasma is in a SNL configuration close to the upper G-coil set in which current flows in the opposite direction to the plasma current, the plasma moves down and approaches the X-point, as the current in the G-coil sets is increased. This plasma movement induces negative currents in the edge region, while the net surface loop voltage drives a positive current compensating the decrease of external linking flux from the upper G-coil set to the plasma.

The perturbed edge current shown in figure 2.3 is approximately proportional to the velocity of the vertical plasma movement, again indicating that the current driven by the net surface loop voltage is relatively small. An additional simulation in which a VDE was triggered by a pulsed magnetic perturbation and an immediate disabling of the control system

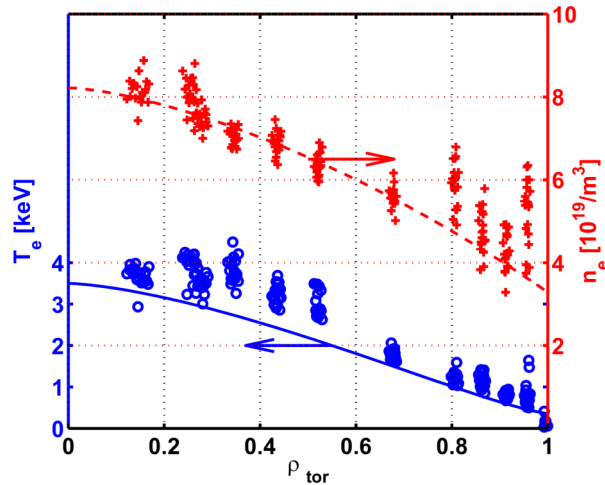


Figure 2.5: Prescribed monotonic electron temperature (blue solid line) and density (red dashed line) profiles used in the simulation of ASDEX Upgrade discharge # 18343. These profiles are chosen based on the measured data. Blue circles and red crosses indicate the measured electron temperature and density, respectively.

is shown in figure 2.4. The edge current evolution is clearly related to the velocity of the vertical plasma motion in the absence of a net surface loop voltage.

2.2.3 Magnetic triggering of ELMs in ASDEX Upgrade

The magnetic triggering of ELMs first demonstrated in TCV was repeated in ASDEX Upgrade [27]. Instead of injecting short and strong pulses into the coil systems, a reference vertical plasma position including a sinusoidal waveform is pre-programmed in the feedback control system to produce the magnetic perturbations. ASDEX Upgrade discharge #18343 showing the ELM frequency locking to the vertical plasma motion [27] is chosen for a free-boundary tokamak simulation. The plasma density and temperature profiles are prescribed with monotonic shapes as shown in figure 2.5. The choice of the temperature profile is made during the initialization of a simulation and is constrained to have a similar shape to the data points. The assumed profiles show some deviations from the data points, since the initial temperature profile has to be consistent with the measured plasma pressure (through β_p) and the assumed density profile.

Simulated plasma responses are shown in figure 2.6. The pre-programmed reference input (z_{ref}) to the feedback control system generates currents in the active control coils (CoIo and

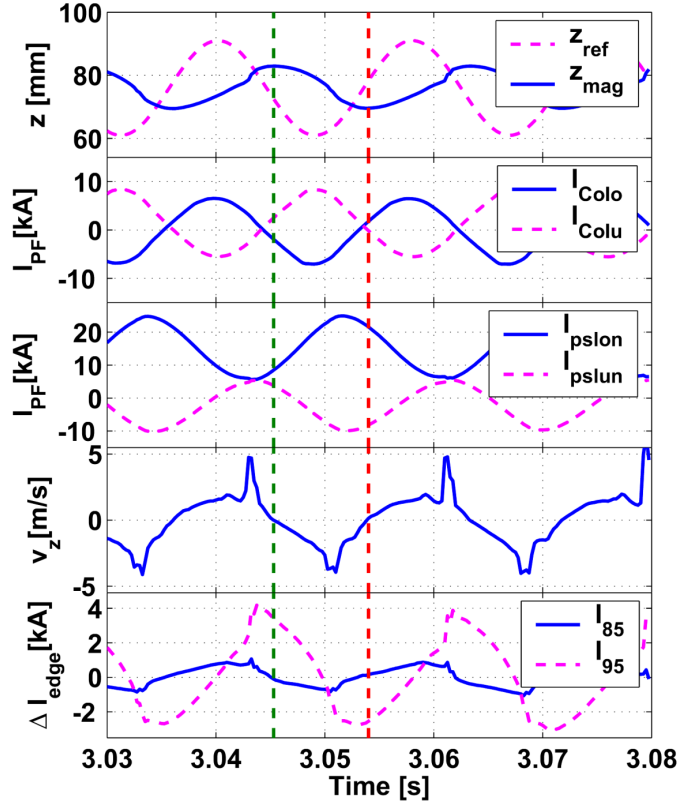


Figure 2.6: Magnetic triggering of ELMs in ASDEX Upgrade discharge #18343 is simulated. Time traces of the reference and controlled vertical positions, the currents in the fast vertical position control coils (I_{CoIo} and I_{CoIu}), the currents in the PSLs (I_{pslon} and I_{pslun}), the velocity of the vertical plasma movement and the variations of edge current densities. I_{85} and I_{95} represent integrated currents outside $\rho_{tor} > 0.85$ and $\rho_{tor} > 0.95$, respectively. ELMs are triggered in the experiments when the plasma is moving down at maximum speed (between dashed green and red) and the edge current density is decreased.

CoIu) for the control of the vertical plasma position (z_{mag}). Eddy currents are induced in the vacuum vessel and passive stabilization loops (PSLs, pslon and pslun), in response to the controlled coil currents and plasma movement. The variation of the plasma current in the edge region (ΔI_{edge}) is again a mixture of motional (v_z) and direct induction contributions (equation (2.1)). I_{85} and I_{95} represent the edge currents integrated outside $\rho_{tor} > 0.85$ and $\rho_{tor} > 0.95$, respectively. The times the plasma is moved up and down are indicated by green and red dashed lines, respectively.

The controlled vertical plasma position responds with a larger phase delay with respect

to the reference waveform in the simulation ($\sim 3\pi/2$) than that observed in the experiment ($\sim \pi$) [27]. However key components representing the dynamic plasma response, such as the magnitude of the vertical excursion ($\Delta z_{mag} \sim \pm 0.7\text{cm}$) and its velocity ($\Delta v_z \sim \pm 3\text{m/s}$), are reproduced similar to the observations in the experiment. The peaks shown in the velocity of the vertical movement originate from a large mesh size used in determining the plasma centre. The edge current (I_{95}), is perturbed mainly by the vertical plasma motion, deduced from the similarity of their evolutions. However, comparing the edge currents, I_{85} and I_{95} , we see that the phase difference with respect to the plasma motion varies with the integration range. When the plasma is moving down, the edge plasma current is reduced by negatively induced currents, and vice versa. In spite of the complexity of the simulated system, this matches well with the observations in the experiments.

The peak to peak variation of ΔI_{edge} ($\sim 7\text{kA}$) is considerably lower than the swing ($\sim 50 - 60\text{kA}$) shown in figure 4 of reference [27]. This difference can be attributed to the lower edge temperature used in the simulation (see figure 2.5). The edge current variation is significantly reduced by the resulting lower plasma conductivity and is further reduced by a slightly lower surface voltage induced by a smaller vertical movement. The lower edge temperature and the absence of pedestal-like edge profiles also reduce the edge bootstrap current which provides the main contribution to the average edge current. Although the absolute value appears to be quite far from the experiment, the normalized edge current variation with respect to the average edge current, which defines the relative strength of the edge current perturbation, is similar for the simulation and the experiment.

2.3 Comparing the two cases of magnetic triggering of ELMs

The type of ELM observed in the magnetic triggering experiments in TCV has recently been identified as type-III [57], whereas type-I ELMs are observed during non-triggering phases in ASDEX Upgrade. This implies that the magnetic perturbations injected into TCV and ASDEX Upgrade discharges might be triggering ELMs in different ways. Different ELM types imply different plasma sensitivities to the dynamic changes of physical quantities such as the edge pressure gradient and plasma current density. The opposite behaviour observed

in the magnetic triggering of ELMs might then require different explanations. However, this issue is beyond our current modelling capability which does not yet simulate the ELMs themselves and therefore can not differentiate between different ELM types.

In the occurrence of natural ELMs, the pedestal pressure gradient increases with a build-up of bootstrap current, until reaching a threshold value, and then it decreases quickly releasing the plasma particles and stored energy. This threshold behaviour is generally believed to be caused by destabilising MHD modes with the increase of pressure gradient and current density in the edge region. If the edge pressure gradient and/or the edge current density are/is significantly perturbed externally, the edge stability and therefore the ELM cycle would clearly be modified. This can either delay or trigger ELMs, leading to synchronization of the ELMs to the perturbation.

2.3.1 Perturbed plasma current density in the edge region

The evolution of the simulated plasma current density in the edge region is shown in figures 2.7(a) and 2.8(a), respectively for TCV and ASDEX Upgrade. A significant feature is observed in the evolution of the plasma current density. When the plasma current density is reduced by negatively induced currents at the plasma boundary, the plasma current density at inner magnetic flux surfaces is increased, and vice versa. In both plasmas, the depth of the skin current calculated with a given edge temperature is comparable with the distance between the magnetic flux surface of $\rho_{tor} = 0.9$ and the plasma boundary. This is the range in which the edge current perturbations are observed. The current diffusion time calculated with this scale length is less than the period of the magnetic perturbation in both plasmas. Therefore, the perturbed current penetrating the edge region and its radial diffusion across flux surfaces produces a complicated pattern of the edge current fluctuation.

Edge current density profiles plotted on the radial grid are given in figure 2.7(c) and 2.8(c) at the moments marked in figure 2.7(b) and 2.8(b), respectively. They clearly show the inverted perturbations. The edge currents integrated outside are normalized with averaged unperturbed edge plasma currents and plotted in figure 2.7(b) and 2.8(b). The min/max variation of the normalized edge current in TCV is about 0.5 (from 0.7 to 1.2), while it is about 0.25 (from 0.9 to 1.15) in ASDEX Upgrade.

The large perturbation in edge current observed in TCV is mainly due to its faster

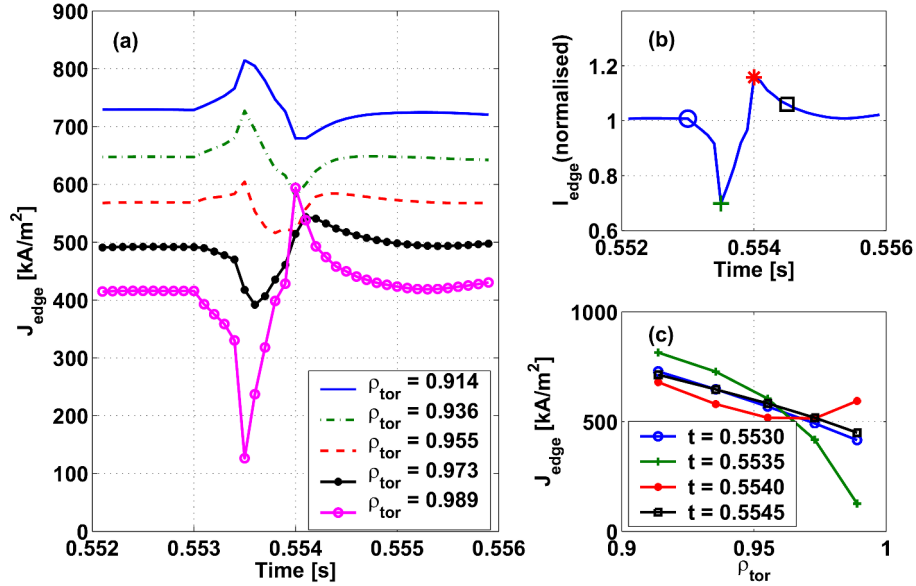


Figure 2.7: Evolution of the plasma current in the simulation of TCV discharge #20333. Edge current density (a), normalized edge current integrated outside $\rho_{\text{tor}} > 0.95$ (b) and radial edge current density profiles (c) at the times indicated by the markers in (b) are shown.

vertical plasma movement ($\pm 20\text{m/s}$). In ASDEX Upgrade, although the speed of the vertical plasma movement ($\pm 3\text{m/s}$) is relatively low, it produces a large perturbation due to its higher edge temperature. However, triggered ELMs in the ASDEX Upgrade experiments are observed when the edge current is reduced by negatively induced currents. Although there is a controversy over the destabilising effect of the edge current gradient increase, the edge current reduction generally has a strong stabilising effect. Therefore, a simple explanation based on the sign of the induced edge current perturbation is inadequate to explain both the magnetic triggering of ELMs in ASDEX Upgrade and the observed opposite ELM behaviour between two plasmas. In ASDEX Upgrade, we should therefore explore the possibility that ELMs might be triggered by another perturbed physical quantity.

2.3.2 Perturbed local plasma pressure gradient in the edge region

The response of the plasma to the magnetic perturbation not only induces a plasma motion but also produces a deformation of the plasma shape. The latter results in a perturbation of the local plasma pressure gradient in the edge region as shown in figure 2.9. Assuming a non-

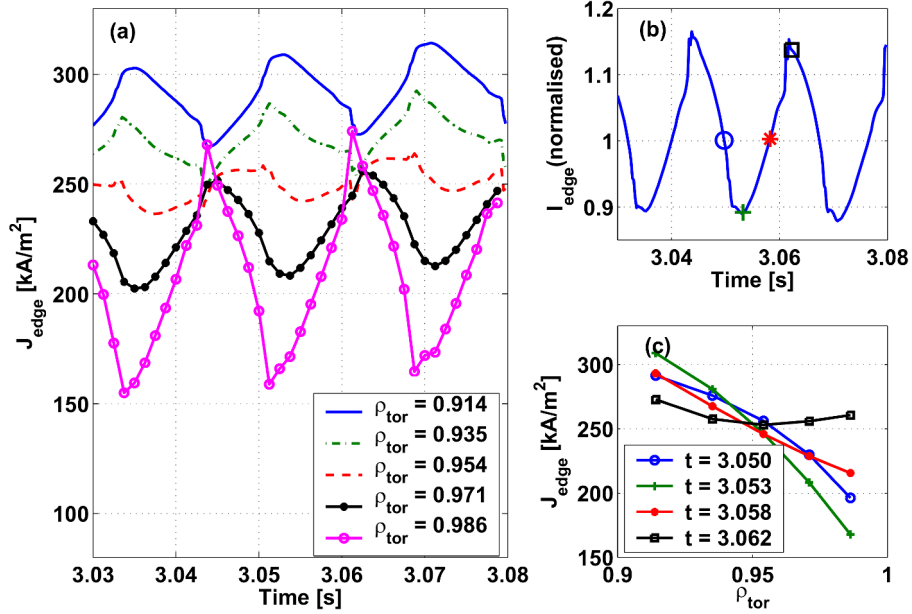


Figure 2.8: Evolution of the plasma current in the simulation of ASDEX Upgrade discharge #18343. Edge current density (a), normalized edge current integrated outside $\rho_{\text{tor}} > 0.95$ (b) and radial edge current density profiles (c) at the times indicated by the markers in (b) are shown.

variant pressure difference between two neighbouring magnetic flux surfaces, the variation of the local pressure gradient is calculated from the flux surface separation along the poloidal angle. This is given by

$$\frac{\Delta(dp/dr|_{\theta})}{dp/dr|_{\theta}} \sim \frac{x_0 - x_1}{x_1} \Big|_{\theta} \quad (2.2)$$

where, x_0 and x_1 are the distances between two neighbouring magnetic flux surfaces at the beginning and at the end of an upward or downward vertical movement.

The variations are less than 10% of the unperturbed averaged value. In both TCV and ASDEX Upgrade, an increase of the local pressure gradient is produced by a downward plasma movement. In a SNL configuration, both plasmas are shrinking when they are moving down closer to the X-point, and vice versa. Therefore, although the increase of the local pressure gradient is destabilizing the edge in ASDEX Upgrade, it can not be an answer for the observed opposite ELM behaviour between the two devices. In particular, the upward movement associated with the magnetic triggering of ELMs in TCV reduces the local pressure gradient in the edge region.

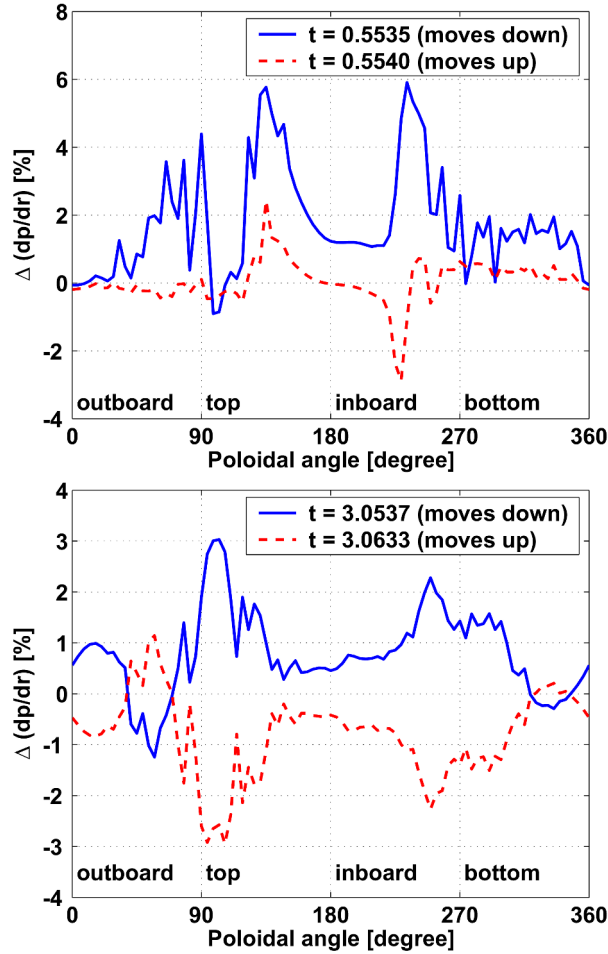


Figure 2.9: Local pressure gradient change in the edge region is calculated as a function of the poloidal angle. Downward (solid blue) and upward (red dashed) movements in TCV discharge #20333 (top) and ASDEX upgrade discharge #18343 (bottom) are compared.

2.3.3 Flux surface deformation and its pattern in the edge region

An interesting feature is observed in the deformation of the plasma shape in ASDEX Upgrade. The plasma experiences a localized expansion of the flux surfaces near the upper PSL during its downward movement. In TCV, a similar flux surface expansion near the upper G-coil set is produced with an upward movement. These are compared in figure 2.10. The PSLs located inside the vacuum vessel of ASDEX Upgrade play a similar role to that of the G-coil sets in TCV due to their proximity to the plasma boundary. Positive eddy currents are induced in the upper PSL as a result of the downward plasma movement and direct induction by currents in active and passive conducting structures. They create a localized

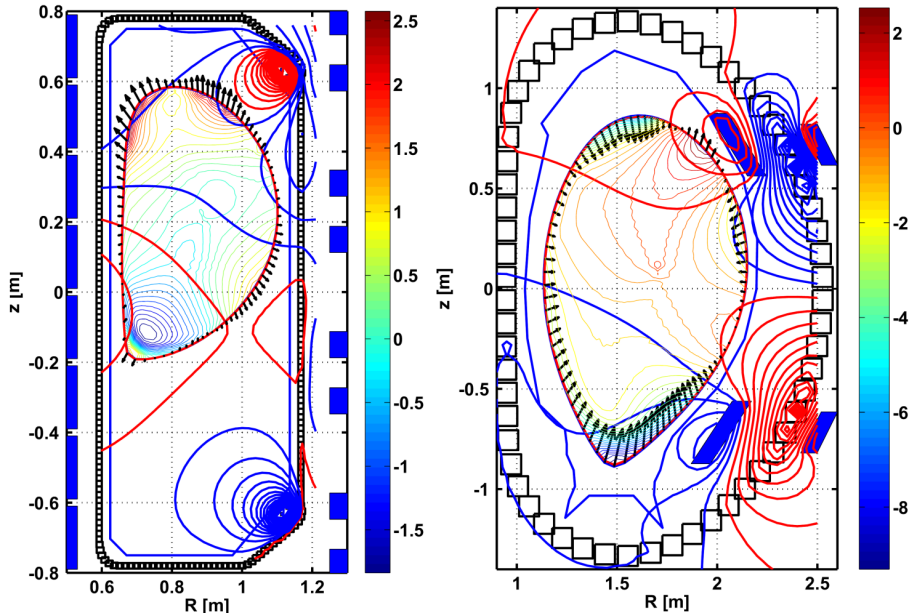


Figure 2.10: Flux surface deformations and vacuum flux changes are shown for upward plasma movement in TCV discharge #20333 (left) and downward plasma movement in ASDEX Upgrade discharge #18343 (right). ELMs are triggered in the experiments for these plasma movements. The arrows are amplified by a factor 20 for visibility.

expansion of the flux surfaces near the upper PSL compared with the overall shrinkage of plasma column. Both plasma movements generating a localized expansion of flux surfaces, upward in TCV and downward in ASDEX Upgrade, trigger ELMs in the experiments. The opposite plasma movement, downward in TCV and upward in ASDEX Upgrade, creates localized shrinkage of flux surfaces as shown in figure 2.11. In these figures, the deformation of the plasma flux surfaces is calculated by using a moving frame in which the origin is fixed to the magnetic axis. The arrows, magnified 20 times for visibility, represent the deformation of the last closed flux surface. The increase and decrease of the external linking fluxes are shown in red and blue, respectively.

The responses of plasma shape parameters to the magnetic perturbations are shown in figure 2.12. The red dashed lines indicate the times ELMs are triggered in the experiments [26, 27]. In both plasmas, the plasma elongation is slightly delayed with respect to the vertical plasma movement and the size of the elongation perturbations is less than 1%. The plasma triangularities respond promptly and exhibit a few percent variation. These global parameters do not reveal any additional clue for the opposite behaviour observed in the

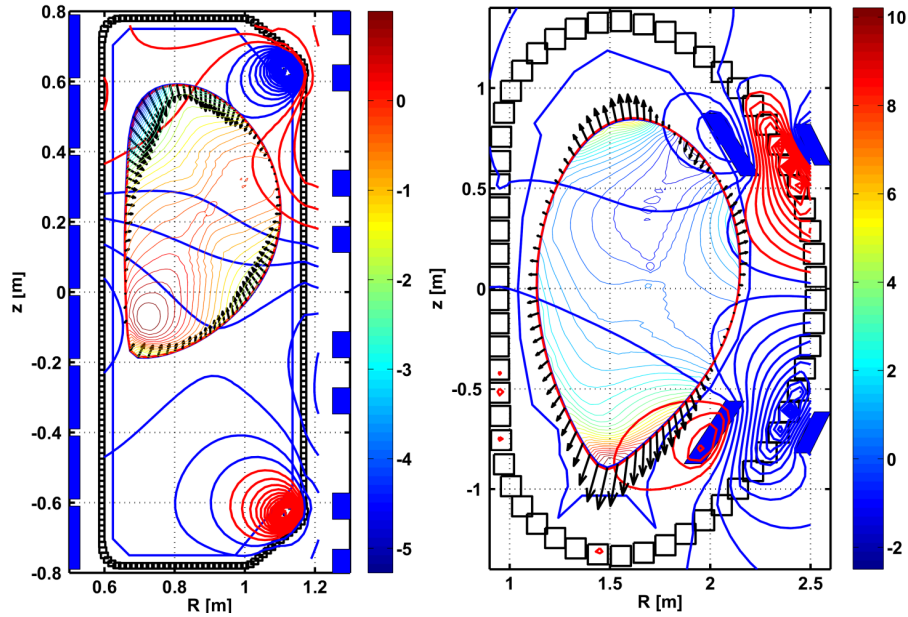


Figure 2.11: Flux surface deformations and vacuum flux changes are shown for downward plasma movement in TCV discharge #20333 (left) and upward plasma movement in ASDEX Upgrade discharge #18343 (right). ELMs are not observed in the experiments for these plasma movements. The arrows are amplified by a factor 20 for visibility.

magnetic triggering of ELMs. However, a stability study on the ASDEX Upgrade plasmas, including the separatrices, showed that the increase of the plasma squareness in the low field side (LFS) and upper half plane of the poloidal cross section has a tendency to destabilize the plasma edge [56]. This tendency matches well with the localized expansion of flux surfaces near the upper PSL during the downward plasma movement in ASDEX Upgrade.

Although the localized expansion of flux surfaces observed both in the simulation of TCV and ASDEX Upgrade plasmas provides a new clue for understanding the magnetic triggering of ELMs, the shape deformation in TCV plasmas still has some open questions. DINA-CH/SPIDER simulations dedicated to the study of edge stability of TCV plasma during the magnetic triggering of ELMs [58] show that the plasma squareness in the LFS and upper half plane of the poloidal cross section decreases a little during the upward plasma movement resulting in a small stabilising effect.

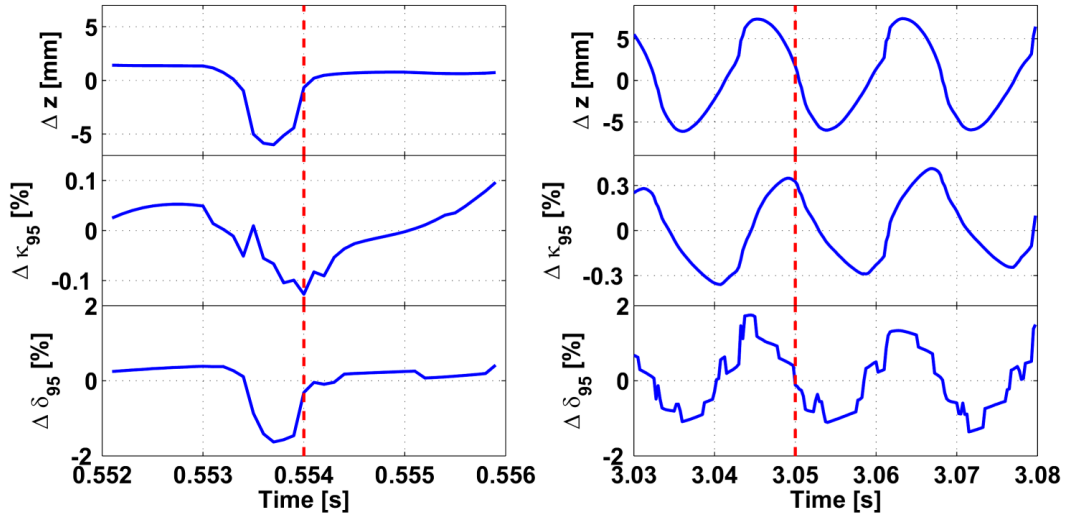


Figure 2.12: Vertical plasma movement and the response of the plasma elongation and triangularity to the magnetic perturbation are shown for TCV discharge #20333 (left) and ASDEX Upgrade discharge #18343 (right). The times ELMs are triggered in the experiment are indicated by red dashed lines.

2.4 Magnetic perturbation with radial plasma movements in ASDEX Upgrade

The effect of the plasma shape deformation was investigated further by minimizing fluctuations in the edge plasma currents. Instead of inducing a vertical plasma motion, a radial motion is induced to produce a different type of magnetic perturbation in the simulation of ASDEX Upgrade discharge #18343. To avoid saturation of the input voltages to the active coils, the amplitude of the reference waveform modulation was reduced to half of that used to control the vertical plasma position.

The plasma shape is easily deformed by a radial plasma movement due to the eddy currents induced in the PSLs and vacuum vessel as shown in figure 2.13. The deformation of the plasma shape shows a weak change in squareness in the LFS and upper half plane. The plasma elongation is the dominant parameter linked to the plasma shape deformation.

The deformation of the plasma boundary during vertical and radial plasma movements is compared in figure 2.14. The deformation patterns which accompany the radial movement (poloidal mode number, $m = 2$) are simpler than those which accompany the vertical move-

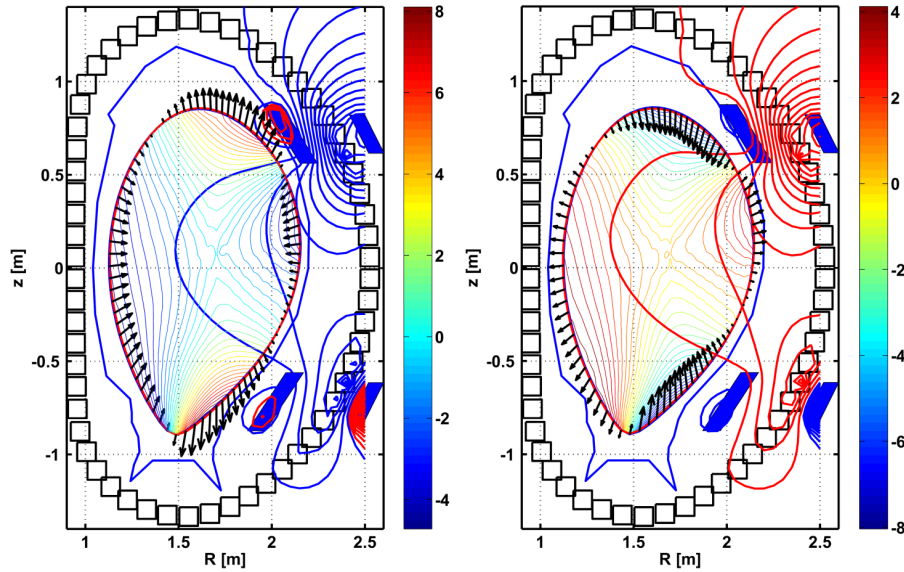


Figure 2.13: Flux surface deformations and vacuum flux changes are shown for inward (left) and outward (right) radial plasma movements in ASDEX Upgrade. The arrows are amplified by a factor 20 for visibility.

ment ($m = 3$) and the area of the plasma column is changed less, compared with the case of vertical plasma movement. In particular, the strongly localized expansion of the flux surface near the upper PSL against the shrinkage of the plasma column is observed only with the downward plasma movement, as indicated by blue circles.

The experiments reported in ASDEX Upgrade showed that the plasma shape deformation produced by a radial plasma movement does not trigger ELMs [59] and this observation is supported by a stability analysis with the KINX code [60]. The detailed analysis of the plasma boundary curvature perturbation shows similar changes for vertical and radial movement in the LFS and upper half plane. However, there is a difference affecting the edge stability in ASDEX Upgrade. The plasma boundary curvature in the LFS and lower half plane is increased only when the plasma column size is reduced by the downward plasma movement.

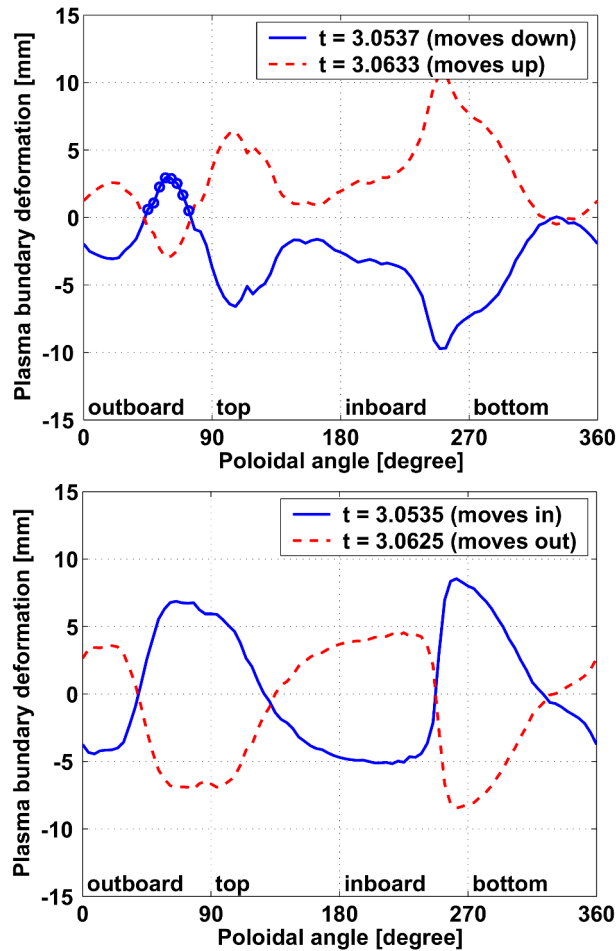


Figure 2.14: Plasma boundary deformations for vertical movement (top) and for radial movement (bottom) in ASDEX Upgrade. Localized expansion of the flux surfaces near the upper PSL is indicated (blue circles).

2.5 Discussion

The experimental evidence for ELM triggering from TCV and ASDEX Upgrade is clear, and has been subsequently confirmed on JET [61]. The original explanation by TCV was an inductive increase in the edge current due to the plasma movement away from the divertor current. The observations on ASDEX Upgrade and JET confirmed that the original prediction that the effect would become clearer on larger plasmas with higher edge temperatures was correct. However, the change in sign of the edge current density change indicated that the simplicity of the original TCV explanation is probably inadequate. In this chapter, we have explored the physics of this phenomenon with two advanced codes, namely a

free-boundary evolution code, DINA-CH, and a free boundary stability code including the separatrix, KINX. The qualitative observations obtained with these two models are summarized in table 2.1.

The preceding discussions on the various effects investigated have not clearly defined a unique mechanism for destabilizing the ELMs. While the edge current increase by an upward vertical movement is the strongest candidate in TCV, in ASDEX Upgrade the onset of ELMs seems to depend not only on the equilibrium quantities such as the edge pressure and current gradients, but also on free-boundary motion and deformation. The role of the PSL in changing the separatrix shape during fast transients has been exposed. Localized expansion of the flux surfaces near the upper PSL in ASDEX Upgrade, compared with the overall shrinkage of the plasma column accompanied by the downward plasma movement, shows a tendency to destabilize the plasma edge in the KINX stability analysis. The perturbation induced by a radial plasma movement, such as a strong elongation change, seems not sufficient to trigger ELMs by itself.

The explorations conducted in this paper have underlined the difficulty in attributing a complex phenomenon to a single effect, since for a single given cause, namely fast stimulation of an equilibrium change, all potentially relevant mechanisms are excited, namely changes to the spatial pressure and current gradients, to the edge current density (averaged and local), to the boundary shape, to the plasma column size and to its position. Since all these effects are demonstrably linked to MHD instability, there is a worrying possibility of erroneously attributing causality in the presence of all correlated effects. Furthermore, since such fast effects are intimately linked to the physical construction of the passive and active conductors, with possible 3-D effects not excludable, there is even a strong possibility that similar plasmas in different tokamaks might behave differently, underlining the risk of extrapolating the results from these three experiments to ITER. However, the fact remains that the phenomenon of magnetic triggering might offer a control mechanism for ELMs in ITER, with no additional infrastructure required since internal coils have already been added.

Table 2.1: The observations in the experiments and simulations of magnetic triggering of ELMs are summarized

Observations	TCV	ASDEX Upgrade		Comments
Plasma movement	Upward	Downward	Inward	
Type of natural ELMs	Type III	Type I	Type I	
Triggered ELMs	Observed	Observed	Not observed	
Edge current density	Increased ^b	Decreased	-	
Edge current gradient	Decreased (locally increased)	Increased (locally decreased)	-	Mixed contributions
Edge pressure gradient	Decreased	Increased ^b	-	
Plasma area	Expanded	Shrunk ^b	-	
Shape deformation	Locally expanded in upper LFS ^b	Locally expanded in upper LFS ^b	Elongated	
Squareness (upper LFS) ^a	Decreased	Increased ^b	-	Squareness decrease in TCV is not yet clearly explained
Curvature (upper LFS) ^a	-	Locally increased or decreased	Locally increased or decreased	Similar patterns
Curvature (lower LFS) ^a	-	Increased ^b	Decreased	Systematic differences in the stability margin behaviour

^a Observations from the KINX analysis [58, 60]

^b Possible candidates for triggering ELMs

Chapter 3

Plasma dynamic response to disturbances

3.1 Introduction

Strong plasma disturbances, such as an uncontrolled ELM and a fast H-L mode transition, cause the plasma to release its stored energy and particles on plasma facing components resulting in a plasma movement. If the plasma movement is fast and beyond the capability of the plasma vertical position controller, the discharge is terminated through a VDE. Recently, specifications of plasma disturbances anticipated in ITER have been updated to cover a wider range of plasma disturbances observed in present tokamak experiments [28]. The updated specifications could exceed the capability of the present ITER control systems and may require an upgrade of them. A new assessment of the control systems is indispensable to investigate this issue. Although the main focus is on the plasma position control system, the plasma current and shape control system should be investigated together. In ITER, the plasma position control system only slows down the speed of the vertical plasma movement. The plasma position in a stationary state is determined by the slow control of the plasma boundary shape. The slow power supplies for the shape control are also used for the control of the total plasma current. These issues require a non-linear free-boundary plasma equilibrium evolution code, such as DINA-CH, which can model the non-linear dynamic plasma responses to a plasma disturbance.

The updated plasma disturbances in ITER with high priorities are controlled and uncontrolled ELMs, transport barrier collapse, minor disruptions and fast H-L mode transitions [28]. In this chapter, we have modelled the uncontrolled ELMs and fast H-L mode transitions in inductive 15MA ITER scenario 2 [6] using the updated specifications. The efforts are concentrated on preparing a target plasma by simulating the ITER scenario 2 and developing a systematic procedure, in which plasma disturbances are automatically pre-programmed based on the given specifications.

In section 3.2, the pre-programming of plasma disturbances, the uncontrolled ELMs and fast H-L mode transitions, are described. The non-linear dynamic plasma response to the applied plasma disturbances is investigated in section 3.3. A bug in DINA-CH which artificially stabilised the plasma dynamic responses has been fixed. A discussion is presented in section 3.4.

3.2 Pre-programming appropriate plasma disturbances

A simple routine has been developed to pre-program the plasma disturbances in a reproducible and systematic way. This routine basically controls the release and recovery of the total stored plasma energy to follow a prescribed waveform. In this routine, the heat conductivity profiles consistent with the initial plasma profiles are prescribed. These heat conductivity profiles are then multiplied by a time-varying factor which controls the global energy confinement of the plasma. This factor is determined by taking the difference between the present and reference stored plasma energy into account. As a result, the electron and ion temperature profiles are controlled with a prescribed plasma density profile. The multiplication factor to the heat conductivity profiles, C_m , is given by

$$C_m = 1 + C_{sd} \frac{W_{th} - W_{th}^{ref}}{W_{th}^{ref}}, \quad \text{in range } [10^{-3}, 10^3] \quad (3.1)$$

where, W_{th} and W_{th}^{ref} represent the present and reference stored plasma energy. C_{sd} is a coefficient determining the speed of the dynamics. Localized release of plasma energy from the pedestal is modelled by imposing a heat conductivity at the plasma boundary, χ_b . The heat conductivity profiles are smoothed to make the pedestal nicely continuous with reduced

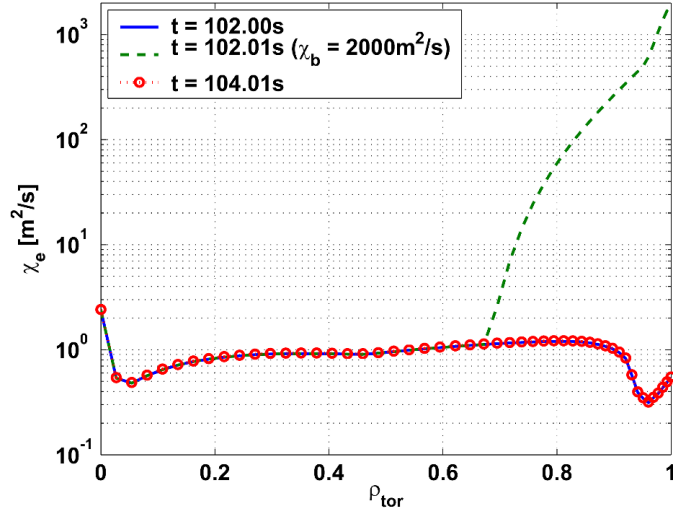


Figure 3.1: Pre-programmed evolution of the electron heat conductivity profile to simulate an uncontrolled ELM. The electron heat conductivity at the plasma boundary is temporarily increased up to $2000\text{m}^2\text{s}^{-1}$ for 1ms.

edge gradients. Uncontrolled ELMs and fast H-L transitions are pre-programmed in this routine.

3.2.1 Uncontrolled ELMs

In ITER, the uncontrolled ELMs in an H-mode plasma are expected to release plasma energy of about 20-25MJ in $200\mu\text{s}$. This disturbance would produce a decrease of β_p of about 0.05 (from 0.65 to 0.60) and an increase of l_i of about 0.05 (from 0.85 to 0.9) on a similar time-scale. At a later time, as the plasma current diffuses, the slow increase of l_i could be up to 0.1 as an upper range. In our simulations, this fast plasma energy release is pre-programmed by imposing a very high heat conductivity at the plasma boundary ($\chi_b = 500 \sim 2000\text{m}^2\text{s}^{-1}$) for 1ms. Although this time duration is much longer than specified for the uncontrolled ELMs, the plasma control does not feel any significant change and is found to produce similar dynamic responses. This also accelerates the simulation by allowing a larger maximum time-step. On the contrary, if a smaller duration ($< 1\text{ms}$) is used for pre-programming the fast plasma energy release, the simulation is not only decelerated, but also becomes unstable numerically with a smaller time-step. After this fast loss of plasma energy, the original heat conductivity profiles are re-assigned to increase the total stored plasma energy back to the previous level. The speed of this recovery process mainly depends on the coefficient, C_{sd} .

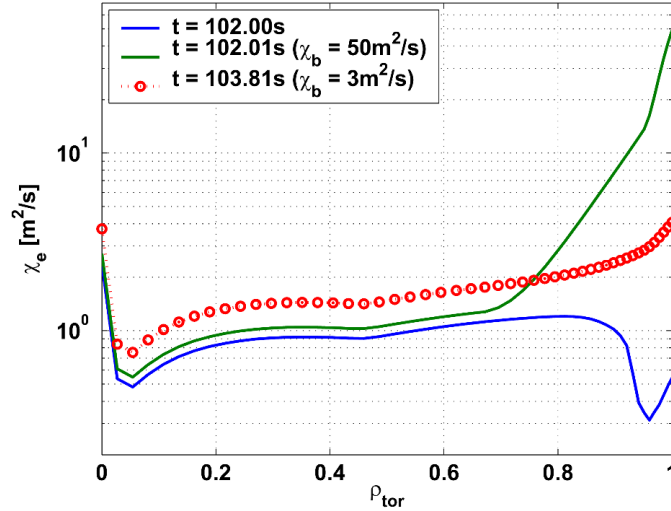


Figure 3.2: Pre-programmed evolution of the electron heat conductivity profile to simulate a fast H-L mode transition. The electron heat conductivity at the plasma boundary is increased up to $50 \text{ m}^2\text{s}^{-1}$ for 10ms at the first stage, then reduced down to $3 \text{ m}^2\text{s}^{-1}$. The heat conductivity profiles are dynamically controlled to simulate L-mode after the disturbance.

An example of the electron heat conductivity profile evolution is shown in figure 3.1.

3.2.2 Fast H-L mode transitions

The fast H-L mode transition in ITER can be divided into 2 stages. First, plasma energy of about 20-40MJ is expected to be released from the pedestal with an exponential time-scale of 10-100ms. This corresponds to a decrease of β_p of about 0.05-0.08 (from 0.65 to 0.57-0.60) and an increase of l_i of about 0.05 (from 0.85 to 0.90). Then, a slower decrease of the plasma energy is followed with an exponential time-scale of 1.8s completing a mode transition to L-mode. This slow change corresponds to a decrease of β_p of about 0.37-0.50 (from 0.57-0.60 to 0.10-0.20) and an increase of l_i of about 0.05-0.20 (from 0.9 to 0.95-1.10).

The first stage is pre-programmed by imposing a high heat conductivity at the plasma boundary, $\chi_b = 50 \text{ m}^2\text{s}^{-1}$ for 100ms. After the first stage, this imposed boundary heat conductivity is reduced to $3 \text{ m}^2\text{s}^{-1}$ to produce L-mode edge. The profile evolution is shown in figure 3.2. The exponential decay of the total stored plasma energy during a fast H-L mode transition is shown in figure 3.3. The reference stored plasma energy, W_{th}^{ref} , is prescribed to be decreased with exponential time-scales of 0.10s and 1.80s for the first and second stages,

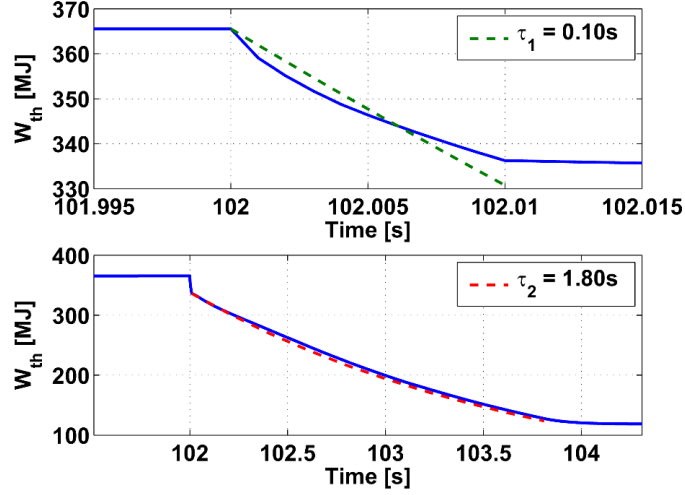


Figure 3.3: Release of the plasma energy (solid lines) following a preprogrammed waveform (dashed lines). The stored plasma energy is decreased quickly with an exponential time-scale of τ_1 at the first stage (top) and slowly reaches to L-mode with an exponential time-scale of τ_2 (bottom).

respectively. The decrease of stored plasma energy in each stage is simply defined using the following expression.

$$W_{th}^{ref}(t) = W_{th}^{ref}(t_{start}) \exp\left(\frac{t - t_{start}}{\tau}\right) \quad (3.2)$$

where, t_{start} is the starting time of plasma energy release and τ is the exponential time-scale. Therefore, the final state is determined by the duration of each stage.

3.2.3 Transport simulation with frozen heat conductivity profiles

At the early stage of preparing the routine controlling the heat conductivity profiles, a series of simulations has been performed to answer a simple question: What is the consequence if frozen heat conductivity profiles are used in modelling the plasma transport? In other words, if the heat conductivity obtained from a stationary plasma state is reused in the modelling of plasma transport, can the plasma find the same stationary state again? To answer this question, first, heat conductivity profiles are obtained from a stationary plasma state. Then these are frozen in time and re-used in the same simulation. In the second simulation, the plasma temperature evolves exponentially, and then either reaches a new stationary state with much lower plasma temperature or diverges to very high plasma temperature. These

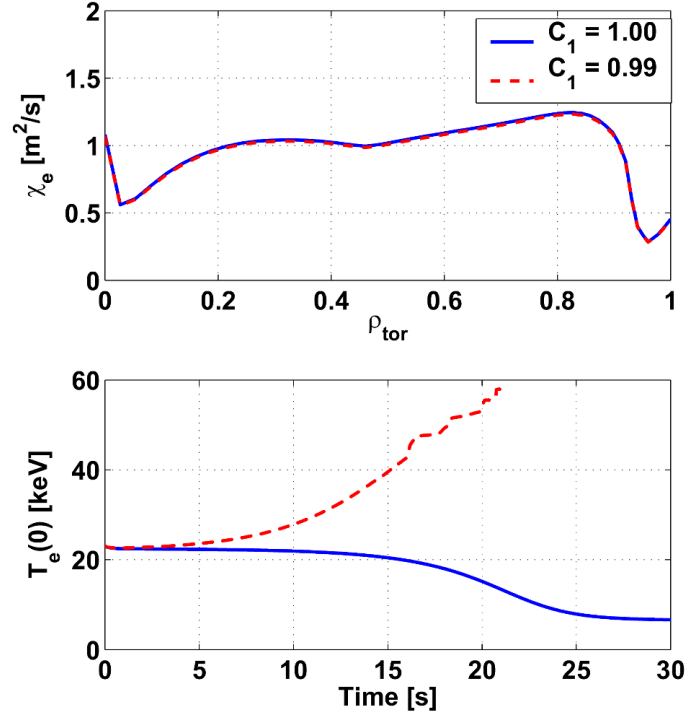


Figure 3.4: Comparison of electron temperature evolution calculated by DINA-CH. The electron and ion heat conductivity profiles are multiplied by C_1 and frozen in time.

are shown in figure 3.4. A very small difference in the multiplication factor ($< 1\%$) produces completely different final states. Similar behaviour was reproduced in other transport modelling codes, namely CRONOS and ASTRA [62]. It seems that the stationary plasma state maintained by heat conductivity profiles being controlled continuously is a meta-stable state which is very sensitive to a small change. Having a stable point at a very low plasma temperature implies that alpha particle heating is responsible for these behaviours. This is checked with CRONOS and the results are shown in figure 3.5. When the alpha particle heating profiles are frozen together with the heat conductivity profiles, the plasma reaches a new stationary state very quickly near the original state.

3.3 Dynamic plasma responses

Dynamic plasma responses to the disturbances, uncontrolled ELMs and fast H-L mode transitions, has been studied by using a non-linear plasma response modelling code, DINA-CH

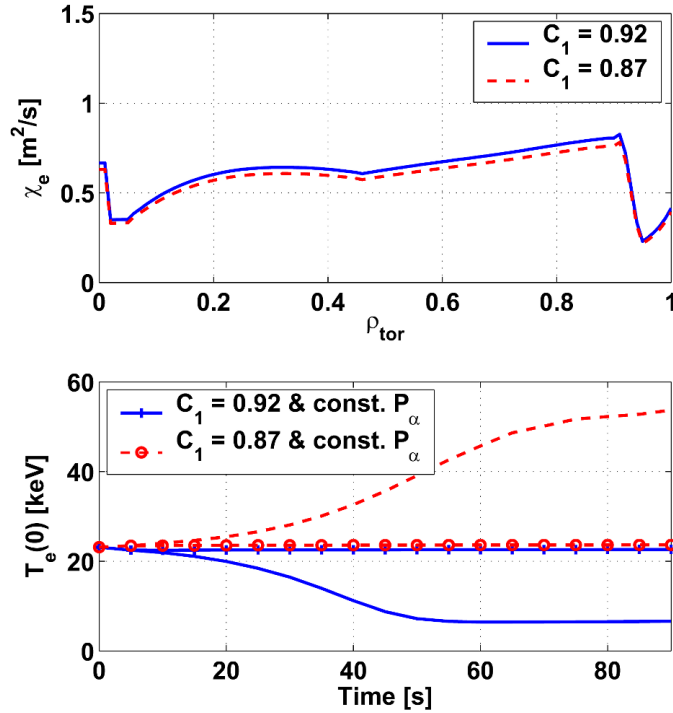


Figure 3.5: Comparison of electron temperature evolution calculated by CRONOS. The electron and ion heat conductivity profiles are multiplied by C_1 and frozen in time. When the alpha heating powers are constant, the electron temperature profiles are stabilized quickly

and an updated electromagnetic ITER description [63], in which the geometry of the poloidal field coils, limiters, passive stabilizers and diverters were slightly modified (see figure 7.2) Input profiles for the inductive 15MA H-mode ITER plasma are taken from the full tokamak discharge simulation introduced in chapter 5 in this thesis. The disturbances are generated in a pre-programmed manner by using the simple routine controlling heat conductivity profiles as explained in section 3.2.

The density profiles are prescribed with a flat profile shape and the electron temperature at the pedestal top is about 3keV. The external source profiles obtained from a time-slice of the full simulation is assumed to be non-varying in time. The H-L mode transition is simulated by increasing the level of heat conductivity instead of decreasing the additional H&CD power. The non-linear changes of the plasma-antenna coupling power during the disturbances are not explicitly considered. The ohmic and alpha particle heating powers are self-consistently calculated with the evolution of the plasma profiles at every time-step. Both the uncontrolled ELMs and fast H-L mode transitions are simulated with a time-step

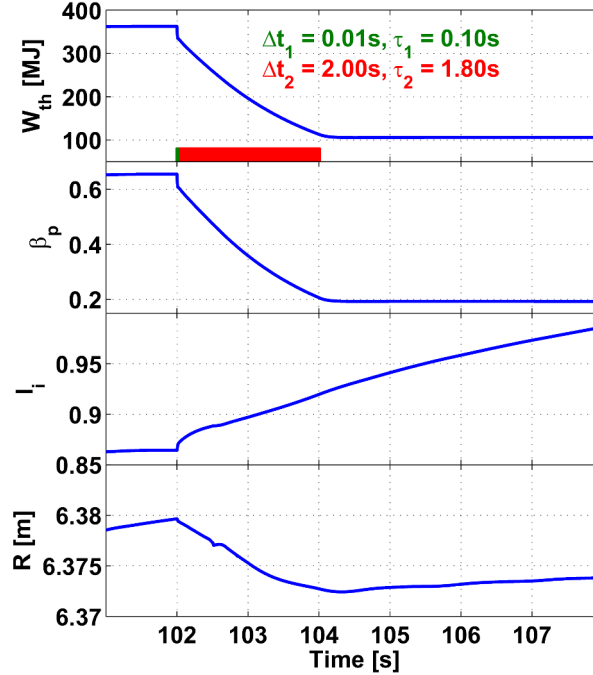


Figure 3.6: Dynamic plasma response to a pre-programmed fast H-L mode transition. The release of the plasma energy consists of two successive stages, fast energy release from the pedestal (green) and slow mode transition to L-mode (red). The radial plasma movement is underestimated in this simulation.

of 1ms.

The plasma current, position and shape controllers used in this simulation work are equivalent to those presented in reference [63] except the time constant of the first-order filter for the vertical plasma position. In this work, the time constant is set equal to the time-step of the simulations. The changes in the plasma dynamic responses due to this modification were checked with uncontrolled ELMs resulting in a fast vertical plasma movement. The simulated plasma dynamic responses with a time constant of 1ms, 3ms [63] and 7ms were almost indistinguishable.

3.3.1 First trial simulations and a bug

In the first trial simulations performed using the version of DINA-CH which was used for the full tokamak discharge simulator in chapter 5, the radial dynamic response during the L-H and H-L mode transitions was unfortunately underestimated. At the first stage of the

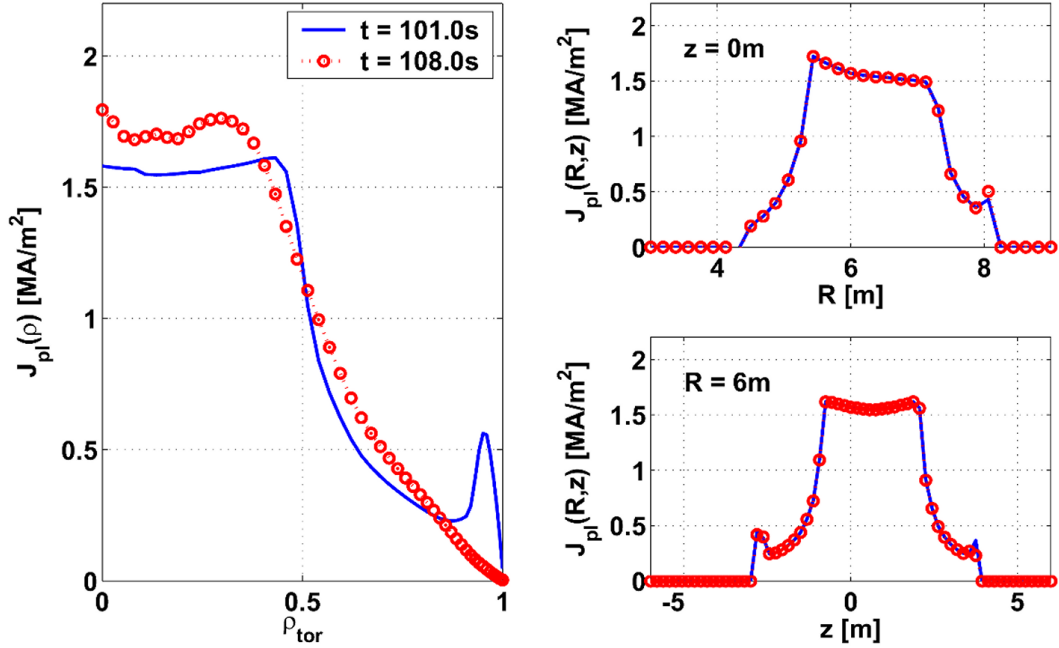


Figure 3.7: Comparison of 1D (left) and 2D (right) plasma current density profiles before and after a fast H-L mode transition. 2D plasma current density was frozen in time resulting in an artificial stabilization of the free-boundary plasma equilibrium evolution.

L-H mode transition with the pedestal energy loss (indicated in green in figure 3.6), β_p was reduced from 0.65 to 0.60 and l_i was increased a little, but less than expected. At the second stage of slow mode transition to L-mode (indicated in red in figure 3.6), the β_p was reduced as pre-programmed while the l_i was slowly increasing. The resulting radially inward plasma movement was less than 15mm. This value is very small compared with the expected one of about 100mm.

The reason for this smaller radial dynamic response was a bug in the source code. The shape of the 2D current profile used for the free-boundary equilibrium calculation had been fixed and re-scaled to the total plasma current during the simulation. Therefore, the initial 2D current profile was frozen in time, while the 1D current profile evolves as a result of the 1D transport calculation. These profile changes are shown in figure 3.7. The figure in the left compares 1D current profiles at different times before and after the disturbance. The figures in the right compare 2D current profiles along radial and vertical chords. This bug is fixed to study the free-boundary dynamic responses to the disturbances in this work. However, a consistent version for the full tokamak discharge simulator is now being prepared.

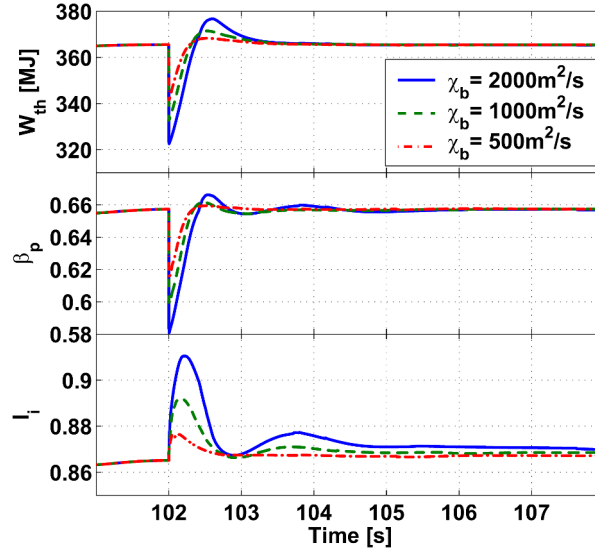


Figure 3.8: Dynamic plasma responses to pre-programmed uncontrolled ELMs. The amount of released plasma energy is varied by imposing a heat conductivity at the plasma boundary ($2000\text{m}^2\text{s}^{-1}$, $1000\text{m}^2\text{s}^{-1}$ and $500\text{m}^2\text{s}^{-1}$). The time traces of stored plasma energy, β_p and l_i are compared.

3.3.2 Uncontrolled ELMs

The uncontrolled ELMs in an H-mode ITER plasma are simulated with different heat conductivity values ($\chi_b = 500 \sim 2000\text{m}^2\text{s}^{-1}$) at the plasma boundary as shown in figure 3.8. Stored plasma energy of about $20 \sim 45\text{MJ}$ is released about in 1ms and recovered within $0.5 \sim 1.0\text{s}$. This cycle corresponds to a $1 \sim 2\text{Hz}$ ELM frequency. The decrease of β_p is about $0.04 \sim 0.08$ for the simulated plasma energy release from the pedestal. These values are similar to the value (0.05) given in the disturbance specifications. The fast increase of l_i is about 0.045 , when 43MJ of the plasma energy is released. However, this l_i change is smaller than expected one (see table 3.1). When 24MJ of plasma energy is released, the l_i increases by only about 0.01 . The slow increase of l_i up to 0.95 at a later time was not observed due to the pre-programmed recovery of the plasma profiles.

The evolution of the electron temperature and plasma current density profiles is shown in figure 3.9. The stored plasma energy is released from the pedestal resulting in the relaxation of the pedestal gradient. The current density profile shows a relatively small change due to the fast recovery of pedestal and a very slow radial current diffusion.

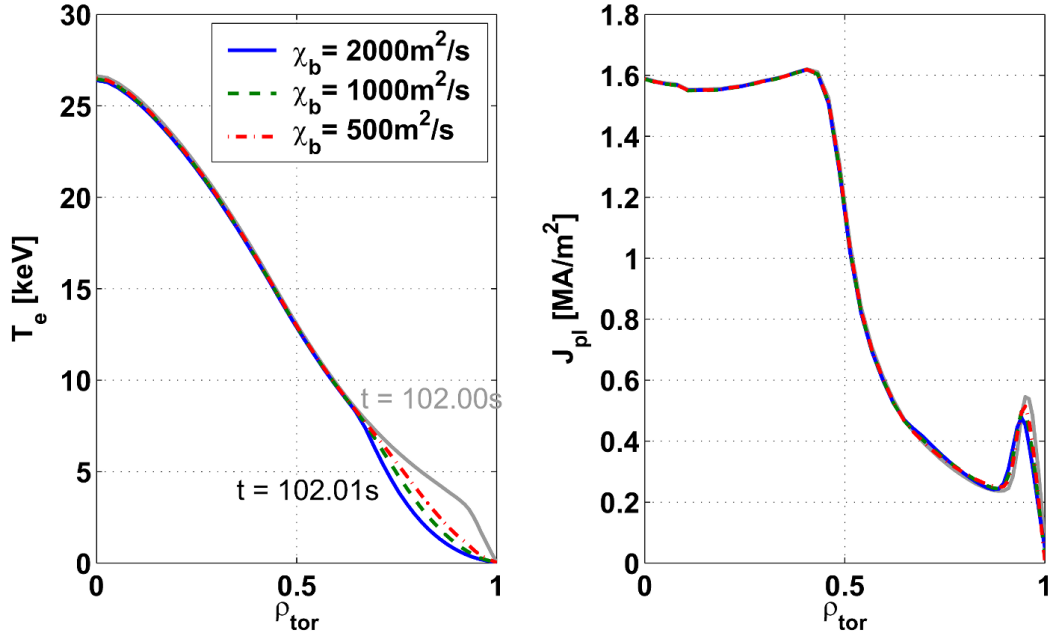


Figure 3.9: Dynamic plasma responses to pre-programmed uncontrolled ELMs. The evolutions of electron temperature and plasma current density profiles are compared. The stored plasma energy in the pedestal was released in 1ms. The plasma current density profile experienced a little change due to a slow current diffusion and a fast recovery of the pedestal.

The dynamic plasma responses are shown in figure 3.10. Larger releases of the plasma energy produce larger fluctuations in the total plasma current, radial and vertical position, and minor radius. The evolution of the 6 gaps between the plasma boundary and wall is shown in figure 3.11. The plasma position and shape are well-controlled overcoming the vertical instability during the disturbances. The separatrix expands during the release of plasma energy. Full recovery of the plasma current, position and shape was possible within 4 seconds. The given specifications of this disturbance and the observed plasma responses are summarized in table 3.1.

3.3.3 Fast H-L mode transition

The fast H-L mode transitions in ITER are simulated with several variants. The amount of released plasma energy and its rate of change in the second stage (slow mode transition to L-mode) have been varied.

Firstly, the amount of released plasma energy during the mode transition to L-mode

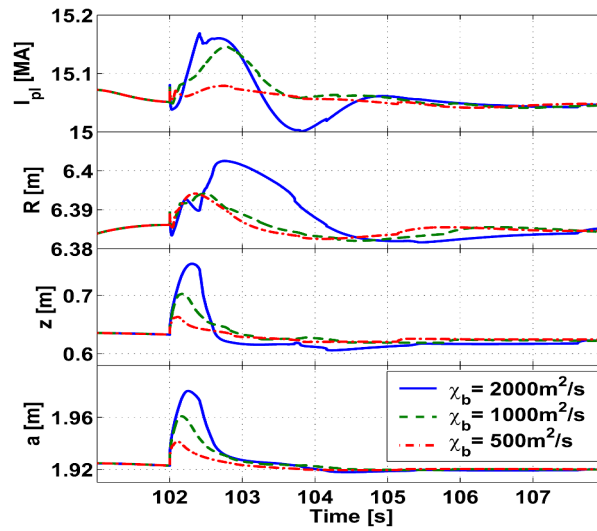


Figure 3.10: Dynamic plasma responses to pre-programmed uncontrolled ELMs. The time trace of the total plasma current, plasma centre and minor radius are compared. The fluctuations caused by the disturbances are stabilized quickly within 4 seconds.

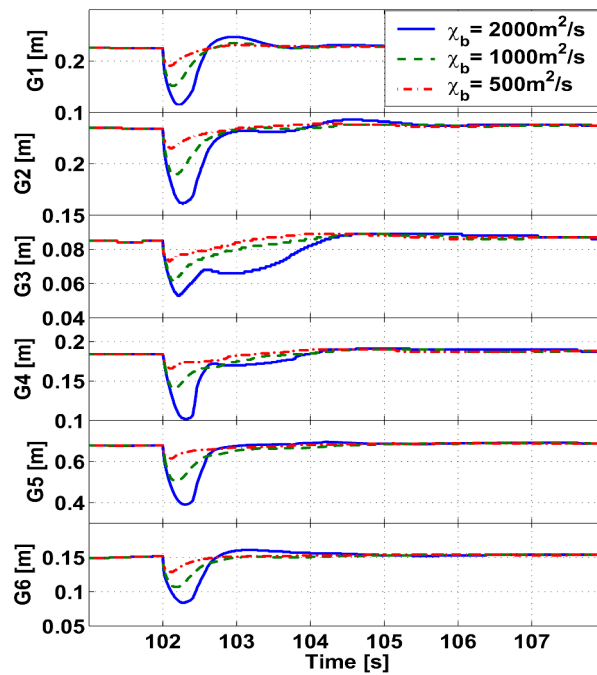


Figure 3.11: Dynamic plasma responses to pre-programmed uncontrolled ELMs. The time traces of the 6 gap measurements are compared. The fluctuations caused by the disturbances are stabilized quickly within 4 seconds.

Table 3.1: The given specification for uncontrolled ELMs and simulated dynamic plasma responses to the disturbances are summarised. The released plasma energy by the ELM is varied by imposing electron and ion heat conductivities at the plasma boundary. * indicates the specification at a later time as the plasma current diffuses.

Plasma responses	Given specifications	Simulation 1 ($\chi_b = 2000\text{m}^2/\text{s}$)	Simulation 2 ($\chi_b = 1000\text{m}^2/\text{s}$)	Simulation 3 ($\chi_b = 500\text{m}^2/\text{s}$)
W_{th} drop	-20~-25MJ in 200 μs	-43MJ in 1ms	-33MJ in 1ms	-24MJ in 1ms
β_p drop	-0.05 (0.65 to 0.60)	-0.077 in 1ms	-0.058 in 1ms	-0.043 in 1ms
$l_i(3)$ increase	+0.05 (0.85 to 0.90) +0.10 (0.85 to 0.95)*	+0.045 in 200ms +0.006 after 8s	+0.027 in 200ms +0.003 after 8s	+0.011 in 150ms +0.0015 after 8s
ΔR_{mag}	-	+15mm in 1s	+8mm in 500ms	+7mm in 350ms
ΔR_{mag}	-	+120mm in 300ms	+70mm in 200ms	+30mm in 100ms
Δa_{minor}	-	+60mm in 250ms	+38mm in 160ms	+19mm in 100ms
ΔI_{pl}	-	+100kA in 400ms	+80kA in 800ms	+30kA in 800ms
Shape transition	-	No	No	No

is varied with the period of the second stage, Δt_2 , as shown in figure 3.12. The speed of energy release is pre-programmed to be similar to the given specifications for this disturbance ($\tau_1 = 100\text{ms}$ and $\tau_2 = 1.8\text{s}$). The l_i increases fast as the edge bootstrap current is reduced by the relaxation of the pedestal pressure gradients. The slow increase of the l_i after the mode transition to L-mode is affected by the plasma boundary shape evolution. The details of this will be addressed later.

The evolution of the electron temperature and plasma current density profiles is shown in figure 3.13. The fast plasma energy release from the pedestal for 10ms significantly reduces the pedestal gradients and edge bootstrap currents. Then the mode transition to L-mode results in a decrease of the plasma temperature (pressure) across the entire plasma column.

The dynamic plasma responses are compared in figure 3.14. When Δt_2 is set to 1.8s, the

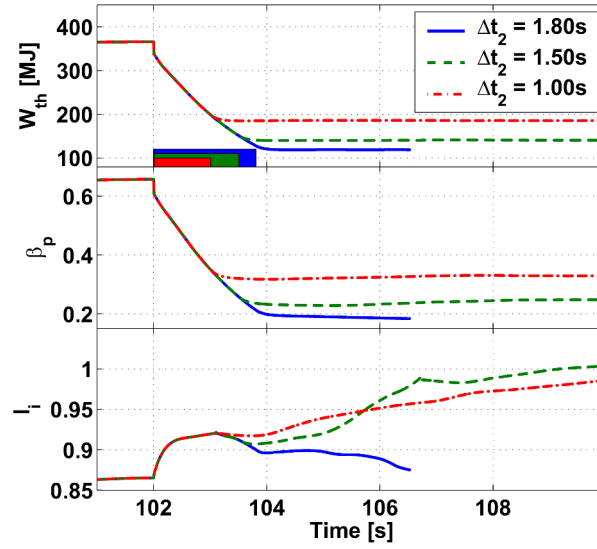


Figure 3.12: Dynamic plasma responses to pre-programmed fast H-L mode transitions. The amount of released plasma energy is varied by imposing the duration of slow energy release at second phase, Δt_2 . The time traces of stored plasma energy, β_p and l_i are compared.

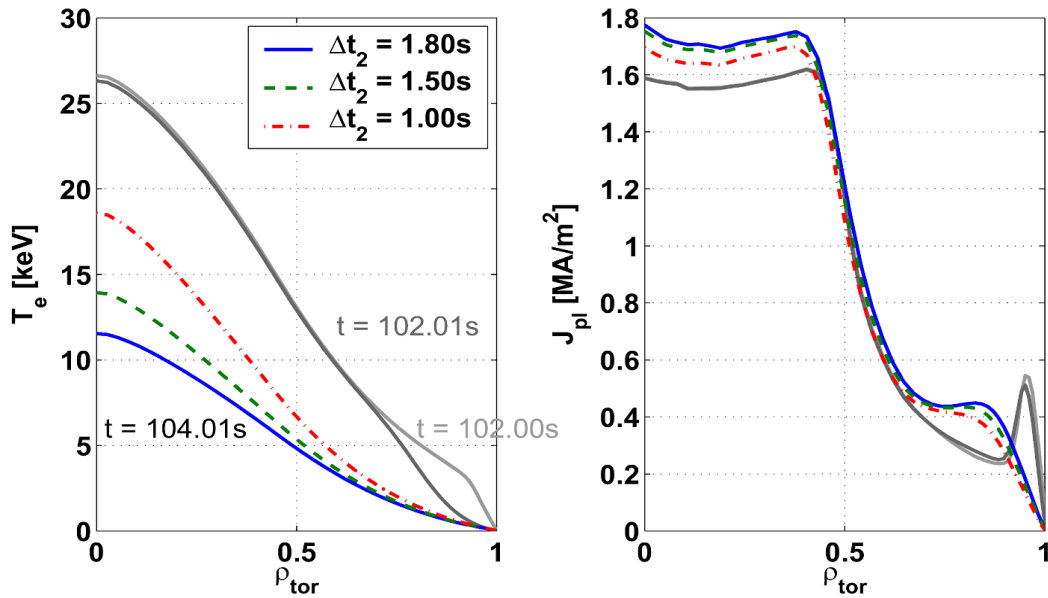


Figure 3.13: Dynamic plasma responses to pre-programmed fast H-L mode transitions. The evolutions of electron temperature and plasma current density profiles are compared. The stored plasma energy in the pedestal was released in 10ms at the first stage and the electron plasma temperature is slowly reduced during the mode transition to L-mode. The edge bootstrap current is reduced and diffuses into the plasma centre.

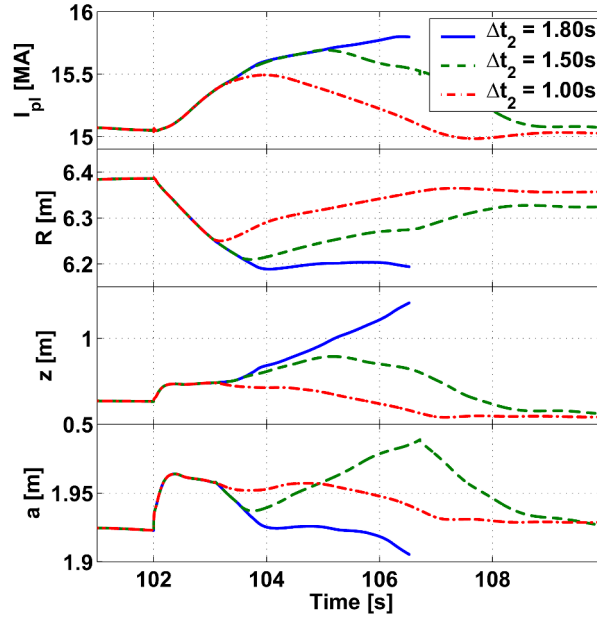


Figure 3.14: Dynamic plasma responses to pre-programmed fast H-L mode transitions. The time trace of the total plasma current, plasma centre and minor radius are compared. The fluctuations caused by the disturbances are stabilised within 10 seconds, unless the plasma experience a strong disturbance causing a VDE.

plasma experiences a VDE due to a large inward radial movement which makes the plasma limited and smaller in volume resulting in a decrease of l_i after the H-L mode transition as already shown in figure 3.12. When Δt_2 is reduced to 1.50s, although the plasma is limited for several seconds, it recovers a diverted shape. After the limiting phase, the total plasma current, position and minor radius are re-stabilized. The l_i is again closely linked to the plasma volume change as deduced from the similarity of its evolution to the minor radius variations. When Δt_2 is further reduced to 1.0s, the plasma is well-controlled without experiencing a shape transition. The fluctuations are quickly stabilized producing a monotonic increase of the l_i . In these simulations, the minimum inward movement caused by the disturbances is larger than 130mm. This is about 10 times larger than observed in the previous simulations with the frozen 2D current profile.

The evolutions of the 6 gaps are compared in figure 3.15. Full recovery of the total plasma current, position and shape is achieved within 10 seconds, unless the plasma experiences a strong disturbance causing a VDE. As the released plasma energy is smaller, the recovery takes less time. The given specifications of this disturbance and observed plasma responses

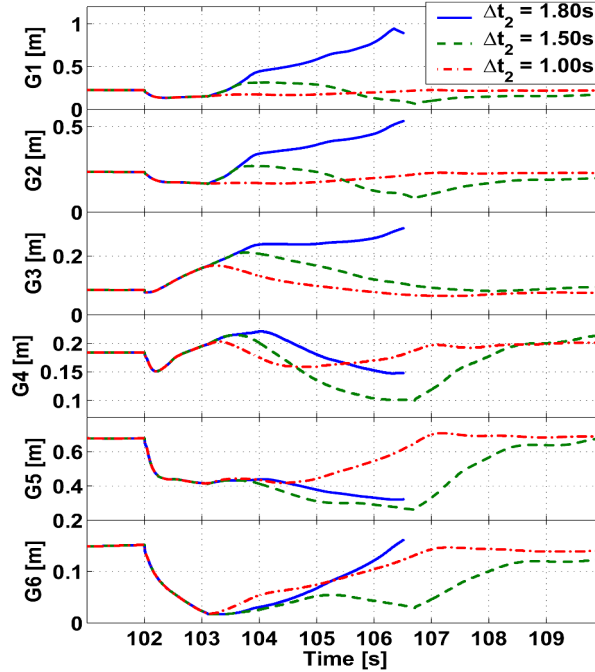


Figure 3.15: Dynamic plasma responses to pre-programmed fast H-L mode transitions. The time traces of the 6 gap measurements are compared.

are summarised in table 3.2. The specifications for fast H-L mode transitions, such as the decrease of β_p down to $0.1 \sim 0.2$, were not fully demonstrated due to the onset of a VDE.

Secondly, the speed of plasma energy release during the mode transition to L-mode is varied by changing the exponential time-scale in the second stage, τ_2 . In these simulations, Δt_2 is varied to produce same amount of plasma energy release as shown in figure 3.16. A fast plasma disturbance produced by imposing $\tau_2 = 1.30\text{s}$ causes the plasma to experience a VDE. This VDE is very similar to the previous one caused by a large plasma energy release.

The l_i decreases and fluctuates similar to the evolution of the minor radius shown in figure 3.17. As the release of plasma energy is slower, the recovery of a stable L-mode state is slightly easier. When τ_2 is set to 2.30s , the inward plasma movement is slow and small. The l_i monotonically increases after the disturbance. Full recovery of the total plasma current, position and shape again takes less than 10 seconds, unless the plasma experiences a strong disturbance causing a VDE. However, slowing down the release of plasma energy does not significantly reduce the recovery time (see figure 3.17).

Additional simulations have performed with an increased maximum control voltage in the

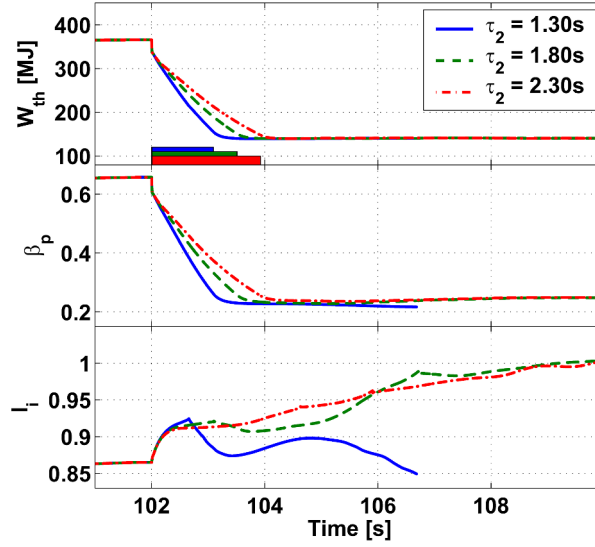


Figure 3.16: Dynamic plasma responses to pre-programmed fast H-L mode transitions. The speed of plasma energy release is varied by imposing the exponential time-scale of slow energy release at second phase, τ_2 . The time traces of stored plasma energy, β_p and l_i are compared.

vertical stabilization (VS) loop. The maximum VS voltage originally set to 6kV is increased to 9kV. However, this modification does not improve the controllability during the fast H-L mode transitions, because the VDEs observed in the previous simulations are caused by an inward plasma movement resulting in the plasma touching the wall located in the high field side (HFS). At that time, the vertical motion was not large and the voltage in the VS loop was not yet saturated. However, stronger and faster disturbances, such as larger uncontrolled ELMs than those simulated in this work, could be vertically unstable saturating the voltages in the VS loop.

3.4 Discussion

The specifications regarding the plasma disturbances in ITER has recently been updated. The capability of the present control systems in rejecting these disturbances is studied using a non-linear free-boundary equilibrium evolution code, DINA-CH. Uncontrolled ELMs and fast H-L mode transitions are pre-programmed. The target H-mode plasma is obtained from a full tokamak discharge simulation of the inductive 15MA ITER scenario 2. A routine controlling the stored plasma energy by modifying the plasma heat conductivity profiles is

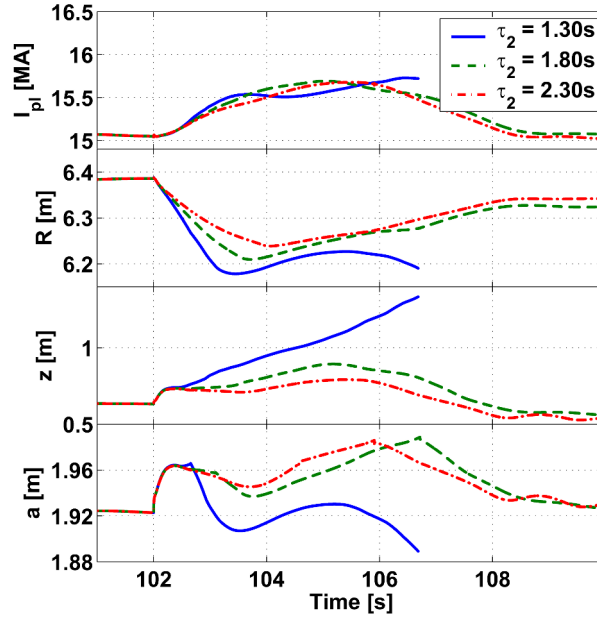


Figure 3.17: Dynamic plasma responses to pre-programmed fast H-L mode transitions. The time trace of the total plasma current, plasma centre and minor radius are compared. The fluctuations caused by the disturbances are stabilised within 10 seconds, unless the plasma experience a strong disturbance causing a VDE.

developed and used to pre-programme the plasma disturbances. A bug found in DINA-CH was investigated and fixed for this task.

Stronger uncontrolled ELMs than the given specifications were controllable with the present feedback control systems. However, the specifications for fast H-L mode transitions were not fully achievable due to a VDE caused by a strong inward plasma movement. A stepwise reduction of additional plasma heating and current drive powers before the H-L mode transition might be required with the present control systems, to reduce the β_p , although the precise details of the back-transitions are not well enough known to assure this could help. The maximum voltage in the VS loop seems not to need an increase for the updated disturbances, fast H-L transitions and uncontrolled ELMs. The disturbances not yet investigated in this task, such as a minor disruption and uncontrolled ELMs in ITER scenario 4, could be studied in a similar manner.

It is worth mentioning the challenges of this task. First, the target H-mode ITER plasma and the vacuum field produced by currents in the poloidal field coils and surrounding passive

conductors only represent a time-slice of the whole tokamak operation. Therefore, the dynamic responses reported in this chapter do not guarantee a successful disturbance rejection for whole ITER operation phase. Second, as briefly addressed before, the minimum time-step in the simulations are set to 1ms due to the computational performance and numerical stability. Although the time-step seems to be reasonably chosen for both the uncontrolled ELMs and fast H-L mode transitions, it is necessary to try a smaller time-step after identifying the numerical problems. One of the possible reasons is that the 2D rectangular grid used in the free-boundary plasma equilibrium evolution is not dense enough to distinguish small equilibrium changes made in a given time-step, therefore sometimes resulting in a jump. For smaller time-steps, the impact of discontinuous jumps could be larger for the controllers. Third, the requirements for plasma-wall clearance [28] may require a strategic modification to the shape references during the disturbances. This has not yet been attempted.

Table 3.2: The given specification for fast H-L mode transitions and simulated dynamic plasma responses to the disturbances are summarised. The released plasma energy during the transition to L-mode is varied by imposing the duration of slow energy release at second phase, Δt_2 . $\Delta t_1 (=10\text{ms})$ is same for all cases.

Plasma responses	Given specifications	Simulation 1 ($\Delta t_2 = 1.80\text{s}$)	Simulation 2 ($\Delta t_2 = 1.50\text{s}$)	Simulation 3 ($\Delta t_2 = 1.00\text{s}$)
W_{th} drop (Δt_1)	-20~-40MJ with t1=10~100ms	-29MJ with $\tau_1=100\text{ms}$	-29MJ with $\tau_1=100\text{ms}$	-29MJ with $\tau_1=100\text{ms}$
W_{th} drop (Δt_2)	Back to L-mode with $\tau_2 \sim 1.8\text{s}$	-210MJ with $\tau_2 = 1.8\text{s}$	-185MJ with $\tau_2 = 1.8\text{s}$	-138MJ with $\tau_2 = 1.8\text{s}$
β_p drop (Δt_1)	-0.05~-0.08 (0.65 to 0.60~0.57)	-0.05	-0.05	-0.05
β_p drop (Δt_2)	-0.37~-0.50 (0.60~0.57 to 0.10~0.20)	-0.40	-0.35	-0.26
$l_i(3)$ increase (Δt_1)	+0.05 (0.85 to 0.90)	+0.005	+0.005	+0.005
$l_i(3)$ increase (Δt_2)	+0.10~+0.25 (0.85 to 0.95~1.10)	+0.05	+0.052 +0.14 after 8s	+0.05 +0.12 after 8s
ΔR_{mag}	-	-190mm	-170mm	-130mm
Δz_{mag}	-	+100mm in 400ms VDE after 1.1s	+100mm in 400ms +200mm after 3s	+100mm in 400ms
Δa_{minor}	-	+40mm in 400ms	+40mm in 400ms +70mm after 4.7s	+40mm in 400ms
ΔI_{pl}	-	Increasing	+650kA after 3s	+450kA after 2s
Shape transition	-	Limited after 1.1s	Limited after 1.1s and diverted after 4.7s	No

Part II

Full tokamak discharge simulations

Chapter 4

Full tokamak discharge simulator

In this chapter, we present the combined full tokamak discharge simulator developed by combining DINA-CH and CRONOS. Although both codes have the same equilibrium and transport physics, they have been used in different research areas. DINA-CH is a non-linear free-boundary plasma equilibrium evolution code which self-consistently calculates dynamic response of the free-boundary equilibrium to currents flowing in the PF coil and surrounding conducting systems. CRONOS is an advanced transport modelling code which self-consistently calculates plasma profile evolution with source profiles. These two codes are combined maintaining their original strengths in each research area. Firstly, we introduce the plasma equilibrium and transport implemented in the both codes. Secondly, we present algorithms used for evolving the free-boundary plasma equilibrium in DINA-CH and the plasma transport in CRONOS. Lastly, we present the code coupling scheme and challenges met during the code integration. In this chapter, we derive ‘standard’ formulations of the plasma equilibrium and transport in MKS units. These formulations are compared with both CRONOS and DINA-CH ones which are additionally introduced in Appendix A. Units are omitted in deriving these formulations for simplicity.

4.1 Plasma equilibrium

Both DINA-CH and CRONOS calculate the plasma equilibrium using the non-linear Grad-Shafranov equation [1]. However, while CRONOS calculates 2D fixed boundary plasma equilibrium [64] taking the plasma boundary as an input, DINA-CH calculates 2D free-boundary

plasma equilibrium consistent with currents in the PF coil and surrounding conducting coil systems.

4.1.1 Non-linear Grad-Shafranov equation

The plasma equilibrium is determined by the following set of coupled equations assuming stationary ideal MHD conditions.

$$\mathbf{j} \times \mathbf{B} = \nabla p \quad (4.1)$$

$$\nabla \cdot \mathbf{B} = 0 \quad (4.2)$$

$$\nabla \times \mathbf{B} = \mu_0 \mathbf{j} \quad (4.3)$$

where p , \mathbf{j} and \mathbf{B} are respectively the plasma pressure, current density and magnetic field.

Introducing a flux function ψ defined as the poloidal flux per radian in ϕ and relating $\nabla \cdot \mathbf{B} = 0$ and $\mathbf{B} \cdot \nabla \psi = 0$, the poloidal component of the magnetic fields can be expressed as follows.

$$B_R = -\frac{1}{R} \frac{\partial \psi}{\partial z}, \quad B_z = \frac{1}{R} \frac{\partial \psi}{\partial R}. \quad (4.4)$$

From the symmetry of \mathbf{j} and \mathbf{B} in the force balance equation, the poloidal component of the plasma current can be expressed using a current flux function f .

$$j_R = -\frac{1}{R} \frac{\partial f}{\partial z}, \quad j_z = \frac{1}{R} \frac{\partial f}{\partial R}. \quad (4.5)$$

Comparing these relations with Ampère's law

$$j_R = -\frac{1}{\mu_0} \frac{\partial B_\phi}{\partial z}, \quad j_z = \frac{1}{\mu_0 R} \frac{\partial (RB_\phi)}{\partial R}, \quad (4.6)$$

the current flux function f is given as

$$f = \frac{RB_\phi}{\mu_0}. \quad (4.7)$$

Since the plasma pressure p is a function of ψ , the poloidal current function f is also a function of ψ .

Decomposing the poloidal and toroidal components of the plasma current and magnetic fields in the force balance equation

$$\mathbf{j}_p \times \mathbf{i}_\phi B_\phi + j_\phi \mathbf{i}_\phi \times \mathbf{B}_p = \nabla p, \quad (4.8)$$

and substituting the poloidal components using the flux functions

$$\mathbf{B}_p = \frac{1}{R}(\nabla\psi \times \mathbf{i}_\phi) \quad \text{and} \quad \mathbf{j}_p = \frac{1}{R}(\nabla f \times \mathbf{i}_\phi), \quad (4.9)$$

the force balance equation can be rewritten as

$$j_\phi = R \frac{dp}{d\psi} + \frac{\mu_0}{R} f \frac{df}{d\psi}. \quad (4.10)$$

The toroidal current density, j_ϕ , can also be written in terms of ψ using Ampère's law as follows

$$-\mu_0 R j_\phi = R \frac{\partial}{\partial R} \left(\frac{1}{R} \frac{\partial \psi}{\partial R} \right) + \frac{\partial^2 \psi}{\partial z^2}. \quad (4.11)$$

Substituting the j_ϕ into this equation, the non-linear Grad-Shafranov equation (standard formulation with MKS units) is written as

$$R \frac{\partial}{\partial R} \left(\frac{1}{R} \frac{\partial \psi}{\partial R} \right) + \frac{\partial^2 \psi}{\partial z^2} = -\mu_0 R \left(R \frac{dp}{d\psi} - \frac{\mu_0}{2R} \frac{df^2}{d\psi} \right) = -\mu_0 R^2 \frac{dp}{d\psi} - \mu_0^2 f \frac{df}{d\psi}. \quad (4.12)$$

The non-linear Grad-Shafranov equations in DINA-CH and CRONOS are derived using different units and expressions. The detail derivations are shown in Appendix A.1.

DINA-CH : CGS units

$$R \frac{\partial}{\partial R} \left(\frac{1}{R} \frac{\partial \psi}{\partial R} \right) + \frac{\partial^2 \psi}{\partial z^2} = -4\pi R^2 \frac{dp}{d\psi} - \frac{1}{2} \frac{dF^2}{d\psi} = -4\pi R^2 \frac{dp}{d\psi} - \left(\frac{4\pi}{c} \right)^2 f \frac{df}{d\psi}, \quad (4.13)$$

where

$$F = RB_\phi = \frac{4\pi f}{c}.$$

CRONOS : MKS units

$$R \frac{\partial}{\partial R} \left(\frac{1}{R} \frac{\partial \psi}{\partial R} \right) + \frac{\partial^2 \psi}{\partial z^2} = -R^2 \frac{dp_1}{d\psi} - F \frac{dF}{d\psi} = -\mu_0 R^2 \frac{dp}{d\psi} - \mu_0^2 f \frac{df}{d\psi}, \quad (4.14)$$

where

$$F = RB_\phi = \mu_0 f, \quad p_1 = \mu_0 p.$$

4.1.2 Free-boundary plasma equilibrium

The fixed boundary plasma equilibrium is determined by solving the non-linear Grad-Shafranov equation with the toroidal plasma current density j_ϕ for a given plasma boundary. In the case of calculating a free-boundary plasma equilibrium, external circuit currents are additionally taken into account in solving the Grad-Shafranov equation.

$$R \frac{\partial}{\partial R} \left(\frac{1}{R} \frac{\partial \psi}{\partial R} \right) + \frac{\partial^2 \psi}{\partial z^2} = \begin{cases} -\mu_0 R j_\phi & \text{if } (R, z) \in S \\ -\mu_0 \sum_{i=1}^N R_i I_i \delta(R - R_i) \delta(z - z_i) & \text{if } (R, z) \notin S \end{cases} \quad (4.15)$$

where N external toroidal circuits with current I_i are located in the position (R_i, z_i) . S is the poloidal cross-section of the plasma. The plasma boundary is iteratively determined by defining the boundary flux of the plasma.

4.2 Plasma transport

Both DINA-CH and CRONOS calculate the plasma transport by solving a set of coupled 1D plasma transport equations averaged on the magnetic flux surface, such as the plasma current diffusion, particle and heat transport. CRONOS is a transport modelling code, in which all the transport equations are self-consistently calculated while the evolution of the plasma boundary is given as an input. On the other hand, DINA-CH is a free-boundary plasma equilibrium evolution code which calculates the plasma current diffusion self-consistently with the evolution of the free-boundary plasma equilibrium. In this code, the coupling between the plasma current diffusion and the particle and heat transport is slightly relaxed to improve the computational performance.

4.2.1 Magnetic flux surface averaging technique

The average of an arbitrary quantity A over a magnetic surface S which is labeled by ρ is defined

$$\langle A \rangle = \frac{\partial}{\partial V} \int_V A dV = \frac{1}{V'} \int_S A \frac{dS}{|\nabla \rho|}, \quad (4.16)$$

where

$$V' = \frac{\partial V}{\partial \rho} = \int_S \frac{dS}{|\nabla \rho|}. \quad (4.17)$$

V is the volume enclosed inside the magnetic surface S . This averaging has the properties (see Appendix A.2 for proofs),

$$\langle \nabla \cdot \mathbf{H} \rangle = \frac{\partial}{\partial V} \langle \mathbf{H} \cdot \nabla V \rangle, \quad \forall \mathbf{H}, \quad (4.18)$$

$$\frac{d}{dt} (V' \langle A \rangle) = V' \left\langle \frac{\partial A}{\partial t} \right\rangle + \frac{\partial}{\partial \rho} \langle A \mathbf{u}_\rho \cdot \nabla V \rangle, \quad \forall A, \quad (4.19)$$

where d/dt is the time derivative at a fixed ρ and $\partial/\partial t$ is the time derivative at a fixed point (R, z) . Using these properties, the 1D transport equations defined on the flux surface can have the time derivative d/dt .

The velocity of a constant ρ surface \mathbf{u}_ρ is defined by

$$\frac{d\rho}{dt} = \frac{\partial \rho}{\partial t} + \mathbf{u}_\rho \cdot \nabla \rho = 0 \quad (4.20)$$

4.2.2 Magnetic field diffusion

The 1D magnetic field diffusion equation can be derived starting from the generalized Ohm's law averaged on the magnetic flux surface.

$$\langle \mathbf{j} \cdot \mathbf{B} \rangle = \sigma \langle \mathbf{E} \cdot \mathbf{B} \rangle + \langle \mathbf{j}_{\text{ni}} \cdot \mathbf{B} \rangle \quad (4.21)$$

Using the following definitions

$$\mathbf{B} = \mathbf{B}_p + \mathbf{B}_\phi = \frac{1}{R} \nabla \psi \times \mathbf{i}_\phi + B_\phi \mathbf{i}_\phi \quad (4.22)$$

$$\mathbf{j} = \mathbf{j}_p + \mathbf{j}_\phi = \frac{1}{R} \nabla f \times \mathbf{i}_\phi + j_\phi \mathbf{i}_\phi \quad (4.23)$$

$$\oint_C \mathbf{E} \cdot d\mathbf{l} = E_\phi (2\pi R) - 2\pi \frac{\partial \psi}{\partial t} = 0 \quad (4.24)$$

$$\frac{d\psi}{dt} = \frac{\partial \psi}{\partial t} + \mathbf{u}_\rho \cdot \nabla \psi \quad (4.25)$$

$$\frac{\partial \psi}{\partial t} + \mathbf{u}_\psi \cdot \nabla \psi = 0 \quad (4.26)$$

$$\nabla \psi = \nabla \rho \frac{\partial \psi}{\partial \rho} \quad (4.27)$$

$\langle \mathbf{j} \cdot \mathbf{B} \rangle$ is given as (see Appendix A.3)

$$\langle \mathbf{j} \cdot \mathbf{B} \rangle = -f^2 \frac{1}{V'} \frac{\partial}{\partial \rho} \left(\frac{c_2}{f} \frac{\partial \psi}{\partial \rho} \right), \quad (4.28)$$

where

$$c_2 = \left\langle \frac{|\nabla \rho|^2}{R^2} \right\rangle = \int_S \frac{|\nabla \rho|^2}{R^2} \frac{dS}{|\nabla \rho|}. \quad (4.29)$$

$\langle \mathbf{E} \cdot \mathbf{B} \rangle$ is given as (see Appendix A.3)

$$\langle \mathbf{E} \cdot \mathbf{B} \rangle = -\mu_0 f \left\langle \frac{1}{R^2} \right\rangle \frac{d\psi}{dt}. \quad (4.30)$$

Inserting these $\langle \mathbf{E} \cdot \mathbf{B} \rangle$ and $\langle \mathbf{j} \cdot \mathbf{B} \rangle$ into the generalized Ohm's law, we have

$$\begin{aligned} \frac{d\psi}{dt} &= -\frac{\langle \mathbf{j} \cdot \mathbf{B} \rangle}{\sigma \mu_0 f \left\langle \frac{1}{R^2} \right\rangle} + \frac{\langle \mathbf{j}_{ni} \cdot \mathbf{B} \rangle}{\sigma \mu_0 f \left\langle \frac{1}{R^2} \right\rangle} \\ &= \frac{f}{\sigma \mu_0 \left\langle \frac{1}{R^2} \right\rangle} \frac{\partial}{\partial \rho} \left(\frac{c_2}{f} \frac{\partial \psi}{\partial \rho} \right) + \frac{\langle \mathbf{j}_{ni} \cdot \mathbf{B} \rangle}{\sigma \mu_0 f \left\langle \frac{1}{R^2} \right\rangle} \\ &= \frac{f}{\sigma \mu_0 c_3} \frac{\partial}{\partial \rho} \left(\frac{c_2}{f} \frac{\partial \psi}{\partial \rho} \right) + \frac{V' \langle \mathbf{j}_{ni} \cdot \mathbf{B} \rangle}{\sigma \mu_0 f c_3}, \end{aligned} \quad (4.31)$$

where

$$c_3 = \left\langle \frac{1}{R^2} \right\rangle V'. \quad (4.32)$$

The magnetic field diffusion equations in DINA-CH and CRONOS are respectively expressed as (see Appendix A.3)

DINA-CH : CGS units

$$\frac{d\psi}{dt} = \frac{c c_2 C_3}{4\pi\sigma} \frac{\partial^2 \psi}{\partial \rho^2} + \frac{c C_3^2 \rho}{4\pi\sigma} \frac{\partial}{\partial \rho} \left(\frac{c_2}{C_3 \rho} \right) \frac{\partial \psi}{\partial \rho} + \frac{V'}{4\pi\sigma\rho} \langle \mathbf{j}_{ni} \cdot \mathbf{B} \rangle, \quad (4.33)$$

where $C_3 = c_3^{-1}$ and $f = c\rho/c_3$.

CRONOS : MKS units

$$\frac{d\psi}{dt} = \frac{c_2}{\sigma \mu_0 c_3} \frac{\partial^2 \psi}{\partial \rho^2} + \frac{F}{\sigma \mu_0 c_3} \frac{\partial}{\partial \rho} \left(\frac{c_2}{F} \right) \frac{\partial \psi}{\partial \rho} + \frac{V'}{\sigma F c_3} \langle \mathbf{j}_{ni} \cdot \mathbf{B} \rangle, \quad (4.34)$$

where $F = RB_\phi = \mu_0 f$.

The evolution of the poloidal flux at the plasma boundary is given by

$$\begin{aligned}\frac{d\psi_b}{dt} &= \frac{d\psi_{pl}}{dt} + \frac{d\psi_{ext}}{dt} \\ &= \frac{d}{dt} (L_p I_p) + \frac{d\psi_{ext}}{dt}.\end{aligned}\quad (4.35)$$

Using an implicit discretization scheme

$$\frac{\psi_b^{n+1} - \psi_b^n}{\tau} = \frac{L_p^{n+1} I_p^{n+1} - L_p^n I_p^n}{\tau} + \frac{\psi_{ext}^{n+1} - \psi_{ext}^n}{\tau}\quad (4.36)$$

and the relation of the total plasma current (see appendix A.4)

$$I_p = -\frac{1}{2\pi\mu_0} c_2 V' \frac{\partial\psi}{\partial\rho} \Big|_{\rho=\rho_b},\quad (4.37)$$

the mixed boundary condition can be written as

$$\frac{1}{2\pi\mu_0} c_2 V' L_p^{n+1} \frac{\partial\psi}{\partial\rho} \Big|_b^{n+1} + \psi_b^{n+1} = \psi_b^n + \psi_{ext}^{n+1} - \psi_{ext}^n - L_p^n I_p^n.\quad (4.38)$$

In the fixed boundary equilibrium case, there are usually 5 options for imposing the boundary condition:

1. Prescribe the external poloidal flux, ψ_{ext}^{n+1} .
2. Prescribe the boundary poloidal flux, $\psi_b(t)$.
3. Prescribe the boundary loop voltage, $V_{loop}(t) = -2\pi \frac{d\psi}{dt} \Big|_b + \frac{1}{q_b} \frac{d\Phi}{dt} \Big|_b$.
4. Prescribe the boundary surface voltage, $V_{surf}(t) = -2\pi \frac{d\psi}{dt} \Big|_b$.
5. Prescribe the total plasma current, $I_p(t) = -\frac{1}{2\pi\mu_0} c_2 V' \frac{\partial\psi}{\partial\rho} \Big|_b$.

In the free-boundary equilibrium case, the poloidal flux at the plasma boundary ψ_b^{n+1} is self-consistently calculated with the external poloidal flux ψ_{ext}^{n+1} provided by currents in the PF coil and surrounding conducting systems.

4.2.3 Particle transport

The evolution of the density of a species indicated by j is described by the continuity equation

$$\frac{\partial n_j}{\partial t} + \nabla \cdot (n_j \mathbf{u}_j) = S_j. \quad (4.39)$$

Averaging this equation over the flux surface and multiplying by V' , we have

$$\left\langle \frac{\partial n_j}{\partial t} \right\rangle V' + \langle \nabla \cdot (n_j \mathbf{u}_j) \rangle V' = \langle S_j \rangle V'. \quad (4.40)$$

Using the properties of the flux surface average, this equation can be rewritten as

$$\frac{d}{dt} (V' \langle n_j \rangle) - \frac{\partial}{\partial \rho} \langle n_j \mathbf{u}_\rho \cdot \nabla V \rangle + \frac{\partial}{\partial V} \langle n_j \mathbf{u}_j \cdot \nabla V \rangle V' = \langle S_j \rangle V'. \quad (4.41)$$

Converting $\nabla V = \nabla \rho \frac{\partial V}{\partial \rho}$, this equation is further rewritten as

$$\frac{d}{dt} (V' \langle n_j \rangle) + \frac{\partial}{\partial \rho} [\langle n_j (\mathbf{u}_j - \mathbf{u}_\rho) \cdot \nabla \rho \rangle V'] = \langle S_j \rangle V'. \quad (4.42)$$

Defining the particle flux relative to a constant ρ surface by $\Gamma_j = \langle n_j (\mathbf{u}_j - \mathbf{u}_\rho) \cdot \nabla \rho \rangle$, the final equation can be simplified as

$$\frac{d}{dt} (n_j V') + \frac{\partial}{\partial \rho} (\Gamma_j V') = S_j V'. \quad (4.43)$$

Here the density and source are defined as functions of ρ . The particle flux can be defined as a sum of diffusion (D) and inward pinch velocity (\mathbf{V}_p) terms by

$$\Gamma_j = n_j (\mathbf{u}_j - \mathbf{u}_\rho) = -D \nabla n_j + n_j \mathbf{V}_p. \quad (4.44)$$

Using this definition, the particle flux relative to a constant ρ surface is written as

$$\Gamma_j = -D \langle |\nabla \rho|^2 \rangle \frac{\partial n_j}{\partial \rho} + n_j \langle \mathbf{V}_p \cdot \nabla \rho \rangle. \quad (4.45)$$

The particle transport equations in DINA-CH and CRONOS are identical.

4.2.4 Electron heat transport

Neglecting the viscosity terms, the energy balance equation of the electrons can be written as

$$\frac{3}{2} \frac{\partial p_e}{\partial t} + \nabla \cdot \left(\mathbf{q}_e + \frac{5}{2} p_e \mathbf{u}_e \right) = \mathbf{j} \cdot \mathbf{E} - Q_{ei} - \mathbf{u}_i \cdot \nabla p_i + Q_e, \quad (4.46)$$

where p_e and p_i are respectively the electron and ion pressure. \mathbf{u}_e and \mathbf{u}_i are respectively the electron and ion velocities and \mathbf{q}_e is the electron heat flux. Q_{ei} is the electron-ion equipartition power and Q_e is the electron heat source.

Since $\mathbf{j} = \mathbf{j}_e + \mathbf{j}_i \approx \mathbf{j}_e$, j^2 can be given as

DINA-CH : CGS units

$$j^2 = \mathbf{j} \cdot \mathbf{j} = \sigma_{\parallel} \left(\mathbf{E} + \frac{\mathbf{u}_e \times \mathbf{B}}{c} \right) \cdot \mathbf{j} = \sigma_{\parallel} \mathbf{E} \cdot \mathbf{j} + \sigma_{\parallel} \mathbf{u}_e \cdot \frac{(\mathbf{j} \times \mathbf{B})}{c} = \sigma_{\parallel} \mathbf{E} \cdot \mathbf{j} + \sigma_{\parallel} \mathbf{u}_e \cdot \nabla p \quad (4.47)$$

CRONOS : MKS units

$$j^2 = \mathbf{j} \cdot \mathbf{j} = \sigma_{\parallel} (\mathbf{E} + \mathbf{u}_e \times \mathbf{B}) \cdot \mathbf{j} = \sigma_{\parallel} \mathbf{E} \cdot \mathbf{j} + \sigma_{\parallel} \mathbf{u}_e \cdot (\mathbf{j} \times \mathbf{B}) = \sigma_{\parallel} \mathbf{E} \cdot \mathbf{j} + \sigma_{\parallel} \mathbf{u}_e \cdot \nabla p \quad (4.48)$$

From these equations, $\mathbf{j} \cdot \mathbf{E}$ is given as

$$\mathbf{j} \cdot \mathbf{E} = \mathbf{u}_e \cdot \nabla p + \frac{j^2}{\sigma_{\parallel}} = \mathbf{u}_e \cdot \nabla p + Q_{ohm}, \quad (4.49)$$

where Q_{ohm} is the ohmic heat source.

Using this expression, the energy balance equation of the electrons is rewritten as

$$\frac{3}{2} \frac{\partial p_e}{\partial t} + \nabla \cdot \left(\mathbf{q}_e + \frac{5}{2} p_e \mathbf{u}_e \right) - \mathbf{u}_e \cdot \nabla p + \mathbf{u}_i \cdot \nabla p_i = Q_e + Q_{ohm} - Q_{ei}. \quad (4.50)$$

Averaging this equation over the flux surface and multiplying by V' , we have

$$\frac{3}{2} \left\langle \frac{\partial p_e}{\partial t} \right\rangle V' + \left\langle \nabla \cdot \left(\mathbf{q}_e + \frac{5}{2} p_e \mathbf{u}_e \right) \right\rangle V' - \langle \mathbf{u}_e \cdot \nabla p + \mathbf{u}_i \cdot \nabla p_i \rangle V' = \langle Q_e + Q_{ohm} - Q_{ei} \rangle V'. \quad (4.51)$$

The left-hand side of this equation can be rewritten as (see Appendix A.5)

$$\begin{aligned} & \frac{3}{2} \left\langle \frac{\partial p_e}{\partial t} \right\rangle V' + \left\langle \nabla \cdot \left(\mathbf{q}_e + \frac{5}{2} p_e \mathbf{u}_e \right) \right\rangle V' - \langle \mathbf{u}_e \cdot (\nabla p - \nabla p_i) \rangle V' \\ &= \frac{3}{2V'^{2/3}} \frac{d}{dt} (p_e V'^{5/3}) + \frac{\partial}{\partial \rho} \left[\left(q_e + \frac{5}{2} T_e \Gamma_e \right) V' \right] + \frac{\Gamma_e}{n_e} \frac{\partial p_e}{\partial \rho} V'. \end{aligned} \quad (4.52)$$

The electron heat transport equation is finally given by

$$\frac{3}{2} \frac{d}{dt} (p_e V'^{5/3}) + V'^{2/3} \frac{\partial}{\partial \rho} \left[\left(q_e + \frac{5}{2} T_e \Gamma_e \right) V' \right] = V'^{5/3} \left(Q_e + Q_{ohm} - Q_{ei} + \frac{\Gamma_e}{n_e} \frac{\partial p_e}{\partial \rho} \right). \quad (4.53)$$

In this equation, the electron heat flux and sources generally defined as

$$\mathbf{q}_e = -\chi_e n_e \nabla T_e - p_e V_e^q \nabla \rho, \quad (4.54)$$

$$q_e = \langle \mathbf{q}_e \cdot \nabla \rho \rangle = -\chi_e n_e \langle |\nabla \rho|^2 \rangle \frac{\partial T_e}{\partial \rho} - p_e V_e^q \langle |\nabla \rho|^2 \rangle, \quad (4.55)$$

$$Q_e = Q_{e,add} + Q_{e,fus} - Q_{line} - Q_{cyclo} - Q_{brem}, \quad (4.56)$$

where χ_e and V_e^q are respectively the electron heat conductivity and convective velocity. $Q_{e,add}$ and $Q_{e,fus}$ are respectively the additional electron heat source and alpha particle self-heating power to electrons. Q_{line} , Q_{cyclo} and Q_{brem} are respectively the line radiation, cyclotron and bremsstrahlung heat losses.

The electron heat transport equations in DINA-CH and CRONOS are identical.

4.2.5 Ion heat transport

Neglecting the viscosity terms, the energy balance equation of the ions can be written as

$$\frac{3}{2} \frac{\partial p_i}{\partial t} + \nabla \cdot \left(\mathbf{q}_i + \frac{5}{2} p_i \mathbf{u}_i \right) = Q_{ei} + \mathbf{u}_i \cdot \nabla p_i + Q_i, \quad (4.57)$$

where \mathbf{q}_i is the ion heat flux and Q_i is the ion heat source. Averaging this equation over the flux surface and multiplying by V' , we have

$$\frac{3}{2} \left\langle \frac{\partial p_i}{\partial t} \right\rangle V' + \left\langle \nabla \cdot \left(\mathbf{q}_i + \frac{5}{2} p_i \mathbf{u}_i \right) \right\rangle V' - \langle \mathbf{u}_i \cdot \nabla p_i \rangle V' = \langle Q_i + Q_{ei} \rangle V'. \quad (4.58)$$

The left hand side of the above equation is rewritten as (see Appendix A.6)

$$\begin{aligned} & \frac{3}{2} \left\langle \frac{\partial p_i}{\partial t} \right\rangle V' + \left\langle \nabla \cdot \left(\mathbf{q}_i + \frac{5}{2} p_i \mathbf{u}_i \right) \right\rangle V' - \langle \mathbf{u}_i \cdot \nabla p_i \rangle V' \\ &= \frac{3}{2V'^{2/3}} \frac{d}{dt} (p_i V'^{5/3}) + \frac{\partial}{\partial \rho} \left[\left(q_i + \frac{5}{2} T_i \Gamma_i \right) V' \right] + \frac{\Gamma_e}{n_e} \frac{\partial p_i}{\partial \rho} V'. \end{aligned} \quad (4.59)$$

The ion heat transport equation is finally given by

$$\frac{3}{2} \frac{d}{dt} (p_i V'^{5/3}) + V'^{2/3} \frac{\partial}{\partial \rho} \left[\left(q_i + \frac{5}{2} T_i \Gamma_i \right) V' \right] = V'^{5/3} \left(Q_i + Q_{ei} + \frac{\Gamma_e}{n_e} \frac{\partial p_i}{\partial \rho} \right). \quad (4.60)$$

In this equation, the ion heat flux and sources are generally given as

$$\mathbf{q}_i = -\chi_i n_i \nabla T_i - p_i V_i^q \nabla \rho, \quad (4.61)$$

$$q_e = \langle \mathbf{q}_i \cdot \nabla \rho \rangle = -\chi_i n_i \langle |\nabla \rho|^2 \rangle \frac{\partial T_i}{\partial \rho} - p_i V_i^q \langle |\nabla \rho|^2 \rangle, \quad (4.62)$$

$$Q_i = Q_{i,add} + Q_{i,fus}, \quad (4.63)$$

where χ_i and V_i^q are respectively the ion heat conductivity and convective velocity. $Q_{i,add}$ and $Q_{i,fus}$ are respectively the additional ion heat source and alpha particle self-heating power to ions.

The ion heat transport equations in DINA-CH and CRONOS are identical.

4.3 Plasma transport evolution scheme in CRONOS

The transport equations of the magnetic field, particles and heat can be rewritten in the following form which can be solved in either implicit or explicit mode.

$$\frac{dF}{dt} = A \frac{\partial^2 F}{\partial \rho^2} + B \frac{\partial F}{\partial \rho} + CF + D \quad (4.64)$$

The computational mode is defined by a scalar f in the range of $[0, 1]$.

$$f = \begin{cases} 0 & \text{Pure implicit} \\ 0.5 & \text{Crank-Nicolson} \\ 1 & \text{Pure explicit} \end{cases} \quad (4.65)$$

For the prediction of F_i^{n+1} located i th radial position at the time of $(n+1)\Delta t$, the above equation can be rewritten as

$$\frac{F_i^{n+1} - F_i^n}{\Delta t} = A_i^{n+f} \frac{\partial^2 F}{\partial \rho^2} \Big|_i^{n+f} + B_i^{n+f} \frac{\partial F}{\partial \rho} \Big|_i^{n+f} + C_i^{n+f} F_i^{n+f} + D_i^{n+f}. \quad (4.66)$$

Using the central difference scheme, the time derivatives are rewritten as

$$\frac{\partial F}{\partial \rho} \Big|_i^{n+f} = \frac{1}{2\Delta\rho} \left(F_{i+1}^{n+f} - F_{i-1}^{n+f} \right), \quad (4.67)$$

$$\left. \frac{\partial^2 F}{\partial \rho^2} \right|_i^{n+f} = \frac{1}{(\Delta \rho)^2} \left(F_{i+1}^{n+f} - 2F_i^{n+f} + F_{i-1}^{n+f} \right). \quad (4.68)$$

Using these relations, the differential equation can be simplified to the following form (see Appendix A.7)

$$a_i F_{i+1}^{n+1} + b_i F_i^{n+1} + c_i F_{i-1}^{n+1} = d_i. \quad (4.69)$$

The coefficients are given by

$$\begin{aligned} a_i &= (1-f) \left(\frac{fA_i^n + (1-f)A_i^{n+1}}{(\Delta \rho)^2} + \frac{fB_i^n + (1-f)B_i^{n+1}}{2\Delta \rho} \right), \\ b_i &= (1-f) \left(-2\frac{fA_i^n + (1-f)A_i^{n+1}}{(\Delta \rho)^2} + fC_i^n + (1-f)C_i^{n+1} \right) - \frac{1}{\Delta t}, \\ c_i &= (1-f) \left(\frac{fA_i^n + (1-f)A_i^{n+1}}{(\Delta \rho)^2} - \frac{fB_i^n + (1-f)B_i^{n+1}}{2\Delta \rho} \right), \\ d_i &= -f \left(\frac{fA_i^n + (1-f)A_i^{n+1}}{(\Delta \rho)^2} + \frac{fB_i^n + (1-f)B_i^{n+1}}{2\Delta \rho} \right) F_{i+1}^n \\ &\quad + \left\{ -f \left(-2\frac{fA_i^n + (1-f)A_i^{n+1}}{(\Delta \rho)^2} + fC_i^n + (1-f)C_i^{n+1} \right) - \frac{1}{\Delta t} \right\} F_i^n \\ &\quad - f \left(\frac{fA_i^n + (1-f)A_i^{n+1}}{(\Delta \rho)^2} - \frac{fB_i^n + (1-f)B_i^{n+1}}{2\Delta \rho} \right) F_{i-1}^n \\ &\quad + fD_i^n + (1-f)D_i^{n+1}. \end{aligned}$$

By collecting this relation for all radial points, a matrix relation can be constructed.

$$\begin{bmatrix} b_0 & a_0 & 0 & \cdots & 0 & 0 \\ c_1 & b_1 & a_1 & \cdots & 0 & 0 \\ 0 & c_2 & b_2 & \cdots & 0 & 0 \\ \vdots & \vdots & \vdots & \ddots & \vdots & \vdots \\ 0 & 0 & 0 & \cdots & b_{N-1} & a_{N-1} \\ 0 & 0 & 0 & \cdots & c_N & b_N \end{bmatrix} \begin{bmatrix} F_0^{n+1} \\ F_1^{n+1} \\ F_2^{n+1} \\ \vdots \\ F_{N-1}^{n+1} \\ F_N^{n+1} \end{bmatrix} = \begin{bmatrix} d_0 \\ d_1 \\ d_2 \\ \vdots \\ d_{N-1} \\ d_N \end{bmatrix}, \quad (4.70)$$

where the boundary condition is applied for $i = 1$ and N . The following scheme is used to solve this matrix relation with an implicit method:

1. Calculate the coefficients a_i , b_i , c_i and d_i using the explicit method ($f = 1$) at the first iteration.
2. Calculate the explicit solution F_i^{n+1} by solving the matrix relation.

3. Recalculate the coefficients using the implicit method ($f \neq 1$) and F_i^{n+1} .
4. Calculate the implicit solution F_i^{m+1} by solving the matrix relation.
5. Repeat these procedures until a good convergence is achieved.
6. If the convergence is not achieved, decrease the transport time-step and restart from the first step.

4.4 Free-boundary plasma equilibrium evolution scheme in DINA-CH

To calculate the non-linear free-boundary plasma evolution, the free-boundary plasma equilibrium has to be self-consistently calculated with a set of the plasma transport equations and circuit equations for the PF coil and surrounding conducting systems. DINA-CH self-consistently calculates the magnetic field diffusion with the evolution of the free-boundary plasma equilibrium and circuit currents, using an iterative implicit scheme. The particle and heat transport are coupled to the free-boundary plasma equilibrium evolution using an explicit scheme.

4.4.1 Circuit equations

The toroidal current density in the i th axisymmetric external toroidal circuit located in the position (r_i, z_i) is given by

$$j_i = \sigma_i E_i, \quad (4.71)$$

where σ_i is the electrical conductivity. The toroidal electric field E_i is given by

$$E_i = \frac{1}{2\pi r_i} \left(-\frac{\partial \psi_i}{\partial t} + V_i \right), \quad (4.72)$$

where $-\partial \psi_i / \partial t$ is the induced voltage in the i th circuit and V_i is the applied voltage to the i th circuit. Using the definition of electrical resistivity of the element with the area S_i , $R_i = \sigma_i S_i / 2\pi r_i$, the above equation can be written as

$$-\frac{\partial \psi_i}{\partial t} + V_i = R_i I_i \quad (4.73)$$

The poloidal flux ψ_i for each current element is given by

$$\psi_i = L_i I_i + \sum_{j \neq i} M_{ij} I_j + \sum_k M_{ik}^{cp} I_k \quad (4.74)$$

where M_{ij} is the mutual inductance between the i th and j th conducting element, M_{ik}^{cp} is the mutual inductance between the i th conducting element and k th filament current in the plasma.

Combining the two equations and assuming the self-inductance and mutual inductance are time independent for a solid conductor, we can get the following equation.

$$L_i \frac{\partial I_i}{\partial t} + \sum_{j \neq i} M_{ij} \frac{\partial I_j}{\partial t} + \sum_k M_{ik}^{cp} \frac{\partial I_k}{\partial t} + R_i I_i = V_i \quad (4.75)$$

Using the matrix and vector notations, this equation is rewritten as

$$M \frac{\partial I_c}{\partial t} + M^{cp} \frac{\partial I_p}{\partial t} + R I_c = V_c \quad (4.76)$$

where

$$M = \begin{bmatrix} L_1 & M_{12} & \cdots & M_{1n_c} \\ M_{12} & L_2 & \cdots & M_{2n_c} \\ \vdots & \vdots & \ddots & \vdots \\ M_{1n_c} & M_{2n_c} & \cdots & L_{n_c} \end{bmatrix}, \quad M^{cp} = \begin{bmatrix} 0 & M_{12} & \cdots & M_{1n_p} \\ M_{12} & 0 & \cdots & M_{2n_p} \\ \vdots & \vdots & \ddots & \vdots \\ M_{n_c 1} & M_{n_c 2} & \cdots & 0 \end{bmatrix},$$

$$R = \begin{bmatrix} R_1 & 0 & \cdots & 0 \\ 0 & R_2 & \cdots & 0 \\ \vdots & \vdots & \ddots & \vdots \\ 0 & 0 & \cdots & R_{n_c} \end{bmatrix}, \quad I_c = \begin{bmatrix} I_1 \\ I_2 \\ \vdots \\ I_{n_c} \end{bmatrix}, \quad I_p = \begin{bmatrix} I_1 \\ I_2 \\ \vdots \\ I_{n_p} \end{bmatrix}, \quad \text{and } V_c = \begin{bmatrix} V_1 \\ V_2 \\ \vdots \\ V_{n_a} \\ 0 \\ \vdots \\ 0 \end{bmatrix}$$

The numbers of the conductors and plasma elements are respectively n_c and n_p . Voltages in the n_a active conductors can be non-zeros.

4.4.2 Free-boundary plasma equilibrium evolution algorithm

1. At the beginning of n th time-step, the following information is obtained from the previous $(n-1)$ th time-step results: the toroidal current density $j_\phi(t_n, R, z) = j_{pl}(t_n, R, z) + j_{ext}(t_n, R, z)$, poloidal flux $\psi(t_n, R, z)$, normalized magnetic flux surface coordinate $(\rho(t_n, R, z), \theta(t_n, R, z))$ and flux surface averaged 1D plasma profiles $\psi(t_n, \rho)$, $n_{e,i}(t_n, \rho)$ and $p_{e,i}(t_n, \rho)$.
2. At the beginning of s th iteration in the n th time-step, solve the magnetic field diffusion with a given time-step Δt to get the s th estimate of the poloidal flux for the $(n+1)$ th time-step $\psi^{s*}(t_{n+1}, \rho)$.
 - (a) For the first iteration ($s = 1$), use an explicit scheme with $\psi(t_n, \rho)$
 - (b) From the second iteration ($s > 1$), use an implicit scheme with $\psi(t_n, \rho)$ and $\psi^{(s-1)}(t_{n+1}, \rho)$.
3. Calculate the plasma current $j_{pl}^{s*}(t_{n+1}, R, z)$ using the estimate of the poloidal flux.
4. Solve the circuit equations to get the external circuit current $j_{ext}^{s*}(t_{n+1}, R, z)$.
5. Solve the free-boundary G-S equation using $j_\phi^{s*}(t_{n+1}, R, z) = j_{pl}^{s*}(t_{n+1}, R, z) + j_{ext}^{s*}(t_{n+1}, R, z)$ to get the poloidal flux $\psi^s(t_{n+1}, R, z)$.
6. Calculate the normalized magnetic flux surface coordinate $(\rho^{s*}(t_{n+1}, R, z), \theta^{s*}(t_{n+1}, R, z))$ and the flux surface averaged 1D plasma profiles, such as $\psi^{s*}(t_{n+1}, \rho)$, $n_{e,i}^{s*}(t_{n+1}, \rho)$ and $p_{e,i}^{s*}(t_{n+1}, \rho)$
7. Check the convergence condition for the poloidal flux given by

$$\left| \frac{\psi^s(t_{n+1}, R, z) - \psi^{(s-1)}(t_{n+1}, R, z)}{\psi^{(s-1)}(t_{n+1}, R, z)} \right| < \epsilon_\psi, \quad \forall (R, z). \quad (4.77)$$

If the convergence condition is not satisfied, go to the step 2.

8. Calculate the particle and heat transport using an explicit scheme.
9. Check the constraint on the vertical plasma motion given by

$$\left| \frac{\dot{z}_{pl}(t_{n+1}) - \dot{z}_{pl}(t_n)}{\dot{z}_{pl}(t_n)} \right| < \epsilon_{\dot{z}_{pl}}, \quad (4.78)$$

where

$$z_{pl} = \frac{\int_S z j_{pl}(R, z) dS}{\int_S j_{pl}(R, z) dS}. \quad (4.79)$$

If this constraint is not satisfied, decrease the time-step Δt and go to the step 1. Otherwise, go to the next $(n + 1)$ th time-step.

4.5 Combined tokamak discharge simulator

Coupling two physics codes is a general method of studying the effect of non-linear coupling of the different physics represented by each code independently. However, this requires a reliable code coupling scheme to prevent the coupled system from being subjected to significant uncertainty caused by the coupling itself in conditions in which each code normally behaves correctly.

4.5.1 Code coupling scheme

In the combined tokamak discharge simulator, DINA-CH provides the non-linear evolution of the free-boundary plasma equilibrium self-consistently calculated with the plasma current diffusion, in response to both controlled PF coil currents and inductively driven currents in the surrounding conducting system. CRONOS provides the evolution of the plasma profiles by self-consistently solving heat and particle transport with source profiles. The free-boundary plasma equilibrium provided by DINA-CH is directly used for CRONOS transport and source calculations. The plasma and source profiles provided by CRONOS are directly used for DINA-CH in calculating the free-boundary equilibrium and current diffusion.

The code coupling scheme used for the combined tokamak discharge simulator is shown in figure 4.1. All the exchanged data between DINA-CH and CRONOS are passed as SIMULINK variables explicitly treated in time. Therefore, the heat and particle transport calculated by CRONOS and the plasma current diffusion are not implicitly coupled. This slightly deteriorates the consistency in implicitly solving a complete set of coupled transport equations. Nevertheless, this was an inevitable choice to guarantee computational performance and reliability of the combined tokamak discharge simulator. The computational performance of the combined simulation was not significantly deteriorated by the

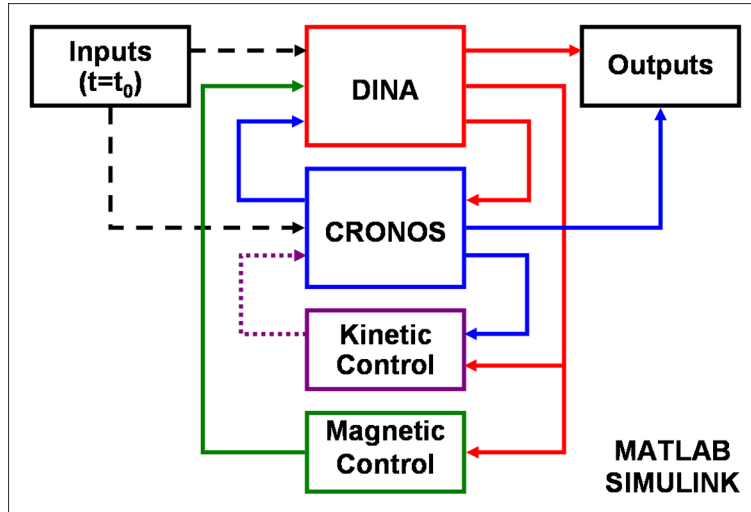


Figure 4.1: Code coupling scheme used for the combined tokamak discharge simulator. Inputs provide initial plasma equilibrium information only at the beginning of simulation (dashed lines). Control of the kinetic plasma profiles is not yet in the closed loop (dotted line).

explicit data exchange scheme and propagation of numerical errors between the two codes was avoided. With this code coupling scheme, the two codes were combined maintaining their original code structures.

Inputs for a full tokamak discharge simulation consist of initial plasma profiles and a reference operation scenario. The initial plasma profiles are prepared by performing a preliminary CRONOS simulation with a prescribed plasma boundary given by the reference operation scenario. The reference operation scenario provides guidance for the tokamak discharge evolution. The evolution of the total plasma current, position and shape are guided by pre-programmed PF coil current waveforms and also feedback controlled respecting their target waveforms. The average electron density evolution and the H&CD scheme are generally prescribed. At the first time-step, an initial free-boundary plasma equilibrium is calculated by DINA-CH with the input plasma profiles. In order to make the initial plasma boundary close to that given by the reference operation scenario, the initial currents in the PF coils are determined by trial. Initial eddy currents in the surrounding conducting systems are extrapolated back from the stationary currents built up after the simulation starts. Once the tokamak discharge simulation starts with a reasonable plasma configuration, the two codes exchange data at every subsequent time step.

This combined tokamak discharge simulator inherits much useful functionality from both

DINA-CH and CRONOS. DINA-CH provides magnetic diagnostic models, such as the magnetic probes and flux loops, and kinetic diagnostic models, such as the interferometer, bolometer and neutron camera. These measurements can be used for either magnetic or kinetic plasma control, by reconstructing the plasma equilibrium in the feedback loop. Magnetic plasma control provides PF coil voltages through the power supplies linked to the controllers for the total plasma current, position and shape. Kinetic plasma control, which is work in progress, provides auxiliary H&CD power for controlling the plasma profiles. Various auxiliary H&CD source modules, such as SINBAD [71, 72] for NBH&CD, PION [73] for ICRH&FWCD, DELPHINE [74] and LUKE [75] for LHH&CD, REMA [76] for ECH&CD and SPOT [77] for alpha particle self-heating, are available in CRONOS. CRONOS also provides various transport models based on either empirical formulation or theory, such as NCLASS [78], Weiland model [79], GLF23 [80] and KIAUTO [37]. Toroidal plasma rotation can be included into the set of coupled transport equations. The SIMULINK graphical user interface (see figure 4.2) of the combined DINA-CH and CRONOS simulator provides improved accessibility to this tokamak model for non-programmer users.

4.5.2 Challenges met during the code coupling

DINA-CH has a free-boundary equilibrium solver and CRONOS has a fixed boundary equilibrium solver. The same plasma equilibrium is implemented in the two codes with slightly different expressions and assumptions [23, 24, 25]. Therefore, in principle, CRONOS can reconstruct a DINA-CH free-boundary equilibrium taking the plasma boundary information and use it for its own plasma transport and source profile calculations. However, the reconstructed equilibrium would be slightly different from the original DINA-CH equilibrium and this inconsistency can be a possible seed for numerical errors in a time simulation. A safe coupling method avoiding this problem [65] is to directly provide the DINA-CH equilibrium for CRONOS transport and source calculations [66]. This also improves the computational performance and does not cause any loss of information in studying the physics as far as the selected code has superior functionality. The heat and particle transport solver in DINA-CH has to be turned off for the same reason.

The choice of data exchange scheme is another issue which has an influence on the computational performance, consistency and numerical stability. The simplest way to exchange data between two codes avoiding these difficulties is to use an explicit scheme in time. This

scheme does not require any additional iteration which can significantly deteriorate the computational performance and possibly cause continuous propagation of numerical errors. This is also useful for maintaining the original code structures and therefore to independently manage and upgrade each code. To ensure the convergence of this explicit data exchange scheme, a sufficiently small time-step is used.

Computational performance of the combined tokamak discharge simulations is reduced with respect to the sum of the independent computational performance of each code. DINA-CH already uses a fixed time-step in advancing the free-boundary plasma equilibrium evolution and has no modification which slowed down the computation, except preparing additional outputs for CRONOS. However, CRONOS, which originally used an advanced acceleration scheme while solving the plasma transport, is significantly slowed down by limiting the maximum time-step of the acceleration scheme. In the combined simulator, the fixed time-step of DINA-CH is used as the maximum time-step of the CRONOS acceleration scheme. In order to improve this computational performance, a time-varying source profile update interval is used. For a time-consuming source profile calculation, frequent source profile updating is only prescribed when the plasma state is changing fast or significantly enough. During the test of this idea, it was identified that several source profiles are erroneously dependent on the source profile update interval. This problem was resolved by upgrading the CRONOS source modules.

Several new numerical instabilities were observed in the combined tokamak discharge simulations. The SPIDER equilibrium solver [67] was adopted to resolve a numerical difficulty that occurred when treating a highly peaked edge bootstrap current profile in ITER. The density of the original 2D grid points used for calculating the free-boundary equilibrium was insufficient to correctly represent the peaked edge bootstrap current. As a new candidate to further improve the numerical stability, an adaptive grid solver is now being developed. Another numerical difficulty was identified in the heat transport calculation. This was an exceptional situation for a transport modelling code with a fixed boundary equilibrium solver, such as CRONOS. When a diverted plasma experiences a back-transition to a limited configuration and moves fast in the radial direction, the plasma temperature profile at the edge is set to a prescribed minimum value, resulting in a discontinuity in the radial gradient. The heat loss during a particular transport time-step was unexpectedly high. This difficulty was resolved by allowing the transport solver to use a much smaller internal time-step when the convergence is poor.

Validation of the combined tokamak discharge simulator for present experiments is a remaining issue. DINA-CH, originally used to study non-linear plasma responses to the plasma disturbances, was validated for TCV plasmas for the dynamic plasma response to PF coil voltage stimulation and non-linear evolution of the vertical displacement events (VDEs) [24, 34, 35, 36]. At the same time it was benchmarked against several linear plasma dynamic response models. The plasma transport modelling of CRONOS and its source calculation modules were validated for Tore Supra plasmas [25, 37, 38, 39] and benchmarked on JET experiments [68, 69, 70]. Although the combined tokamak discharge simulator has not yet been validated as a whole against present experiments, we have directly used it for simulating ITER discharges. The code coupling scheme used for this simulator does not appear to add any significant additional uncertainty which invalidates the previously conducted validation of each code, since each code in the combined simulator still keeps its original structure and physics by treating the exchanged data explicitly in time. The exchanged data in the combined simulation simply plays a role of experimental inputs in an independently conducted simulation using the original code. We will demonstrate the capability of the combined tokamak discharge simulator by simulating ITER scenario 2 in chapter 5, as well as the 12MA hybrid mode scenario in chapter 7 of this thesis.

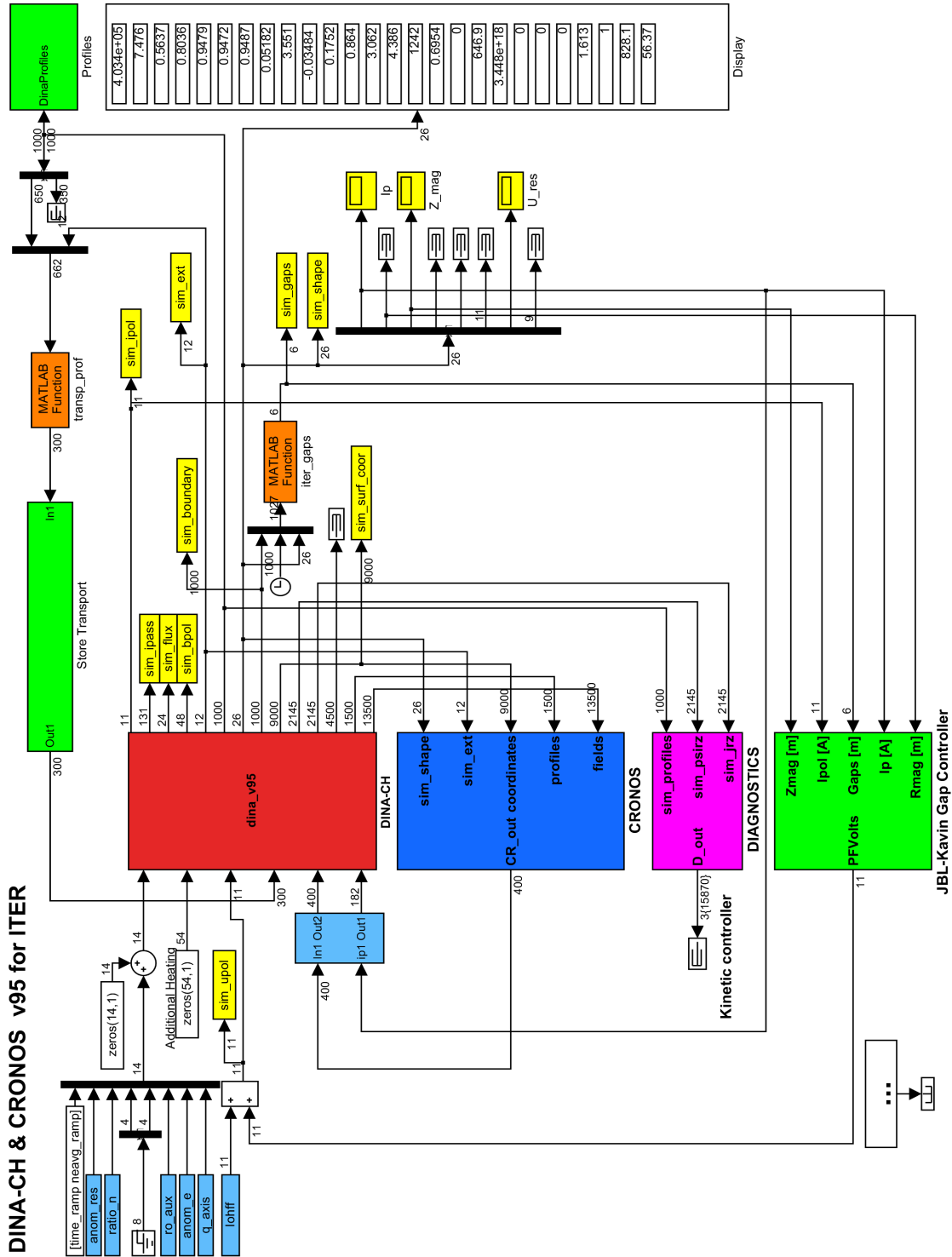


Figure 4.2: Simulink model of ITER in the combined tokamak discharge simulator

Chapter 5

Full tokamak discharge simulation of ITER scenario 2

5.1 Introduction

Understanding non-linearly coupled physics between plasma transport and free-boundary equilibrium evolution is essential to successfully achieving advanced tokamak operation in future devices, such as ITER and DEMO.

Tailoring the plasma current density profile by injecting a non-inductively driven current source during the plasma current ramp-up phase is an example which clearly shows non-linear coupling. Auxiliary H&CD applied during the plasma current ramp-up results in changes not only in the plasma profiles, but also in the dynamic evolution of the plasma equilibrium. First, the applied auxiliary heat and current sources modify the plasma pressure and current density profiles through the transport process. Then, these changes modify the force balance between the plasma and the surrounding conducting systems and lead to modifications of the evolution of the poloidal field (PF) coil currents. All these changes force the plasma to be in a new free-boundary equilibrium configuration with different plasma position and shape. Finally the location of the power deposition, source profile shape and absorbed power of auxiliary H&CD are non-linearly modified by these changes. In addition to this basic mechanism, modifications to the plasma state, such as the plasma confinement, transport and stability, non-linearly interact with each other. The constraints in operating

the tokamak device, such as the coil current and force limits, also can provide additional non-linearities into the tokamak. To study these non-linearly coupled physics in a tokamak, we need a simulation tool which can self-consistently take all the related plasma physics and operational constraints into account.

For this reason, we have developed a full tokamak discharge simulator by combining DINA-CH and CRONOS (see chapter 4). This combined simulator self-consistently calculates the plasma transport and source profiles with the free-boundary plasma equilibrium evolution non-linearly determined in response to currents flowing in the surrounding conducting and PF coil systems. Using this simulator, a full tokamak discharge simulation of inductive 15MA ITER operation scenario 2 has been successfully simulated taking the operational constraints into account [81]. This simulation demonstrates the present capability of the combined tokamak discharge simulator in simulating a full tokamak discharge. Many physics and tokamak operation issues, such as the PF coil current limits, vertical instability, poloidal flux consumption, confinement mode transition, application of H&CD power, free-boundary plasma shape evolution and plasma control, are studied to achieve the full tokamak discharge simulation of the ITER scenario operation 2. Details of the PF coil current limits, vertical stability and poloidal flux consumption, are presented in section 5.4.

5.2 Setting up the simulation of ITER operation scenario 2

ITER operation scenario 2 aims at inductively driving the plasma current up to 15MA and operating it for about 400s of plasma burn in ELMy H-mode conditions as shown in figure 5.1 [6]. In this scenario, the total plasma current is ramped up to 15MA at 100s starting from 0.4MA at 1.6s, and then it is maintained for about 400s of a flat-top phase. After consuming the available poloidal flux supplied by the super-conducting PF coils, the total plasma current is ramped down at a slow rate compared with the current ramp-up rate to avoid peaking the plasma current profile, for a safe plasma termination. The average electron density is assumed to be linearly ramped up along with the total plasma current, starting from $4 \times 10^{18} \text{m}^{-3}$ at 1.6s and reaching $4 \times 10^{20} \text{m}^{-3}$ at 100s, and then it is ramped further up to $1 \times 10^{20} \text{m}^{-3}$ within 30s along with the application of the main H&CD [82].

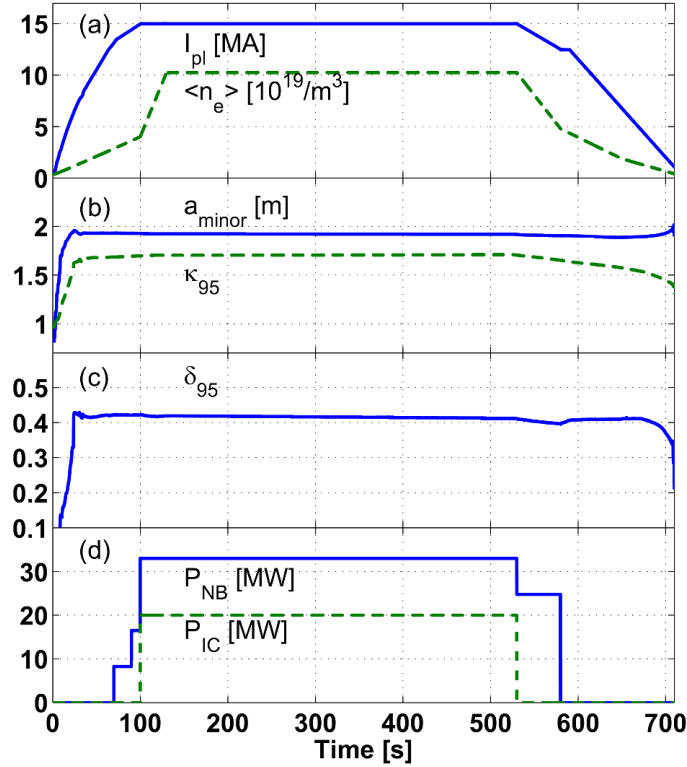


Figure 5.1: Inductive 15MA ITER ELMy H-mode operation scenario (ITER operation scenario 2). (a) The total plasma current, average electron density, (b) minor radius, plasma elongation, (c) plasma triangularity and (d) auxiliary H&C&D powers (20MW of IC and 33MW of NB) are shown.

The ramp-down of the average electron density is imposed by trial to avoid the onset of a radiative collapse during the termination of the plasma pulse. The electron density profile is prescribed to experience a smooth transition from a parabolic profile at the beginning of the current ramp-up to a flat profile as the average electron density reaches its maximum value. The ion and impurity density profiles are self-consistently calculated with an effective charge profile which is assumed to be flat and to decrease monotonically as the electron density increases [82]. The ratio of deuterium to tritium is assumed to be 50:50 and the impurities species, He (3% of D), Be (respecting the assumed average effective charge) and Ne (10% of Be) are assumed.

The evolution of the plasma shape is guided by the coil current waveforms which are pre-programmed inputs to the shape controller. The plasma starts with a small bore, $a(t = 1.6s) = 0.8m$, and then experiences a transition to a diverted single null lower (SNL)

configuration from a limited configuration at about 29s. The minor radius in the fully diverted configuration is about 2.0m. The plasma elongation increases as the plasma column expands, and then it is gradually reduced during the plasma termination to avoid the onset of disruptive VDEs.

53MW of total auxiliary H&CD power is proposed to trigger an L-H mode transition and to maintain the plasma burn during the flat-top phase. 33MW of NBI provides plasma heating and non-inductively driven current with a broad profile shape. 20MW of ICRH provides localized on-axis heat deposition at a frequency of 55MHz using a second harmonic of tritium. 8.25MW of NBI is applied earlier starting from 70s, and then the power is stepped up to 16.5MW at 90s. Although the total NBI power in ITER appears to be varied only with a few steps, we have allowed more flexibility of controlling the power in the simulations. Applying H&CD during the current ramp-up phase was an obligatory choice to avoid the coil current limits by effectively reducing the resistive ohmic flux consumption and adding non-inductively driven current. The early NBI can be replaced by other H&CD sources, such as EC and LH, in which the power can be modulated to provide the best source profiles.

The KIAUTO transport model [37] controls the plasma energy confinement and mode transitions respecting the global energy confinement time scaling laws. It gives gyroBohm-like radial profile dependence for the core plasma. The pedestal width and height can be either prescribed by a scaling law or calculated using the critical pressure gradient. The thermal collapse and plasma current redistribution at the plasma centre during sawtooth crashes are synchronized between the two codes. When the sawtooth is triggered in DINACH (Kadomtsev model), the plasma current is redistributed. When this event is detected from the safety factor profile change, CRONOS produce an effective thermal collapse by applying high enough heat conductivities inside the inversion radius.

The electromagnetic definition of ITER used for simulating this operation scenario is shown in figure 5.2. A toroidally axi-symmetric plasma surrounded by limiters, passive stabilizers, vacuum vessel shells and poloidal field coils is assumed. The electromagnetic interaction between the plasma current and the surrounding conducting system is self-consistently calculated using these ITER design parameters [6].

The ITER plasma control system consists of two feedback loops, a fast vertical stabilization loop and a slow loop providing control of the plasma current and shape [63]. The fast

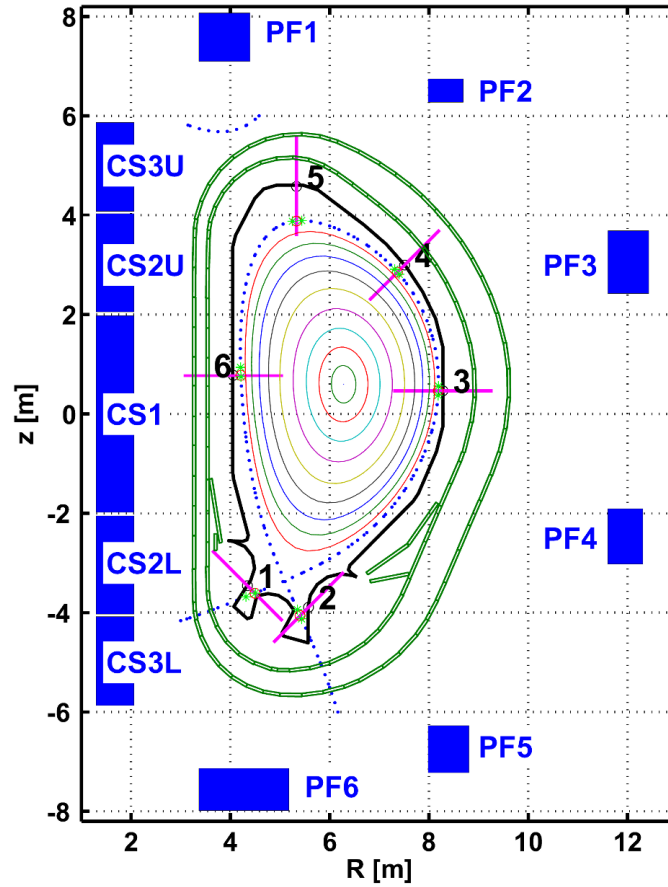


Figure 5.2: Electromagnetic definition of ITER used for simulating 15MA ELMy H-mode operation scenario. The poloidal field coils (blue closed squares), vacuum vessel shells (green open squares), limiters (thick black lines), separatrix (blue dotted lines), 6 gap measurements between the plasma boundary and wall (violet lines with numbers) are shown.

vertical stabilization loop feedback controls the vertical plasma motion taking the vertical velocity of the plasma current centroid as input. The slow plasma shape controller feedback controls 6 gaps between the plasma boundary and wall in the diverted plasma configurations. This ITER controller was originally developed to operate around 15MA total plasma current. It has been modified to function with a varying plasma current [83], enabling its use for a full operation scenario including the plasma current ramp-up and ramp-down. The position and shape control inputs, the vertical plasma velocity and 6 gaps, are multiplied by the plasma current to generate control parameters which are directly related to the flux produced by the PF coil voltages. Standard ITER power supplies [63] are used to provide the PF coil voltages for both the fast vertical stabilization and slow plasma shape control.

Including an integral control into the slow plasma shape feedback loop to eliminate the offset will be the object of further work.

In the early phase of the plasma current ramp-up, the plasma is in a limited configuration, without feedback control of the plasma shape, but with pre-programmed reference PF coil currents. In this phase, a radial position controller is applied to stabilize the plasma boundary evolution. Both vertical and radial position controls are additionally weighted at low plasma current (0.4-7.5MA) to enhance the controllability. The radial position controller is switched to the plasma shape controller with a smooth transition after the plasma has a fully diverted configuration at around 29s.

5.3 Full tokamak discharge simulation results

The combined tokamak discharge simulation results are shown in figure 5.3. The non-inductively driven current was produced by the application of NBI and the bootstrap current fraction was varied in response to the plasma heating and density evolution. The alpha particle self-heating power is slightly over 100MW during the flat-top phase, indicating that Q is close to 10. The time traces of the β_p , l_i and q values at the centre and edge are similar to those given by the reference operation scenario. The β_p increases fast around the L-H mode transition triggered by the application of the main H&CD at the start of the flat-top phase (SOF). It then decreases with a stepwise reduction of auxiliary power during the plasma termination. The l_i at SOF is slightly higher than the value given by the reference operation scenario. However, the vertical instability associated with a high l_i was controllable with the vertical position control system. The central q was reduced fast at the beginning of the plasma current ramp-up, causing an early onset of sawtooth events.

The evolution of the currents in the CS and PF coils is shown in figure 5.4. All the CS coil currents are within the coil current limits [63] for all the operation phases. The current in the PF6 coil approached its limit at the beginning of the flat-top phase and the current in the PF2 coil briefly violated its limit around the end of the flat-top phase (EOF). However, this violation seems avoidable by either changing the plasma shape evolution or increasing the coil current limit itself, as addressed in the recent ITER design review [84]. The coil voltages were automatically within the coil voltage limits [63], since they were imposed in the control system as power supply voltage saturation limits.

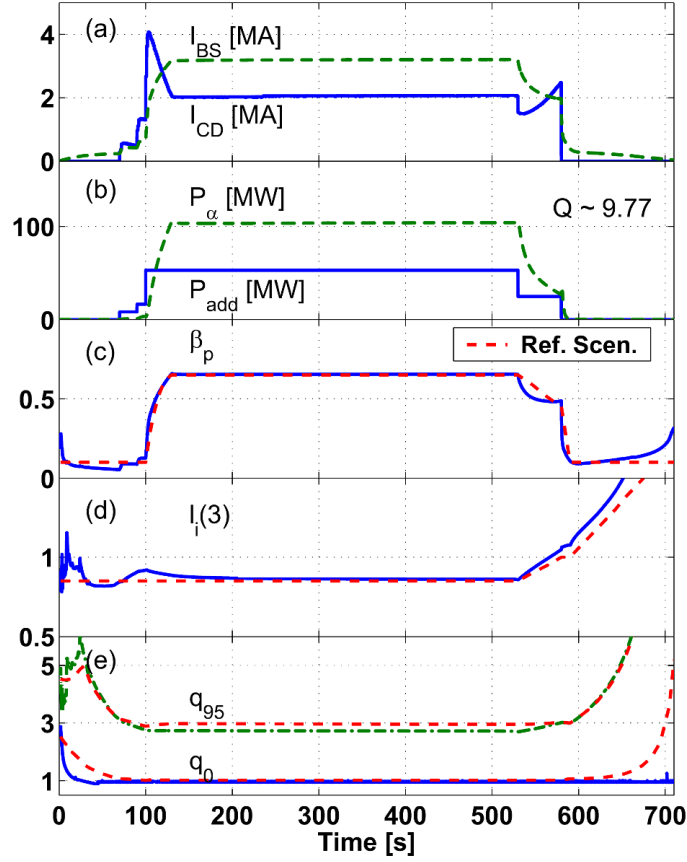


Figure 5.3: Time traces of (a) bootstrap and driven currents, (b) alpha particle and auxiliary heating powers, (c) β_p , (d) l_i and (e) q values (q_0 and q_{95}). Values given by the reference ITER operation scenario 2 are shown as red dashed lines.

The consumption of the poloidal flux provided by the coil system is slightly less than the estimated one in the reference operation scenario, figure 5.5. Either the total H&CD power can be reduced or the burn duration can be extended with 53MW of total H&CD power. The imbalance current flowing in the vertical stabilization converter (VSC), $I_{imb} = I_{PF2} + I_{PF3} - I_{PF4} - I_{PF5}$ [A], and the total active power provided by the power supply system, $P_{act} = \sum_k V_k I_k + V_{VSC} I_{imb}$ [W], are well within the operational limits [63]. The electromagnetic force on CS and PF coils which has not yet been evaluated in this simulation will be the subject of further work.

The time traces of 6 gap measurements reflecting the evolution of the plasma shape are shown in figure 5.6. At the beginning of the plasma current ramp-up, the evolution of the plasma boundary in a limited shape configuration was guided by the pre-programmed coil

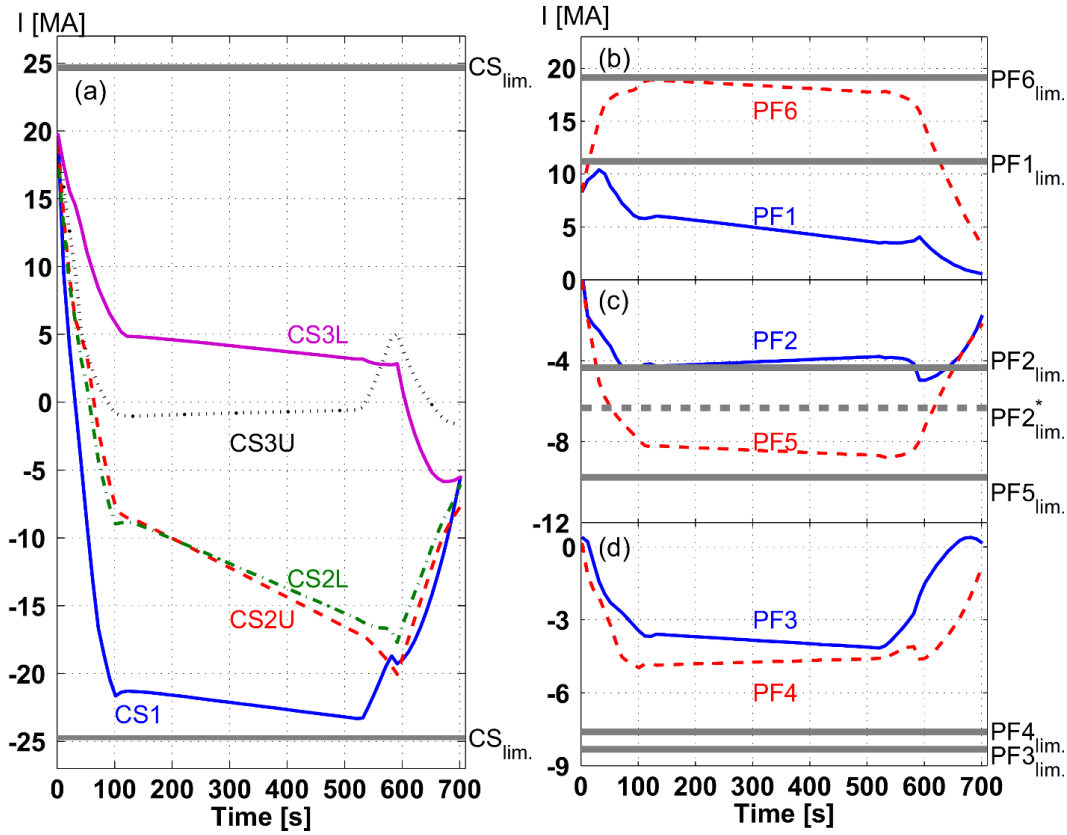


Figure 5.4: Time traces of currents in the PF coils. The coil current limits are shown as thick gray lines. The PF2 coil current violated its limit ($PF2_{lim}$) around the end of the flat-top phase. However, in the recent ITER design review [84], this coil current limit has been increased in absolute value ($PF2^*_{lim}$).

current and prescribed feed-forward voltage waveforms. After the plasma had a fully diverted configuration at about 29s, the shape controller started to control the 6 gaps and continued until the end of the current ramp-down.

5.4 Issues related to the ITER tokamak operation

Several issues related to the ITER tokamak operation and their details are introduced in this section.

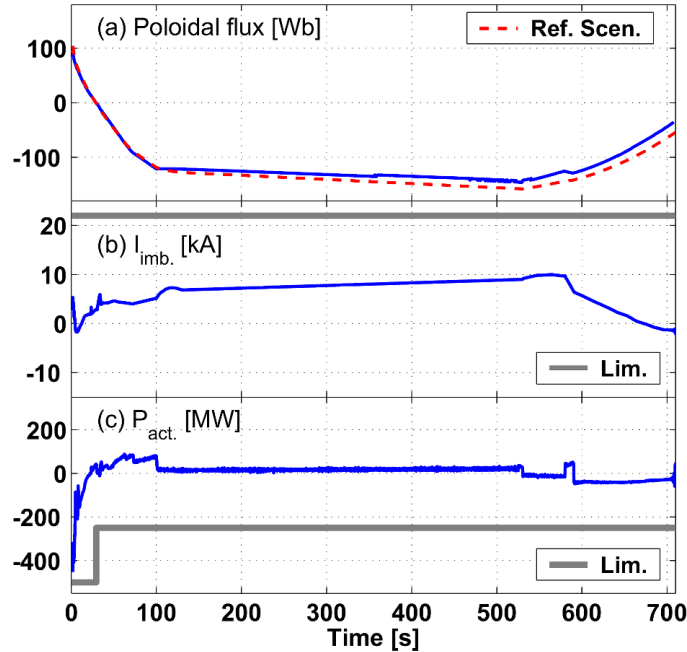


Figure 5.5: Time traces of the poloidal flux, imbalance current flowing in the vertical stabilization converter and total active power of the power supply system. The limits of the imbalance current and total active power are shown as gray lines.

5.4.1 Avoiding the PF coil current limit

The coil current limit in operating the super-conducting PF coils is a critical issue not only in safely operating the tokamak, but also in studying burning plasma physics in ITER. As any PF coil current reaches its limit, the operation scenario will have to be modified in real-time to protect the PF coil itself and to prevent the loss of plasma control. Uncontrolled plasma termination in ITER would result in dangerous electromagnetic and thermal loads onto the tokamak system. This issue is particularly critical for inductive ITER operation scenario 2 which is designed to use the maximum capability of the coil system in inductively driving the plasma current. In this scenario, the PF coil currents are close to their limits at the end of the current ramp-up phase.

The most critical coils, in which the currents approach their limits, are CS1 and PF6 (see figure 5.4). The CS1 coil located close to the plasma is designed to fully consume its volt-seconds mainly in inductively driving the plasma current. The PF6 coil, in which the current flows in the same direction to the plasma current, is mainly responsible for maintaining the diverted SNL configuration. Therefore, as the plasma current increases, the CS1 coil current

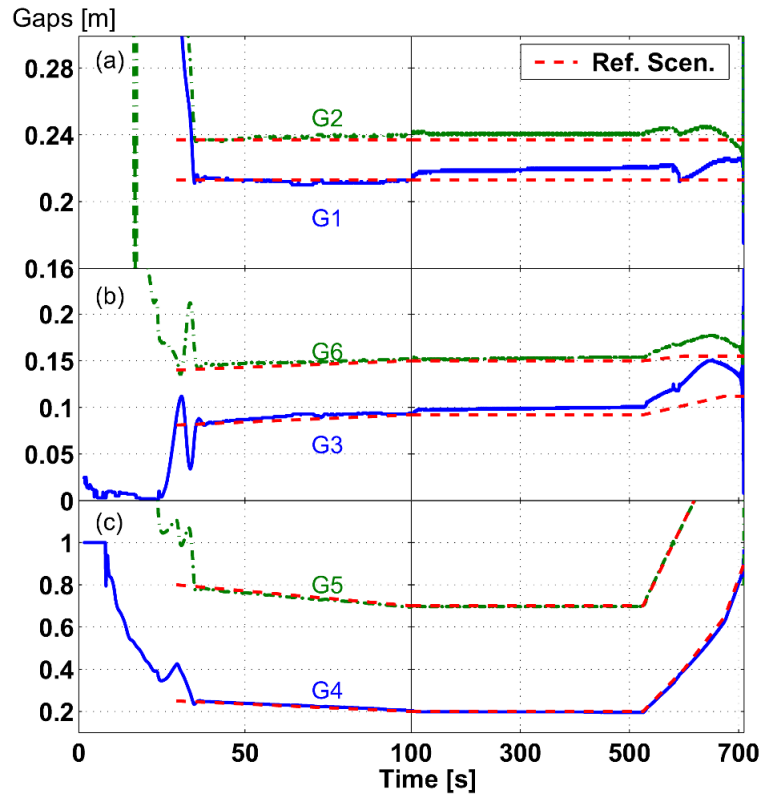


Figure 5.6: Time traces of 6 gap measurements. (a) Gaps measured from the divertor legs, G1 and G2. (b) Outboard and inboard gaps, G3 and G6. (c) Gaps measured at the upper low field side and top, G4 and G5. Locations of the gap measurements are shown in figure 5.2. The plasma shape controller is switched on after the plasma has a fully diverted configuration at about 29s.

approaches its minimum limit and the PF6 coil current approaches its maximum limit. In the simulation of ITER operation scenario 2 without the application of auxiliary H&CD during the current ramp-up phase, CS1 coil current violated its coil current limit at the end of the current ramp-up. The time traces of the coil currents in this reference simulation are shown as dashed lines in figure 5.7 and 5.8. To find an effective method of avoiding this violation of the CS1 coil current limit, applying early H&CD and modifying the coil current evolution were investigated.

Applying an early H&CD was very effective in saving volt-seconds of the PF coils by reducing the resistive ohmic flux losses as shown in figure 5.7. Volt-seconds in all CS, PF1 and PF6 coils are saved by injecting 8.25MW of NBI, starting at 70s. The resistive ohmic

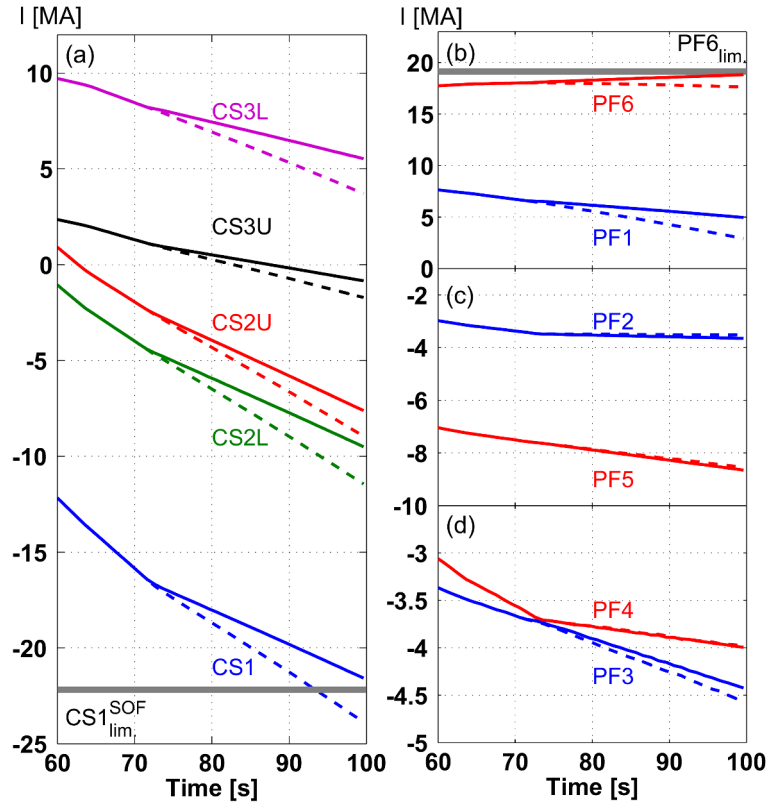


Figure 5.7: Time traces of currents in the PF coils. 8.25MW of NB injected starting at 70s to avoid the CS1 coil current limit at SOF. Time traces of coil currents in the reference simulation (no auxiliary H&CD during the current ramp-up phase) are shown as dashed lines.

flux losses are reduced due to the higher plasma conductivity resulting from the plasma heating. In this method, although the violation of the CS1 coil current limit was avoided, the current in the PF6 coil was actually closer to its limit. This would be dangerous if too much auxiliary H&CD power is applied without paying attention to the resulting changes to the coil current evolution.

As an alternative to the previous method, in the absence of the early H&CD the evolution of the PF coil currents was modified in such a way that the volt-seconds of the CS1 coil is saved. The pre-programmed current waveforms of the CS2U, CS2L, CS3U, CS3L, PF1 and PF6 coils were modified to provide additional volt-seconds. The results of this simulation are shown in figure 5.8. The volt-seconds of the CS1 coil were saved, however it was not sufficient to allow the CS1 coil current to avoid the violation of its limit. This method appears to be

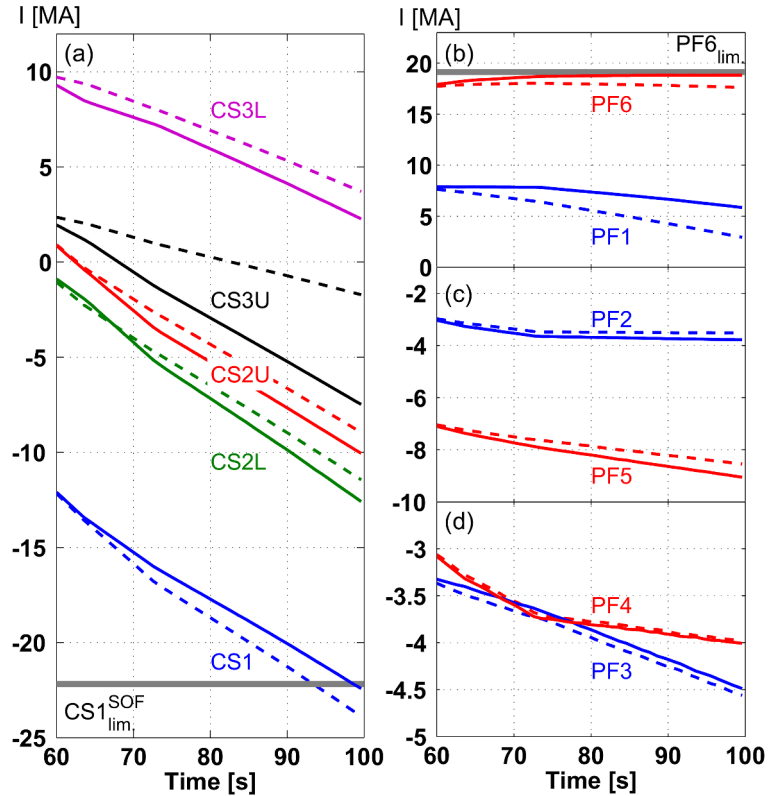


Figure 5.8: Time traces of currents in the PF coils. The pre-programmed current waveforms of CS2U, CS2L, CS3U, CS3L, PF1 and PF6 coils were modified to provide additional volt-seconds. Time traces of coil currents in the reference simulation are shown as dashed lines.

less effective due to a conflict between controls. The plasma shape control strongly rejects any coil current modifications resulting in a deviation of 6 gaps from their target values. Therefore, the PF1 and PF6 coil currents increased to more positive values, opposite to the modification to the pre-programmed coil current waveforms, and the change of the plasma boundary was very small as shown in figure 5.9.

5.4.2 Vertical stability with high l_i

In ITER, the plasma current ramp-up rate is limited by the engineering constraints in operating super-conducting PF coils and this makes it difficult to prevent the plasma current density profile from being peaked at the centre. Particularly at the SOF of the reference ITER operation scenario 2, l_i can be very high above the assumed value in the reference scenario, due to the absence of non-inductively driven current and a very low bootstrap cur-

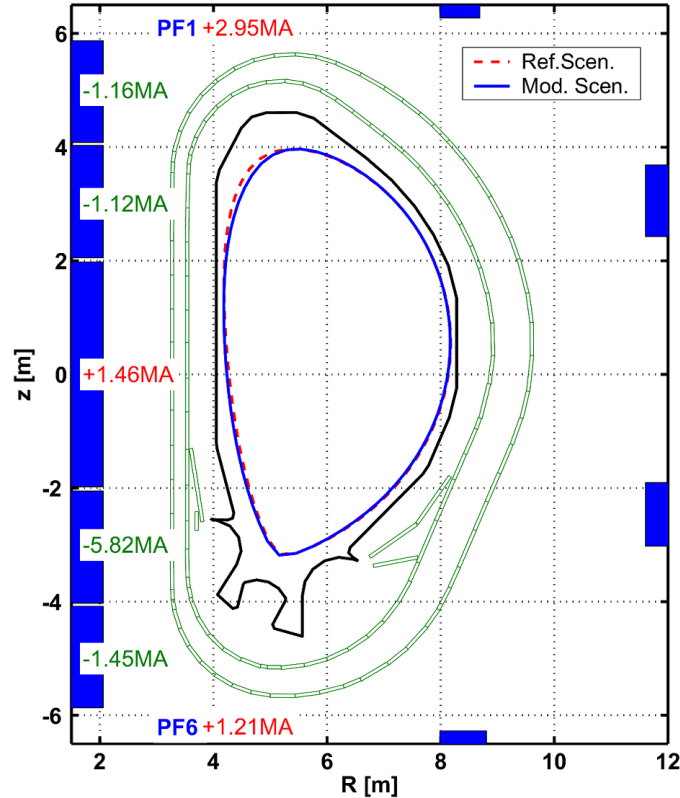


Figure 5.9: Plasma boundaries at SOF in the reference simulation and in the simulation in which the pre-programmed current waveforms of CS2U, CS2L, CS3U, CS3L, PF1 and PF6 coils were modified. Increase and decrease of coil currents with respect to those in the reference simulation are respectively indicated by upward and downward arrows.

rent fraction. In this condition, the vertical instability associated with a high l_i can trigger the onset of dangerous VDEs. Although the vertical instability in the simulation of ITER operation scenario 2 was controllable with the present ITER control system (see section 5.2), there is still an uncertainty on the appropriate range of l_i . Recent JET and ASDEX Upgrade experiments [85] demonstrated that the l_i can be much higher than the assumed maximum value ($l_i=1.0$) in the reference ITER scenario 2 [6].

Therefore, we examined the vertical instability growth rates ($\gamma[\text{s}^{-1}]$) of the plasmas with different l_i and β_p . The growth rate is calculated from either upward or downward drift motion of the plasma in the absence of the feedback control of the plasma position and shape (see figure 5.10). The plasma drift motion is fitted to an exponential function $f(t) = a\exp(\gamma t) + b$ and the result is confirmed by using the logarithm method [86] which gives

Table 5.1: Vertical instability growth rates calculated from DINA-CH simulations. The plasmas are assumed to be at SOF in the ITER operation scenario 2.

	$l_i(3)$	β_p	γ_{fit}^{dn}	γ_{fit}^{up}
Ref.sim.	1.0	0.055	11.36	12.09
Low l_i	0.7	0.1	6.93	7.95
Middle l_i	1.0	0.1	10.58	12.22
High l_i	1.2	0.1	12.71	13.34

time-varying growth rate $\gamma(t)$ (see figure 5.11). The growth rates obtained using the two methods were very similar for the downward plasma drift continued for a longer time before the simulation has stopped. The downward plasma drift was about 0.7m for 0.5 ~ 1.0s, while the upward drift was about 0.2m for 0.3 ~ 0.6s.

The results are summarized in table 5.1. The vertical instability growth rate is higher for the plasma with higher l_i and lower β_p , similar to the previously reported results using the CREATE plasma response model [87]. As clearly shown in our results, reducing l_i and increasing β_p can improve the vertical stability of the plasma. Applying early H&CD would be a good solution as introduced in the next section. Enhancing the control of the vertical plasma position, for example by adding an additional control loop [87], could be a direct solution for widening the tokamak operation widow.

A very high l_i deteriorating the vertical stability of the plasma can be produced by ramping down the plasma current too fast (see figure 5.3 (d)). In this case, progressively reducing the plasma elongation during the plasma current ramp-down is an effective method. This method is already applied in the simulation of ITER scenario 2 to achieve a safe plasma termination (see figure 5.1).

5.4.3 Reducing the poloidal flux consumption

The plasma burn duration can be significantly extended by reducing the poloidal flux consumption during the current ramp-up phase. Injecting early H&CD with sufficient power is the most plausible method, if the resulting plasma disturbances can be safely rejected. This

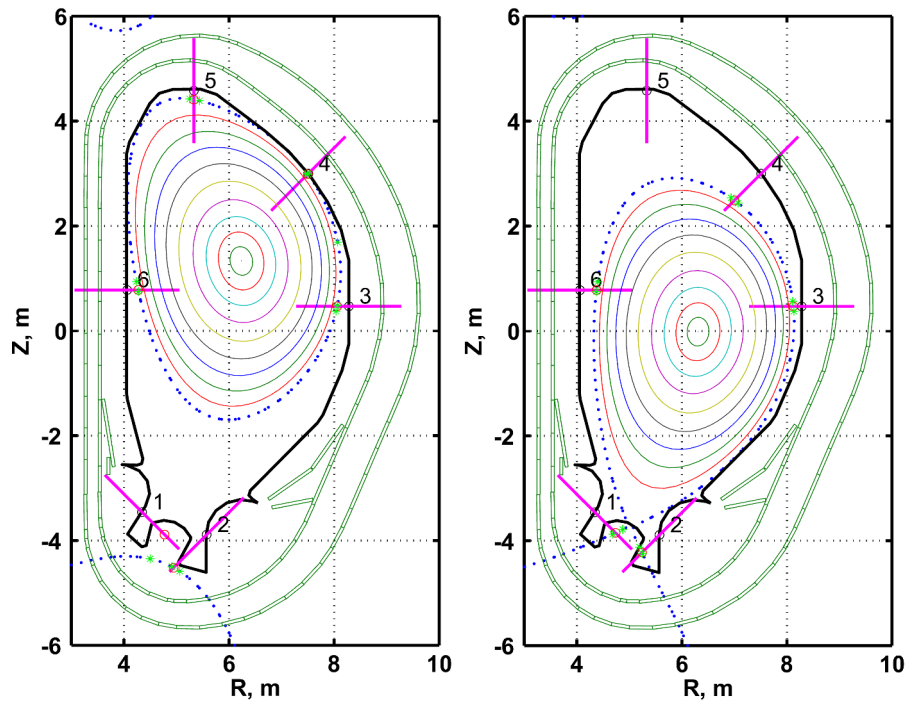


Figure 5.10: (a) Upward and (b) downward vertical plasma drift motions after disconnecting the feedback control of PF coil currents.

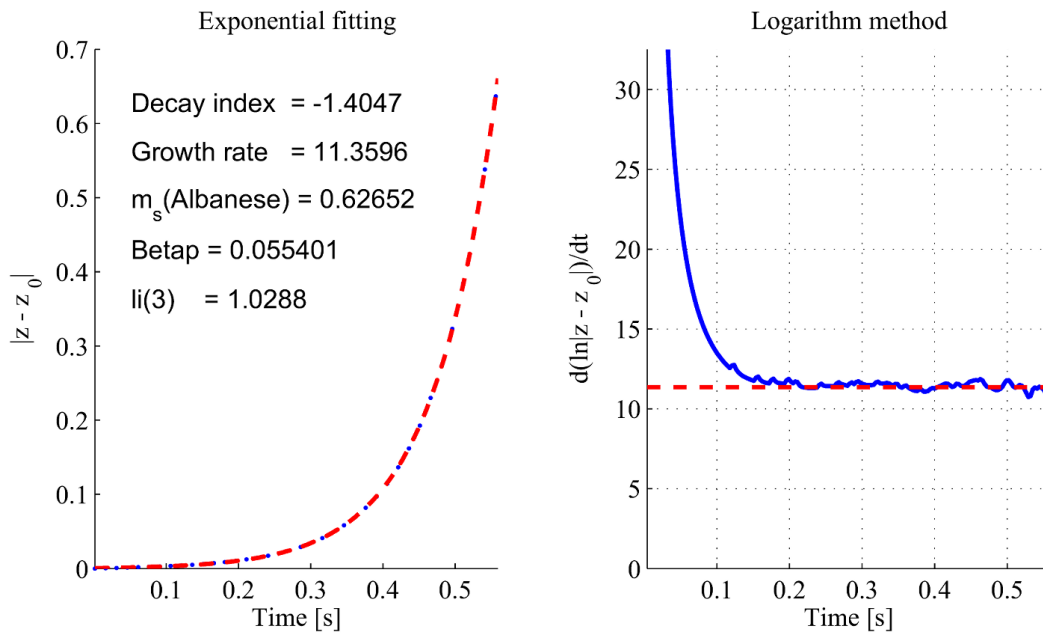


Figure 5.11: Vertical instability growth rates calculated by (a) fitting vertical plasma drift to an exponential function and (b) using the logarithm method [86]

can be very effective not only in saving the poloidal flux consumption and extending the plasma burn duration, but also in reducing the l_i and preventing the CS coil currents from approaching their limits. Previously reported simulations of lower hybrid assisted plasma current ramp-up in ITER [88] were very successful in demonstrating these capabilities. This simulation was conducted with a large bore start-up scenario including the recently updated ITER design [84]. The l_i was reduced to 0.71 and about 43Wb of poloidal flux was saved at the end of the current ramp-up phase by progressively increasing the LH power up to 20MW, starting from 8s. The details are presented in chapter 6.

5.5 Summary and Discussion

A full tokamak discharge simulator has been developed by combining two codes, DINA-CH and CRONOS. This tool enables us to study the non-linearly coupled free-boundary physics between the plasma equilibrium evolution and transport. A full simulation of the ITER reference scenario 2 has been successfully conducted as a demonstration of the capabilities of the combined simulator, as well as being a design study in itself.

The non-inductively driven current was produced by the application of NBI and the alpha particle self-heating power was slightly over 100MW during the flat-top phase ($Q \sim 10$). A L-H confinement mode transition was triggered by the application of the main H&CD at SOF. The time traces of the β_p , l_i and q values are similar to those given by the reference operation scenario. The vertical instability associated with a high l_i was controllable with the vertical position control system. The central q was reduced fast at the beginning of the plasma current ramp-up, causing an early onset of sawtooth events.

All the CS coil currents were within the coil current limits for all the operation phases. The current in the PF2 coil briefly violated its limit around the EOF. However, this violation seems avoidable by either changing the plasma shape evolution or increasing the coil current limit itself, as addressed in the recent ITER design review. The consumption of the poloidal flux provided by the coil system was slightly less than the estimated one in the reference operation scenario. Either the total H&CD power can be reduced or the burn duration can be extended with 53MW of total H&CD power. The imbalance current flowing in the VSC and the total active power provided by the power supply system were well within the operational

limits. The evolution of the plasma boundary in a limited shape configuration was guided by the pre-programmed coil current and prescribed feed-forward voltage waveforms. After the plasma had a fully diverted configuration at about 29s, the shape controller started to control the 6 gaps and continued until the end of the current ramp-down.

Several issues related to ITER operation have been studied. Avoiding the violation of coil current limits were possible either by applying early heating or by modifying the evolution of the PF coil currents during the current ramp-up phase. The vertical instability growth rates of the plasma with different l_i and β_p were investigated to find ways of meeting this problem. Application of early LH was effective to save the poloidal flux consumption and to reduce l_i down to the level at which the vertical instability is sufficiently controllable.

Avoiding possible disruptive plasma behaviours by intelligently self-regulating the operational scenario and actively controlling the plasma profiles can be studied with the present capability of the combined tokamak discharge simulator and will be the subject of future study. Considering 3D effects, such as the toroidal magnetic field (TF) ripple and the ferromagnetic inserts [89, 90], would be possible by applying an estimated correction term to the 2D free-boundary equilibrium in near future.

Chapter 6

Lower Hybrid assisted plasma current ramp-up in ITER

6.1 Introduction

The engineering constraints in operating the superconducting poloidal field coils in ITER [6] limit both the poloidal flux available for inductively driving the plasma current and its rate of change. These give rise to difficulties in designing plasma current ramp-up scenarios. First, the lack of poloidal flux provided by the PF coils can either limit the maximum total plasma current or reduce the duration of the plasma burn required for the study of advanced tokamak operation in ITER. Second, a slow plasma current ramp-up can lead the plasma current density profile to be too peaked in the plasma core. This not only brings unfavourable sawtooth activity into the current ramp-up phase, but also can reduce the vertical control margins associated with a high l_i . Therefore a tool which can reduce the demand on the poloidal flux by reducing resistive ohmic flux consumption and can control the l_i by tailoring the plasma current density profile, becomes indispensable for advanced tokamak operation in ITER. As a candidate solution [91], LHCD is considered in this chapter.

Previous studies on the plasma current ramp-up conducted using a transport modelling code with a prescribed plasma boundary have shown the capabilities of using LH [92]. However, these studies were not complete in the strict sense, because missing free-boundary features could alter their conclusions, and not only increase the uncertainties in the results. The plasma transport during the plasma current ramp-up can non-linearly interact

with the free-boundary equilibrium. The evolution of the plasma profiles and PF coil currents should therefore be self-consistently calculated with eddy currents in the surrounding conducting systems and controlled within the operational limits of the PF coil system. The free-boundary full tokamak discharge simulator, the combined DINA-CH and CRONOS simulator [81], has been used to take all the necessary physics and engineering constraints into account.

6.2 Modelling the plasma current ramp-up

The plasma current ramp-up scenario used in this study is shown in figure 6.1. The total plasma current is ramped up to 15MA at 100s, starting from 0.5MA at 1.55s. Linear ramp-up of the averaged electron density is prescribed with a profile shape given by $f(\rho_{tor}) = 0.4 + 0.6 \times (1 - \rho_{tor}^3)$ where ρ_{tor} is the square root of the normalized toroidal flux. The average effective charge monotonically decreases in time together with the electron density rise and has a flat profile. The ion and impurity densities are calculated from the electron density and effective charge profiles. Anomalous electron and ion heat conductivity profiles are prescribed by using a shaping function, $g(\rho_{tor}) = 1 + 6\rho_{tor}^2 + 80\rho_{tor}^{20}$ and normalized in the KIAUTO transport model [37] which controls the plasma confinement level and mode transitions in such a way as to respect the global energy confinement time scaling laws. The choice of this particular profile shape for the heat conductivity comes from the analysis of JET current ramp-up experiments reported in [93, 94]. Based on this work, we assume that the plasma stays in L-mode confinement during the whole current ramp-up phase and the L-mode confinement is given by the IPB98(y,2) H-mode scaling using a low correction factor, $H_{98} = 0.5$. Initial eddy currents in the passive conducting systems are determined by trial and then self-consistently calculated with the evolution of the free-boundary plasma equilibrium. Sawtooth events are synchronized between the two codes by triggering an effective thermal collapse in CRONOS when the plasma current is redistributed in DINA-CH.

The plasma starts with a large bore, $a(t = 1.55s) = 1.6m$, and then forms a diverted shape in a single null lower (SNL) configuration at about 20s. For the initial phase with limited plasma, the feedback control system is programmed to control only the total plasma current and position, focusing on the stabilization of the plasma motion and on the plasma

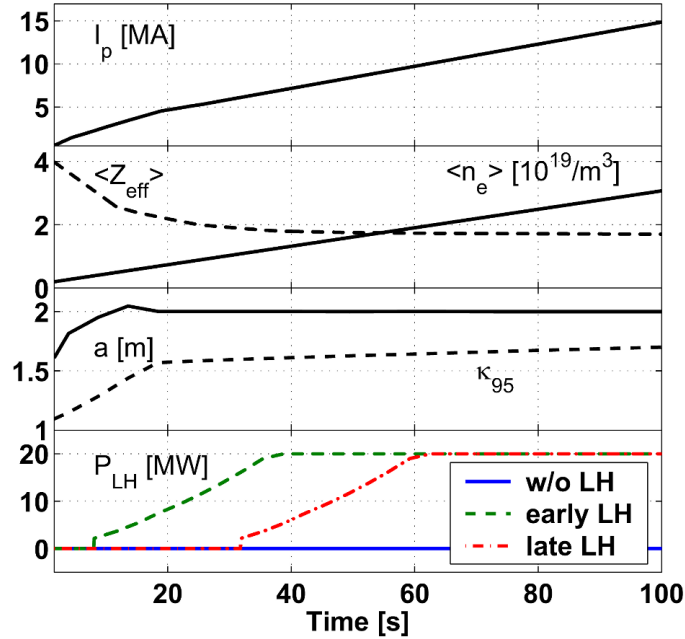


Figure 6.1: Plasma current ramp-up scenario. The total plasma current, averaged effective charge and electron density, minor radius and plasma elongation, and three variants of applied LH (without/early/late LH) are shown.

size. Once the plasma shape becomes diverted due to the reference waveforms of the PF coil currents, a shape controller is switched on with a smooth transition minimizing the disturbance to position control.

Three variants of LHCD have been simulated to investigate their effect on the plasma current ramp-up in ITER as shown in figure 6.1. In the first, fully inductive current ramp-up without any additional current drive source is simulated as a reference. Then two plasma current ramp-up scenarios, in which LH is applied either before or after the plasma has a diverted configuration, are simulated for comparison. In the early LH application scenario, the LH power starts at $t = 8$ s and is progressively ramped up to its maximum value of 20MW over about 30 seconds. The purpose of this power waveform is to drive the maximum fraction of the plasma current with LH waves while avoiding overdriving it. In the late LH application scenario, the same power waveform is moved later in time, resulting in a power ramp-up between $t = 32$ s and 62s.

Heat deposition and LH driven current profiles are calculated every 3.4s by a combined toroidal ray-tracing/Fokker Planck code, DELPHINE [74]. The 20MW of LH power is

distributed among two peaks of the power spectrum. 70% of the power (14MW) belongs to a co-current peak with a maximum at $n_{\parallel} = 2.0$ and the remaining 30% (6MW) belongs to a counter-current peak with a maximum at $n_{\parallel} = -6.0$. The latter lobe of the power spectrum, owing to its large n_{\parallel} absolute value, drives a very small amount of counter-current far off-axis. The calculated LH power deposition and driven current profiles are then slightly broadened just prior to solving the transport equations. The broadening is done by considering the RT/FP output as the source term of a simple radial diffusion equation with diffusion coefficient $D = 1.0\text{m}^2\text{s}^{-1}$ and a slowing down time $\tau = 5\text{ms}$. Note that in this simple procedure, there is no consistency between the diffused fast electron profiles and the wave absorption. The steady-state solution of the radial diffusion equation is then used as input for the source terms (electron heat and current drive) to the CRONOS transport equations. This method, implemented in the DELPHINE/CRONOS coupling [74], is useful to avoid possible numerical difficulties in the transport evolution owing to the sometimes sharp deposition profiles given by the RT/FP calculation. Physically, this empirical method is also a way to qualitatively account for the fact that measured LH power deposition profiles are systematically broader than the prediction of standard RT/FP codes [95]. However, for $D = 1.0\text{m}^2\text{s}^{-1}$ the broadening is quite small and results only in a slight smoothing of the RT/FP profiles.

6.3 Lower Hybrid assisted plasma current ramp-up

Full simulation results are compared in figure 6.2. Early application of LH provides a large fraction of the plasma current until the LH power reaches its maximum at about 38s. The LH driven current then remains approximately constant until $t = 50\text{s}$. A possible reason for this high level of LHCD is that the increase of the plasma current may enhance the current drive efficiency [74] and compensate the density increase during this phase. After $t = 50\text{s}$, the LH driven current decreases as the plasma density increases further. The current driven by late application of LH reaches its maximum at about 60s. However the fraction of LH driven current during the LH power rise is much smaller, because the total plasma current has already reached a higher value. In both cases, the plasma temperatures are quickly increased by the LH heating, resulting in a rise of β_p . The LH deposition and driven currents become very similar in both early and late application cases, once the same LH power level is reached at about $t = 60\text{s}$.

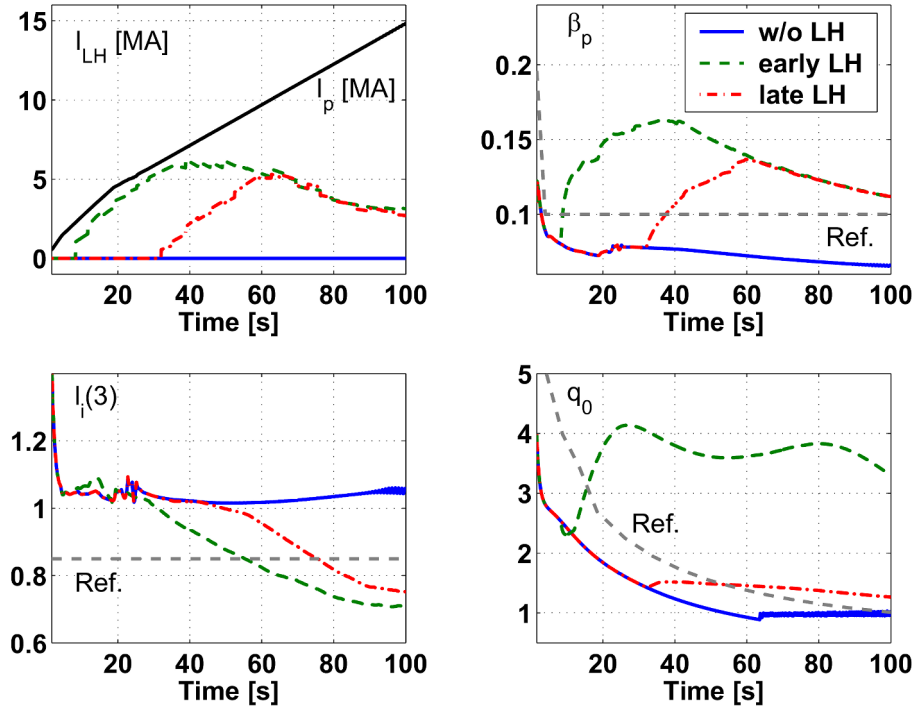


Figure 6.2: Time traces of LH driven currents, poloidal plasma betas, l_i and central q values. Three cases, without/early/late LH, are compared.

The l_i is reduced by the off-axis current driven by the LH application. At the end of plasma current ramp-up, it is reduced to 0.71 by the early LH application and to 0.75 by the late LH application. These values are considered to be low enough to control the vertical instability with the present PF coil limits [87]. Even without the application of LH, and therefore with a higher l_i compared with the reference value, it was possible to avoid loss of vertical control by only slightly reducing the plasma elongation. Further details of this will be the subject of future work. The late LH application shows a faster decrease of the l_i than the early application.

When LH is not applied, the q value at the plasma centre, q_0 , decreases progressively and stays around 1.0 due to the onset of sawtooth activity. Early LH application initially increases q_0 up to 4 and keeps it above 3 producing a negative or very low magnetic shear at the plasma centre. The late LH maintains q_0 above 1, barely avoiding the sawtooth instability during the plasma current ramp-up, showing a capability of exploiting hybrid scenario operation conditions. The q profiles at the end of the current ramp-up are compared in figure 6.3. With early LH, the LH driven off-axis currents are initially concentrated near the plasma

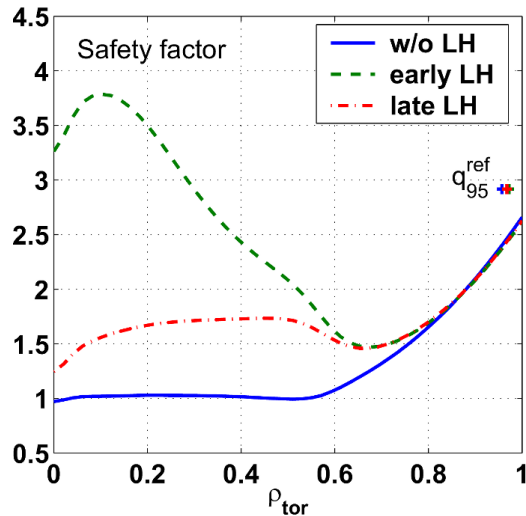


Figure 6.3: q profiles at the end of the current ramp-up ($t = 100s$). Three cases, without/early/late LH, are compared. Smaller q_{95} values (~ 2.5) than the reference scenario value ($q_{95}^{ref} \sim 2.9$) are induced by the change of the plasma boundary (the plasma elongation is reduced to improve the vertical stability in these simulations).

centre ($\rho_{tor} \approx 0.2$) with a very high fraction of the total plasma current. This makes it very efficient for increasing q_0 . As the plasma temperature is increased by LH heating and the total plasma current and electron density increase, the location of the LH driven off-axis current progressively moves outward radially (up to $\rho_{tor} \approx 0.6$) as shown in figure 6.4.

The evolution of the poloidal flux supplied by the PF coils and consumed for the inductively driven plasma current fraction is calculated for the three variants of LH application, compared in figure 6.5. Without LH, the consumption of poloidal flux is slightly above the reference scenario, possibly causing a shortage of poloidal flux available for the required plasma burn duration in ITER scenario 2 [6]. With the early LH, the poloidal flux consumption at the end of the plasma current ramp-up phase is reduced from -124Wb to -81Wb saving 43Wb . This amount is equivalent to about 500s of additional burn duration if the poloidal flux is consumed at the rate assumed in the ITER reference scenario 2, in which about 30Wb is consumed for the plasma burn of about 400s [6]. The ITER reference scenario 2 was originally designed to use maximum inductive plasma current ramp-up capacity to reach 15MA plasma current at the beginning of the flat-top phase, and then the ELMy H-mode burning plasma sustained by 53MW of auxiliary H&CD power consumes the poloidal flux until to reach the coil current limits. Therefore, this scenario is very challenging for the

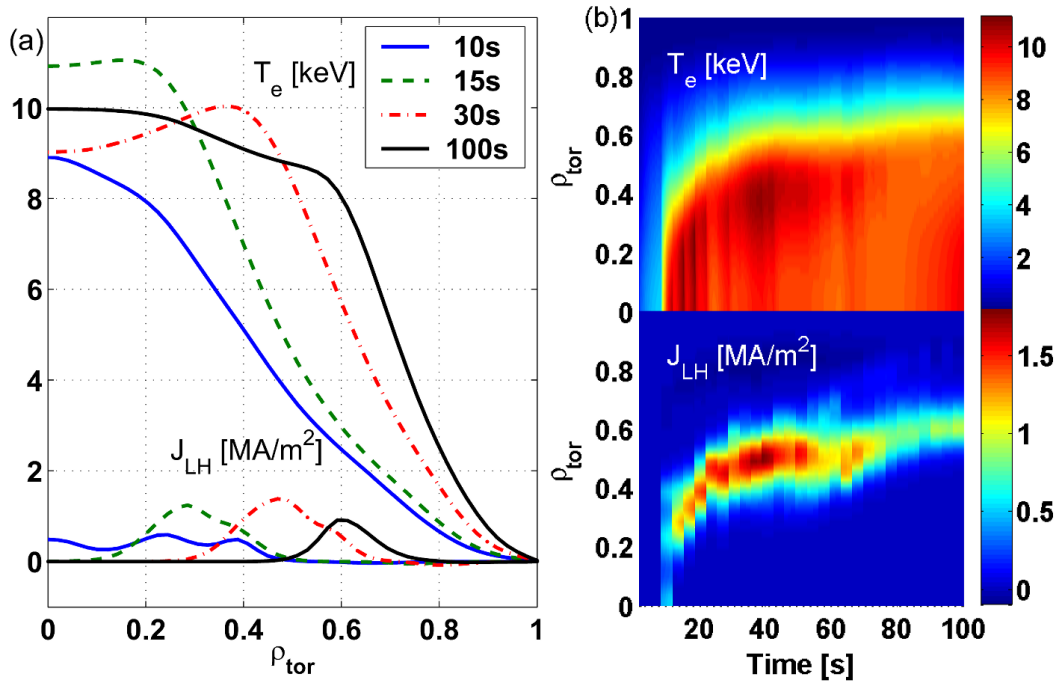


Figure 6.4: (a) Radially outward shift of LH driven currents during the current ramp-up assisted by an early LH and simultaneous broadening of electron temperature profiles. (b) Detail evolution of electron temperature and currents driven by LH.

ITER PF coil system.

To estimate the separate contributions of the plasma heating and the non-inductively driven current to the volt-second saving, an additional simulation has been performed with only early LH heating. LH heating profiles are obtained from the previous early LH simulation results and prescribed for this simulation. This case is additionally shown as a black dotted line in figure 6.5. The contribution from the LH heating is about 35.5Wb (82%) while the remaining contribution from LH current drive is estimated to be about 7.5Wb (18%). The increased electron temperature resulting from LH heating is therefore mostly responsible for reducing the resistive ohmic flux consumption. The LH non-inductively driven current replaces part of the inductively driven current and further reduces the consumption of poloidal flux.

The shape and position feedback control system generates PF coil demand voltages within their prescribed limits [63]. The evolution of the controlled currents in the CS1 and PF6 coils, which are the most critical in the avoidance of the PF coil current limits, are shown in

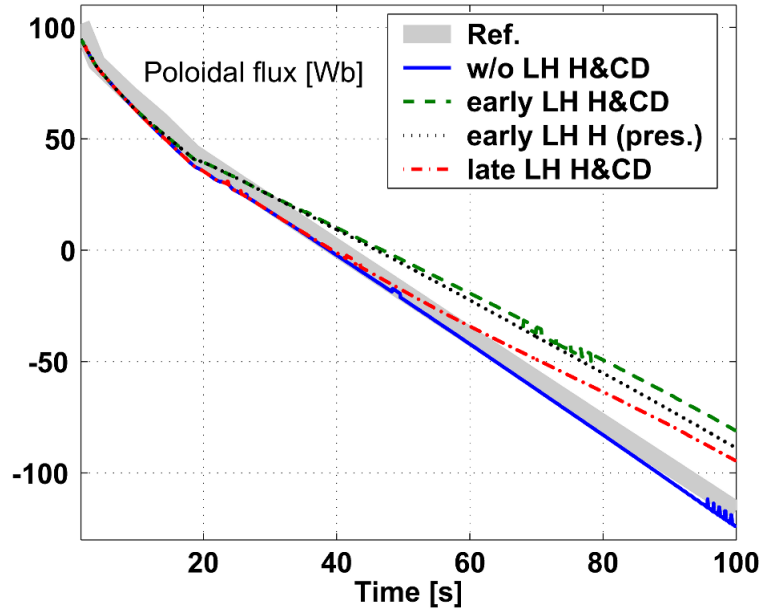


Figure 6.5: Time traces of poloidal fluxes. Four cases, without LH H&CD, early LH H&CD, early LH H (heating profiles are obtained from early LH H&CD case, and then prescribed) and late LH H&CD are compared.

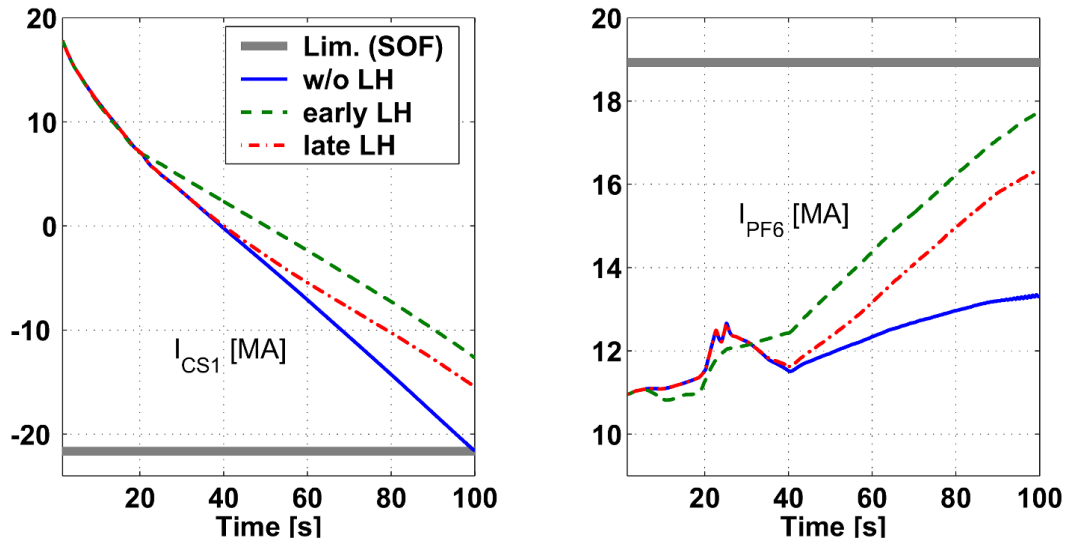


Figure 6.6: Time traces of currents in CS1 (left) and PF6 (right) coils. Three cases, without/early/late LH, are compared.

figure 6.6. The CS coils, which primarily provide poloidal flux and therefore plasma current, generally benefit from increased safety margins with the application of LH. However, the currents in the outer PF coils can actually become closer to the limits, unless the prescribed plasma shape evolution is redesigned.

6.4 Free-boundary plasma evolution

A critical problem related specifically to free-boundary features has been identified, when LH is applied before the plasma has a fully diverted shape. The early LH produces large changes in the plasma profiles, exceeding the uncertainties assumed in designing the reference scenario PF coil currents. These changes can cause the plasma to remain limited over the whole ramp-up phase, unless the reference coil current waveforms are modified. If the plasma fails to form a diverted shape, the shape controller is never turned on. In this study, instead of fully redesigning the operation scenario, an elongation controller is added with a weight determined by trial to force a transition to a diverted shape. This elongation controller provides modification to the PF coil currents which in turn modify the inboard and outboard gaps between the plasma boundary and wall, according to the heating and current drive scheme in the operation scenario. Plasma shapes with this elongation control are compared with those without the control at the times before and after the preset time of the shape transition, $t_{XPF} = 20 \sim 25$ s in figure 6.7. When LH is applied after the plasma has a diverted shape, the back-transition to a limited shape is not seen. The reason appears to be that the relative strength of LHCD is lower owing to the higher total plasma current at later times. The development of explicit strategies considering this effect will be the object of further work.

Vertical position oscillations are observed at the end of plasma current ramp-up in the reference scenario, in which LH is not applied, shown in figure 6.8. These oscillations appear to be caused by the interaction between the feedback control and the plasma profile and shape evolution. In the simulation with the original reference shape, the vertical oscillations grow until control is lost at the end of the plasma current ramp-up phase. When the plasma elongation is reduced by modifying the reference Gap5 (see insert in figure 6.8), the oscillations are significantly reduced and the plasma survives until the end of the ramp-up phase. The application of LH added to the modification of Gap5 (red dash-dot line in figure 6.8)

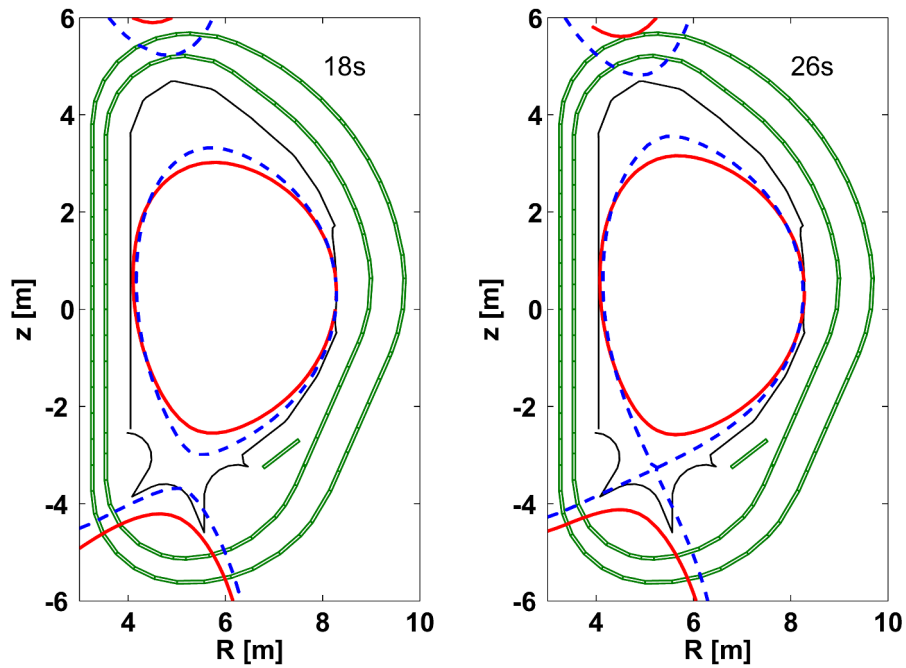


Figure 6.7: Plasma shapes with the elongation control (dashed blue) are compared with those without the control (red solid) at the time before (left) and after (right) the preset time of shape transition.

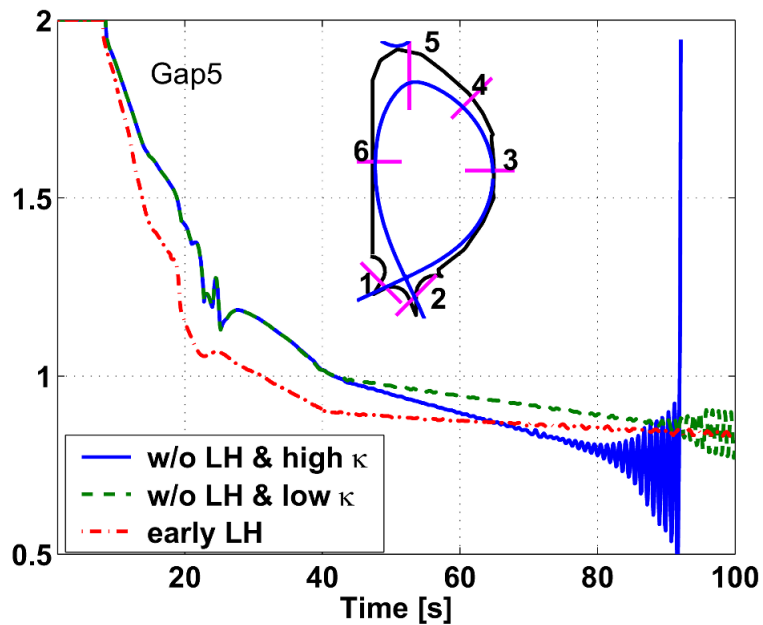


Figure 6.8: Time traces of Gap5 indicated at the top of vacuum vessel in the nested small figure.

completely removes the oscillations. However, the changes of the plasma boundary adopted in our simulations (with and without LHCD) induce lower q_{95} the q value at the 95% normalized poloidal flux surface, than the reference ITER shape (see figure 6.3). This aspect may require further optimization to operate with larger margins regarding the avoidance of an external kink mode.

6.5 Conclusions

By simulating the LH assisted plasma current ramp-up in ITER with the combined full tokamak discharge simulator, the capacity of LH for saving the poloidal flux consumed to produce plasma current and for increasing the safety margins in operating the superconducting poloidal field coils are self-consistently studied. With an early application of 20MW of LH power during the current ramp, up to 43Wb of flux consumption can be saved with respect to the ohmic ramp-up case. A range of slightly reversed to flat target q profile shapes can be achieved, as is needed to operate ITER in advanced scenarios, as well as avoiding the onset of sawteeth during the ramp-up. By reducing l_i , LHCD also makes the vertical position stabilization much easier. The early application of LH before the plasma has a diverted shape requires either redesigning the reference coil current waveforms or adding additional shape controls, such as an elongation control, due to the importance of the changes to the current profile. The latter option has been successfully implemented and applied in the simulation. These simulations demonstrate LHCD as a useful and effective tool for reducing the flux consumption and controlling the target q profile during the ITER current ramp-up, while remaining fully compatible with the constraints of the present PF coil system design.

Chapter 7

ITER hybrid mode operation

7.1 Introduction

ITER hybrid mode operation aims at operating the plasma for a long plasma burn time ($> 1000\text{s}$) with sufficient fusion gain ($Q > 5$) [6]. The plasma is operated at lower plasma current compared with the ITER operation scenario 2 to provide the poloidal flux for a long flat-top. Slightly lower average electron density is assumed to reduce the resistive ohmic flux losses by increasing the plasma conductivity for a given plasma pressure. The plasma burn time in ITER can be further extended, if the plasma confinement is higher than ELMy H-mode confinement as observed in present experiments [96, 97, 98]. In these experiments, operating the plasma with a stationary flat q profile above 1.0 at the plasma centre was the key element in achieving the improved confinement regime. A low magnetic shear appears to be favourable for stabilizing MHD instabilities and the sawtooth crash has been avoided by a self-regulating mechanism, such as 3/2 NTM in DIII-D and fishbone (in the core) and/or 3/2 NTM in ASDEX Upgrade, preventing the central q value from being decreased below 1.0 [97, 99, 100]. Although the central q value is observed to be maintained above 1.0 by virtue of the existence of this self-regulating mechanism, the possibility of obtaining a flat q profile at the beginning of the flat-top phase and sustaining it as long as possible by combining various non-inductively driven current sources still has to be studied in view of operation of ITER.

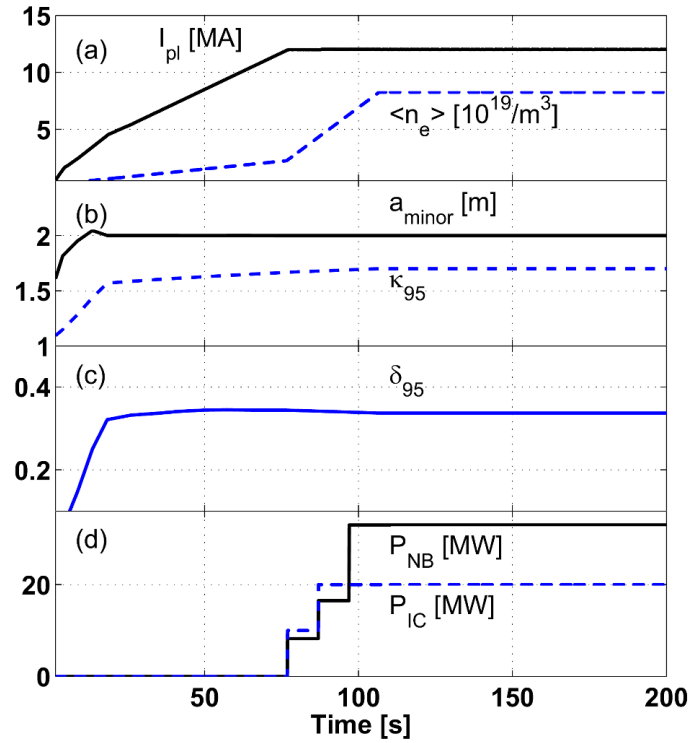


Figure 7.1: ITER 12MA hybrid mode operation scenario (ITER operation scenario 3). (a) The total plasma current, average electron density, (b) minor radius, plasma elongation (c) plasma triangularity and (d) auxiliary H&C&D powers (20MW of IC and 33MW of NB) are shown.

7.2 Modelling the plasma current ramp-up

The plasma current ramp-up scenario for ITER hybrid mode operation is generated by tailoring the initial part of the 15MA ELMy H-mode ITER operation scenario 2 presented in chapter 6, figure 7.1. The total plasma current is ramped up to 12MA at 77s starting from 0.5MA at 1.5s. The average electron density is again assumed to be linearly ramped up along with the total plasma current, starting from $2.125 \times 10^{18} \text{m}^{-3}$ at 1.5s and reaching $2.5 \times 10^{19} \text{m}^{-3}$ at 77s, and then it is ramped further up to $8.5 \times 10^{19} \text{m}^{-3}$ within 30s. The density profile starts with a parabolic shape at 1.5s and becomes completely flat in the core at 107s. The electron density at the separatrix is assumed to be 35% of the central value. The pedestal top is assumed to be at $\rho_{tor} = 0.95$, where ρ_{tor} is the square root of the normalized toroidal flux.

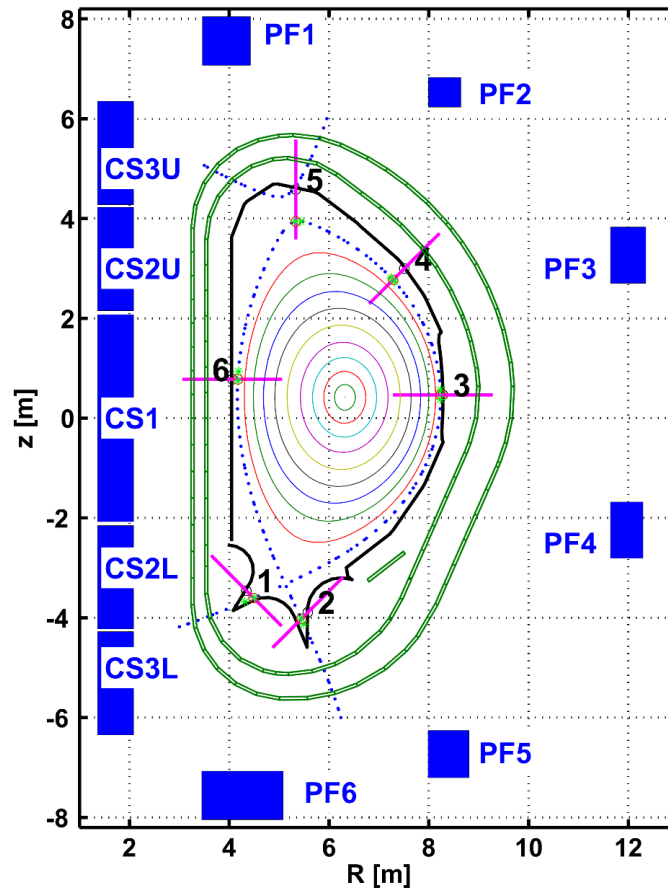


Figure 7.2: Electromagnetic definition of ITER used for simulating the 12MA hybrid mode operation scenario. The poloidal field coils (blue closed squares), vacuum vessel shells (green open squares), limiters (thick black lines), separatrix (blue dotted lines), 6 gap measurements between the plasma boundary and wall (violet lines with numbers) are shown.

The plasma starts with a large bore, $a(t = 1.6s) = 1.6m$. It then experiences a transition to a diverted SNL configuration at about 20s. This is clearly shown in the evolution of plasma elongation and triangularity. At the beginning of the flat-top phase, 33MW of NBI and 20MW of ICRH are applied to trigger an L-H mode transition and to initiate the plasma burn. Shifted deuterium beams with 1MeV energy are applied to provide off-axis plasma H&CD (see figure 7.7) and the second harmonic of tritium at a frequency of 55MHz has been used to provide on-axis plasma heating.

The electromagnetic definition of ITER [63] used for simulating this operation scenario is shown in figure 7.2. The geometry of limiters, passive stabilizers, vacuum vessel shells and poloidal field coils is slightly changed compared with the previous design [6] (see figure 5.2).

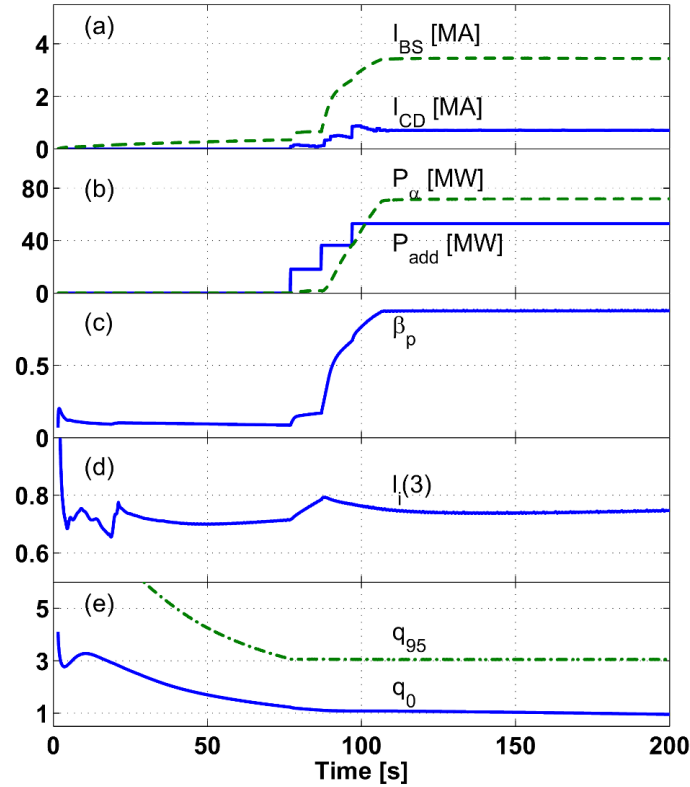


Figure 7.3: Time traces of (a) bootstrap and driven currents, (b) alpha particle and auxiliary heating powers, (c) β_p , (d) l_i and (e) q values (q_0 and q_{95}).

Anomalous electron and ion heat conductivity profiles are calculated by the KIAUTO transport model. To take into account the confinement improvement observed in the experiments targeting hybrid mode operation, a confinement enhancement factor for the H-mode scaling, $H_{98} = 1.2$, is used as a multiplication factor on the confinement time. These are the assumptions used for our simulation of ITER hybrid mode operation, which is referred as reference simulation in this section.

The combined tokamak discharge simulation results are shown in figure 7.3. The non-inductively driven current was produced by the application of NBI and the bootstrap current fraction evolved in response to the plasma heating and density evolution. The alpha particle self-heating power is slightly over 70MW during the flat-top phase, indicating that the fusion gain Q is about 6~7. β_p is increased by the application of the main H&CD up to about 0.85 and l_i is maintained around 0.75 during the flat-top phase. The central q value was slightly above 1.0 at the SOF, avoiding an early onset of sawtooth crashes during the current ramp-up phase. At $t = 200$ s of this simulation, the electron temperature at the centre and

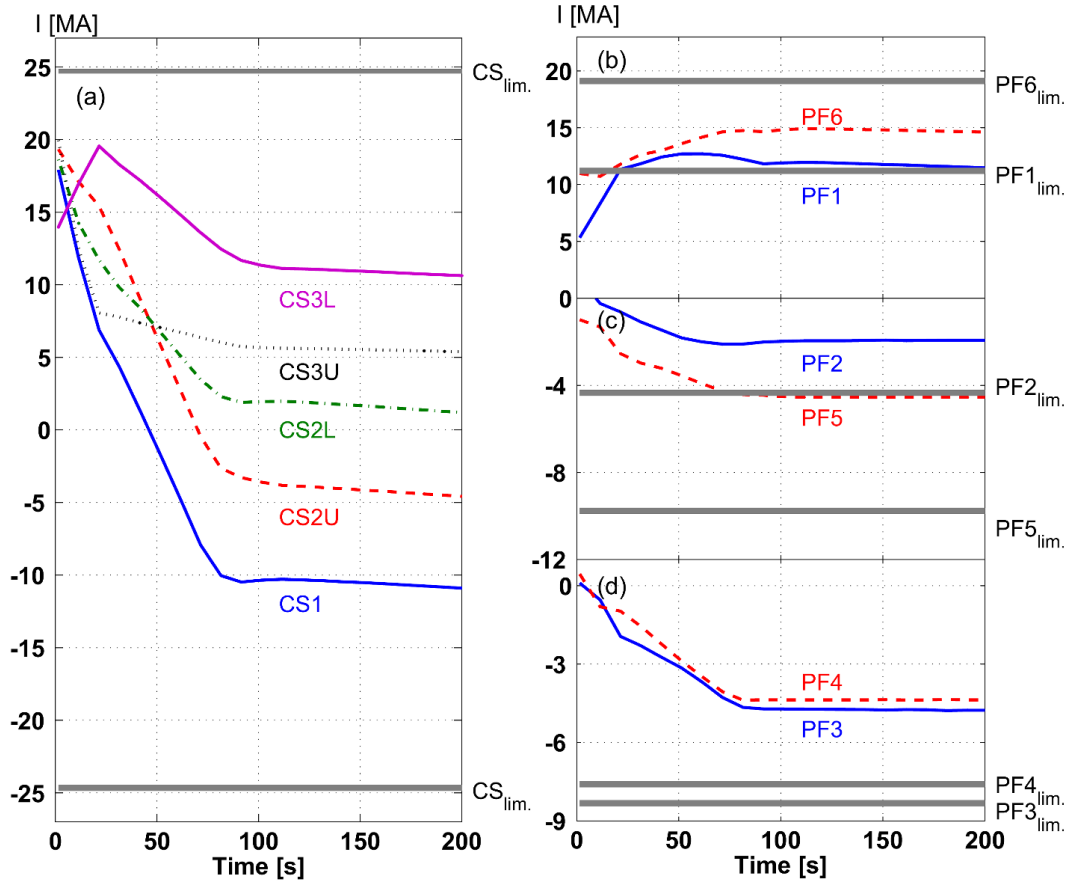


Figure 7.4: Time traces of currents in the PF coils. The coil current limits are shown as thick gray lines. The PF1 coil current violated its limit ($PF1_{lim.}$) around the plasma shape transition to a diverted configuration.

pedestal top were about 25.5keV and 3.14keV, respectively. The normalized plasma beta ($\beta_N = \beta/(I_p/aB_T)$) was slightly over 2.0 and l_i was about 0.76. The central q value was 0.94 and Q was about 6.75. These values are summarized in table 7.1.

The evolution of the currents in the CS and PF coils is shown in figure 7.4. All the CS coil currents evolve far away from the coil current limits [63] due to the reduced volt-second consumption during the current ramp-up phase. However, the PF1 coil violated its limit around the plasma shape transition to a diverted configuration. The cause of this violation is investigated and a possible method avoiding it is studied in section 7.5. The coil voltage limits [63] were imposed in the control system as power supply voltage saturation limits.

The time traces of 6 gap measurements reflecting the evolution of the plasma shape are

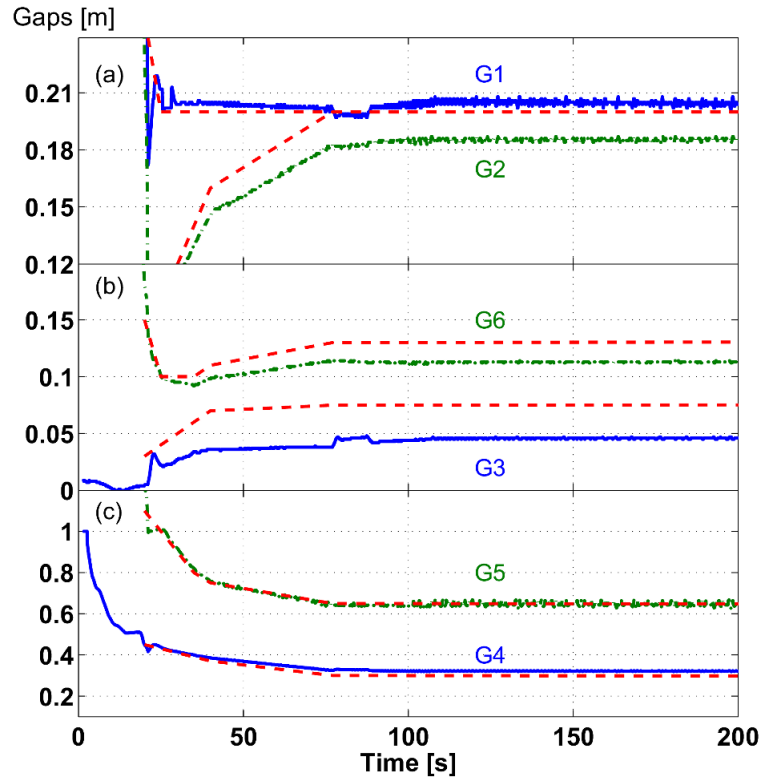


Figure 7.5: Time traces of 6 gap measurements. (a) Gaps measured from the divertor legs, G1 and G2. (b) Outboard and inboard gaps, G3 and G6. (c) Gaps measured at the upper low field side and top, G4 and G5. Locations of the gap measurements are shown in figure 7.2. The plasma shape controller is switched on after the plasma has a fully diverted configuration at about 20s.

shown in figure 7.5. After the plasma had a fully diverted configuration at about 20s, the shape controller started to control the 6 gaps and continued until the end of the current ramp-down. The outboard (G3) and inboard (G6) gaps show significant offsets from the reference inputs indicating that the pre-programmed coil current waveforms are not fully compatible with the desired plasma shape evolution.

7.3 Achieved plasma parameters

Various simulations with slightly different assumptions are compared to examine the achievable range of plasma parameters in ITER hybrid mode operation and to test feasibility to

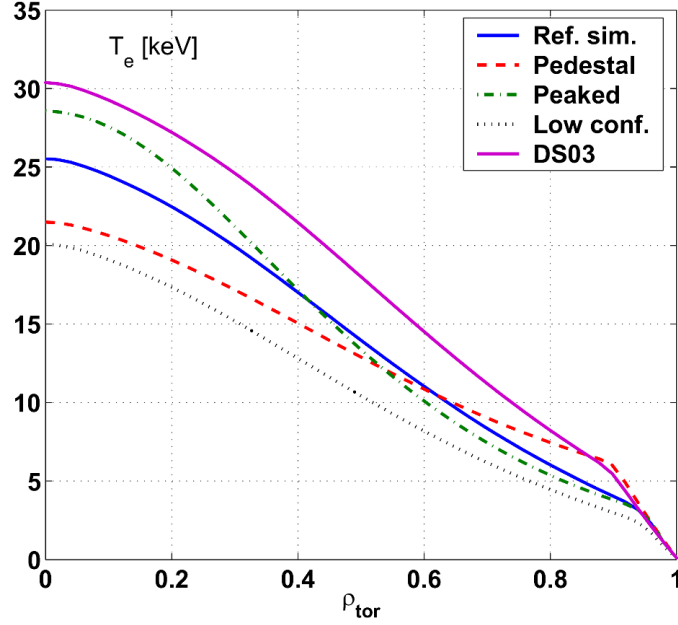


Figure 7.6: Electron temperature profiles at $t = 200$ s. Five cases are compared. (a) Reference simulation, (b) with wider and higher pedestal assumption, (c) with an assumed heat conductivity profile resulting in a peaked plasma temperature profile shape, (d) without considering confinement enhancement and (e) with DS03 confinement time scaling law.

these assumptions. The results are summarized in table 7.1 and the electron temperature profiles are compared in figure 7.6.

Firstly, a wider and higher pedestal was applied assuming the pedestal top at $\rho_{tor} = 0.92$ and about twice the stored energy of the reference pedestal. The electron temperature at the centre is significantly reduced due to the re-normalization by the KIAUTO transport model, while it is much higher at the pedestal compared with the reference simulation. l_i is reduced by the increased bootstrap current at the edge.

Secondly, the heat conductivity profile was imposed with a shaping function, $f(\rho) = 1 + 3\rho^2$, to produce a more peaked temperature profile. The peaked temperature profile resulted in a higher l_i and slow decrease of the central q value. The neutral beam driven current is slightly increased.

Thirdly, $H_{98} = 1.0$ was assumed to examine the case in which the plasma stays in a standard ELMy H-mode confinement. The electron temperature, β_N and Q were significantly reduced and higher l_i was produced.

Table 7.1: Plasma parameters achieved at $t = 200s$ in various simulations of ITER hybrid mode operation.

	Ref. sim.	Pedest.	Peaked	Low conf.	DS03	EC	LH	EC &LH
W_{th} (MJ)	291	286	287	220	369	312	314	330
H_{98}	1.18	1.19	1.17	0.97	1.39	1.20	1.20	1.20
β_N	2.07	2.03	2.05	1.56	2.62	2.21	2.22	2.33
$l_i(3)$	0.76	0.68	0.82	0.82	0.66	0.75	0.70	0.70
$q(0)$	0.94	0.90	1.00	0.96	1.25	1.31	0.96	1.23
$T_e(0)$ (keV)	25.5	21.5	28.6	20.1	30.4	30.3	27.3	31.2
$T_i(0)$ (keV)	23.8	20.0	26.5	19.0	27.9	23.5	25.3	25.1
$T_e^{Ped.}$ (keV)	3.14	5.48	3.14	2.34	4.87	3.41	3.46	3.66
$(\rho_{tor}^{Ped.})$	(0.95)	(0.92)	(0.95)	(0.95)	(0.92)	(0.95)	(0.95)	(0.95)
I_{BS} (MA)	3.44	3.51	3.37	2.51	4.65	3.79	3.84	4.10
I_{NB} (MA)	0.71	0.66	0.83	0.46	0.99	0.65	0.67	0.67
I_{EC} (MA)	-	-	-	-	-	0.41	-	0.33
I_{LH} (MA)	-	-	-	-	-	-	0.89	0.94
P_α (MW)	71.9	65.4	72.1	41.8	109.7	76.3	82.1	84.7
Q	6.75	6.19	6.79	3.92	10.27	4.98	5.61	4.55

Lastly, purely gyroBohm global energy confinement scaling law (DS03) proposed by McDonald [102] was applied without the multiplication factor which enhances the H-mode confinement. In this case, the wider and higher pedestal was again assumed to generate an acceptable electron temperature at the centre and pedestal. Estimated H_{98} was about 1.39 and β_N was 2.62. l_i is reduced down to 0.66 and the central q values are maintained above 1.0.

These simulations show that the reference simulation is in the middle of parameter space bounded by conservative and promising plasma confinement assumptions.

7.4 q profile evolution

To study the effect of different H&CD method on the evolution of the q profile, slightly off-axis ECH&ECCD and/or far off-axis LHH&LHCD were/was added to the reference H&CD scheme, starting from 110s. The results are shown in the three last columns of table 2. The current density profiles modified with different H&CD methods are compared in figure 7.7. Application of 20MW of additional EC though the upper launchers mainly modified the plasma current density profile at the centre by adding a slightly off-axis current in which its maximum is localized inside $\rho_{tor} = 0.2$. Application of 20MW of additional LH provides a localized far off-axis current in which its maximum is localized around $\rho_{tor} = 0.8$.

The evolution of the central q value and the q profiles at $t = 200$ s are compared in figure 7.8. The slightly off-axis EC driven current was effective in modifying the central q value, while the far off-axis LHCD had a small and delayed influence on the central q profile. When the far off-axis LH driven current was applied, q values were increased around the deposition location. Although the contribution of the far off-axis LHCD over a longer time scale has not been investigated, it appears less effective for an active control of q profile during the flat-top phase, in which the plasma current is high. Although the application of ECCD was effective in modifying the central profile, the resulting profile was not flat at the centre. Application of an off-axis current located near the centre with a broad shape would be more promising for achieving a stationary flat q profile above 1.0. Application of both ECCD and LHCD, in which half of the power is stepped up at 160s, showed combined contributions at different locations.

7.5 Coil current limits

In the reference simulation of the ITER hybrid mode operation, a violation of the PF1 coil current limit was identified after the plasma configuration is fully diverted at 20s, as shown again in figure 7.9. This appears to be caused by imposing a heat conductivity profile which produces a relatively broad temperature profile. The PF1 coil current is increased above its limit due to the reduction of volt-second consumption caused by the confinement improvement.

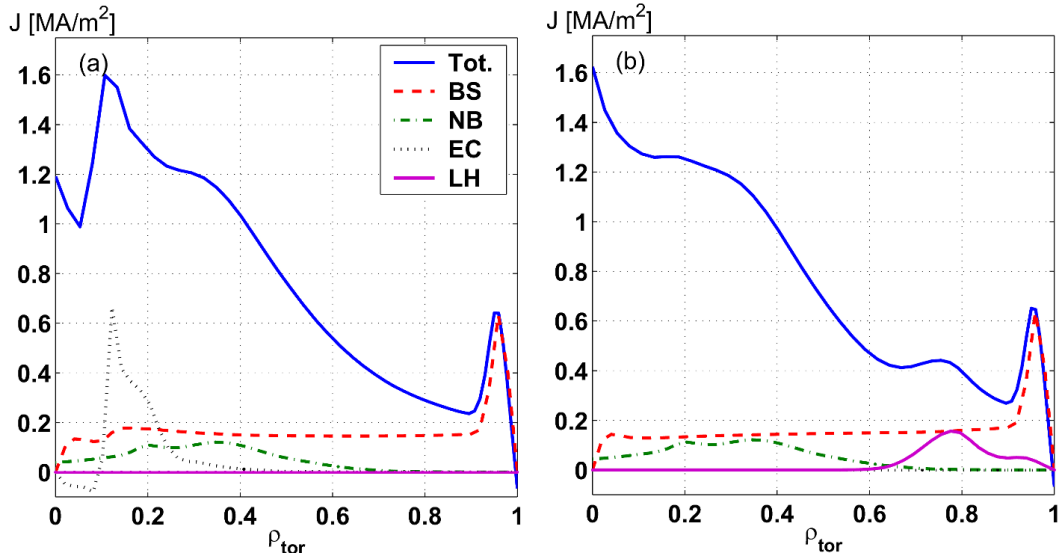


Figure 7.7: The total plasma, bootstrap and source current density profiles at $t = 200\text{s}$ are compared. (a) 20MW of EC is added to the reference H&CD scheme (33MW of NB and 20MW of IC). (b) 20MW of LH is added to the reference H&CD scheme.

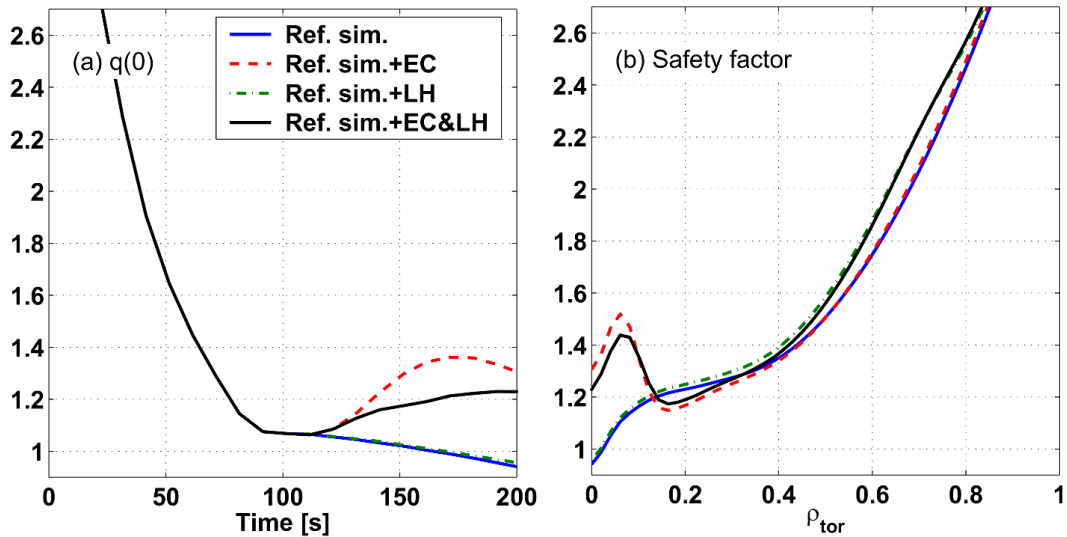


Figure 7.8: (a) Time traces of central q values and (b) q profiles at $t = 200\text{s}$. Four cases are compared. Reference simulation, with additional 20MW of EC, with additional 20MW of LH and with both additional 20MW of EC and 20MW of LH.

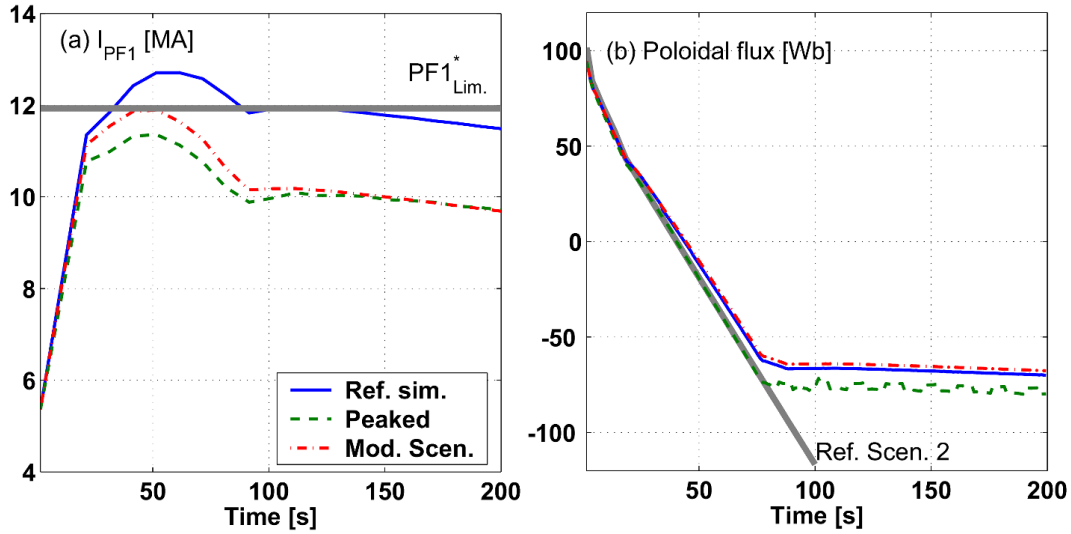


Figure 7.9: Time traces of (a) currents in PF1 coil and (b) poloidal fluxes. Three cases, reference simulation, with an assumed heat conductivity profile resulting in a peaked plasma temperature profile shape and with modified pre-programmed coil current waveforms, are compared. The PF1 coil current limit ($PF1_{lim.}^*$) given in the recent ITER design review [84] is shown in (a). The poloidal flux evolution given in the reference ITER operation scenario 2 is shown in (b).

Another simulation has been performed following the assumptions used in the simulation of ITER operation scenario 2 [88]. In this simulation, the heat conductivity profile is prescribed by using a shaping function, $f(\rho_{tor}) = 1 + 6\rho_{tor}^2 + 80\rho_{tor}^{20}$ and L-mode confinement is assumed during the plasma current ramp-up using a correction factor, $H_{98} = 0.5$. These original assumptions were chosen based on JET plasma current ramp-up experiments [40-41]. In this simulation, the plasma temperature profile was more peaked and the violation of the PF1 coil current limit was easily avoided while more poloidal flux was consumed. The time trace of the PF1 coil current is compared with that of the reference simulation in figure 7.4.

An active method to avoid the violation of the PF1 coil current limit was attempted by modifying the evolution of the PF coil currents of the reference simulation. Although the violation of the PF1 coil current limit was only just avoided with this method, the vertical stability of the plasma was significantly deteriorated leading to a VDE at SOF. To avoid this difficulty, the evolution of the plasma shape was additionally modified in such a way to reduce the plasma elongation [17]. The time trace of the PF1 coil current in this simulation is additionally shown in figure 7.9.

7.6 Summary and discussion

Hybrid mode operation has been simulated, focusing on the study of the operational capability of obtaining a stationary flat q profile at SOF and sustaining it as long as possible by combining various non-inductively driven current sources. Achievable range of plasma parameters in ITER hybrid mode operation is examined by comparing various simulations with slightly different assumption. Application of a slightly off-axis ECCD appears to be effective compared to the far off-axis LHCD, at least on short time scales. The violation of the PF1 coil current limit has been investigated and an active method of avoiding it is further studied. Modifying the evolution of the PF coil currents has shown its potential, although the vertical stability of the plasma is deteriorated. The study of the advanced tokamak operations in ITER, such as the hybrid and steady-state operations, is the main subject of future work which requires theory-based transport models including the related physics.

Part III

Active control of the kinetic plasma profiles

Chapter 8

Simplifying plasma profile control in ITER

8.1 Introduction

Advanced tokamak operations in ITER, such as the steady-state and hybrid modes [3], require an active real-time control of several kinetic plasma profiles to achieve the advanced regimes for sustained operation. Experiments on this active plasma profile control have been conducted on several devices, including JET [41, 42], Tore-Supra [43, 44] and DIII-D [45, 46]. Particularly, the experiments and simulations in JET using a model-based technique for integrated real-time profile control [47, 48, 49, 50] demonstrated its capability of simultaneously controlling several plasma profiles. The response model of the plasma profiles to power changes of auxiliary H&CD systems was deduced from identification experiments and was then used to control the plasma profiles.

However, there is still concern on the range of applicability of this experimentally deduced plasma profile response model. This model might be not valid if the plasma state varies away from the reference state achieved in the identification experiments. Real-time update of the plasma profile response model would be the most plausible approach to resolving this difficulty. This is possible either by selecting an adequate plasma profile response model from an existing database or by identifying one in real-time. Both methods are worth trying. However, due to the cost of preparing a database of plasma profile response models, the latter

will be more attractive if an adequate method for calculating the plasma profile response model in real-time without consuming too much computational time is provided.

In this chapter, we propose and test a robust control technique that simplifies the active real-time control of plasma profiles in ITER. The plasma profile responses to the power changes of several H&CD systems are modelled by simplifying the related physics, to allow real-time update of them. In section 8.2, the incremental electron temperature and q profile response models are introduced. In section 8.3, ITER hybrid mode operation has been simulated using the CRONOS transport modelling code [25] and the feasibility of control based on the incremental plasma profile response models is investigated. In section 8.4, the capability of the developed active plasma profile control technique has been shown by applying it to simulations of the ITER hybrid mode operation. A summary and discussion is presented in section 8.5.

8.2 Plasma profile response models

In this section, the electron temperature profile response is modelled by simplifying the electron heat transport equation and the q profile response is modelled by directly relating it to the changes of the source current density profiles. These plasma profile response models are based on the dual assumptions of linearity and time-invariance. In reality, the response of the plasma is neither linear, since the electron and ion pressure profiles on which we estimate the coefficients will change with the changes of H&CD, nor time-invariant, due to the strong evolution of the profiles themselves. In our electron temperature profile response model, the dependence of the alpha particle self-heating on the ion temperature profile evolution and the influence of the electron-ion equipartition power change are not included. Most importantly, confinement degradation with the additional H&CD power is ignored. In our q profile response model, the dependence on the self-generating bootstrap current on the pressure profile change and the diffusion of the plasma current are not included. We therefore do not expect our incremental plasma profile response models to predict the exact evolution of the plasma profiles.

The formulations introduced to describe the plasma transport in CRONOS [25] are used to derive the incremental profile response models. This allows direct application of the

plasma profile response models to CRONOS simulations. For simplicity, the clear radial and time dependence of the variables is omitted in the formulations unless it is explicitly required.

8.2.1 Incremental electron temperature profile response model

The evolution of the electron pressure [25] is given by

$$\frac{3}{2} \frac{\partial}{\partial t} \left(P_e V'^{\frac{5}{3}} \right) + V'^{\frac{2}{3}} \frac{\partial}{\partial \rho} \left[V' \langle |\nabla \rho|^2 \rangle (q_e + \lambda T_e \gamma_e) \right] = V'^{\frac{5}{3}} Q_e \quad (8.1)$$

where P_e , q_e , T_e , γ_e and Q_e are respectively the local electron pressure (Pa), heat flux (Wm^{-2}), temperature (eV), particle flux ($\text{m}^{-2}\text{s}^{-1}$) and heat source (Wm^{-3}). V' , $\langle |\nabla \rho|^2 \rangle$ and γ are the derivative plasma volume element $dV/d\rho$, a geometric coefficient averaged on the magnetic flux surface and a parameter to take into account the contribution of the particle flux to the heat flux. The radial coordinate, ρ , is defined by

$$\rho = \sqrt{\frac{\Phi}{\pi B_0}} \quad (8.2)$$

where Φ and B_0 are respectively the toroidal magnetic flux (Tm^2) and magnetic field (T) on the geometric axis. The electron heat flux [25] is calculated with

$$q_e = -\chi_e n_e \frac{\partial T_e}{\partial \rho} - P_e V_e^q \quad (8.3)$$

where χ_e , n_e and V_e^q are respectively the electron heat conductivity (m^2s^{-1}), density (m^{-3}) and convective speed (ms^{-1}).

Assuming a stationary state, no electron particle flux and zero electron heat convective speed, the electron heat transport equation is simplified as

$$\frac{\partial}{\partial \rho} \left[V' \langle |\nabla \rho|^2 \rangle \left(-\chi_e n_e \frac{\partial T_e}{\partial \rho} \right) \right] = V' Q_e \quad (8.4)$$

Integrating this equation twice along the radial coordinate ρ , we have

$$T_e(\rho) - T_e(\rho_{max}) = \int_{\rho}^{\rho_{max}} \left(\frac{1}{V' \langle |\nabla \rho|^2 \rangle \chi_e n_e} \int_0^{\rho} V' Q_e d\rho \right) d\rho \quad (8.5)$$

The electron heat source contains the following contributions.

$$Q_e = Q_{e,EC} + Q_{e,IC} + Q_{e,LH} + Q_{e,NB} + Q_{e,etc} \quad (8.6)$$

where $Q_{e,index}$ is the electron heat source provided by each auxiliary H&CD listed in $index \in \{EC, IC, LH, NB\}$. $Q_{e,etc}$ is the sum of the other electron heat sources including ohmic heating, alpha particle self-heating, radiative loss, neoclassical sources and electron-ion equipartition power. This term is assumed to be non-time-varying on a short timescale for simplicity while each electron heat source quickly responds to its auxiliary H&CD power change. Furthermore, assuming that the radial profile shapes of the electron heat sources are non-time-varying for given launching conditions, each electron heat source can be expressed as a product of two factors, the auxiliary heating power $p_{e,index}(t)$ and normalized electron heat source profile $\hat{Q}_{e,index}(\rho)$. The electron heat source can be rewritten as

$$Q_e(\rho, t) = \sum_{index} p_{e,index}(t) \hat{Q}_{e,index}(\rho) + Q_{e,etc}(\rho), \text{ for } index \in \{EC, IC, LH, NB\} \quad (8.7)$$

Inserting this into equation (8.5), the electron temperature profile response to the power changes of the auxiliary H&CD systems is given by

$$\Delta T_e(\rho, t) = \sum_{index} C_{e,index}(\rho) \Delta p_{e,index}(t), \text{ for } index \in \{EC, IC, LH, NB\} \quad (8.8)$$

where

$$C_{e,index}(\rho) = \int_{\rho}^{\rho_{max}} \left(\frac{1}{V' \langle |\nabla \rho|^2 \rangle \chi_e n_e} \int_0^{\rho} V' \hat{Q}_{e,index}(\rho) d\rho \right) d\rho \quad (8.9)$$

This relation shows that an approximation $\Delta T_e^{approx.}(\rho, t)$ to the desired change of the electron temperature profile $\Delta T_e^{desired}(\rho, t)$ can be provided by linearly combining several auxiliary H&CD power changes $\Delta p_{e,index}(t)$ for given electron temperature profile responses $C_{e,index}(\rho)$ in such a way as to minimize the error between the two profiles

$$\min \left\| \Delta T_e^{desired}(\rho, t) - \Delta T_e^{approx.}(\rho, t) \right\| \quad (8.10)$$

The assumptions used in deriving this electron temperature profile response model are linearity and time-invariance. These assumptions are those generally used for simple identification of a system to be controlled. This incremental electron temperature profile response model can be updated in real-time in ITER, if the equilibrium quantities and source profile shapes are provided within the control interval with a modest accuracy.

8.2.2 Incremental q profile response model

The q profile is directly related to the source current density profiles in this model. The q profile [25] is given by

$$q = -\frac{V'F \left\langle \frac{1}{R^2} \right\rangle}{4\pi^2} \frac{1}{\frac{\partial \Psi}{\partial \rho}} \quad (8.11)$$

where F and $\langle 1/R^2 \rangle$ are the diamagnetic function (Tm) and a geometric coefficient averaged on the magnetic flux surface. The plasma current density (Am^{-2}) profile averaged on the magnetic flux surface [25] is given by

$$j_{pl} = -\frac{1}{\mu_0 V' \left\langle \frac{1}{R} \right\rangle} \frac{\partial}{\partial \rho} \left[V' \left\langle \frac{|\nabla \rho|^2}{R^2} \right\rangle \frac{\partial \Psi}{\partial \rho} \right] \quad (8.12)$$

where Ψ and μ_0 are the poloidal flux (Tm²) and vacuum permeability (TmA⁻¹). $\langle |\nabla \rho|^2 / R^2 \rangle$ and $\langle 1/R \rangle$ are geometric coefficients.

Integrating this equation along the radial coordinate ρ and inserting it into the equation (8.11), we have

$$q = \frac{C_1}{\int_0^\rho C_2 j_{pl} d\rho} \quad (8.13)$$

where

$$C_1 = \frac{V'^2 F \left\langle \frac{1}{R^2} \right\rangle \left\langle \frac{|\nabla \rho|^2}{R^2} \right\rangle}{4\pi^2 \mu_0} \quad \text{and} \quad C_2 = V' \left\langle \frac{1}{R} \right\rangle \quad (8.14)$$

The plasma current density contains the following contributions.

$$j_{pl} = j_{bs} + j_{ohm} + j_{EC} + j_{IC} + j_{LH} + j_{NB} \quad (8.15)$$

where j_{index} is the driven current source provided by each H&CD system listed in $index \in \{ohm, EC, IC, LH, NB\}$. j_{bs} is the bootstrap current density assumed for simplicity to be non-time-varying while the ohmic and driven currents quickly respond to the loop voltage and auxiliary H&CD power changes, respectively. This assumption would be not valid for steady-state operation in which the bootstrap current fraction is usually above 50%, as well

as during fast L-H and H-L confinement mode transitions. This model will be applicable only when the bootstrap current density is either stationary or slowly evolving compared with the change rates of the driven current density profiles. Furthermore, assuming that the radial profile shapes of the driven currents are non-time-varying for given launching conditions, each current source can be expressed as a product of two factors, the H&CD power $p_{q,index}(t)$ and normalized current density profile $\hat{j}_{index}(\rho)$. The plasma current density can then be rewritten as

$$j_{pl}(\rho, t) = \sum_{index} p_{q,index}(t) \hat{j}_{index}(\rho) + j_{bs}(\rho), \text{ for } index \in \{ohm, EC, IC, LH, NB\} \quad (8.16)$$

Inserting this into equation (8.13), we have

$$q(\rho, t) = \frac{C_1(\rho)}{C_3(\rho) + \sum_{index} C_{i(index)}(\rho) p_{q,index}(t)},$$

$$\text{for } index \in \{ohm, EC, IC, LH, NB\} \ \& \ i(index) \in \{4, 5, 6, 7, 8\} \quad (8.17)$$

where

$$C_3(\rho) = \int_0^\rho C_2(\rho) j_{bs}(\rho) d\rho \quad (8.18)$$

and

$$C_{i(index)}(\rho) = \int_0^\rho C_2(\rho) \hat{j}_{index}(\rho) d\rho \quad (8.19)$$

The q profile response to the power changes of the H&CD systems is then given by

$$\Delta q(\rho, t) = \sum_{index} \Delta p_{q,index}(t) C_{i(index)}(\rho),$$

$$\text{for } index \in \{ohm, EC, IC, LH, NB\} \ \& \ i(index) \in \{10, 11, 12, 13, 14\} \quad (8.20)$$

where

$$C_{i(index)}(\rho) = \frac{-C_1(\rho)}{C_9(\rho)} \times C_{i(index)-6}(\rho) \quad (8.21)$$

and

$$C_9(\rho) = \left(C_3(\rho) + \sum_{index} p_{q,index}(t) C_{i(index)-6}(\rho) \right)^2 \quad (8.22)$$

In general, the ohmic current is controlled by the applied loop voltage to satisfy the constraints on the total plasma current. Therefore, we have assumed that the ohmic current

counteracts each auxiliary driven current in such a way that the edge q value is not time-varying for given total plasma current and shape. The ohmic power change is divided into 4 parts to independently compensate the edge q variation resulting from each auxiliary driven current change.

$$\Delta q(\rho, t) = \sum_{index} (C_{10}(\rho)\Delta p_{q,ohm}^{index}(t) + C_{i(index)}(\rho)\Delta p_{q,index}(t)),$$

$$\text{for } index \in \{EC, IC, LH, NB\} \ \& \ i(index) \in \{11, 12, 13, 14\} \quad (8.23)$$

Following the assumption that each pair results in no edge q variation, we have

$$\Delta p_{q,ohm}^{index}(t) = -\frac{C_{i(index)}(\rho = \rho_{max})}{C_{10}(\rho = \rho_{max})}\Delta p_{q,index}(t),$$

$$\text{for } index \in \{EC, IC, LH, NB\} \ \& \ i(index) \in \{11, 12, 13, 14\} \quad (8.24)$$

Inserting this relation into equation (8.23), the q response to the power changes of the auxiliary H&CD systems is finally given by

$$\Delta q(\rho, t) = \sum_{index} C_{q,index}(\rho)\Delta p_{q,index}(t),$$

$$\text{for } index \in \{EC, IC, LH, NB\} \ \& \ i(index) \in \{11, 12, 13, 14\} \quad (8.25)$$

where

$$C_{q,index}(\rho) = C_{i(index)}(\rho) - \frac{C_{i(index)}(\rho = \rho_{max})}{C_{10}(\rho = \rho_{max})}C_{10}(\rho) \quad (8.26)$$

This relation shows that an approximation $\Delta q^{approx.}(\rho, t)$ to the desired change of the q profile $\Delta q^{desired}(\rho, t)$ can be provided by linearly combining several auxiliary H&CD power changes $\Delta p_{q,index}(t)$ for given q profile responses $C_{q,index}(\rho)$ in such a way as to minimize the error between the two profiles

$$\min \left\| \Delta q^{desired}(\rho, t) - \Delta q^{approx.}(\rho, t) \right\| \quad (8.27)$$

The assumptions used in deriving this q profile response model are again linearity and time-invariance. Therefore, the diffusion of the plasma current which is very slow under the ITER operating conditions is not considered. This incremental q profile response model can be updated in real-time in ITER, if the equilibrium quantities and source profile shapes are provided within the control interval with a modest accuracy

8.2.3 Simultaneous control of the electron temperature and q profiles

The electron temperature profile can be controlled using the incremental electron temperature profile response model. For example, assuming 5 radial control locations, we can construct a matrix relation such as

$$\begin{bmatrix} \Delta T_e(\rho_{e,1}) \\ \Delta T_e(\rho_{e,2}) \\ \Delta T_e(\rho_{e,3}) \\ \Delta T_e(\rho_{e,4}) \\ \Delta T_e(\rho_{e,5}) \end{bmatrix} = \begin{bmatrix} C_{e,EC}(\rho_{e,1}) & C_{e,IC}(\rho_{e,1}) & C_{e,LH}(\rho_{e,1}) & C_{e,NB}(\rho_{e,1}) \\ C_{e,EC}(\rho_{e,2}) & C_{e,IC}(\rho_{e,2}) & C_{e,LH}(\rho_{e,2}) & C_{e,NB}(\rho_{e,2}) \\ C_{e,EC}(\rho_{e,3}) & C_{e,IC}(\rho_{e,3}) & C_{e,LH}(\rho_{e,3}) & C_{e,NB}(\rho_{e,3}) \\ C_{e,EC}(\rho_{e,4}) & C_{e,IC}(\rho_{e,4}) & C_{e,LH}(\rho_{e,4}) & C_{e,NB}(\rho_{e,4}) \\ C_{e,EC}(\rho_{e,5}) & C_{e,IC}(\rho_{e,5}) & C_{e,LH}(\rho_{e,5}) & C_{e,NB}(\rho_{e,5}) \end{bmatrix} \begin{bmatrix} \Delta p_{e,EC} \\ \Delta p_{e,IC} \\ \Delta p_{e,LH} \\ \Delta p_{e,NB} \end{bmatrix} \quad (8.28)$$

Simplifying this relation using matrix and vector notations, we have

$$\Delta \mathbf{T}_e = \mathbf{C}_e \Delta \mathbf{p}_e \quad (8.29)$$

The required power changes of the auxiliary H&CD systems are obtained by solving

$$\Delta \mathbf{p}_e = g_e \mathbf{C}_e^{-1} \Delta \mathbf{T}_e, \quad (8.30)$$

where g_e is the proportional gain of the electron temperature control loop.

In the same way, the q profile can be controlled using the incremental q profile response model. For example, assuming 3 radial control locations, we can construct a matrix relation such as

$$\begin{bmatrix} \Delta q(\rho_{q,1}) \\ \Delta q(\rho_{q,2}) \\ \Delta q(\rho_{q,3}) \end{bmatrix} = \begin{bmatrix} C_{q,EC}(\rho_{q,1}) & C_{q,IC}(\rho_{q,1}) & C_{q,LH}(\rho_{q,1}) & C_{q,NB}(\rho_{q,1}) \\ C_{q,EC}(\rho_{q,2}) & C_{q,IC}(\rho_{q,2}) & C_{q,LH}(\rho_{q,2}) & C_{q,NB}(\rho_{q,2}) \\ C_{q,EC}(\rho_{q,3}) & C_{q,IC}(\rho_{q,3}) & C_{q,LH}(\rho_{q,3}) & C_{q,NB}(\rho_{q,3}) \end{bmatrix} \begin{bmatrix} \Delta p_{q,EC} \\ \Delta p_{q,IC} \\ \Delta p_{q,LH} \\ \Delta p_{q,NB} \end{bmatrix} \quad (8.31)$$

Simplifying this relation using matrix and vector notations, we have

$$\Delta \mathbf{q} = \mathbf{C}_q \Delta \mathbf{p}_q \quad (8.32)$$

The required power changes of the auxiliary H&CD systems are obtained by solving

$$\Delta \mathbf{p}_q = g_q \mathbf{C}_q^{-1} \Delta \mathbf{q} \quad (8.33)$$

where g_q is the proportional gain of the q profile control loop.

To calculate the inverse matrix (\mathbf{C}_e^{-1} or \mathbf{C}_q^{-1}) of either an over-determined ($\Delta\mathbf{T}_e$) or an under-determined ($\Delta\mathbf{q}$) system, the SVD technique is used. The saturation of the auxiliary H&CD power is taken into account in an iteration procedure. If the demand on an auxiliary H&CD power goes either above the maximum or below the minimum, this H&CD power remains unchanged to the previous value and the demand on the H&CD power is recalculated only for the other H&CD systems. At every control time-step, the demand on H&CD power is newly calculated including the previously saturated H&CD systems, in order to see if this new power demand can make the saturated H&CD powers to be controllable. Discretization of the auxiliary power change for a H&CD system which consists of several modules delivering a constant power can be additionally taken into account in the iteration procedure.

Simultaneous control of the electron temperature and q profiles is possible by combining the two incremental plasma profile response models.

$$\begin{bmatrix} \Delta T_e(\rho_{e,1}) \\ \Delta T_e(\rho_{e,2}) \\ \Delta T_e(\rho_{e,3}) \\ \Delta T_e(\rho_{e,4}) \\ \Delta T_e(\rho_{e,5}) \\ \Delta q(\rho_{q,1}) \\ \Delta q(\rho_{q,2}) \\ \Delta q(\rho_{q,3}) \end{bmatrix} = \begin{bmatrix} C_{e,EC}(\rho_{e,1}) & C_{e,IC}(\rho_{e,1}) & C_{e,LH}(\rho_{e,1}) & C_{e,NB}(\rho_{e,1}) \\ C_{e,EC}(\rho_{e,2}) & C_{e,IC}(\rho_{e,2}) & C_{e,LH}(\rho_{e,2}) & C_{e,NB}(\rho_{e,2}) \\ C_{e,EC}(\rho_{e,3}) & C_{e,IC}(\rho_{e,3}) & C_{e,LH}(\rho_{e,3}) & C_{e,NB}(\rho_{e,3}) \\ C_{e,EC}(\rho_{e,4}) & C_{e,IC}(\rho_{e,4}) & C_{e,LH}(\rho_{e,4}) & C_{e,NB}(\rho_{e,4}) \\ C_{e,EC}(\rho_{e,5}) & C_{e,IC}(\rho_{e,5}) & C_{e,LH}(\rho_{e,5}) & C_{e,NB}(\rho_{e,5}) \\ C_{q,EC}(\rho_{q,1}) & C_{q,IC}(\rho_{q,1}) & C_{q,LH}(\rho_{q,1}) & C_{q,NB}(\rho_{q,1}) \\ C_{q,EC}(\rho_{q,2}) & C_{q,IC}(\rho_{q,2}) & C_{q,LH}(\rho_{q,2}) & C_{q,NB}(\rho_{q,2}) \\ C_{q,EC}(\rho_{q,3}) & C_{q,IC}(\rho_{q,3}) & C_{q,LH}(\rho_{q,3}) & C_{q,NB}(\rho_{q,3}) \end{bmatrix} \begin{bmatrix} \Delta p_{EC} \\ \Delta p_{IC} \\ \Delta p_{LH} \\ \Delta p_{NB} \end{bmatrix} \quad (8.34)$$

Simplifying this relation using matrix and vector notations and multiplying by weights w_e and w_q , we have

$$\begin{bmatrix} w_e \Delta \mathbf{T}_e \\ w_q \Delta \mathbf{q} \end{bmatrix} = \begin{bmatrix} w_e \mathbf{C}_e \\ w_q \mathbf{C}_q \end{bmatrix} \begin{bmatrix} \Delta \mathbf{p} \end{bmatrix} \quad (8.35)$$

The electron temperature and q profile responses are appropriately weighted by trials to give a balance between the two profile response models. Otherwise, the SVD would produce a biased result on one of the profile controls. The required power changes of the auxiliary H&CD systems can be obtained by solving

$$\begin{bmatrix} \Delta \mathbf{p} \end{bmatrix} = \begin{bmatrix} w_e \mathbf{C}_e \\ w_q \mathbf{C}_q \end{bmatrix}^{-1} \begin{bmatrix} g_e & 0 \\ 0 & g_q \end{bmatrix} \begin{bmatrix} w_e \Delta \mathbf{T}_e \\ w_q \Delta \mathbf{q} \end{bmatrix} \quad (8.36)$$

In our simulations, the proportional gains of the control loops g_e and g_q are respectively 1.0 and 0.5. The weights w_e and w_q are respectively 1 and 10^5 . These weights can be

determined using a systematic method which contains an appropriate normalization and respects different dynamics of the different plasma profiles.

8.3 Plasma profile responses in ITER hybrid mode operation

The hybrid mode operation in ITER [3] aims at operating the plasma with improved plasma confinement for a long plasma burn time. In this operation mode, maintaining a stationary flat q profile above 1.0 is the key to avoid MHD instabilities deteriorating the plasma confinement. This capability has been experimentally demonstrated in several devices [98, 96, 97]. Active real-time control of the q profile will be an essential tool for achieving the hybrid mode operation for a long time. In this chapter, the ITER hybrid mode operation has been simulated using CRONOS with a prescribed evolution of the plasma boundary. The plasma current ramp-up scenario is generated by tailoring the initial part of the 15MA ITER operation scenario 2 [88]. The evolution of the plasma boundary is prescribed with a large initial bore, $a(t = 1.6\text{s}) = 1.6\text{m}$. During the flat-top phase, the total plasma current is maintained at 12MA and the average electron density is assumed to be $8.5 \times 10^{19}\text{m}^{-3}$. Anomalous heat conductivity profiles are calculated by the KIAUTO transport model [37]. A slight improvement of the plasma confinement observed in the hybrid mode experiments [98, 96, 97] is assumed using a confinement time correction factor for H-mode, $H_{98} = 1.2$. 33MW of slightly off-axis NBI and 20MW of on-axis ICRH are applied as the main H&CD scheme. Hereinafter, the simulation conducted with these assumptions is referred to as reference simulation. The electron and ion temperature profiles, and the safety factor profiles are shown in figure 8.1.

To study the usefulness of the incremental plasma profile response models, additional auxiliary H&CD power is added to the main H&CD scheme, and then the resulting changes of the electron temperature and q profiles are calculated. Our first question is what the difference is between the incremental models and a full plasma evolution simulation.

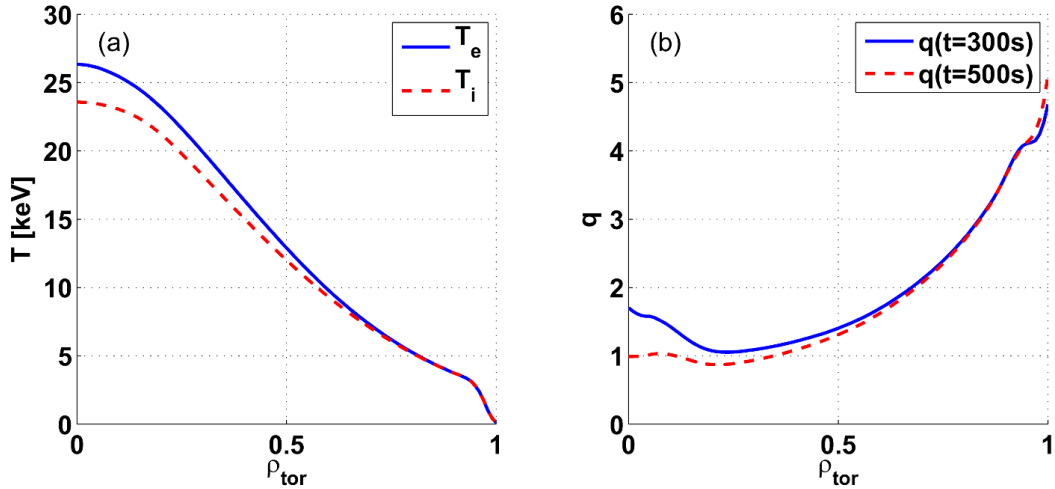


Figure 8.1: Plasma profiles in the reference simulation. (a) Electron and ion temperature profiles at $t = 300$ s. (b) Safety factor profiles at $t = 300$ s and $t = 500$ s.

8.3.1 Plasma profile responses to additional H&CD power

The changes of the electron temperature and q profiles due to the application of 20MW of additional ECH&CD are respectively shown in figure 8.2 (a) and (c). A second case in which 20MW of additional LHH&CD is applied is shown in figure 8.2 (b) and (d). The electron temperature profile changes are calculated about 10 seconds after the application of the additional auxiliary power at which time the electron temperature profile evolution is stationary. These are then compared with the profile changes modelled using our simple incremental electron temperature profile response model. The electron heat source profile is amplified 5 times for visibility. The radial coordinate is given by the square root of the normalized toroidal flux, ρ_{tor} . The q profile changes are calculated about 200 seconds after the application of the additional auxiliary power at which time the fast transient redistribution of the plasma current is almost disappeared and the q profile is slowly evolving. These are then compared with the profile changes modelled using our simple incremental q profile response model. The modelled electron temperature and q profile changes are calculated at the time that the additional auxiliary power is applied.

In both EC and LH cases, the electron temperature profile changes in the simulations are much smaller than the modelled ones (multiplied by 0.4), because a significant amount of the electron heating power is consumed for heating the ions through the electron-ion equipartition power as shown in table 8.1. When 20MW of EC power is applied, the increases

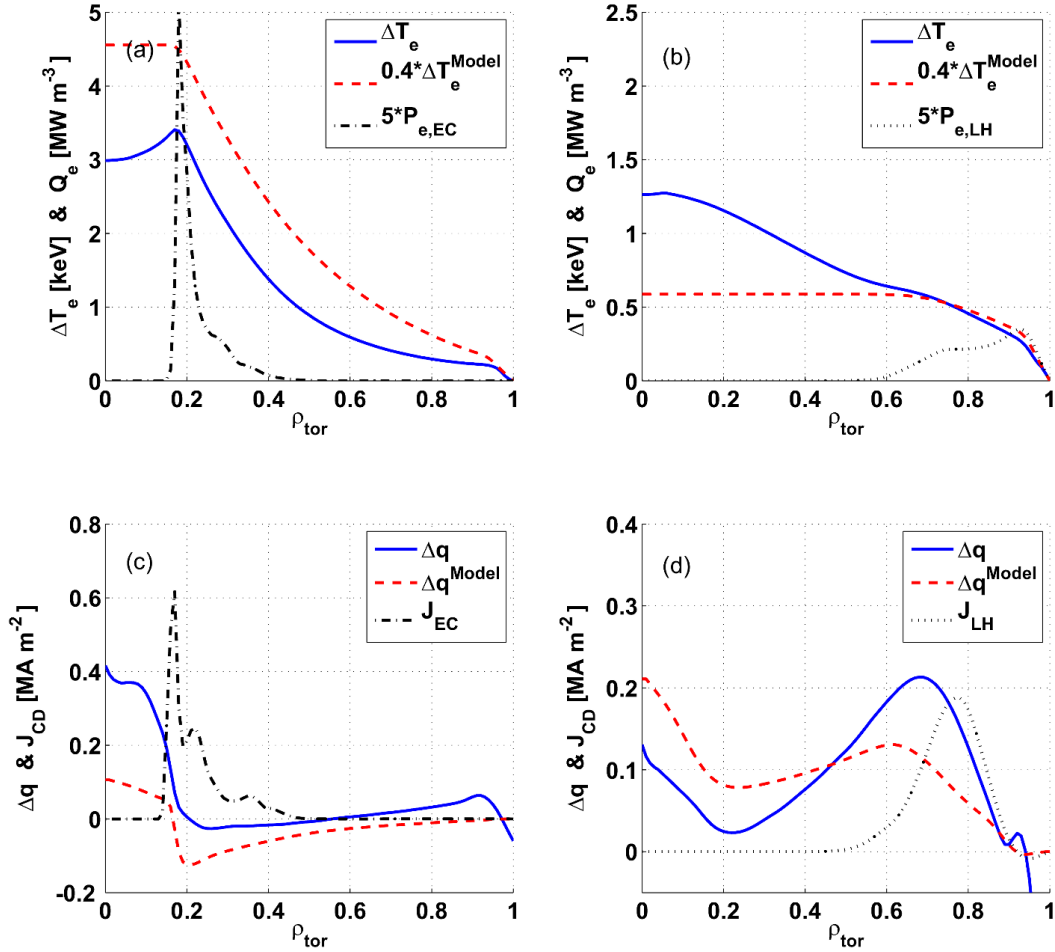


Figure 8.2: Changes of the electron temperature ((a) and (b)) and q ((c) and (d)) profiles with respect to the reference simulation. 20MW of ECH&CD ((a) and (c)) and 20MW of LHH&CD ((b) and (d)) are additionally applied. The changes of the electron temperature profiles modelled using the incremental electron temperature profile response model are multiplied by 0.4 and the electron heat deposition profiles are amplified 5 times for visibility.

of the total electron and ion heating powers are respectively about 8.88 and 10.64MW (see table 8.1). The electron energy confinement time is reduced by about 14%. When 20MW of LH power is applied, the increase of the total electron and ion heating powers are respectively about 15.65 and 7.65MW. Although the LH power consumed for heating ions is relatively smaller than the EC case, the electron energy confinement time is significantly reduced by about 23%. Therefore, the electron temperature profile changes in the simulations generally correspond to about 30 ~ 50% of the modelled profile changes. Including the electron-ion equipartition term and considering the confinement degradation will improve our present

Table 8.1: Increase and decrease of the total electron and ion heating powers, ohmic power, alpha particle self-heating powers to electron and ion, external auxiliary heating powers to electron and ion, electron-ion equipartition and loss power (MW). The electron thermal energy confinement time changes are compared. These values are calculated about 10 seconds after the application of 20MW of EC and/or 20MW of LH.

	$\Delta P_{e,tot}$	$\Delta P_{i,tot}$	ΔP_{ohm}	$\Delta P_{e,\alpha}$	$\Delta P_{i,\alpha}$	$\Delta P_{e,add}$	$\Delta P_{i,add}$	ΔP_{ei}	ΔP_{loss}	$\frac{\Delta\tau_{E,e}}{\tau_{E,e}^{ref.}}$
EC	8.88	10.64	-0.08	0.29	1.98	19.90	-0.92	9.58	1.65	-14%
LH	15.65	7.65	-0.14	4.86	2.49	19.21	-2.48	7.64	0.64	-23%
EC&LH	24.42	19.49	-0.19	4.28	4.29	39.23	-1.30	16.51	2.39	-35%

$\Delta P_{e,tot} \approx \Delta P_{ohm} + \Delta P_{e,\alpha} + \Delta P_{e,add} - \Delta P_{ei} - \Delta P_{loss}$ and
 $\Delta P_{i,tot} \approx \Delta P_{i,\alpha} + \Delta P_{i,add} + \Delta P_{ei}$, where $\Delta P_{loss} \approx \Delta(P_{line} + P_{cyclo} + P_{brem})$

incremental electron temperature profile response model.

Major differences between the simulation and modelled electron temperature profile changes are observed in the central region for both cases. These are mainly due to the simplifications applied to the electron heat transport. In the full plasma evolution simulations, the electron heat conductivity in the central region is increased with the application of EC, while it is reduced with the application of LH.

Application of the near on-axis EC driven current profile increased the central q values while slightly decreasing the q values around the current deposition location. Application of the far off-axis LH driven current increased the q values both around the current deposition location and in the central region. These q profile changes are similar to the modelled ones. However, mainly at the central region, there are significant differences between them. When near on-axis EC was additionally added, the resulting central plasma heating reduced the radial diffusion of the plasma current delaying the evolution of the central q value. When far off-axis LH was additionally added, the plasma current density at the centre region was affected a little due to the very slow radial current diffusion. The changes of inductive/non-inductive currents are shown in table 8.2. The bootstrap and NB driven currents are increased due to the plasma heating and the ohmic current is decreased to maintain the total plasma current.

Table 8.2: Increase and decrease of the ohmic current, EC, LH and NB driven currents, bootstrap current and total plasma current (MA). These currents are calculated about 200 seconds after the application of 20MW of EC and/or 20MW of LH.

	ΔI_{ohm}	ΔI_{EC}	ΔI_{LH}	ΔI_{NB}	ΔI_{BS}	ΔI_{pl}
EC	-0.87	0.43	-	0.18	0.26	0.00
LH	-1.72	-	1.09	0.13	0.53	0.03
EC&LH	-2.53	0.42	1.08	0.29	0.77	0.03

8.3.2 Application of both ECH&CD and LHH&CD

The electron temperature profile change due to the application of both the additional ECH&CD and LHH&CD is compared with the modelled one in figure 8.3 (a). The increases of the total electron and ion heating powers are respectively about 24.42 and 19.45MW as shown in the third row in table 8.1. The electron energy confinement time is reduced by about 35%. Therefore, the electron temperature profile change in the simulation again corresponds to about 40% of the modelled profile change. The shape of the electron heat conductivity profile in the central region is changed less than the previous two cases, by heating the plasma both at the central and outer regions. Therefore, the shape of the electron temperature profile response is very similar to the modelled one.

The most important result from the electron temperature profile responses is not that there is a magnitude error about 60%, but that the shapes of the modelled and simulation profile responses are similar. The direction of the profile change and its relative magnitude on several radial points is likely to be adequate information for setting up feedback control. The differing response amplitude can easily be handled by controller gains.

The q profile change is compared with the modelled one in figure 8.3 (b). The modelled and simulation q profile responses are again similar. However, the simulation q profile response is slightly higher than the modelled one due to the plasma heating effect. Assuming that the ohmic current counteracts the driven source current in such a way as to compensate the edge q variation appears to be an acceptable simplification in deriving the incremental q profile response model. Including the plasma heating effect and considering the current diffusion will improve the accuracy of our incremental q profile response model. However, this would deteriorate the robustness of the simple response models. Although these effects

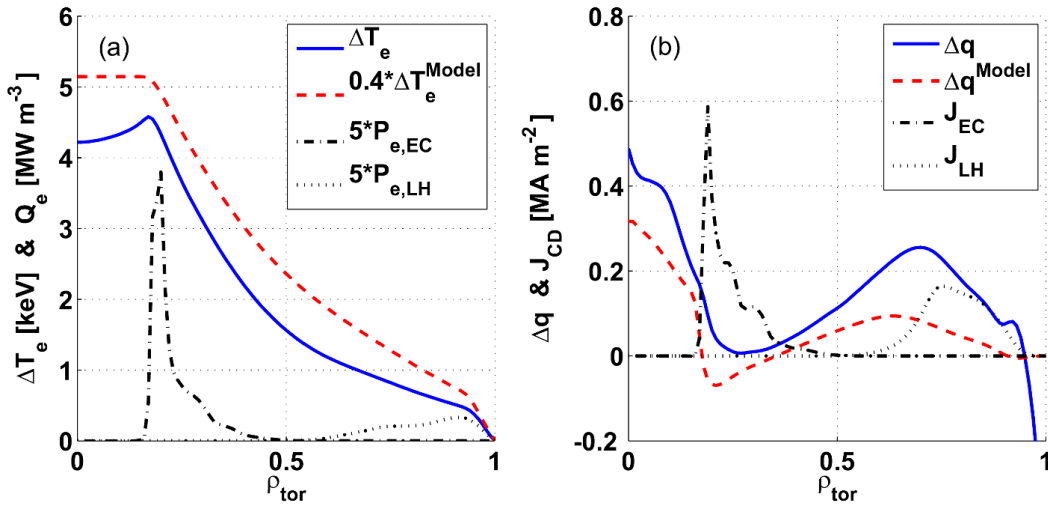


Figure 8.3: Changes of (a) the electron temperature and (b) q profiles with respect to the reference simulation. Both 20MW of ECH&CD and 20MW of LHH&CD are additionally applied. The changes of the electron temperature profiles modelled using the incremental electron temperature profile response model are multiplied by 0.4 and the electron heat deposition profiles are amplified 5 times for visibility.

are not negligible, our simplified incremental q profile response model still provides a fairly good estimate of the q profile change for developing feedback control.

8.4 Active control of kinetic plasma profiles

The incremental plasma profile response models have been used to control the electron temperature and q profiles either independently or simultaneously. The control interval set to 10 seconds appears to be sufficient for real-time update of the plasma profile response models in ITER, since this active plasma profile control technique requires a modest accuracy for the equilibrium reconstruction and source profile calculation.

8.4.1 Controlling the electron temperature profile

The electron temperature profile was controlled starting at about 300s using all the available actuators, EC, IC, LH and NB. The evolution of the electron temperature at 5 radial control

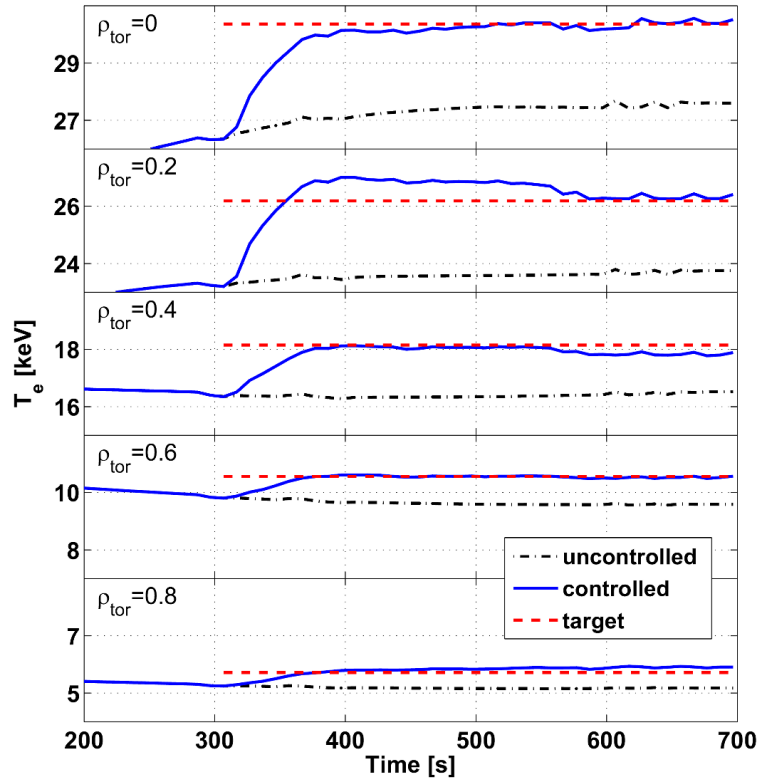


Figure 8.4: Time traces of the electron temperatures at 5 radial control locations. Control of the electron temperature profile was started at about $t = 300$ s.

locations is shown in figure 8.4. The target electron temperature profile is determined by multiplying the electron temperature profile at 700s in the reference simulation by a factor 1.1. The target electron temperature at each radial control location is shown as a dashed line. The evolution of the uncontrolled electron temperatures in the reference simulation is shown as dashed-dotted lines. The controlled electron temperature profile approached the target profile within 100s and was held stationary.

The radial electron temperature profiles at 700s are shown in figure 8.5 (a) and the electron heat source profiles normalized by their auxiliary H&CD powers are shown in figure 8.5 (b). The time traces of the actuator powers are shown in figure 8.6. NB and IC were already used as the main H&CD with their maximum powers. EC and LH powers were additionally applied starting at about 300s. While the LH power reached its maximum at the end of the simulation, the EC power was still controllable, indicating that the control of the electron temperature profile was still active.

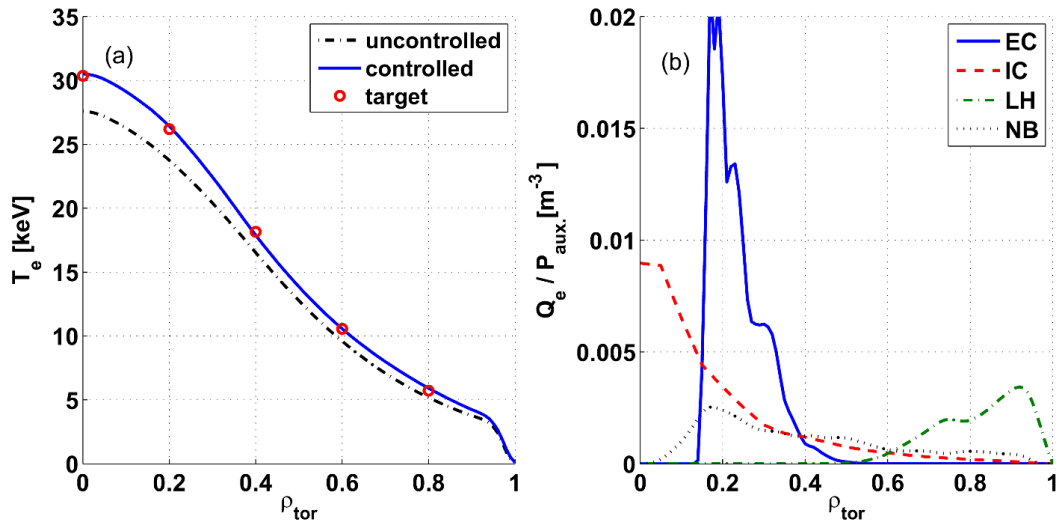


Figure 8.5: (a) The electron temperature profiles and (b) the unit electron heating profiles normalized by their auxiliary H&CD powers at 700s. Control of the electron temperature profile was started at about $t = 300$ s.

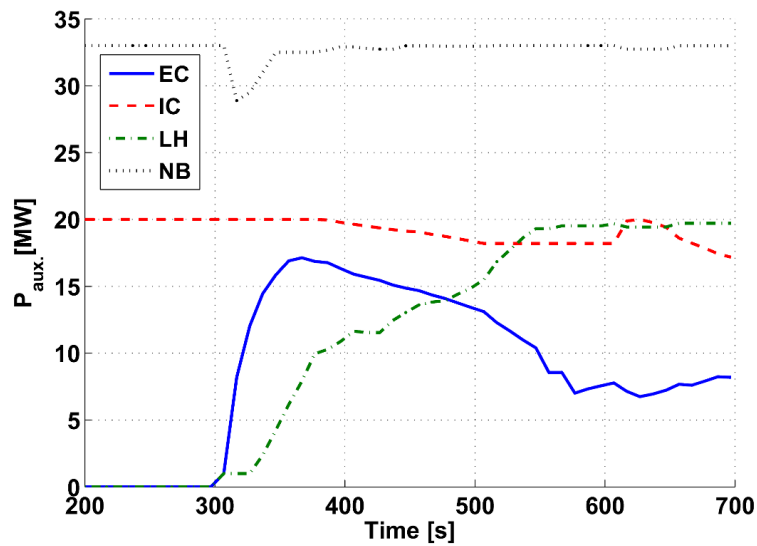


Figure 8.6: Time traces of auxiliary H&CD powers. Control of the electron temperature profile was started at about 300s.

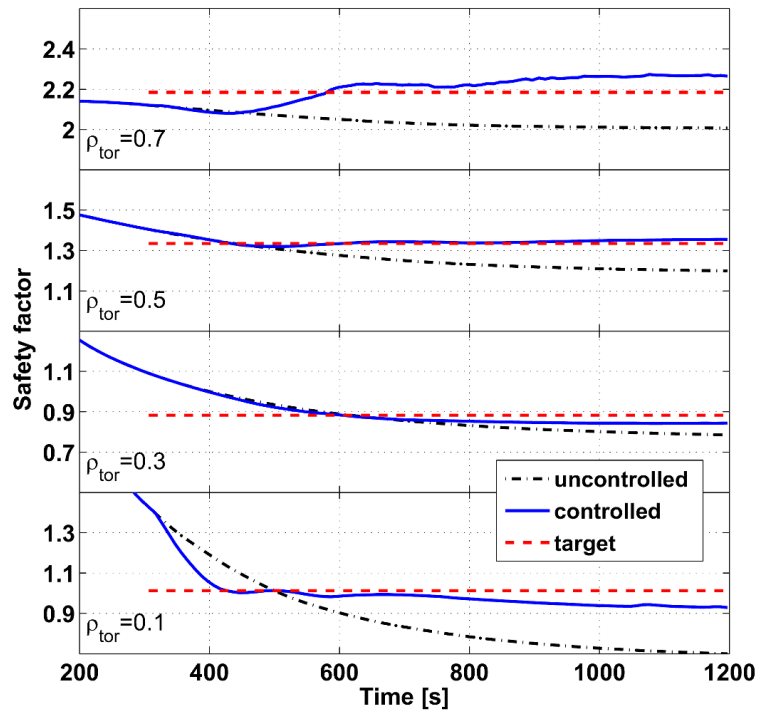


Figure 8.7: Time traces of the q values at 4 radial control locations. Control of the q profile was started at about $t = 300$ s.

It is worth remembering that the achievable target electron temperature profile is strongly limited by the available powers of the auxiliary H&CD systems. In addition, if too broad a target electron temperature profile is requested, the target profile is sometimes not achievable even with adequate power. Any heat source with a localized far off-axis deposition profile inevitably increases the central electron temperature through the transport processes (see figure 8.2 (b)). Thus controllability is limited by both the maximum available power and the lower limit of zero power for each H&CD source.

8.4.2 Controlling the q profile

The q profile was controlled starting at about 300s using these three actuators, EC, LH and NB, which can provide non-inductively driven currents. The evolution of the q values at 4 radial control locations is shown in figure 8.7. The target profile is determined by averaging the two q profiles at 700s obtained from both the reference simulation and the simulation in which maximum LH and EC powers are additionally applied. In this way, the target q profile is known to be accessible with the controlled EC, LH and NB at least until $t = 700$ s.

The target q value in the central region ($\rho_{tor} = 0.1$) is initially much less than the q value in the simulation. This large difference produced a strong action on the central value at the beginning of the control. The central q value became close to the target value within 100s, while the values at other control locations evolved similarly to the uncontrolled evolution. As the demand on the control of the central q value became weaker, the control of the q values at other control locations became more active. This control behaviour is caused by the absence of an actuator which can reduce the central q value while increasing q values at outer region. Therefore, both EC and LH were initially inactive while NB was activated to reduce the central q value.

The radial q profiles at 700s are shown in figure 8.8(a) and the driven current density profiles normalized by their auxiliary H&CD powers are shown in figure 8.8 (b). The time traces of the actuator powers are shown in figure 8.9. The actuator powers are easily saturated in this control simulation for ITER hybrid mode operation. Once the actuator powers are saturated at their maximum values, the q profile inevitably deviates from its target profile. LH power applied to control the naturally decreasing central q value also increases the value at $\rho_{tor} = 0.7$ to above the target value. However, this is inevitable for LH to best control the q profile, unless the shape of the LH driven source current profile is additionally controlled.

8.4.3 Simultaneous control of the electron temperature and q profiles

Finally, simultaneous control of the electron temperature and q profiles has been successfully achieved. The target electron temperature and q profiles were those used in the previous two subsections. The control of the q profile was started first at about 300s and then the control of the electron temperature was started at about 400s, to avoid a strong conflict between the two controls observed when starting them at the same time. The control of the central q value again initially demands a fast decrease of NB power inactivating both EC and LH. Therefore, if the control of the electron temperature profile to reach a higher target electron temperature profile starts with this control at the same time, these controls conflict with each other.

The evolution of the electron temperature and q profiles are shown in figure 8.10. Both profiles are as well controlled as the previous simulations controlling each one of the two

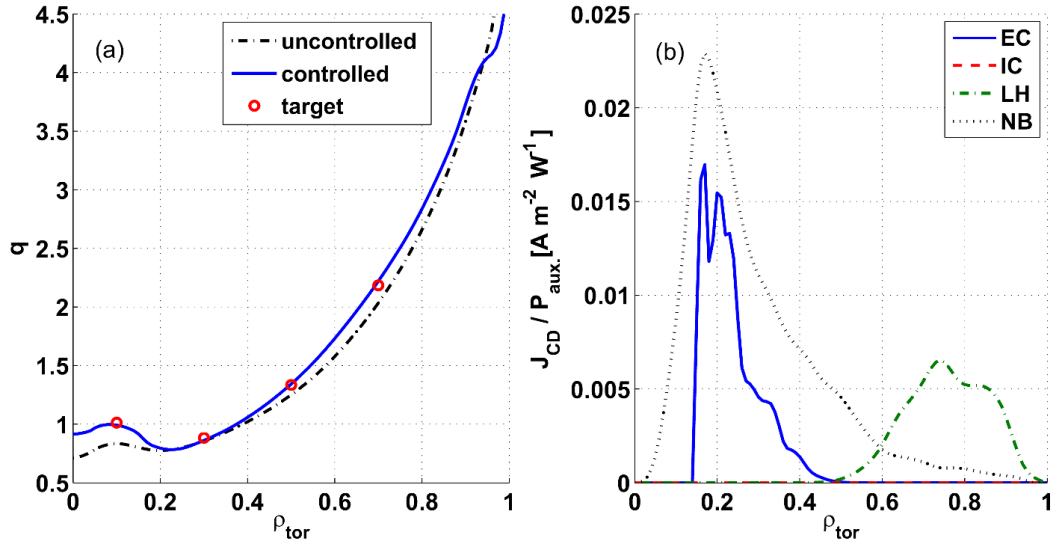


Figure 8.8: (a) The q profiles and (b) the unit driven current source profiles normalized by their auxiliary H&CD powers at $t = 700\text{s}$. Control of the q profile was started at about $t = 300\text{s}$.

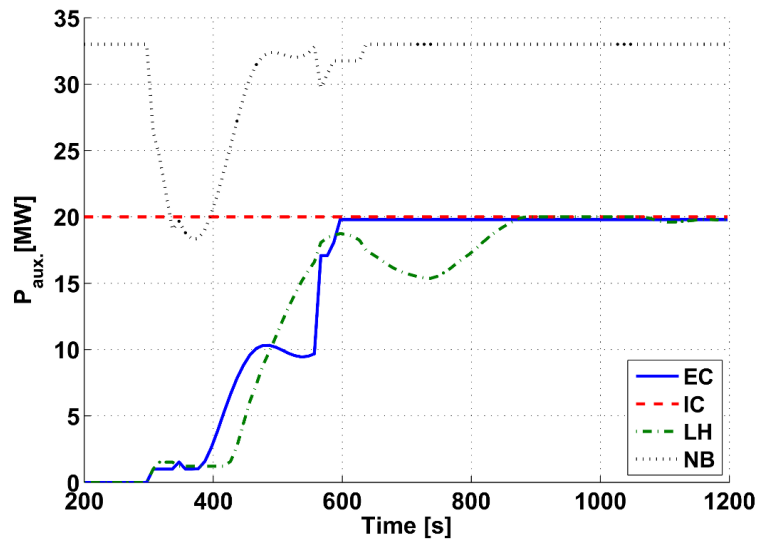


Figure 8.9: Time traces of auxiliary H&CD powers. Control of the q profile was started at about $t = 300\text{s}$.

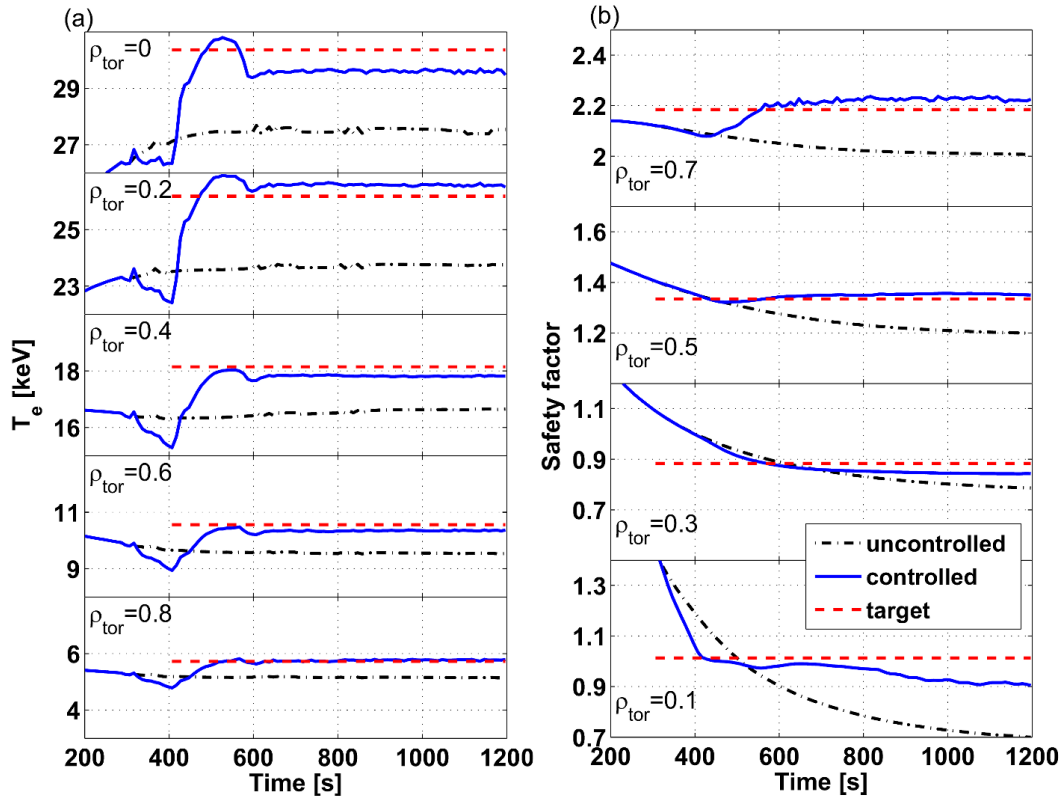


Figure 8.10: Time traces of (a) the electron temperatures at 5 radial control locations and (b) q values at 4 radial control locations. Control of the electron temperature profile was started at about $t = 400$ s and control of the q profile was started at about $t = 300$ s.

plasma profiles separately. The radial profiles at 700s are shown in figure 8.11 and the time traces of the actuator powers are shown in figure 8.12. The actuators for the control of the q profile, EC, LH and NB, already reached their maximum powers at about 600s. However, the control of the electron temperature profile was still active with the IC power until the end of the simulation.

8.5 Summary and Discussion

The main objective in developing this simple and direct plasma profile control method was to explore a robust control technique. Aiming at a real-time update of the plasma profile response model in ITER, simplified incremental electron temperature and q profile response models have been developed. The plasma profile responses calculated by these incremen-

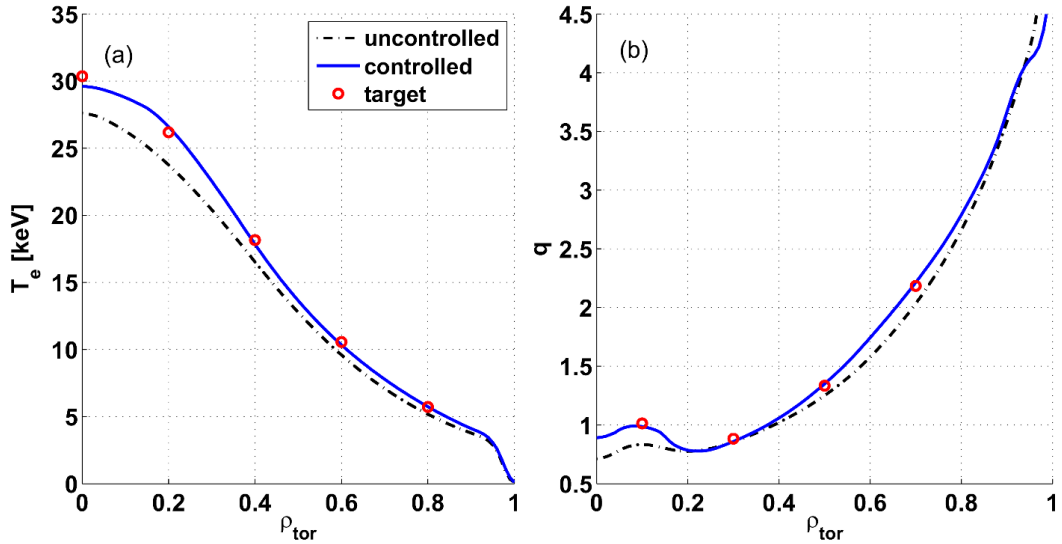


Figure 8.11: (a) The electron temperature profiles and (b) q profiles at $t = 700$ s. Control of the electron temperature profile was started at about $t = 400$ s and control of the q profile was started at about $t = 300$ s.

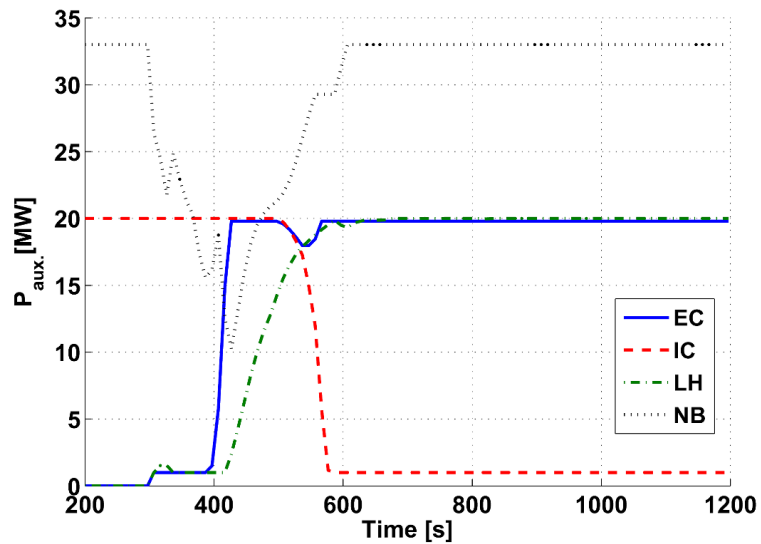


Figure 8.12: Time traces of auxiliary $H\&C\&D$ powers. Control of the electron temperature profile was started at about $t = 400$ s and control of the q profile was started at about $t = 300$ s.

tal models provide adequate information for the feedback control of plasma profiles. It is likely that the simplifying approximations in the linear time-invariant incremental models provide as accurate models as those based on more subtle but less general assumptions. The capability of this control technique has been successfully shown in the CRONOS transport simulations of the ITER hybrid mode operation. Both the electron temperature and q profiles were well controlled. The q profile control revealed that the ITER hybrid mode operation will require additional auxiliary H&CD power to maintain the stationary flat q profile. This control technique could be experimentally demonstrated in present large devices, if fast equilibrium reconstruction and source profile calculation methods are provided.

The plasma current ramp-up and ramp-down phases can be included into the control phase by providing pre-programmed waveforms of the target plasma profiles. For the application of this control technique to ITER steady-state operation, we need an additional technique which can intelligently identify the target plasma profiles taking the dynamic evolution of internal transport barriers into account.

Chapter 9

Conclusions

9.1 Summary

In the first part of this thesis, we have studied two physics questions linked to the non-linear free-boundary plasma equilibrium evolution. We have investigated the dynamic response of the free-boundary plasma equilibrium to either the external voltage perturbations or internal plasma disturbances using DINA-CH.

In the magnetic ELM triggering experiments in ASDEX Upgrade, the ELMs were triggered when the plasma was moving down towards the X-point with a consequent decrease of the plasma current density in the edge region, contrary to the previous observation on TCV in which ELMs were triggered when the edge current was increased by an upward plasma movement. We have investigated this opposite behaviour using DINA-CH, focusing on the free-boundary plasma equilibrium responses. Deformation of the plasma shape is identified as a possible candidate which can explain the observed opposite behaviour. The PSLs located inside the vacuum vessel of ASDEX Upgrade produced similar external linking flux changes to those generated by the G-coil sets in TCV for opposite vertical plasma movements. Therefore, both plasmas experienced similar local flux surface expansions near the upper G-coil set and PSL when the ELMs were triggered. In ASDEX Upgrade, however, the localized expansion of the plasma flux surfaces near the upper PSL was observed with the global shrinkage of the plasma column accompanied by the downward plasma movement. The effect of this plasma shape deformation on the plasma stability at the edge region has

been analyzed using the KINX code. This stability analysis revealed that there is a correlation between the shape deformation and the edge plasma stability. However, this correlation could be different for different type of natural ELMs. Therefore, all the potentially relevant mechanisms for the magnetic triggering of ELMs have been taken into account, not to erroneously attribute causality in the presence of all correlated plasma responses.

The specifications regarding the plasma disturbances in ITER have been recently updated. Therefore, we have re-examined the capability of the feedback control system of ITER in rejecting strong disturbances, such as uncontrolled ELMs and fast H-L mode transitions. These disturbances are pre-programmed using a routine controlling the store plasma energy by modifying the plasma heat conductivity profiles. Stronger uncontrolled ELMs than the updated specifications were controllable with the feedback control system. Full recovery of the plasma current, position and shape took less than 4 seconds. However, the specifications for fast H-L mode transitions were not fully achievable due to a VDE caused by a strong radially inward plasma movement. Full recovery of the plasma current, position and shape took less than 10 seconds, unless the plasma experience a strong disturbances causing a VDE. A stepwise reduction of additional plasma H&CD power across the confinement mode transition would be useful to reduce the magnitude of the disturbance in ITER.

In the second part of this thesis, we firstly have introduced DINA-CH and CRONOS. We have then presented the full tokamak discharge simulator developed by combing these two codes. This full tokamak discharge simulator has been used to study the feasibility of ITER operation scenarios, as well as several issues related to the tokamak operation.

In the combined tokamak discharge simulator, DINA-CH self-consistently calculates the non-linear evolution of free-boundary plasma equilibrium with the plasma current diffusion, in response to both controlled PF coil currents and inductively driven currents in the surrounding conducting system. CRONOS provides the evolution of the kinetic plasma profiles by self-consistently solving heat and particle transport with source profiles. The free-boundary plasma equilibrium provided by DINA-CH is directly used for CRONOS transport and source calculations. The plasma and source profiles provided by CRONOS are directly used for DINA-CH in calculating the free-boundary equilibrium and current diffusion. All the exchanged data between DINA-CH and CRONOS are passed as SIMULINK variables explicitly in time with a sufficiently small time-step to ensure the convergence. This explicit

data exchange scheme slightly deteriorates the consistency of the coupled physics, compared with a fully implicit scheme solving a complete set of coupled transport equations. Nevertheless, this was an inevitable choice to guarantee computational performance and reliability of the combined tokamak discharge simulator. With this code coupling scheme, the two codes are combined maintaining their original code structures. In the combined simulation, the computational performance was not significantly deteriorated with the explicit data exchange scheme, and propagation of numerical errors between the two codes was avoided.

Inductive 15MA ELMy H-mode ITER scenario 2 has been successfully simulated as a demonstration of the capabilities of the combined tokamak discharge simulator, as well as being a design study in itself. The alpha particle self-heating power was slightly over 100MW during the current flat-top phase ($Q \sim 10$). A L-H confinement mode transition was triggered by the application of the main H&CD at SOF. The vertical instability associated with a high l_i was controllable with the vertical position control system. The central q was quickly reduced at the beginning of the plasma current ramp-up, causing an early onset of sawtooth events. Although the current in the PF2 coil briefly violated its limit around the EOF, this violation seems avoidable by either changing the plasma shape evolution or increasing the coil current limit itself, as addressed in the recent ITER design review [84]. The consumption of the poloidal flux provided by the coil system was slightly less than the estimated one in the reference operation scenario. The imbalance current flowing in the VSC and the total active power provided by the power supply system were well within the operational limits. The evolution of the plasma boundary in a limited shape configuration was guided by the pre-programmed coil current and prescribed feed-forward voltage waveforms. After the plasma had a fully diverted configuration at about 29s, the shape controller started to control 6 gaps between the plasma and wall. It then continued until the end of the current ramp-down phase.

Moreover, we have investigated several issues related to ITER operation. The violation of CS coil current limits during the current ramp-up phase was avoided by either applying early heating or modifying the pre-programmed coil current waveforms. The vertical instability growth rates of the plasmas with different β_p and l_i were calculated from the open-loop simulations. It has shown that the vertical stability can be improved by reducing the l_i .

The capacity of LH for saving the poloidal flux consumed to produce plasma current and for increasing the safety margins in operating the superconducting poloidal field coils has

been studied. With an early application of 20MW of LH power during the current ramp, up to 43Wb of flux consumption was saved with respect to the ohmic ramp-up case. A slightly reversed or flat target q profile required to operating ITER in advanced tokamak regimes was achieved avoiding the onset of sawteeth during the current ramp-up. The application of LH also improved the vertical stability of the plasma by reducing l_i . The early application of LH before the plasma has a fully diverted configuration gave a significant modification to the evolution of the plasma shape. Either redesigning the reference coil current waveforms or adding additional shape controls, such as an elongation control, was requested in order to provide an appropriate guidance for desired plasma shape transition. We have used the latter option in our simulations.

We have simulated ITER hybrid mode operation, focusing on the operational capability of obtaining a stationary flat q profile at SOF and sustaining it as long as possible by combining various non-inductively driven current sources. The plasma current ramp-up scenario is generated by tailoring the initial part of the inductive 15MA ELMy H-mode ITER operation. Firstly, we have conducted various simulations with slightly different assumptions to get the achievable range of plasma parameters in the ITER hybrid mode operation. Secondly, we have studied the effect of different H&CD method on the evolution of the q profile. Application of a near on-axis ECCD appears to be effective compared to the far off-axis LHCD, at least on short time scales.

In the last part of this thesis, we have developed a robust control technique that simplifies the active plasma profile control in ITER and its potential has been shown by applying it to the simulation of ITER hybrid mode operation.

The response of the plasma profiles to power changes of auxiliary H&CD systems are modelled by simplifying the related physics to allow real-time update of them. The electron temperature profile response is modelled by simplifying the electron heat transport equation and the q profile response is modelled by directly relating it to the changes of source current density profiles. The required changes of actuator powers are calculated using the SVD technique, taking the saturation of the actuator powers into account. This control technique can be used for real-time active control of the plasma profiles, if a fast equilibrium reconstruction and source profile calculation methods are provided. In the CRONOS simulations with a control interval of 10 seconds, the electron temperature and q profiles were well controlled either independently or simultaneously. The control of q profile revealed that ITER will

require additional auxiliary H&CD power to maintain the stationary flat q profile for the hybrid mode operation.

9.2 Perspective

The study of the plasma dynamic response to either external voltage perturbations or internal plasma disturbances has demonstrated the capability of DINA-CH, a non-linear free-boundary plasma equilibrium evolution code. The full tokamak discharge simulator developed by combining DINA-CH and the advanced plasma transport modelling code, CRONOS has clearly shown its extended capability. The robust control technique developed for real-time active control of kinetic plasma profiles in ITER has shown its strong potential. As a final conclusion, the tasks that we could attempt in near future with these tools, technique and our experience are summarized.

- Improve the studies of the magnetic triggering of ELMs and the plasma dynamic responses to disturbances using the full tokamak discharge simulator.
- Study the feasibility of ITER hybrid and steady-state mode operation scenarios using theory based transport models.
- Test the active plasma profile control technique in ITER hybrid mode and steady-state operations using the full tokamak discharge simulator.
- Demonstrate the active plasma profile control technique in present tokamaks.
- Improve the plasma profile response models in order to include the plasma current ramp-up and ramp-down phases.
- Develop an integrated plasma control system which contains all the magnetic and kinetic plasma controls, with an intelligent plasma disruption avoidance technique.
- Include 3D effects such as the toroidal magnetic field ripple and ferromagnetic inserts.
- Include the plasma-antenna power coupling physics.

- Technically, further improve the full tokamak discharge simulator (consistency, performance, accuracy, stability, reliability and user-friendliness)
- Provide these tools, techniques and simulations to EU-ITM and support developing a new simulation tool.

Appendix A

Details in deriving the theoretical formulations

A.1 Non-linear Grad-Shafranov equation

A.1.1 DINA-CH : CGS units

In DINA-CH, the non-linear Grad-Shafranov equation is derived in CGS units using the following set of coupled assuming stationary ideal MHD conditions.

$$\mathbf{j} \times \mathbf{B} = c \nabla p \quad (\text{A.1})$$

$$\nabla \cdot \mathbf{B} = 0 \quad (\text{A.2})$$

$$\nabla \times \mathbf{B} = \frac{4\pi}{c} \mathbf{j} \quad (\text{A.3})$$

where p , \mathbf{j} and \mathbf{B} are respectively the plasma pressure, current density and magnetic field.

Introducing a flux function ψ defined as the poloidal flux per radian in ϕ and relating $\nabla \cdot \mathbf{B} = 0$ and $\mathbf{B} \cdot \nabla \psi = 0$, the poloidal component of the magnetic fields can be expressed as follows.

$$B_R = -\frac{1}{R} \frac{\partial \psi}{\partial z}, \quad B_z = \frac{1}{R} \frac{\partial \psi}{\partial R}. \quad (\text{A.4})$$

From the symmetry of \mathbf{j} and \mathbf{B} in the force balance equation, the poloidal component of the plasma current can be expressed using a current flux function f .

$$j_R = -\frac{1}{R} \frac{\partial f}{\partial z}, \quad j_z = \frac{1}{R} \frac{\partial f}{\partial R}. \quad (\text{A.5})$$

Comparing these relations with Ampère's law,

$$j_R = -\frac{c}{4\pi} \frac{\partial B_\phi}{\partial z}, \quad j_z = \frac{c}{4\pi R} \frac{\partial(RB_\phi)}{\partial R}, \quad (\text{A.6})$$

the flux function f is defined as

$$f = \frac{cRB_\phi}{4\pi}. \quad (\text{A.7})$$

Since the plasma pressure p is a function of ψ , the poloidal current function f is also a function of ψ .

Decomposing the poloidal and toroidal components of the plasma current and magnetic fields in the force balance equation

$$\mathbf{j}_p \times \mathbf{i}_\phi B_\phi + j_\phi \mathbf{i}_\phi \times \mathbf{B}_p = c\nabla p, \quad (\text{A.8})$$

and substituting the poloidal components using the flux functions

$$\mathbf{B}_p = \frac{1}{R}(\nabla\psi \times \mathbf{i}_\phi) \quad \text{and} \quad \mathbf{j}_p = \frac{1}{R}(\nabla f \times \mathbf{i}_\phi), \quad (\text{A.9})$$

the force balance equation can be rewritten as

$$j_\phi = cR \frac{dp}{d\psi} + \frac{4\pi}{cR} f \frac{df}{d\psi}. \quad (\text{A.10})$$

The toroidal current density, j_ϕ , can also be written in terms of ψ using Ampère's law as follows

$$-\frac{4\pi}{c} R j_\phi = R \frac{\partial}{\partial R} \frac{1}{R} \frac{\partial \psi}{\partial R} + \frac{\partial^2 \psi}{\partial z^2}. \quad (\text{A.11})$$

Substituting the j_ϕ into this equation, the non-linear Grad-Shafranov equation is written as

$$R \frac{\partial}{\partial R} \left(\frac{1}{R} \frac{\partial \psi}{\partial R} \right) + \frac{\partial^2 \psi}{\partial z^2} = -4\pi R^2 \frac{dp}{d\psi} - \left(\frac{4\pi}{c} \right)^2 f \frac{df}{d\psi} = -R \left(4\pi R \frac{dp}{d\psi} + \frac{1}{2R} \frac{dF^2}{d\psi} \right), \quad (\text{A.12})$$

where

$$F = RB_\phi = \frac{4\pi f}{c}.$$

A.1.2 CRONOS : MKS units

In CRONOS, the Grad-Shafranov equation has a slightly different expression compared with the standard formulation that uses MKS units. Since this is confusing, we introduce its derivation here. The ideal MHD equations in the standard formulation in MKS units (section 4.1) can be rewritten using secondary variables, $p_1 = \mu_0 p$ and $\mathbf{j}_1 = \mu_0 \mathbf{j}$.

$$\mathbf{j}_1 \times \mathbf{B} = \nabla p_1 \quad (\text{A.13})$$

$$\nabla \cdot \mathbf{B} = 0 \quad (\text{A.14})$$

$$\nabla \times \mathbf{B} = \mathbf{j}_1 \quad (\text{A.15})$$

where p , \mathbf{j} and \mathbf{B} are respectively the plasma pressure, current density and magnetic field.

Introducing a flux function ψ defined as the poloidal flux per radian in ϕ and relating $\nabla \cdot \mathbf{B} = 0$ and $\mathbf{B} \cdot \nabla \psi = 0$, the poloidal component of the magnetic fields can be expressed as follows.

$$B_R = -\frac{1}{R} \frac{\partial \psi}{\partial z}, \quad B_z = \frac{1}{R} \frac{\partial \psi}{\partial R}. \quad (\text{A.16})$$

From the symmetry of \mathbf{j}_1 and \mathbf{B} in the force balance equation, the poloidal component of the plasma current can be expressed using a current flux function F .

$$j_{1,R} = -\frac{1}{R} \frac{\partial F}{\partial z}, \quad j_{1,z} = \frac{1}{R} \frac{\partial F}{\partial R}. \quad (\text{A.17})$$

Comparing these relations with Ampère's law,

$$j_{1,R} = -\frac{\partial B_\phi}{\partial z}, \quad j_{1,z} = \frac{\partial(RB_\phi)}{\partial R}, \quad (\text{A.18})$$

the flux function F is defined as

$$F = RB_\phi. \quad (\text{A.19})$$

Since the plasma pressure p_1 is a function of ψ , the poloidal current function F is also a function of ψ .

Decomposing the poloidal and toroidal components of the plasma current and magnetic fields in the force balance equation,

$$\mathbf{j}_{1,p} \times \mathbf{i}_\phi B_\phi + j_{1,\phi} \mathbf{i}_\phi \times \mathbf{B}_p = \nabla p_1, \quad (\text{A.20})$$

and substituting the poloidal components using the flux functions

$$\mathbf{B}_p = \frac{1}{R}(\nabla\psi \times \mathbf{i}_\phi) \quad \text{and} \quad \mathbf{j}_{1,p} = \frac{1}{R}(\nabla F \times \mathbf{i}_\phi), \quad (\text{A.21})$$

the force balance equation can be rewritten as

$$j_{1,\phi} = R \frac{dp_1}{d\psi} + \frac{1}{R} F \frac{dF}{d\psi}. \quad (\text{A.22})$$

The toroidal current density, $j_{1,\phi}$, can also be written in terms of ψ from Ampère's law as follows

$$-Rj_{1,\phi} = R \frac{\partial}{\partial R} \frac{1}{R} \frac{\partial \psi}{\partial R} + \frac{\partial^2 \psi}{\partial z^2}. \quad (\text{A.23})$$

Substituting the $j_{1,\phi}$ into this equation, the non-linear Grad-Shafranov equation is written as

$$R \frac{\partial}{\partial R} \left(\frac{1}{R} \frac{\partial \psi}{\partial R} \right) + \frac{\partial^2 \psi}{\partial z^2} = -R^2 \frac{dp_1}{d\psi} - F \frac{dF}{d\psi} = -\mu_0 R^2 \frac{dp}{d\psi} - \mu_0^2 f \frac{df}{d\psi}, \quad (\text{A.24})$$

where

$$F = RB_\phi = \mu_0 f, \quad p_1 = \mu_0 p.$$

A.2 Flux surface average properties

The first flux surface average property is derived as

$$\begin{aligned} \langle \nabla \cdot \mathbf{H} \rangle &= \frac{\partial}{\partial V} \int_V \nabla \cdot \mathbf{H} dV \\ &= \frac{\partial}{\partial V} \int_S \mathbf{H} \cdot \mathbf{n} dS \\ &= \frac{\partial}{\partial V} \int_S \mathbf{H} \cdot \frac{\nabla V}{|\nabla V|} dS \\ &= \frac{\partial}{\partial V} \int_S \mathbf{H} \cdot \frac{\nabla V}{|\nabla \rho|} \frac{\partial \rho}{\partial V} dS \\ &= \frac{\partial}{\partial V} \frac{1}{V'} \int_S \frac{\mathbf{H} \cdot \nabla V}{|\nabla \rho|} dS \\ &= \frac{\partial}{\partial V} \langle \mathbf{H} \cdot \nabla V \rangle. \end{aligned} \quad (\text{A.25})$$

The second flux surface average property is derived from the definition of time derivative of a quantity A ,

$$\frac{dA}{dt} = \frac{\partial A}{\partial t} + \mathbf{u}_\rho \cdot \nabla A. \quad (\text{A.26})$$

Averaging this equation on the flux surface and multiplying by V' , we have

$$\begin{aligned}
 \frac{d}{dt} (V' \langle A \rangle) &= V' \left\langle \frac{\partial A}{\partial t} \right\rangle + \langle \mathbf{u}_\rho \cdot \nabla A \rangle V' \\
 &= V' \left\langle \frac{\partial A}{\partial t} \right\rangle + \langle \nabla \cdot (A \mathbf{u}_\rho) - A (\nabla \cdot \mathbf{u}_\rho) \rangle V' \\
 &= V' \left\langle \frac{\partial A}{\partial t} \right\rangle + \langle \nabla \cdot (A \mathbf{u}_\rho) \rangle V' \\
 &= V' \left\langle \frac{\partial A}{\partial t} \right\rangle + \frac{\partial}{\partial V} \langle A \mathbf{u}_\rho \cdot \nabla V \rangle V' \\
 &= V' \left\langle \frac{\partial A}{\partial t} \right\rangle + \frac{\partial}{\partial \rho} \langle A \mathbf{u}_\rho \cdot \nabla V \rangle, \tag{A.27}
 \end{aligned}$$

where $\nabla \cdot \mathbf{u}_\rho = 0$ from the definition of \mathbf{u}_ρ (see section 4.2.1).

A.3 The magnetic field diffusion equation

A.3.1 Derivation of $\langle \mathbf{j} \cdot \mathbf{B} \rangle$ and $\langle \mathbf{E} \cdot \mathbf{B} \rangle$

$\langle \mathbf{j} \cdot \mathbf{B} \rangle$ in section 4.4.2 is derived as follows.

$$\begin{aligned}
 \langle \mathbf{j} \cdot \mathbf{B} \rangle &= \frac{\partial}{\partial V} \int_V \mathbf{j} \cdot \mathbf{B} dV \\
 &= \frac{\partial}{\partial V} \int_V \left[\left(\frac{1}{R} \nabla \psi \times \mathbf{i}_\phi + B_\phi \mathbf{i}_\phi \right) \cdot \left(\frac{1}{R} \nabla f \times \mathbf{i}_\phi + j_\phi \mathbf{i}_\phi \right) \right] dV \\
 &= \frac{\partial}{\partial V} \int_V \left[\left(\frac{1}{R} \nabla \psi \times \mathbf{i}_\phi + \frac{\mu_0 f}{R} \mathbf{i}_\phi \right) \cdot \left(\frac{1}{R} \nabla f \times \mathbf{i}_\phi - \frac{R}{\mu_0} \nabla \cdot \left(\frac{\nabla \psi}{R^2} \right) \mathbf{i}_\phi \right) \right] dV \\
 &= -\frac{\partial}{\partial V} \int_V \left[f \nabla \cdot \left(\frac{\nabla \psi}{R^2} \right) - \frac{1}{R^2} \nabla \psi \cdot \nabla f \right] dV = -\frac{\partial}{\partial V} \int_V \left[f^2 \nabla \cdot \left(\frac{1}{f} \frac{\nabla \psi}{R^2} \right) \right] dV \\
 &= -f^2 \frac{\partial}{\partial V} \left[\int_V \nabla \cdot \left(\frac{1}{f} \frac{\nabla \psi}{R^2} \right) dV \right] = -f^2 \frac{\partial}{\partial V} \left[\int_S \frac{1}{f} \frac{\nabla \psi}{R^2} \cdot \mathbf{n} dS \right] \\
 &= -f^2 \frac{\partial \rho}{\partial V} \frac{\partial}{\partial \rho} \left[\int_S \frac{1}{f} \frac{\nabla \rho}{R^2} \frac{\partial \psi}{\partial \rho} \cdot \frac{\nabla \rho}{|\nabla \rho|} dS \right] = -f^2 \frac{1}{V'} \frac{\partial}{\partial \rho} \left[\frac{1}{f} \int_S \frac{|\nabla \rho|^2}{R^2} \frac{ds}{|\nabla \rho|} \frac{\partial \psi}{\partial \rho} \right] \\
 &= -f^2 \frac{1}{V'} \frac{\partial}{\partial \rho} \left(\frac{c_2}{f} \frac{\partial \psi}{\partial \rho} \right), \tag{A.28}
 \end{aligned}$$

where

$$c_2 = \left\langle \frac{|\nabla \rho|^2}{R^2} \right\rangle = \int_S \frac{|\nabla \rho|^2}{R^2} \frac{dS}{|\nabla \rho|}. \tag{A.29}$$

$\langle \mathbf{E} \cdot \mathbf{B} \rangle$ in section 4.4.2 is derived as follows.

$$\begin{aligned}
\langle \mathbf{E} \cdot \mathbf{B} \rangle &= \frac{\partial}{\partial V} \int_V \mathbf{E} \cdot \mathbf{B} dV \\
&= \frac{1}{V'} \int_S \mathbf{E} \cdot \mathbf{B} \frac{dS}{|\nabla \rho|} \\
&= \frac{1}{V'} \int_S \mathbf{E} \cdot \mathbf{B}_p \frac{dS}{|\nabla \rho|} + \frac{1}{V'} \int_S \mathbf{E} \cdot \mathbf{B}_\phi \frac{dS}{|\nabla \rho|} \\
&= \frac{1}{V'} \int_S \mathbf{E} \cdot \left(\frac{1}{R} \nabla \psi \times \mathbf{i}_\phi \right) \frac{dS}{|\nabla \rho|} + \frac{1}{V'} \int_S \mathbf{E}_\phi \cdot \mathbf{B}_\phi \frac{dS}{|\nabla \rho|} \\
&= -\frac{1}{V'} \int_S \left(\mathbf{E} \times \frac{\mathbf{i}_\phi}{R} \right) \cdot \nabla \psi \frac{dS}{|\nabla \rho|} + \frac{1}{V'} \int_S \left(-\frac{1}{R} \frac{\partial \psi}{\partial t} \mathbf{i}_\phi \right) \cdot \mathbf{B}_\phi \frac{dS}{|\nabla \rho|} \\
&= -\frac{\partial \psi}{\partial V} \int_S \left(\mathbf{E} \times \frac{\mathbf{i}_\phi}{R} \right) \cdot \frac{\nabla \rho}{|\nabla \rho|} dS + \frac{\partial \psi}{\partial V} \int_S \frac{B_\phi}{R} \mathbf{u}_\psi \cdot \frac{\nabla \rho}{|\nabla \rho|} dS \\
&= -\frac{\partial \psi}{\partial V} \int_S \left(\mathbf{E} \times \frac{\mathbf{i}_\phi}{R} \right) \cdot \mathbf{ndS} + \frac{\partial \psi}{\partial V} \int_S \frac{B_\phi}{R} \mathbf{u}_\rho \cdot \mathbf{ndS} + \frac{\partial \psi}{\partial V} \int_S \frac{B_\phi}{R} (\mathbf{u}_\psi - \mathbf{u}_\rho) \cdot \mathbf{ndS}.
\end{aligned} \tag{A.30}$$

The first term in the right-hand side is further expressed as

$$\begin{aligned}
-\frac{\partial \psi}{\partial V} \int_S \left(\mathbf{E} \times \frac{\mathbf{i}_\phi}{R} \right) \cdot \mathbf{ndS} &= -\frac{\partial \psi}{\partial V} \int_V \nabla \cdot \left(\mathbf{E} \times \frac{\mathbf{i}_\phi}{R} \right) dV \\
&= -\frac{\partial \psi}{\partial V} \int_V (\nabla \times \mathbf{E}) \cdot \frac{\mathbf{i}_\phi}{R} dV \\
&= \frac{\partial \psi}{\partial V} \int_V \frac{d\mathbf{B}}{dt} \cdot \frac{\mathbf{i}_\phi}{R} dV \\
&= \frac{\partial \psi}{\partial V} \int_V \frac{1}{R} \frac{dB_\phi}{dt} dV \\
&= 2\pi \frac{\partial \psi}{\partial V} \frac{d}{dt} \left(\int_V \frac{B_\phi}{2\pi R} dV \right) \\
&= 2\pi \frac{\partial \psi}{\partial V} \frac{d\Phi}{dt}.
\end{aligned} \tag{A.31}$$

The second term in the right-hand side is further expressed as

$$\begin{aligned}
 \frac{\partial \psi}{\partial V} \int_S \frac{B_\phi}{R} \mathbf{u}_\rho \cdot \mathbf{n} dS &= \frac{\partial \psi}{\partial V} \int_V \nabla \cdot \left(\frac{B_\phi}{R} \mathbf{u}_\rho \right) dV \\
 &= \frac{\partial \psi}{\partial V} \int_V \left[\mathbf{u}_\rho \cdot \left(\nabla \frac{B_\phi}{R} \right) + \frac{B_\phi}{R} \nabla \cdot \mathbf{u}_\rho \right] dV \\
 &= \frac{\partial \psi}{\partial V} \int_V \mathbf{u}_\rho \cdot \left(\nabla \frac{B_\phi}{R} \right) dV \\
 &= 2\pi \frac{\partial \psi}{\partial V} \mathbf{u}_\rho \cdot \nabla \left(\int_V \frac{B_\phi}{2\pi R} dV \right) \\
 &= 2\pi \frac{\partial \psi}{\partial V} \mathbf{u}_\rho \cdot \nabla \Phi.
 \end{aligned} \tag{A.32}$$

The last term in the right-hand side is further expressed as

$$\begin{aligned}
 \frac{\partial \psi}{\partial V} \int_S \frac{B_\phi}{R} (\mathbf{u}_\psi - \mathbf{u}_\rho) \cdot \mathbf{n} dS &= \frac{\partial \psi}{\partial V} \int_V \nabla \cdot \left(\frac{B_\phi}{R} (\mathbf{u}_\psi - \mathbf{u}_\rho) \right) dV \\
 &= \frac{\partial \psi}{\partial V} \int_V (\mathbf{u}_\psi - \mathbf{u}_\rho) \cdot \left(\nabla \frac{B_\phi}{R} \right) dV \\
 &= 2\pi \frac{\partial \psi}{\partial V} (\mathbf{u}_\psi - \mathbf{u}_\rho) \cdot \nabla \left(\int_V \frac{B_\phi}{2\pi R} dV \right) \\
 &= 2\pi \frac{\partial \psi}{\partial V} (\mathbf{u}_\psi - \mathbf{u}_\rho) \cdot \nabla \Phi.
 \end{aligned} \tag{A.33}$$

Summing these three terms, $\langle \mathbf{E} \cdot \mathbf{B} \rangle$ is written as

$$\begin{aligned}
 \langle \mathbf{E} \cdot \mathbf{B} \rangle &= 2\pi \frac{\partial \psi}{\partial V} \frac{d\Phi}{dt} + 2\pi \frac{\partial \psi}{\partial V} \mathbf{u}_\rho \cdot \nabla \Phi \\
 &= 2\pi \frac{\partial \psi}{\partial V} \frac{d\Phi}{dt} + 2\pi \frac{\partial \psi}{\partial V} \mathbf{u}_\rho \cdot \nabla \Psi \frac{\partial \Phi}{\partial \Psi} \\
 &= \frac{\partial \Psi}{\partial V} \frac{d\Phi}{dt} - \frac{\partial \Psi}{\partial V} \frac{d\Psi}{dt} \frac{\partial \Phi}{\partial \Psi} \\
 &= \frac{\partial \Psi}{\partial V} \frac{d\Phi}{dt} - \frac{\partial \Phi}{\partial V} \frac{d\Psi}{dt}.
 \end{aligned} \tag{A.34}$$

This equation can be rewritten as

$$\begin{aligned}
\frac{d\Phi}{dt} &= \frac{1}{2\pi} \frac{\partial V}{\partial \psi} \langle \mathbf{E} \cdot \mathbf{B} \rangle + 2\pi \frac{\partial \Phi}{\partial \Psi} \frac{d\psi}{dt} \\
&= \frac{1}{2\pi} \frac{\partial V}{\partial \psi} \langle \mathbf{E} \cdot \mathbf{B} \rangle + \frac{\partial}{\partial \psi} \left(\int_V \frac{B_\phi}{2\pi R} dV \right) \frac{d\psi}{dt} \\
&= \frac{1}{2\pi} \frac{\partial V}{\partial \psi} \langle \mathbf{E} \cdot \mathbf{B} \rangle + \frac{\partial V}{\partial \psi} \frac{\partial}{\partial V} \left(\int_V \frac{\mu_0 f}{2\pi R^2} dV \right) \frac{d\psi}{dt} \\
&= \frac{1}{2\pi} \frac{\partial V}{\partial \psi} \langle \mathbf{E} \cdot \mathbf{B} \rangle + \frac{\mu_0}{2\pi} \frac{\partial V}{\partial \psi} \left\langle \frac{f}{R^2} \right\rangle \frac{d\psi}{dt} \\
&= \frac{1}{2\pi} \frac{\partial V}{\partial \psi} \left[\langle \mathbf{E} \cdot \mathbf{B} \rangle + \mu_0 f \left\langle \frac{1}{R^2} \right\rangle \frac{d\psi}{dt} \right].
\end{aligned} \tag{A.35}$$

By assuming $d\Phi/dt = 0$, we have

$$\langle \mathbf{E} \cdot \mathbf{B} \rangle = -\mu_0 f \left\langle \frac{1}{R^2} \right\rangle \frac{d\psi}{dt}. \tag{A.36}$$

A.3.2 DINA-CH : CGS units

$\langle \mathbf{j} \cdot \mathbf{B} \rangle$ in CGS units is identical to its standard formulation in MKS units. $\langle \mathbf{E} \cdot \mathbf{B} \rangle$ in CGS units is slightly different. Starting from the same equation derived in the standard formulation in MKS units given by

$$\begin{aligned}
\frac{d\Phi}{dt} &= \frac{1}{2\pi} \frac{\partial V}{\partial \psi} \langle \mathbf{E} \cdot \mathbf{B} \rangle + 2\pi \frac{\partial \Phi}{\partial \Psi} \frac{d\psi}{dt} \\
&= \frac{1}{2\pi} \frac{\partial V}{\partial \psi} \langle \mathbf{E} \cdot \mathbf{B} \rangle + \frac{\partial}{\partial \psi} \left(\int_V \frac{B_\phi}{2\pi R} dV \right) \frac{d\psi}{dt} \\
&= \frac{1}{2\pi} \frac{\partial V}{\partial \psi} \langle \mathbf{E} \cdot \mathbf{B} \rangle + \frac{\partial V}{\partial \psi} \frac{\partial}{\partial V} \left(\int_V \frac{4\pi f}{2\pi R^2} dV \right) \frac{d\psi}{dt} \\
&= \frac{1}{2\pi} \frac{\partial V}{\partial \psi} \langle \mathbf{E} \cdot \mathbf{B} \rangle + \frac{2}{c} \frac{\partial V}{\partial \psi} \left\langle \frac{f}{R^2} \right\rangle \frac{d\psi}{dt} \\
&= \frac{1}{2\pi} \frac{\partial V}{\partial \psi} \left[\langle \mathbf{E} \cdot \mathbf{B} \rangle + \frac{4\pi f}{c} \left\langle \frac{1}{R^2} \right\rangle \frac{d\psi}{dt} \right].
\end{aligned} \tag{A.37}$$

By assuming $d\Phi/dt = 0$, we have

$$\langle \mathbf{E} \cdot \mathbf{B} \rangle = -\frac{4\pi f}{c} \left\langle \frac{1}{R^2} \right\rangle \frac{d\psi}{dt}, \tag{A.38}$$

where $f = cRB_\phi/4\pi$.

Inserting $\langle \mathbf{E} \cdot \mathbf{B} \rangle$ and $\langle \mathbf{j} \cdot \mathbf{B} \rangle$ into the generalized Ohm's law averaged on the magnetic flux surface (in the formulation with CGS units, μ_0 is replaced to $4\pi/c$), we have

$$\begin{aligned}
 \frac{d\psi}{dt} &= -\frac{c \langle \mathbf{j} \cdot \mathbf{B} \rangle}{4\pi\sigma f \left\langle \frac{1}{R^2} \right\rangle} + \frac{c \langle \mathbf{j}_{\text{ni}} \cdot \mathbf{B} \rangle}{4\pi\sigma f \left\langle \frac{1}{R^2} \right\rangle} \\
 &= -\frac{V'}{4\pi\sigma\rho} \langle \mathbf{j} \cdot \mathbf{B} \rangle + \frac{V'}{4\pi\sigma\rho} \langle \mathbf{j}_{\text{ni}} \cdot \mathbf{B} \rangle \\
 &= \frac{V'}{4\pi\sigma\rho} f^2 \frac{1}{V'} \frac{\partial}{\partial\rho} \left(\frac{c_2}{f} \frac{\partial\psi}{\partial\rho} \right) + \frac{V'}{4\pi\sigma\rho} \langle \mathbf{j}_{\text{ni}} \cdot \mathbf{B} \rangle \\
 &= \frac{V'}{4\pi\sigma\rho} \left(\frac{c\rho}{c_3} \right)^2 \frac{1}{V'} \frac{\partial}{\partial\rho} \left(\frac{c_2 c_3}{c\rho} \frac{\partial\psi}{\partial\rho} \right) + \frac{V'}{4\pi\sigma\rho} \langle \mathbf{j}_{\text{ni}} \cdot \mathbf{B} \rangle \\
 &= \frac{c\rho}{4\pi c_3^2 \sigma} \frac{\partial}{\partial\rho} \left(\frac{c_2 c_3}{c\rho} \frac{\partial\psi}{\partial\rho} \right) + \frac{V'}{4\pi\sigma\rho} \langle \mathbf{j}_{\text{ni}} \cdot \mathbf{B} \rangle \\
 &= \frac{c C_3^2 \rho}{4\pi\sigma} \frac{\partial}{\partial\rho} \left(\frac{c_2}{C_3 \rho} \frac{\partial\psi}{\partial\rho} \right) + \frac{V'}{4\pi\sigma\rho} \langle \mathbf{j}_{\text{ni}} \cdot \mathbf{B} \rangle \\
 &= \frac{c c_2 C_3}{4\pi\sigma} \frac{\partial^2 \psi}{\partial\rho^2} + \frac{c C_3^2 \rho}{4\pi\sigma} \frac{\partial}{\partial\rho} \left(\frac{c_2}{C_3 \rho} \right) \frac{\partial\psi}{\partial\rho} + \frac{V'}{4\pi\sigma\rho} \langle \mathbf{j}_{\text{ni}} \cdot \mathbf{B} \rangle, \tag{A.39}
 \end{aligned}$$

where $C_3 = c_3^{-1}$ and $f = c\rho/V' \left\langle \frac{1}{R} \right\rangle = c\rho/c_3$. Here, f is derived from the definition of ρ as follows.

$$\begin{aligned}
 \frac{\partial\rho^2}{\partial V} &= 2\rho \frac{\partial\rho}{\partial V} = \frac{\partial\Phi}{\partial V} = \frac{\partial}{\partial V} \int_V \frac{B_\phi}{2\pi R} dV \\
 &= \frac{\partial}{\partial V} \int_V \frac{4\pi f}{2\pi R^2} dV \\
 &= \frac{2f}{c} \frac{\partial}{\partial V} \int_V \frac{1}{R^2} dV \\
 &= \frac{2f}{c} \left\langle \frac{1}{R^2} \right\rangle. \tag{A.40}
 \end{aligned}$$

A.3.3 CRONOS : MKS units

The magnetic field diffusion equation in CRONOS can be simply obtained by replacing f with F/μ_0 in the standard formulations in MKS units.

$$\frac{d\psi}{dt} = \frac{c_2}{\sigma\mu_0 c_3} \frac{\partial^2 \psi}{\partial\rho^2} + \frac{F}{\sigma\mu_0 c_3} \frac{\partial}{\partial\rho} \left(\frac{c_2}{F} \right) \frac{\partial\psi}{\partial\rho} + \frac{V'}{\sigma F c_3} \langle \mathbf{j}_{\text{ni}} \cdot \mathbf{B} \rangle. \tag{A.41}$$

A.4 Plasma current

A.4.1 Standard : MKS units

Using the following relation

$$\begin{aligned}
\left\langle \frac{j_\phi}{R} \right\rangle &= \left\langle -\frac{1}{\mu_0} \nabla \cdot \left(\frac{\nabla \psi}{R^2} \right) \right\rangle = -\frac{1}{\mu_0} \left\langle \nabla \cdot \left(\frac{\nabla \psi}{R^2} \right) \right\rangle \\
&= -\frac{1}{\mu_0} \frac{\partial}{\partial V} \left\langle \frac{\nabla \psi}{R^2} \cdot \nabla V \right\rangle = -\frac{1}{\mu_0} \frac{\partial}{\partial V} \left\langle \frac{\nabla \rho}{R^2} \cdot \nabla \rho \frac{\partial V}{\partial \rho} \frac{\partial \psi}{\partial \rho} \right\rangle \\
&= -\frac{1}{\mu_0} \frac{\partial}{\partial V} \left\langle V' \frac{|\nabla \rho|^2}{R^2} \frac{\partial \psi}{\partial \rho} \right\rangle = -\frac{1}{\mu_0} \frac{\partial}{\partial V} \left\langle c_2 V' \frac{\partial \psi}{\partial \rho} \right\rangle \\
&= -\frac{1}{\mu_0 V'} \frac{\partial}{\partial \rho} \left(c_2 V' \frac{\partial \psi}{\partial \rho} \right), \tag{A.42}
\end{aligned}$$

the plasma current is given by

$$\begin{aligned}
I_p &= \iiint_S \mathbf{j} \cdot \mathbf{i}_\phi dR dz = \iint_S \frac{j_\phi}{R} R dR dz = \iint_S \frac{j_\phi}{R} \sqrt{g} d\theta d\rho \\
&= \int_0^{\rho_m} \left(\int_0^{2\pi} \frac{j_\phi}{R} \sqrt{g} d\theta \right) d\rho = \int_0^{\rho_m} \left(\left\langle \frac{j_\phi}{R} \right\rangle \int_0^{2\pi} \sqrt{g} d\theta \right) d\rho \\
&= \int_0^{\rho_m} \left(\left\langle \frac{j_\phi}{R} \right\rangle \frac{V'}{2\pi} \right) d\rho = -\frac{1}{2\pi \mu_0} \int_0^{\rho_m} \frac{\partial}{\partial \rho} \left(c_2 V' \frac{\partial \psi}{\partial \rho} \right) d\rho \\
&= -\frac{1}{2\pi \mu_0} c_2 V' \frac{\partial \psi}{\partial \rho} \Big|_{\rho=\rho_m}. \tag{A.43}
\end{aligned}$$

A.4.2 DINA-CH : CGS units

Using the following relation

$$\left\langle \frac{j_\phi}{R} \right\rangle = \left\langle -\frac{c}{4\pi} \nabla \cdot \left(\frac{\nabla \psi}{R^2} \right) \right\rangle = -\frac{c}{4\pi V'} \frac{\partial}{\partial \rho} \left(c_2 V' \frac{\partial \psi}{\partial \rho} \right), \tag{A.44}$$

the plasma current in DINA-CH is given by

$$I_p = -\frac{c}{8\pi^2} c_2 V' \frac{\partial \psi}{\partial \rho} \Big|_{\rho=\rho_m}. \tag{A.45}$$

A.5 Electron heat transport equation

The left hand side of the energy balance equation of the electrons (section 4.2.4) can be rewritten as

$$\begin{aligned}
& \frac{3}{2} \left\langle \frac{\partial p_e}{\partial t} \right\rangle V' + \left\langle \nabla \cdot \left(\mathbf{q}_e + \frac{5}{2} p_e \mathbf{u}_e \right) \right\rangle V' - \langle \mathbf{u}_e \cdot (\nabla p - \nabla p_i) \rangle V' \\
&= \frac{3}{2} \frac{d}{dt} \langle p_e \rangle V' - \frac{3}{2} \frac{\partial}{\partial \rho} \langle p_e \mathbf{u}_\rho \cdot \nabla V \rangle + \frac{\partial}{\partial V} \langle \mathbf{q}_e \cdot \nabla V \rangle V' + \frac{\partial}{\partial V} \left\langle \frac{5}{2} p_e \mathbf{u}_e \cdot \nabla V \right\rangle V' \\
&\quad - \langle \mathbf{u}_e \cdot \nabla p_e \rangle V' \\
&= \frac{3}{2} \frac{d}{dt} \langle p_e \rangle V' - \frac{3}{2} \frac{\partial}{\partial \rho} \langle p_e \mathbf{u}_\rho \cdot \nabla V \rangle + \frac{\partial}{\partial \rho} \left\langle \frac{5}{2} p_e \mathbf{u}_e \cdot \nabla V \right\rangle + \frac{\partial}{\partial \rho} \langle \mathbf{q}_e \cdot \nabla V \rangle - \langle \mathbf{u}_e \cdot \nabla p_e \rangle V' \\
&= \frac{3}{2} \frac{d}{dt} (p_e V') + \frac{\partial}{\partial \rho} \left\langle \frac{5}{2} p_e \mathbf{u}_e \cdot \nabla V - \frac{3}{2} p_e \mathbf{u}_\rho \cdot \nabla V \right\rangle + \frac{\partial}{\partial \rho} \langle \mathbf{q}_e \cdot \nabla V \rangle - \langle \mathbf{u}_e \cdot \nabla p_e \rangle V' \\
&= \frac{3}{2} \frac{dp_e}{dt} V' + \frac{3}{2} p_e \frac{dV'}{dt} + \frac{\partial}{\partial \rho} \left[\langle p_e \mathbf{u}_\rho \cdot \nabla V \rangle + \frac{5}{2} T_e \langle n_e (\mathbf{u}_e - \mathbf{u}_\rho) \cdot \nabla \rho \rangle V' \right] \\
&\quad + \frac{\partial}{\partial \rho} \langle \mathbf{q}_e \cdot \nabla \rho \rangle V' - \langle \mathbf{u}_e \cdot \nabla p_e \rangle V' \\
&= \frac{3}{2V'^{2/3}} \frac{d}{dt} (p_e V'^{5/3}) - \frac{5}{2} p_e \frac{dV'}{dt} + \frac{3}{2} p_e \frac{dV'}{dt} + \frac{\partial}{\partial \rho} \langle p_e \mathbf{u}_\rho \cdot \nabla \rho \rangle V' + \frac{\partial}{\partial \rho} \left(\frac{5}{2} T_e \Gamma_e V' \right) \\
&\quad + \frac{\partial}{\partial \rho} q_e V' - \langle \mathbf{u}_e \cdot \nabla p_e \rangle V' \\
&= \frac{3}{2V'^{2/3}} \frac{d}{dt} (p_e V'^{5/3}) - p_e \frac{\partial}{\partial \rho} \langle \mathbf{u}_\rho \cdot \nabla V \rangle + p_e \frac{\partial}{\partial \rho} \langle \mathbf{u}_\rho \cdot \nabla V \rangle + \langle \mathbf{u}_\rho \cdot \nabla p_e \rangle V' \\
&\quad + \frac{\partial}{\partial \rho} \left[\left(q_e + \frac{5}{2} T_e \Gamma_e \right) V' \right] - \langle \mathbf{u}_e \cdot \nabla p_e \rangle V' \\
&= \frac{3}{2V'^{2/3}} \frac{d}{dt} (p_e V'^{5/3}) + \frac{\partial}{\partial \rho} \left[\left(q_e + \frac{5}{2} T_e \Gamma_e \right) V' \right] + \langle (\mathbf{u}_\rho - \mathbf{u}_e) \cdot \nabla p_e \rangle V' \\
&= \frac{3}{2V'^{2/3}} \frac{d}{dt} (p_e V'^{5/3}) + \frac{\partial}{\partial \rho} \left[\left(q_e + \frac{5}{2} T_e \Gamma_e \right) V' \right] + \langle n_e (\mathbf{u}_\rho - \mathbf{u}_e) \cdot \nabla \rho \rangle \frac{1}{n_e} \frac{\partial p_e}{\partial \rho} V' \\
&= \frac{3}{2V'^{2/3}} \frac{d}{dt} (p_e V'^{5/3}) + \frac{\partial}{\partial \rho} \left[\left(q_e + \frac{5}{2} T_e \Gamma_e \right) V' \right] + \frac{\Gamma_e}{n_e} \frac{\partial p_e}{\partial \rho} V'. \tag{A.46}
\end{aligned}$$

A.6 Ion heat transport equation

The left hand side of the energy balance equation of the ions (section 4.2.5) can be rewritten as

$$\begin{aligned}
& \frac{3}{2} \left\langle \frac{\partial p_i}{\partial t} \right\rangle V' + \left\langle \nabla \cdot \left(\mathbf{q}_i + \frac{5}{2} p_i \mathbf{u}_i \right) \right\rangle V' - \langle \mathbf{u}_i \cdot \nabla p_i \rangle V' \\
&= \frac{3}{2} \frac{d}{dt} (\langle p_i \rangle V') - \frac{3}{2} \frac{\partial}{\partial \rho} \langle p_i \mathbf{u}_\rho \cdot \nabla V \rangle + \frac{\partial}{\partial V} \langle \mathbf{q}_i \cdot \nabla V \rangle V' + \frac{\partial}{\partial V} \left\langle \frac{5}{2} p_i \mathbf{u}_i \cdot \nabla V \right\rangle V' \\
&\quad - \langle \mathbf{u}_i \cdot \nabla p_i \rangle V' \\
&= \frac{3}{2} \frac{d}{dt} (\langle p_i \rangle V') - \frac{3}{2} \frac{\partial}{\partial \rho} \langle p_i \mathbf{u}_\rho \cdot \nabla V \rangle + \frac{\partial}{\partial \rho} \left\langle \frac{5}{2} p_i \mathbf{u}_i \cdot \nabla V \right\rangle + \frac{\partial}{\partial \rho} \langle \mathbf{q}_i \cdot \nabla V \rangle - \langle \mathbf{u}_i \cdot \nabla p_i \rangle V' \\
&= \frac{3}{2} \frac{d}{dt} (p_i V') + \frac{\partial}{\partial \rho} \left\langle \frac{5}{2} p_i \mathbf{u}_i \cdot \nabla V - \frac{3}{2} p_i \mathbf{u}_\rho \cdot \nabla V \right\rangle + \frac{\partial}{\partial \rho} \langle \mathbf{q}_i \cdot \nabla V \rangle - \langle \mathbf{u}_i \cdot \nabla p_i \rangle V' \\
&= \frac{3}{2} \frac{dp_i}{dt} V' + \frac{3}{2} p_i \frac{dV'}{dt} + \frac{\partial}{\partial \rho} \left[\langle p_i \mathbf{u}_\rho \cdot \nabla V \rangle + \frac{5}{2} T_i \langle n_i (\mathbf{u}_i - \mathbf{u}_\rho) \cdot \nabla \rho \rangle V' \right] \\
&\quad + \frac{\partial}{\partial \rho} \langle \mathbf{q}_i \cdot \nabla \rho \rangle V' - \langle \mathbf{u}_i \cdot \nabla p_i \rangle V' \\
&= \frac{3}{2V'^{2/3}} \frac{d}{dt} (p_i V'^{5/3}) - \frac{5}{2} p_i \frac{dV'}{dt} + \frac{3}{2} p_i \frac{dV'}{dt} + \frac{\partial}{\partial \rho} \langle p_i \mathbf{u}_\rho \cdot \nabla \rho \rangle V' + \frac{\partial}{\partial \rho} \left(\frac{5}{2} T_i \Gamma_i V' \right) \\
&\quad + \frac{\partial}{\partial \rho} q_i V' - \langle \mathbf{u}_i \cdot \nabla p_i \rangle V' \\
&= \frac{3}{2V'^{2/3}} \frac{d}{dt} (p_i V'^{5/3}) - p_i \frac{\partial}{\partial \rho} \langle \mathbf{u}_\rho \cdot \nabla V \rangle + p_i \frac{\partial}{\partial \rho} \langle \mathbf{u}_\rho \cdot \nabla V \rangle + \langle \mathbf{u}_\rho \cdot \nabla p_i \rangle V' \\
&\quad + \frac{\partial}{\partial \rho} \left[\left(q_i + \frac{5}{2} T_i \Gamma_i \right) V' \right] - \langle \mathbf{u}_i \cdot \nabla p_i \rangle V' \\
&= \frac{3}{2V'^{2/3}} \frac{d}{dt} (p_i V'^{5/3}) + \frac{\partial}{\partial \rho} \left[\left(q_i + \frac{5}{2} T_i \Gamma_i \right) V' \right] + \langle (\mathbf{u}_\rho - \mathbf{u}_i) \cdot \nabla p_i \rangle V' \\
&= \frac{3}{2V'^{2/3}} \frac{d}{dt} (p_i V'^{5/3}) + \frac{\partial}{\partial \rho} \left[\left(q_i + \frac{5}{2} T_i \Gamma_i \right) V' \right] + \langle n_e (\mathbf{u}_\rho - \mathbf{u}_e) \cdot \nabla \rho \rangle \frac{1}{n_e} \frac{\partial p_i}{\partial \rho} V' \\
&= \frac{3}{2V'^{2/3}} \frac{d}{dt} (p_i V'^{5/3}) + \frac{\partial}{\partial \rho} \left[\left(q_i + \frac{5}{2} T_i \Gamma_i \right) V' \right] + \frac{\Gamma_e}{n_e} \frac{\partial p_i}{\partial \rho} V'. \tag{A.47}
\end{aligned}$$

A.7 Plasma transport evolution scheme in CRONOS

The differential equation in section 4.3 can be rewritten as

$$\begin{aligned}
\frac{F_i^{n+1} - F_i^n}{\Delta t} &= A_i^{n+f} \frac{1}{(\Delta\rho)^2} \left(F_{i+1}^{n+f} - 2F_i^{n+f} + F_{i-1}^{n+f} \right) + B_i^{n+f} \frac{1}{2\Delta\rho} \left(F_{i+1}^{n+f} - F_{i-1}^{n+f} \right) \\
&\quad + C_i^{n+f} F_i^{n+f} + D_i^{n+f} \\
&= \left(\frac{1}{(\Delta\rho)^2} A_i^{n+f} + \frac{1}{2\Delta\rho} B_i^{n+f} \right) F_{i+1}^{n+f} + \left(-\frac{2}{(\Delta\rho)^2} A_i^{n+f} + C_i^{n+f} \right) F_i^{n+f} \\
&\quad + \left(\frac{1}{(\Delta\rho)^2} A_i^{n+f} - \frac{1}{2\Delta\rho} B_i^{n+f} \right) F_{i-1}^{n+f} + D_i^{n+f} \\
&= \left(\frac{1}{(\Delta\rho)^2} A_i^{n+f} + \frac{1}{2\Delta\rho} B_i^{n+f} \right) (fF_{i+1}^n + (1-f)F_{i+1}^{n+1}) \\
&\quad + \left(-\frac{2}{(\Delta\rho)^2} A_i^{n+f} + C_i^{n+f} \right) (fF_i^n + (1-f)F_i^{n+1}) \\
&\quad + \left(\frac{1}{(\Delta\rho)^2} A_i^{n+f} - \frac{1}{2\Delta\rho} B_i^{n+f} \right) (fF_{i-1}^n + (1-f)F_{i-1}^{n+1}) + D_i^{n+f}. \tag{A.48}
\end{aligned}$$

Rearranging the terms, we have

$$\begin{aligned}
(1-f) \left(\frac{A_i^{n+f}}{(\Delta\rho)^2} + \frac{B_i^{n+f}}{2\Delta\rho} \right) F_{i+1}^{n+1} + \left\{ (1-f) \left(-\frac{A_i^{n+f}}{(\Delta\rho)^2} + C_i^{n+f} \right) - \frac{1}{\Delta t} \right\} F_i^{n+1} \\
+ (1-f) \left(\frac{A_i^{n+f}}{(\Delta\rho)^2} - \frac{B_i^{n+f}}{2\Delta\rho} \right) F_{i-1}^{n+1} \\
= -f \left(\frac{A_i^{n+f}}{(\Delta\rho)^2} + \frac{B_i^{n+f}}{2\Delta\rho} \right) F_{i+1}^n + \left\{ -f \left(-\frac{A_i^{n+f}}{(\Delta\rho)^2} + C_i^{n+f} \right) - \frac{1}{\Delta t} \right\} F_i^n \\
- f \left(\frac{A_i^{n+f}}{(\Delta\rho)^2} - \frac{B_i^{n+f}}{2\Delta\rho} \right) F_{i-1}^n + D_i^{n+f}. \tag{A.49}
\end{aligned}$$

Rewriting this equation in a simple form, we have

$$a_i F_{i+1}^{n+1} + b_i F_i^{n+1} + c_i F_{i-1}^{n+1} = d_i. \tag{A.50}$$

The coefficients are given by

$$\begin{aligned}
a_i &= (1-f) \left(\frac{fA_i^n + (1-f)A_i^{n+1}}{(\Delta\rho)^2} + \frac{fB_i^n + (1-f)B_i^{n+1}}{2\Delta\rho} \right), \\
b_i &= (1-f) \left(-2\frac{fA_i^n + (1-f)A_i^{n+1}}{(\Delta\rho)^2} + fC_i^n + (1-f)C_i^{n+1} \right) - \frac{1}{\Delta t}, \\
c_i &= (1-f) \left(\frac{fA_i^n + (1-f)A_i^{n+1}}{(\Delta\rho)^2} - \frac{fB_i^n + (1-f)B_i^{n+1}}{2\Delta\rho} \right), \\
d_i &= -f \left(\frac{fA_i^n + (1-f)A_i^{n+1}}{(\Delta\rho)^2} + \frac{fB_i^n + (1-f)B_i^{n+1}}{2\Delta\rho} \right) F_{i+1}^n \\
&\quad + \left\{ -f \left(-2\frac{fA_i^n + (1-f)A_i^{n+1}}{(\Delta\rho)^2} + fC_i^n + (1-f)C_i^{n+1} \right) - \frac{1}{\Delta t} \right\} F_i^n \\
&\quad - f \left(\frac{fA_i^n + (1-f)A_i^{n+1}}{(\Delta\rho)^2} - \frac{fB_i^n + (1-f)B_i^{n+1}}{2\Delta\rho} \right) F_{i-1}^n \\
&\quad + fD_i^n + (1-f)D_i^{n+1},
\end{aligned}$$

where A_i^{n+f} , B_i^{n+f} , C_i^{n+f} , D_i^{n+f} and F_i^{n+f} are written by the relation

$$X_i^{n+f} = fX_i^n + (1-f)X_i^{n+1}. \quad (\text{A.51})$$

Bibliography

- [1] Wesson J A Tokamaks 1997 (Oxford: Clarendon Press) 2nd edition
- [2] Spitzer L The stellarator concept 1958 *Phys. Fluids* **1** 253
- [3] Green B J et al ITER: burning plasma physics experiment 2003 *Plasma Phys. Control. Fusion* **45** 687
- [4] Fisch N J Theory of current drive in plasmas 1987 *Rev. Mod. Phys.* **59** 175
- [5] Peeters A G The bootstrap current and its consequences 2000 *Plasma Phys. Control. Fusion* **42** B231
- [6] ITER Technical Basis 2002 ITER EDA *Documentation Series No 24* (Vienna : IAEA)
- [7] Lister J B, Martin Y, Moret J-M On locating the poloidal field coils for Tokamak vertical position control 1996 *Nucl. Fusion* **36** 1547
- [8] Lazarus E A, Lister J B, Neilson G H Control of the Vertical Instability in Tokamaks 1990 *Nucl. Fusion* **30** 111
- [9] Coutlis A et al Measurement of the open loop plasma equilibrium response in TCV 1999 *Nucl. Fusion* **39** 663
- [10] Jensen T H and Skinner D G Support of the model for "Vertical displacement episodes" from numerical simulation of episodes observed in the DIII-D tokamak. 1990 *Phys. Fluids B* **2** 2358
- [11] Zohm H Edge localized modes 1996 *Plasma Phys. Control. Fusion* **38** 105
- [12] Hubbard A E Physics and scaling of the H-mode pedestal 2000 *Plasma Phys. Control. Fusion* **42** A15

- [13] Conner J W and Wilson H R A review of theories of the L-H transition 2000 *Plasmas Phys. Control. Fusion* **42** R1
- [14] von Goeler S, Stodiek W and Sauthoff N 1974 *Phys. Rev. Lett.* **33** 1201
- [15] Zweben S J et al Alpha-particle physics in the tokamak fusion test reactor DT experiment 1997 *Plasmas Phys. Control. Fusion* **39** A275
- [16] Noterdaeme J-M et al Heating, current drive and energetic particle studies on JET in preparation of ITER operation 2003 *Nucl. Fusion* **43** 202
- [17] Stork D et al Overview of transport, fast particle and heating and current drive physics using tritium in JET plasmas 2005 *Nucl. Fusion* **45** 5181
- [18] Conner J W et al A review of internal transport barrier physics for steady-state operation of tokamaks 2004 *Nucl. Fusion* **44** R1
- [19] Wolf R C Internal transport barriers in tokamak plasmas 2003 *Plasmas Phys. Control. Fusion* **45** R1
- [20] Kim S H, Park J M and Hong S H Predictive Numerical Simulations on the Formation of Internal Transport Barrier in the Reversed Shear Regime of KSTAR Tokamak 2005 *Journal of Korean Physical Society* **46** 861
- [21] Sauter O et al Beta limits in long-pulse tokamak discharges 1997 *Phys. Plasmas* **4** 1654
- [22] Fitzpatrick R and Hender T C The interaction of resonant magnetic perturbations with rotating plasmas 1991 *Phys. Fluids B* **3** 644
- [23] Khayrutdinov R R and Lukash V E Studies of Plasma Equilibrium and Transport in a Tokamak Fusion Device with the Inverse Variable Technique 1993 *Journal of Computational Physics* **109** 193
- [24] Favez J-Y, Khayrutdinov R R, Lister J B and Lukash V E, Comparing TCV experimental VDE response with DINA code simulations 2002 *Plasma Phys. Control. Fusion* **44** 171
- [25] Basiuk V et al Simulations of steady-state scenarios for Tore Supra using the CRONOS code 2003 *Nucl. Fusion* **43** 822

- [26] Degeling A W, Martin Y R, Lister J B, Villard L, Dokouka V N, Lukash V E and Khayrutdinov R R Magnetic triggering of ELMs in TCV 2003 *Plasma Phys. Control. Fusion* **45** 1637
- [27] Lang P T et al Frequency control of type-I ELMs by magnetic triggering in ASDEX Upgrade 2004 *Plasma Phys. Control. Fusion* **46** L31
- [28] Loarte A Summary of kick-off meeting for tasks TW6-TPO-DISLOAD and TW6-TPO-PLASMDYN 2007
- [29] Jardin S C, Pomphrey N and DeLucia J Dynamic modeling of Transport and Positional Control of Tokamaks 1983 *J. Comput. Phys.* **66** 481
- [30] Budny R V, Andre R, Bateman G, Halpern F, Kessel C E, Kritz A and McCune D Predictions of H-mode performance in ITER 2008 *Nucl. Fusion* **48** 075005
- [31] Crotinger J A, LoDestro L, Pearlstein L D, Tarditi A, Casper T A and Hooper E B CORSICA: A Comprehensive Simulation of Toroidal Magnetic-Fusion Devices 1997 *LLNL Report UCRL-ID-126284*
- [32] Jackson G L et al ITER startup studies in the DIII-D tokamak 2008 *Nucl. Fusion* **48** 125002
- [33] Casper T A, Meyer W H, Pearlstein L D, Portone A ITER shape controller and transport simulations 2008 *Fusion Eng. Des.* **83** 552
- [34] Khayrutdinov R R, Lister J B, Lukash V E and Wainwright J P Comparing DINA code simulations with TCV experimental plasma equilibrium responses 2001 *Plasma Phys. Control. Fusion* **43** 321
- [35] Lister J B, Khayrutdinov R R, Limebeer D J N, Lukash V E, Nakamura Y, Sharma A Villone F Wainwright J P and Yoshino R Linear and non-linear plasma equilibrium responses on the JT-60U and TCV tokamaks 2001 *Fusion Eng. Des.* **56-57** 755
- [36] Kim S H et al Comparing magnetic triggering of ELMs in TCV and ASDEX Upgrade 2009 *Plasma Phys. Control. Fusion* **51** 055021
- [37] Artaud J F et al Predictive integrated modelling for ITER scenarios 2005 *Proc. 32nd EPS Conf. on Plasma Physics (Tarragona, Spain)* vol 29C (ECA) P-1.035

- [38] Garcia J, Giruzzi G, Artaud J F, Baisuk V, Decker J, Imbeaux F, Peysson Y and Schneider M Integrated modeling of ITER steady-state scenarios 2008 *Plasma Phys. Control. Fusion* **50** 124032
- [39] Turco F, Giruzzi G, Artaud J F, Barana O, Basiuk V, Huysmans G, Imbeaux F, Maget P, Mazon D and Ségui J-L Investigation of MHD phenomena on Tore Supra by localised eccd perturbation experiments 2008 *Plasma Phys. Control. Fusion* **50** 035001
- [40] EFDA Task Force on Integrated Tokamak Modelling <http://www.efda-itm.eu>
- [41] Mazon D et al Active control of the current density profile in JET 2003 *Plasma. Phys. Control. Fusion* **45** L47
- [42] Mazon D et al Real-time control of internal transport barriers in JET 2002 *Plasma. Phys. Control. Fusion* **44** 1087
- [43] Barana O, Basiuk V, Ducobu L, Laborde L, Mazon D, Moreau P and Saint-Laurent F Integration of advanced feedback control technique on Tore Supra 2007 *Fusion Eng. Des.* **82** 1023
- [44] Joffrin E et al, Integrated plasma controls for steady state scenarios 2007 *Nucl. Fusion* **47** 1664
- [45] Ferron J R et al Feedback control of the safety factor profile evolution during formation of an advanced tokamak discharge 2006 *Nucl. Fusion* **46** L13
- [46] Gohil P et al Control of plasma profiles in DIII-D discharges 2006 *Plasma. Phys. Control. Fusion* **48** A45
- [47] Laborde L et al A model-based technique for integrated real-time profile control in the JET tokamak 2005 *Plasma. Phys. Control. Fusion* **47** 155
- [48] Joffrin E et al Integrated scenario in JET using real-time profile control 2003 *Plasma. Phys. Control. Fusion* **45** A367
- [49] Moreau D et al Real-time control of q -profile in JET for steady state advanced tokamak operation 2003 *Nucl. Fusion* **43** 870
- [50] Tala T et al Predictive transport simulations of real-time profile control in JET advanced tokamak plasmas 2005 *Nucl. Fusion* **45** 1027

- [51] Stober J, Marascheck M, Conway G D, Gruber O, Herrmann A, Sips A C C, Treutterer W, Zohm H and ASDEX Upgrade Team Type II ELMy H modes on ASDEX Upgrade with good confinement at high density 2001 *Nucl. Fusion* **41** 1123
- [52] Saibene G et al Improved performance of ELMy H-mode at high density by plasma shaping in JET 2002 *Plasma Phys. Control. Fusion* **44** 1769
- [53] Lang P T et al ELM pace making and mitigation by pellet injection in ASDEX Upgrade 2004 *Nucl. Fusion* **44** 665
- [54] Evans T E et al Suppression of large edge localized modes in high confinement DIII-D plasmas with a stochastic magnetic boundary 2005 *J. Nucl. Mater.* **337-339** 691
- [55] Degtyarev L, Martynov A, Medvedev S, Troyon F, Villard L and Gruber R The KINX ideal MHD stability code for axisymmetric plasmas with separatrix 1997 *Comput. Phys. Comm.* **103** 10
- [56] Medvedev S Yu, Ivanov A A, Martynov A A, Poshekhonov Yu Yu, Kim S H, Lister J B, Martin Y R, Sauter O, Villard L and Khayrutdinov R R Magnetic ELM Triggering and Edge Stability of Tokamak Plasma 2005 *Proc. 32nd EPS Conf. on Plasma Physics (Tarragona, Spain)* vol 29C (ECA) P-5. 064
- [57] Behn R, Alfier A, Medvedev S Yu, Zhuang Ge, Pasqualotto R, Nielsen P, Martin Y and the TCV team Edge profiles of electron temperature and density during ELMy H-mode in ohmically heated TCV plasmas 2007 *Plasma Phys. Control. Fusion* **49** 1289
- [58] Medvedev S Yu et al Edge Stability of TCV Plasma 2006 *Proc. 33rd EPS Conf. on Plasma Physics (Rome, Italy)* vol 30I (ECA) P-1. 146
- [59] Lang P T et al Impact of fast vertical and radial plasma movement on type-I ELMs in ASDEX Upgrade 2006 *Czech. J. Phys.* **56** 1329
- [60] Medvedev S Yu, Ivanov A A, Martynov A A, Poshekhonov Yu Yu, Kim S H, Lister J B, Martin Y R, Sauter O, Villard L and Lang P T Edge Stability and Boundary Shaping in Tokamak 2007 *Proc. 34th EPS Conf. on Plasma Physics (Warsaw, Poland)* vol 31F (ECA) P-4. 078

- [61] Sartori F, Piccolo F, Zedda M K and JET-EFDA contributors Synchronous ELM Pacing at JET using the Vertical Stabilisation 2008 *Proc. 35th EPS Conf. on Plasma Physics (Hersonissos, Greece)* vol 32D (ECA) P-5. 045
- [62] Pereverenzev G V and Yushmanov P N, ASTRA Automated System for TRansport Analysis in a Tokamak 2002 *Report IPP* 5/98
- [63] Gribov Y Engineering limits and other data related to analysis of ITER plasma equilibria, poloidal field scenarios and plasma control 2006 *ITER_D_247JZD*
- [64] Huysmans G T A, Goedbloed J P and Kerner W 1991 *CP90 Conf. on Comp. Physics (Singapore, Word Scientific)* p 371
- [65] Kim S H, Artaud J F, Basiuk V, Khayrutdinov R R, Dokuka V, Lister J B and Lukash V E Combined DINA-CH and CRONOS Simulations of ITER 2005 *Proc. 32nd EPS Conf. on Plasma Physics (Tarragona, Spain)* vol 29C (ECA) P-2.072
- [66] Lukash V E, Artaud J F, Basiuk V, Dokuka V, Khayrutdinov R R, Kim S H and Lister J B Progress on Combined DINA-CH and CRONOS Simulator 2006 *Proc. 33rd EPS Conf. on Plasma Physics (Rome, Italy)* vol 30I (ECA) P-5.150
- [67] Ivanov A A, Khayrutdinov R R, Medvedev S Yu and Poshekhonov Yu Yu New Adaptive Grid Plasma Evolution Code SPIDER 2005 *Proc. 32nd EPS Conf. on Plasma Physics (Tarragona, Spain)* vol 29C (ECA) P-5.063
- [68] Tala T et al Full predictive time-dependent transport simulations of ITB plasmas in JET, JT-60U and DIII-D 2006 *Nucl. Fusion* **46** 548
- [69] Imbeaux F et al Multi-machine transport analysis of hybrid discharge from the ITPA profile database 2005 *Plasma Phys. Control. Fusion* **47** B179
- [70] Litaudon X et al Towards fully non-inductive current drive operation in JET 2002 *Plasma Phys. Control. Fusion* **44** 1057
- [71] Feng Y, Wolle B and Hübner K New, simplified technique for calculating particle source rates due to neutral beam injection into tokamaks 1995 *Comput. Phys. Commun.* **88** 161

- [72] Wolle B, Eriksson L-G, Gerstel U and Sadler G Time-dependent neutron-rate interpretation of neutral-beam-heated tokamak plasmas 1994 *Plasma Phys. Control. Fusion* **36** 1051
- [73] Eriksson L-G, Hellsten T and Willen U Comparison of time dependent simulations with experiments in ion cyclotron heated plasmas 1993 *Nucl. Fusion* **33** 1037
- [74] Imbeaux F and Peysson Y Ray-tracing and Fokker-Planck modelling of the effect of plasma current on the propagation and absorption of lower hybrid waves 2005 *Plasma Phys. Control. Fusion* **47** 2041
- [75] Peysson Y, Decker J and Basiuk V 2007 Simulations of Tore Supra Lower Hybrid Current Drive Experiments *Proc. 34th EPS Conf. on Plasma Physics (Warsaw, Poland)* vol 31F (ECA) P-4.164
- [76] Krivenski V, Fidone I, Giruzzi G, Granata G, Meyer R L and Massucato E Improving current generation in a tokamak by electron cyclotron waves 1985 *Nucl. Fusion* **25** 127
- [77] Schneider M Eriksson L-G, Basiuk V and Imbeaux F On alpha particle effects in tokamaks with a current hole 2005 *Plasma Phys. Control. Fusion* **47** 2087
- [78] Houlberg W A, Shaing K C, Hirshman S P and Zarnstorff M C Bootstrap current and neoclassical transport in tokamaks of arbitrary collisionality and aspect ratio 1997 *Phys. Plasmas* **4** 3230
- [79] Strand P, Nordman H, Weiland J and Christiansen J P Predictive transport simulations of JET L and H mode gyro-radius scaling experiments 1998 *Nucl. Fusion* **38** 545
- [80] Kinsey J E, Staebler G M and Waltz R E Predicting core and edge transport barriers in tokamaks using the GLF23 drift-wave transport model 2005 *Phys. Plasmas* **12** 052503
- [81] Kim S H, Artaud J F, Basiuk V, Dokuka V, Khayrutdinov R R, Lister J B and Lukash V E Full tokamak simulation of ITER scenario 2 using the combined DINA-CH and CRONOS simulator 2008 *Proc. 35th EPS Conf. on Plasma Physics (Hersonissos, Greece)* vol 32D (ECA) O-2.004
- [82] Lukash V E, Gribov Y, Kavin A, Khayrutdinov R R and Cavinato M Simulations of ITER scenarios 2005 *Plasma Devices and Operations* **13** 143

- [83] Kim S H, Artaud J F, Basiuk V, Dokuka V, Khayrutdinov R R, Lister J B and Lukash V E Plasma Current Ramp-up Phase Simulation of ITER 2007 *Proc. 34th EPS Conf. on Plasma Physics (Warsaw, Poland)* vol 31F (ECA) P-5.142
- [84] Gribov Y CS and PF coils data and requirements to separatrix positioning for analysis of ITER plasma equilibria and poloidal field scenarios 2008 *ITER_D_2ACJT3*
- [85] Sips A C C et al Current rise studies at ASDEX Upgrade and JET in preparation for ITER 2008 *Proc. 35th EPS Conf. on Plasma Physics (Hersonissos, Greece)* vol 32D (ECA) O-2.003
- [86] Favez J-Y Enhancing the control of tokamaks via a continuous nonlinear control law 2004 PhD Thesis No. 3034 Ecole Polytechnique Fédérale de Lausanne
- [87] Portone A, Albanese R, Fresa R, Mattei M, Rubinacci G and Villone F Vertical stability of ITER plasmas with 3D passive structures and a double-loop control system 2005 *Fusion Eng. Des.* **74** 537
- [88] Kim S H, Artaud J F, Basiuk V, Bécoulet A, Dokuka V, Hoang G T, Imbeaux F, Khayrutdinov R R, Lister J B and Lukash V E Lower hybrid assisted plasma current ramp-up in ITER 2009 *Plasma Phys. Control. Fusion* **51** 065020
- [89] Shinohara K, Oikawa T, Urano H, Oyama N, Lonroth J, Saibene G, Parail V and Kamada Y Effects of ferromagnetic components on energetic ion confinement in ITER 2009 *Fusion Eng. Des.* **84** 24
- [90] Zwingmann W, Moreau D and Saint-Laurent F Equilibrium reconstruction of tokamak discharges with toroidal variation 2005 *Proc. 32nd EPS Conf. on Plasma Physics (Tarragona, Spain)* vol 29C (ECA) P-2.044
- [91] Hoang G T et al A Lower Hybrid Current Drive system for ITER 2009 *Nucl. Fusion* **49** 175001
- [92] Kessel C E et al Simulation of the hybrid and steady state advanced operating modes in ITER 2007 *Nucl. Fusion* **47** 1274
- [93] Hogeweyj G M D, Imbeaux F, Köchl F, Litaudon X, Parail V and Sips A C C Simulation of the current ramp-up phase of ITER discharges 2008 *Proc. 35th EPS Conf. on Plasma Physics (Hersonissos, Greece)* vol 32D (ECA) P-5.034

- [94] Parail V et al Integrated modelling for ITER in EU 2008 *22nd Int. Conf. on Fusion Energy Conference 2008 (Geneva, Switzerland)* IT/P6-7
- [95] Peysson Y and the Tore Supra team Progress towards high-power lower hybrid current drive in TORE SUPRA 2000 *Plasma Phys. Control. Fusion* **42** B87
- [96] Joffrin E et al The ‘hybrid’ scenario in JET: towards its validation for ITER 2005 *Nucl. Fusion* **45** 626
- [97] Staebler A et al The improved H-mode at ASDEX Upgrade: a candidate for an ITER hybrid scenario 2005 *Nucl. Fusion* **45** 617
- [98] Luce T C et al Stationary high-performance discharges in the DIII-D tokamak 2003 *Nucl. Fusion* **43** 321
- [99] Chu M S et al Maintaining the quasi-steady state central current density profile in hybrid discharges 2007 *Nucl. Fusion* **27** 434
- [100] Casper T A et al Evidence for anomalous effects on the current evolution in the tokamak hybrid operating scenarios 2007 *Nucl. Fusion* **47** 825
- [101] ITER Physics Basis 1999 *Nucl. Fusion* **39** 2204-2206
- [102] McDonald et al The beta scaling of energy confinement in ELMy H-modes in JET 2004 *Plasma Phys. Control. Fusion* **46** A215

Acknowledgments

I would like to thank everyone who has directly contributed to this thesis work.

Foremost, I am deeply grateful to my thesis supervisor, Dr. Jo Lister, for his support and guidance in my work. His experience and knowledge on the plasma physics and controlled fusion were fundamental of this thesis work. He also has been for me a wonderful reference as a husband and father. Many thanks to his wife, Judy Lister, for her support in many ways.

I am very thankful to my colleagues, Drs. J-F. Artaud, V. Basiuk, V. Dokuka, R.R. Khairoutdinov and V.E. Lukash for providing their codes, knowledge and experience. This international collaboration was very successful and for me a wonderful experience.

Many important contributions were provided by Drs. A. Bécoulet, M.M. Cavinato, Y. Gribov, G.T. Hoang, F. Imbeaux, A.A. Ivanov, P.T. Lang and S Yu Medvedev. I wish to thank them for their advices and many encouraging discussions.

I am indebted with many CRPP colleagues. In particular, I would like to thank Drs. O. Sauter, L. Villard, H. Weisen, S. Coda, J-M. Moret, Y.R. Martin and B. Duval for their help and many discussions, Prof. M. Quang Tran and Dr. K. Appert for giving me the opportunity to work in CRPP, and Karim Besseghir, the successor of this project, for his support and contribution.

Finally, I will never thank enough my wife endured painful treatments, and my daughter suffered from the absence of her mother.

This work has been partly supported by the Swiss National Foundation and Euratom.

Curriculum Vitae

Born 18th of October 1976 in Incheon, Republic of Korea

2004-2009 Doctoral student in Physics

Ecole Polytechnique Fédérale de Lausanne (EPFL), Lausanne, Switzerland

2002-2004 Master of Science in Nuclear Engineering

Seoul National University, Seoul, Republic of Korea

1995-2002 Bachelor of Science in Nuclear Engineering

Seoul National University, Seoul, Republic of Korea

Publications

As first author

1. Kim S H and Lister J B Simplifying plasma profile control in ITER 2009 to be submitted to *Plasma Phys. and Control. Fusion*
2. Kim S H, Artaud J F, Basiuk V, Dokuka V, Khayrutdinov R R, Lister J B and Lukash V E Full tokamak discharge simulation of ITER by combining DINA-CH and CRONOS 2009 submitted to *Plasma Phys. and Control. Fusion*
3. Kim S H, Artaud J F, Basiuk V, Bécoulet A, Dokuka V, Hoang G T, Imbeaux F, Khayrutdinov R R, Lister J B and Lukash V E Lower hybrid assisted plasma current ramp-up in ITER 2009 *Plasma Phys. Control. Fusion* **51** 065020
4. Kim S H, Cavinato M M, Dokuka V, Ivanov A A, Khayrutdinov R R, Lang P T, Lister J B, Lukash V E, Martin Y R, Medvedev S Yu and Villard L Comparing magnetic triggering of ELMs in TCV and ASDEX Upgrade 2009 *Plasma Phys. Control. Fusion* **51** 055021
5. Kim S H, Park J M and Hong S H Predictive Numerical Simulations on the Formation of Internal Transport Barrier in the Reversed Shear Regime of KSTAR Tokamak 2005 *Journal of Korean Physical Society* **46** 861

As a co-author

1. Hoang G T et al A Lower Hybrid Current Drive system for ITER 2009 *Nucl. Fusion* **49** 175001
2. Lang P T et al Impact of fast vertical and radial plasma movement on type-I ELMs in ASDEX Upgrade 2006 *Czech. J. Phys.* **56** 1329